Laser Spectroscopic Studies of Plasmas

Samuel D. A. Rogers
Christ Church
University of Oxford

A thesis submitted for the degree of
Doctor of Philosophy
Michaelmas 2022

Spectroscopic Investigations of Plasmas

Samuel D. A. Rogers
Christ Church
University of Oxford

A thesis submitted for the degree of
Doctor of Philosophy

Michaelmas 2022

Abstract

This thesis describes the application of sensitive optical absorption techniques in order to probe inductively coupled plasmas of oxygen and nitrogen. Radio frequency plasmas formed from these simple molecular species have found an increasingly important role in many industrial applications and high resolution spectroscopy provides a means to probe their chemistry with unrivalled specificity and sensitivity. In particular, this work applies the technique of cavity ringdown spectroscopy (CRDS) to detect atomic, ionic and electronically excited molecular species as a function of plasma operating conditions. The plasma probed in this work is created in a low pressure ($10-100$ mTorr) inductively coupled plasma chamber by application of up to 500 W of 13.56 MHz radio frequency power via a 1.5 turn double spiral antenna in a stove top arrangement. The optical cavity utilised in the measurements probes the plasma 120 mm below to top window (which separates the driven coil from the plasma) and 50 mm above the lower, ground electrode. CRDS results are supplemented with observations of plasma emission spectra and comprehensively interpreted by kinetic modelling.

The work is divided into two sections according to the plasma being probed. The first section concerns oxygen plasma with CRDS measurements of $O(^3P)$ and $O_2(a^1\Delta_g)$ utilising forbidden transitions. These measurements reveal dissociation fractions as high as $\approx 15\%$, metastable molecule fractions of $\approx 5\%$ and translation temperatures up to ≈ 450 K. The target species, by virtue of their different threshold energies for electron impact production, provide insight into different regions of the electron energy distribution function (EEDF). As a result, measurements of $O(^3P)$ and $O_2(a^1\Delta_g)$ in combination with a volume averaged kinetic plasma model allow changes in the EEDF to be investigated as the plasma transitions from the E to the H-mode of operation. In addition, aspects of the spectroscopy of $O_2(a^1\Delta_g)$ are

clarified with respect to the appropriate sum rule for Hönl-London factors, necessary in order to properly deduce absolute concentrations.

The volume averaged modelling, although quantitatively useful, does not account for spatial inhomogeneity within the plasma. This inhomogeneity is investigated using measurements of $O_2(X^3\Sigma_g^-)$ in the $v = 0$ and $v = 1$ vibrational states. These observations also elucidate the degree of vibrational excitation within the plasma and reveal a vibrational temperature (amongst the low v states) of $\approx 750 \pm 150$ K at 100 mTorr and 300 W. A 1D model utilising physically reasonable line of sight variation in plasma temperature and composition corroborates the CRDS measurements.

The second section of this thesis concerns nitrogen plasma and focuses on CRD measurements of the molecular cation, $N_2^+(X^2\Sigma_g^+)$, and the electronically excited $N_2(A^3\Sigma_u^+)$ state. These species can be probed using allowed transitions, but due to their low density, the sensitivity enhancement afforded by CRDS is still advantageous. Notably, the use of large intracavity radiation intensities to probe allowed transitions results in optical saturation, the effects of which must be carefully accounted for when determining species temperatures and densities.

With adjustments made for the effects of optical saturation the CRD measurements show ion (and therefore electron) densities of the order of $10^9 - 10^{10}$ cm^{-3} in the plasma bulk (depending on operating conditions) and metastable densities an order of magnitude higher. Interestingly the two species show rather different translational temperatures with the ions typically ≈ 1000 K and the metastables ≈ 600 K. Once again the absolute density measurements are interpreted in terms of a volume averaged kinetic model. The model reveals a limitation in the understanding of nitrogen discharges that has arisen consistently in the literature, namely, the inability to account quantitatively for the density of $N_2(A^3\Sigma_u^+)$ using the literature rate coefficients for the processes typically deemed most important in its production and loss. The possible reasons for the discrepancy are explored in depth.

In addition, spatially resolved measurements of the same nitrogen species are presented, with particular reference to how ion densities change as the edge of the chamber is approached (in regions known as the plasma pre-sheath and sheath). Measurements with a spatial resolution of ≈ 100 μm show that the ion density is reduced by almost an order of magnitude close to the chamber's lower electrode.

Finally, the effects of saturation on the CRD spectra are explored and the possible contributions to the Lamb dip width are discussed in the context of spectral broadening mechanisms. The laser linewidth is measured by a self-heterodyne beat note experiment to be < 100 kHz indicating that it contributes little to the observed Lamb

dip widths (> 100 MHz) and that other processes are dominant. It is concluded that, whilst power broadening plays a significant role in explaining the width of the Lamb dips, the dominant cause of the broadening is unresolved hyperfine structure arising due to the non-zero nuclear spin of ^{14}N.

For my parents, Janis and Andrew
and my grandparents
George, Maud, Mitchell and Maureen.

Acknowledgements

There are many people without whom this thesis would not have been possible. First and foremost, I must thank Grant Ritchie. Grant has not only been a tutor and supervisor to me, but also a hugely inspiring example. Neither of us could have foreseen that, in offering me an undergraduate place at Worcester college nine years ago, he would find himself stuck with me for the best part of a decade, but I hope he agrees that the past 9 years have proved a success! I also owe the most sincere and heartfelt thanks to Rob "Pev" Peverall. Rob's ample supply of both expertise and patience have been vital ingredients in carrying out the work in this thesis and his sense of humour has been a particular highlight of my time in the Ritchie group. Huge thanks must also go to Gus Hancock, whose probing questions (usually delivered with either a thoughtful countenance or a mischievous grin) and encyclopaedic knowledge have aided my understanding of the results presented here a great deal.

On a more personal note, my time in the Ritchie group has been hugely enhanced by the friends I have made. Particular gratitude must be expressed to those with whom I've shared several years in the group. Nick, for his jollity, love of walking around university parks and undying support for Portsmouth F. C. (no matter how far down the league they might slip). Dáire, for her willingness to listen to my complaints about all manner of things and always have a solution. Lorenzo, for his extensive provision of both colomba pasquale and panettone, and his comprehensive knowledge of English grammar. Graham, for his tablet (and assorted baked goods), his sense of humour and for being the world's leading LabVIEW expert. Dom, for his culinary expertise and for putting up with my clutter sometimes spilling onto his desk. John, for his supreme knowledge of fibre-optics, lasers and horticulture.

I have had the good fortune, during my time as a DPhil student, to work with three highly motivated and capable part II students. I must therefore

thank Millie, Ben and Charlie for their investments in their respective part II projects. I flatter myself to think that I may have played a small role in the decisions of all three to pursue doctorates, even if working with me for a year was enough to motivate one of them to flee to Antarctica for their doctoral research!

I have worked with many other people who've passed through the Ritchie group over the last five years and here I mention a few who stick out in my memory for having inspired, entertained or amused me (in no particular order). To An, Katherine, Hamza, Tomas, Colin, Fiona, Ellana, Pippa, Sarah, Evan, Alex, Tom and Scott, thank you!

Away from the Ritchie group, I must thank some of my teachers, in particular, Rachel, Ann, Martin, Mr Miles, Mr Whitehead, Dr Champion and Mr Bailey for their encouragement and patience in teaching me and encouraging me to pursue my interests.

I must also thank my family. Without their support and belief in me this thesis and the work herein would not have been possible. I must thank my brother for setting the bar (sometimes rather too high) and thereby motivating me to strive for success. My grandparents too have been an inspiration to me, placing particular value on education and always doing your best and I feel that they have played an important role in enabling my academic success such that it is. My parents of course deserve extra special thanks for their encouragement which, whether firm or gentle, is and has always been delivered with love.

Finally, to Melly, for putting up with me for so many years, for your belief in me and for your constant reassurance, particularly during the production of this thesis, thank you.

List of publications

- R. Peverall, **S. D. A. Rogers** and G. A. D. Ritchie, "Quantitative measurements of oxygen atom and negative ion densities in a low pressure oxygen plasma by cavity ringdown spectroscopy", *Plasma Sources Science and Technology*, **29**, 045004 (2020), https://doi.org/10.1088/1361-6595/ab7840

- **S. D. A. Rogers**, A. Bond, R. Peverall, G. Hancock, C. M. Western and G. A. D. Ritchie, "Quantitative measurements of singlet molecular oxygen in a low pressure ICP", *Plasma Sources Science and Technology*, **30**, 09LT02 (2021), https://doi.org/10.1088/1361-6595/ac2044

- **S. D. A. Rogers**, A. Bond, B. J. Rhodes, R. Peverall, G. Hancock and G. A. D. Ritchie, "Cavity ringdown studies of the E-H transition in an inductively coupled oxygen plasma: comparison of spectroscopic measurements and modelling", *Plasma Sources Science and Technology*, **31**, 115006 (2022), Plasma Sources Science and Technology, https://doi.org/10.1088/1361-6595/ac9d62

- **S. D. A. Rogers**, A. Bond, R. Peverall, G. Hancock and G. A. D. Ritchie, "Probing spatial inhomogeneity in oxygen plasma using cavity ringdown spectroscopy", *In preparation*

- **S. D. A. Rogers**, C. Kniebe-Evans, B. J. Rhodes, R. Peverall, G. Hancock and G. A. D. Ritchie, "Quantitative measurements of N_2^+ densities and temperatures in low pressure nitrogen plasma by saturated cavity ringdown spectroscopy", *In preparation*

Contents

Part I

Introduction

Chapter 1

Introduction I: The physics, chemistry and industrial application of plasma

Almost a century ago, Irving Langmuir coined the term plasma to refer to a state of matter in which there are significant but equal amounts of positively and negatively charged species[1]. Naturally occurring plasmas were known to humans long before this in the form of lightning, auroras, and flames, and in 1913 it was correctly predicted by Kristian Birkeland that the interstellar medium consists of plasma, a fact that has since been directly verified by the Voyager spacecraft[2]. As well as natural plasma, which makes up 99% of the observable universe, plasma can also be produced artificially, typically by applying an electric field to a gas sample such that some of the sample becomes ionised. Such plasmas are found in several important practical, industrial, and research areas[3,4], including plasma arc welding[5], plasma enhanced chemical vapour deposition (PECVD)[6] important for semiconductor manufacturing, diamond coating technology[7], plasma medicine[8], and nuclear fusion research[9]. Given this huge range of applications, it is no surprise that understanding the fundamental physics and chemistry of various types of plasma has become a highly desirable target for researchers and one in which interest continues to grow. This chapter will first introduce several of the important physical and chemical characteristics common to many different types of plasma. The discussion will then focus on the specifics of low pressure radio frequency driven plasmas confined to a chamber; this type of plasma is of particular importance in the semiconductor industry and studying this type of plasma in oxygen or nitrogen is the focus of this thesis. Finally, the plasma chamber used throughout the work presented in this thesis will be described.

1.1 Defining a plasma

1.1.1 Plasma density

The key property that distinguishes a plasma from a gas is the presence of an abundance of charged species (*i.e.* electrons and ions). By far the most important charged species in plasmas is the electron, and the density (n_e) and temperature (T_e) of the electrons in any given plasma are amongst its most important defining characteristics. When electrons are the only important negatively charged species in a plasma, then the plasma density is equivalent to the electron density (such plasmas are termed electropositive). On the other hand, if negative ions are present in significant quantities, the plasma density usually refers to the total density of electrons and negative ions and will be somewhat higher than the electron density alone (these plasmas are termed electronegative).

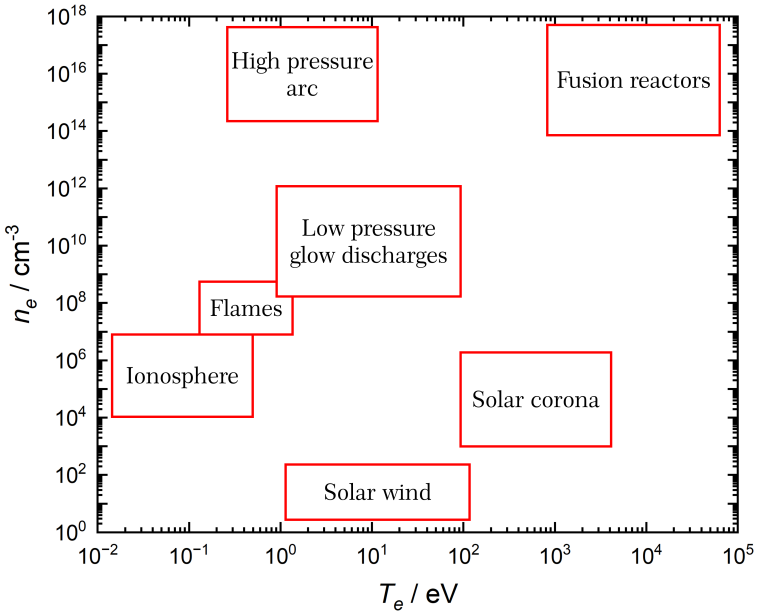

Figure 1.1: Examples of both artificial and naturally occurring plasmas at a wide range of both electron density and temperature.

Plasmas exist with a huge range of electron densities (covering 18 or more orders of magnitude) and temperatures (covering at least 7 orders of magnitude) and examples are shown in figure 1.1. It should be noted that, when discussing plasma, electron

'temperatures' are often expressed in units of electronvolts, even though the electronvolt is in fact a unit of energy. The key points to remember when interpreting information given under this convention are: that the temperature in electronvolts ($T_e(eV)$) can be converted to a real temperature ($T_e(K)$) according to $T_e(K) = T_e(eV)\frac{e}{k_B}$ such that an electron temperature of 1 eV corresponds to ≈ 11600 K and; that the mean energy of the electrons (in Joules) is $\frac{3e}{2}T_e(eV)$ (taking a value of 2.85×10^{-16} J for $T_e(eV) = 1$). Amongst the plasmas in figure 1.1 there is also a diverse degree of ionisation, from fusion plasmas with a degree of ionisation of ≈ 1 to low pressure glow discharges which are industrially important and typically have a degree of ionisation of $\approx 10^{-4} - 10^{-7}$.

1.1.2 Quasi-neutrality and the Debye length

From Langmuir's definition, a plasma must contain an equal amount of positive and negative charge. This requirement for the bulk plasma is encapsulated in the quasi-neutrality condition which may be expressed as:

$$n_e + \sum_i |z_i| n_i^- = \sum_j |z_j| n_j^+, \tag{1.1}$$

where z_i is the charge of the i^{th} ion and n^- and n^+ refer to the negative and positive ion densities respectively. In the plasmas discussed in this thesis, all the ions of importance are singly charged and thus for electronegative plasma the condition can be written

$$n_e + \sum_i n_i^- = \sum_j n_j^+, \tag{1.2}$$

and for electropositive plasmas

$$n_e = \sum_j n_j^+. \tag{1.3}$$

If one chooses a very small volume of plasma it could conceivably contain an ion but no electrons (or visa versa) and thus at this small scale the plasma is not neutral. The length scale over which quasi-neutrality is invalid can be approximated by considering a negatively charged surface within the plasma. Such a surface will have a negative potential, Φ_0, which will exert a repulsive force on the nearby electrons and an attractive force on nearby ions. These forces will alter the density of electrons and ions close to the surface. The depletion of the highly mobile and low mass electrons will be much more significant than the increase of the heavier and less mobile ions, thus to a first approximation the change in ion density can be ignored. The change in

electron density will vary with the local potential, $\Phi(x)$, according to the Boltzmann equation:

$$n_e(x) = n_0 \exp \frac{\Phi(x)}{T_e}, \tag{1.4}$$

where n_0 is the density of electrons (and ions) far from the surface, x is the distance from the surface ($x > 0$), and T_e is in eV. The variation of the potential, $\Phi(x)$, as a function of position in the presence of a charge distribution (of electrons and ions) is given by the Poisson equation which can be written:

$$\frac{\mathrm{d}^2\Phi(x)}{\mathrm{d}x^2} = -\frac{e}{\epsilon_0}(n_i(x) - n_e(x)), \tag{1.5}$$

where e is the elementary charge. Combining equations 1.4 and 1.5 and assuming immobile ions ($n_i(x) = n_0$) yields

$$\frac{\mathrm{d}^2\Phi(x)}{\mathrm{d}x^2} = \frac{en_0}{\epsilon_0}\left(\exp \frac{\Phi(x)}{T_e} - 1\right) \approx \frac{en_0}{\epsilon_0}\frac{\Phi(x)}{T_e}, \tag{1.6}$$

where the approximation utilises the Taylor expansion assuming that $\Phi(x) << T_e$. The relevant solution to this equation, with the boundary conditions $\Phi(0) = \Phi_0$ and $\Phi(\infty) = 0$, is

$$\Phi(x) = \Phi_0 \exp\left(-\left(\frac{en_0}{\epsilon_0 T_e}\right)^{\frac{1}{2}} x\right). \tag{1.7}$$

Thus the potential of the surface is effectively shielded such that the potential experienced by electrons and ions drops off exponentially with distance from the surface. The characteristic length of this decay is known as the Debye length, λ_D, defined as

$$\lambda_D = \left(\frac{\epsilon_0 T_e}{en_0}\right)^{\frac{1}{2}}. \tag{1.8}$$

Thus, within a volume of the order of λ_D^3, the densities of ions and electrons can be different and quasi-neutrality may break down but on larger scales, plasma meets the quasi-neutrality condition. For low pressure discharges of the type investigated in this thesis, the Debye length typically around 0.1 mm

1.1.3 Equilibrium and temperature

Broadly speaking, laboratory plasmas can be divided into two categories, those that are in thermal equilibrium and those that are not. In particular, electrons and atoms (or molecules) can exhibit different temperatures within the plasma, as can different molecular degrees of freedom. By definition, in a non-equilibrium system the

temperature is poorly defined. In laboratory plasmas it is usually possible to assign well-defined rotational and translational temperatures, the vibrational energy distribution on the other hand can be significantly non-Boltzmann (see for example the Treanor distribution[10]) and thus a single temperature can only approximately describe such a population.

When a plasma is generated by the application of an electric field the vast majority of the energy that enters the plasma does so through acceleration of the highly mobile electrons. The energy gained by these electrons can be transferred to atoms and molecules (referred to as *heavy species*) by various collisional processes causing excitation, dissociation, secondary ionisation, and Joule or Ohmic heating[3]. With strong enough fields and/or low pressures, the electrons can gain a relatively high energy from the applied field, driving the electron temperatures to be much higher than the temperatures of the heavy species[4].

The inherent disequilibrium in driven plasmas can also result in a marked disequilibrium between the various degrees of freedom of molecules. This arises because of the sometimes pronounced differences in the efficiency of inelastic collisions to excite different molecular degrees of freedom combined with the disparate rates of energy transfer in molecular collisions. In particular, whilst electron impact vibrational excitation can be quite efficient, the vastly different masses of electrons and heavy species mean that electron impact processes are extremely inefficient at transferring translational energy to heavy species. Much of the translation heating in such plasma happens by V-T energy transfer from the vibrational modes of the molecules, and when the collision frequency is low, the rate of this transfer is insufficient to allow translational and vibrational degrees of freedom to attain thermal equilibrium. Translational and rotational degrees of freedom tend to exchange energy much more efficiently and hence these degrees of freedom tend to be in equilibrium and much closer to ambient temperatures. Thus in non-equilibrium plasma it is normally expected that $T_e > T_v > T_r \approx T_i \approx T_g$ where the temperatures, in descending order, describe the energy of electrons, vibrational motion, rotational motion, (bulk) ion, and neutral translational motions.

1.1.4 The EEDF

Electron impact (EI) processes are of particular importance to the chemistry of laboratory plasmas. The rates of EI processes are intrinsically linked to the energy distribution of the electrons (and hence the electron temperature). In the simplest

and most widely used approximation, only the elastic electron collisions are considered, and the resulting equilibrium distribution of electron energies, as described by the electron energy distribution function (EEDF), $f(E)$, is given by a (normalised) Maxwellian:

$$f(E)\mathrm{d}E = \frac{2\sqrt{E}}{\sqrt{\pi}(k_B T_e)^{\frac{3}{2}}} \exp\left(\frac{-E}{k_B T_e}\right) \mathrm{d}E, \tag{1.9}$$

where all the values are in SI units (*i.e.* T_e is expressed in Kelvin). The Maxwellian distribution has an average energy $\langle E \rangle$ equal to $\frac{3}{2}k_B T_e$ (or $\frac{3}{2}eT_e$ if T_e is expressed in eV). Because the Maxwellian is the most fundamental form of the EEDF, it is often desirable to see how the real distribution of electron energies deviates from this ideal case, and therefore it is convenient to define an electron energy probability function (EEPF), $g(E)$, as:

$$g(E) = \frac{f(E)}{\sqrt{E}}, \tag{1.10}$$

such that a plot of the logarithm of the EEPF produces a straight line for a Maxwellian distribution. Maxwellian EEDFs and EEPFs are displayed in figure 1.2 for a range of electron temperatures.

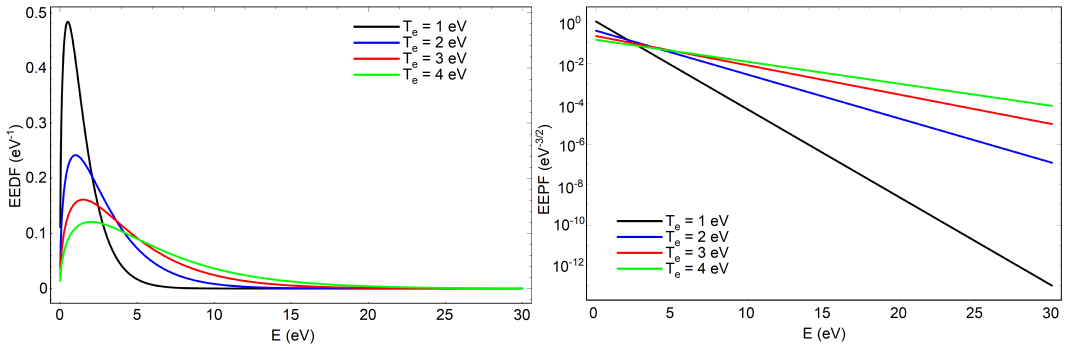

(a) **(b)**

Figure 1.2: (a) Maxwellian electron energy distribution functions (EEDFs) for several electron temperatures. (b) Maxwellian electron energy probability functions (EEPFs) for a range of electron temperatures, note that a Maxwellian EEPF is linear.

Clearly, if electrons are able to drive energetic chemistry via their collisions, then the assumption that they only undergo elastic collisions isn't perfect. In real plasma, therefore, the EEDF can deviate from the ideal case. The most common deviation is a depletion in high energy electrons because these are the electrons that have sufficient energy to engage in the most inelastic processes. A more general form of the EEDF in such cases was given by Gudmundsson[11] as

$$f(E)\mathrm{d}E = c_1\sqrt{E}\exp(-c_2 E^x)\mathrm{d}E, \tag{1.11}$$

with

$$c_1 = \frac{x}{\langle E \rangle^{\frac{3}{2}}} \frac{\left[\Gamma\left(\frac{5}{2x}\right)\right]^{\frac{3}{2}}}{\left[\Gamma\left(\frac{3}{2x}\right)\right]^{\frac{5}{2}}} \quad \text{and} \quad c_2 = \frac{1}{\langle E \rangle^x} \left[\frac{\Gamma\left(\frac{5}{2x}\right)}{\Gamma\left(\frac{3}{2x}\right)}\right]^x, \tag{1.12}$$

and the gamma function, $\Gamma(z)$, defined as

$$\Gamma(z) = \int_0^\infty t^{z-1} \exp(-t) \mathrm{d}t. \tag{1.13}$$

In the special case when $x = 1$, equation 1.11 gives the Maxwellian distribution and in the case when $x = 2$, the resulting EEDF is referred to as a Druyvesteyn distribution which is a commonly used non-ideal EEDF showing a depletion of high energy electrons compared to a Maxwellian with the same average energy. When $x \neq 1$ the electron temperature is ill defined, nevertheless an effective temperature is often reported, defined in terms of the mean electron energy according to $T_e(\mathrm{K}) = \frac{2}{3k_B}\langle E \rangle$ (or $T_e(eV) = \frac{2}{3e}\langle E \rangle$). Several EEDFs and EEPFs ranging from Maxwellian to Druyvesteyn are shown in figure 1.3 all with effective electron temperatures of 1 eV and showing clearly the depletion in high energy electrons for the Druvesteyn distribution in comparison to the Maxwellian.

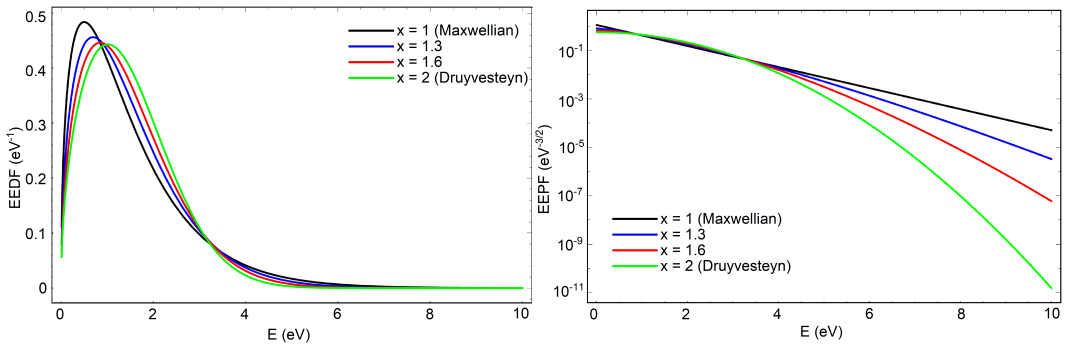

(a) **(b)**

Figure 1.3: (a) EEDFs ranging from Maxwellian to Druyvesteyn. Each EEDF has a mean electron energy of 1.5 eV corresponding to an effective temperature of 1 eV. (b) EEDFs ranging from Maxwellian to Druyvesteyn illustrating the deviation of the EEPF from linearity in the non-Maxwellian cases.

Even more generally the behaviour of electrons in a plasma can be described by a distribution function, $\mathscr{F}(\mathbf{r}, \mathbf{v}, t)$, which exists in a six-dimensional phase space (three position components and three velocity components) such that $\mathscr{F}(\mathbf{r}, \mathbf{v}, t)\mathrm{d}x\mathrm{d}y\mathrm{d}z\mathrm{d}v_x\mathrm{d}v_y\mathrm{d}v_z$ is the number of electrons within the 6D phase volume $(\mathrm{d}x\mathrm{d}y\mathrm{d}z\mathrm{d}v_x\mathrm{d}v_y\mathrm{d}v_z)$ at time t.

The evolution of $\mathscr{F}(\mathbf{r}, \mathbf{v}, t)$ is then described by the Boltzmann equation[3]:

$$\frac{\mathrm{d}\mathscr{F}}{\mathrm{d}t} = -\mathbf{v} \cdot \nabla_{\mathbf{r}}\mathscr{F} - \frac{\mathbf{F}}{m} \cdot \nabla_{\mathbf{v}}\mathscr{F} + \left.\frac{\mathrm{d}\mathscr{F}}{\mathrm{d}t}\right|_{coll}, \tag{1.14}$$

where the first term on the right hand side accounts for the changes in $\mathscr{F}$ with position (*i.e.* diffusion), the second term accounts for the effect of externally applied forces (F), and the third term accounts for changes due to collisional processes. The process of solving the Boltzmann equation requires simplifying assumptions. The approximation most often used in the context of plasma electrons is the two-term approximation whereby the distribution $\mathscr{F}$ is assumed to be nearly spherically symmetric[12]. In this case the distribution may be expanded in terms of spherical harmonics and the expansion truncated after two terms. Combined with knowledge of the collision cross sections for the relevant inelastic processes (which contribute to the third term on the right of equation 1.14) involving the electrons in a specific plasma this approximation can allow real EEDFs to be approximated.

The EEDF is particularly important for describing the plasma chemistry because the rates of electron impact processes depend implicitly on the energies of the electrons involved. The rate coefficient, k_r, for a given EI process can be calculated according to[4]:

$$k_r = \sqrt{\frac{2}{m_e}} \int_0^\infty \sqrt{E}\sigma(E)f(E)\mathrm{d}E, \tag{1.15}$$

where $\sigma(E)$ is the electron energy dependent cross section for the inelastic process.

1.1.5 Plasma chemistry

In industrially important plasmas used for surface processing (like the ones studied in this thesis), the chemistry is invariably driven by electron impact processes[4] (whose rates can be found by equation 1.15). In particular, in a laboratory plasma formed from a feedstock of diatomic molecules (X_2), a typical electron temperature of around 1-3 eV provides a sufficient population of high energy electrons ($E > 10$ eV) to cause *electron impact ionisation* (R1), electronic or vibrational *excitation* (R2) and *dissociation* (R3):

$$e^- + X_2 \longrightarrow e^- + X_2^+ \tag{R1}$$

$$e^- + X_2 \longrightarrow e^- + X_2^* \tag{R2}$$

$$e^- + X_2 \longrightarrow e^- + 2\,X. \tag{R3}$$

Electrons may also form atomic ions directly from diatomic molecules by the processes of *dissociative attachment* (R4) and *dissociative ionisation* (R5)

$$e^- + X_2 \longrightarrow X + X^- \tag{R4}$$

$$e^- + X_2 \longrightarrow 2\,e^- + X + X^+. \tag{R5}$$

The atoms produced in processes R3, R4 and R5 may be created in an electronically excited state or become excited or ionised by further electron impact processes. Finally electrons can also destroy the ions that they create. For positive ions this happens by *recombination* (R6), a process usually requiring a third body and thus only important at high pressures (radiative recombination being inefficient compared with recombination taking place at pressures pertinent to industrial processing), or by *dissociative recombination* (R7) which can be important at all pressures. Meanwhile *electron impact detachment* (R8) can be important for the loss of negative ions.

$$e^- + {X_2}^+ + M \longrightarrow X_2 + M \tag{R6}$$

$$e^- + {X_2}^+ \longrightarrow 2\,X \tag{R7}$$

$$e^- + X^- \longrightarrow 2\,e^- + X. \tag{R8}$$

Although electron impact processes are the most important factor in producing reactive species inside a plasma, the species that are produced can undergo a vast array of subsequent reactions that do not involve free electrons. Amongst the most important of these reactions are *charge transfer* (R9), *ion-ion recombination* (R10), *associative detachment* (R11), *quenching* of excited states (R12) and energy *pooling* (both vibrational and electronic) (R13).

$${X_2}^+ + X \longrightarrow X_2 + X^+ \tag{R9}$$

$${X_2}^+ + X^- \longrightarrow X_2 + X \tag{R10}$$

$$X^- + X \longrightarrow e^- + X_2 \tag{R11}$$

$${X_2}^* + X \longrightarrow X_2 + X \tag{R12}$$

$${X_2}^* + {X_2}^* \longrightarrow {X_2}^{**} + X_2. \tag{R13}$$

Notably, the multitude of chemical pathways mentioned here can be accessed without the need to significantly heat the bulk gas[4]. In this way, high energy species, that can engage in useful chemistry, can be produced with a much smaller energy input than would be required to generate them thermally[4]. This makes non equilibrium plasma potentially useful in achieving industrial scale chemical transformations whilst reducing the energetic cost.

1.1.6 The plasma sheath

When a plasma is confined to a chamber it necessarily interacts with the chamber walls. The result of this interaction is the formation of a plasma sheath, a region characterised by a breakdown of quasi-neutrality and visible in some plasmas as a dark space, from which little or no optical emission can be observed, close to the chamber walls. The reason for the formation of a sheath can be established through a similar thought experiment as was utilised in the context of Debye shielding (section 1.1.2).

Suppose an uncharged conducting surface is introduced into a plasma which, for the sake of simplicity, consists only of neutral species, electrons and singly charged cations. This surface will gain positive charge from the flux of ions, j_i, incident upon it and also gain negative charge from the flux of electrons, j_e. Kinetically the two initial fluxes to the surface can be expressed as:

$$j_i = \frac{1}{4} n_i \bar{v_i} \quad \text{and} \quad j_e = \frac{1}{4} n_e \bar{v_e}, \tag{1.29}$$

where $\bar{v_i}$ and $\bar{v_e}$ are the mean speeds of the ions and electrons respectively (given by kinetic theory for species j as $\bar{v}_j = \left(\frac{8k_B T_j}{\pi m_j}\right)^{\frac{1}{2}}$). For the types of non-equilibrium plasma investigated in this thesis, ion temperatures are typically of the order of 500 K, corresponding to mean velocities of the order of 1000 ms^{-1} (exact values depend on the ion mass), whilst electron temperatures are typically 2 eV (≈20,000 K) corresponding to mean velocities of the order of 10^6 ms^{-1}. The flux of electrons to the surface is therefore initially much greater than the flux of ions due to their higher mobility. As a result, the surface begins to become negatively charged such that low energy electrons are repelled and ions are attracted to the surface. Eventually, sufficient charge builds up such that $j_i = j_e$ and the surface reaches a constant negative potential, V_f, referred to as the *floating potential*. If the difference between this floating potential, V_f, and the potential in the plasma bulk, V_p, is greater than a few T_e (in eV), then the plasma acts as a potential well that can contain the majority of electrons.

The rapidly falling potential near the chamber walls leads to a repulsion (and thus absence) of electrons from the sheath, whilst the acceleration of the ions towards the wall leads to a decrease in their density across the sheath. Overall this means that the plasma sheath has an excess of positive charge and quasi-neutrality breaks down. The ion acceleration across the sheath is a major factor in plasma's ability to process surfaces and by applying a bias potential to the substrate being processed the ion acceleration (and thus the rate of etching for example) can be carefully controlled.

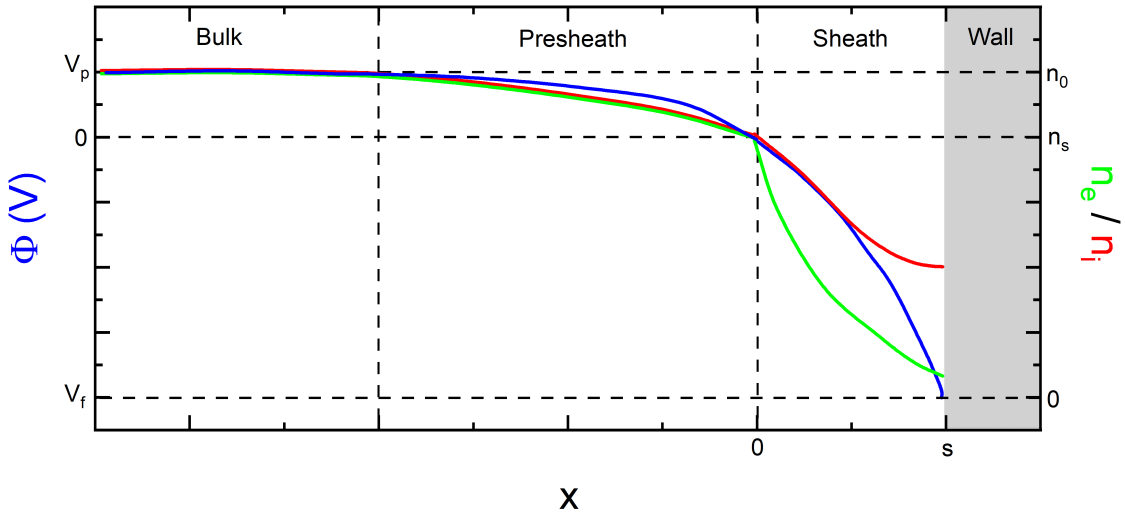

Figure 1.4: A schematic of the variation of electron density (green), ion density (red) and potential (blue) as the wall of a plasma chamber is approached showing the bulk of the plasma, the presheath and the sheath.

A sketch of the potentials and densities as a function of position within the sheath is shown in figure 1.4, note that the origin ($x = 0$) is defined as the point where the sheath and the plasma meet and that this point is also defined as having zero potential ($\Phi(0) = 0$) such that V_p is positive and V_f negative.

If several simplifying assumptions are applied, namely that electrons obey a Maxwellian EEDF, that ions are cold ($T_i = 0$ K) before being launched into the sheath, and that quasi-neutrality holds at the sheath edge ($n_{i,s} = n_{e,s}$ where the subscript s refers to the value at the plasma sheath interface), then the velocity of ions as they traverse the sheath is described by:

$$\frac{1}{2}m_i v_i(x)^2 = \frac{1}{2}m_i v_{i,s}^2 - e\Phi(x), \tag{1.30}$$

where $v_{i,s} = v_i(0)$ is the velocity with which ions are launched into the sheath, and the potential $\Phi(x)$ is negative for positive x such that the ion velocities increase through the sheath. If the sheath is also assumed to be collisionless, such that no ions are created or destroyed as they traverse the sheath and by definition there are no velocity changing collisions, then it can be assumed that the flux of ions is constant for all positions x within the sheath:

$$n_i(x)v_i(x) = n_{i,s}v_{i,s}. \tag{1.31}$$

Combining equations 1.30 and 1.31 yields an expression for the variation of ion density within the sheath:

$$n_i(x) = n_{i,s}\left(1 - \frac{2e\Phi(x)}{m_i v_{i,s}^2}\right)^{-\frac{1}{2}}, \tag{1.32}$$

whilst the variation of the electron density is dictated by a modified form of the Boltzmann relation (1.4):

$$n_e(x) = n_{e,s} \exp \frac{\Phi(x)}{T_e}. \tag{1.33}$$

Inserting the spatial dependences of the ion and electron densities into Poisson's equation (1.5) and noting that $n_{i,s} = n_{e,s} = n_s$ by quasi-neutrality yields:

$$\frac{\mathrm{d}^2\Phi(x)}{\mathrm{d}x^2} = \frac{en_s}{\epsilon_0}\left(\exp\frac{\Phi(x)}{T_e} - \left(1 - \frac{2e\Phi(x)}{m_i v_{i,s}^2}\right)^{-\frac{1}{2}}\right). \tag{1.34}$$

Stable solutions to this formulation of Poisson's equation are found only to exist when:

$$v_{i,s} \geq \sqrt{\frac{eT_e}{m_i}}. \tag{1.35}$$

Equation 1.35 is known as the *Bohm sheath criterion* and it requires that, for a sheath to be stable, ions must enter with a velocity not less than the Bohm velocity $v_B = \sqrt{\frac{eT_e}{m_i}}$. If the ions enter the sheath with velocities below the Bohm velocity, then the flux of ions to the wall will be less than the flux of electrons (hence the dependence of the Bohm criterion on electron temperature) and thus the wall potential will not be stable and the sheath will grow. To attain the Bohm velocity in this simple model, an ion must be accelerated across a potential equivalent to $T_e/2$ and thus the potential at the sheath edge must already have deviated by $T_e/2$ away from the bulk plasma potential. This leads to the concept of the presheath, a region between the true bulk and the plasma sheath in which quasi-neutrality is still approximately valid and where ions are accelerated such that they obtain the Bohm velocity before entering the sheath.

Figure 1.4 depicts the sheath, presheath and the plasma bulk. It should be noted that while this formulation in which the plasma is divided into the sheath, presheath and bulk is more or less arbitrary, it provides a framework within which one can understand the behaviour of plasmas that are confined to a chamber. Real plasmas have a quasi-neutral bulk which transitions gradually to a region near the wall in which there is an excess of positive charge. This change occurs in a continuous manner and not by two discrete steps as the sheath/presheath model might imply. Nevertheless the idea of defining a sheath edge (often defined by use of the Bohm criterion) can

still be useful in describing the behaviour of a given plasma. Within this simple model it is possible to find the expected energy of ions incident upon the floating surface. The ions first undergo an acceleration up to the Bohm velocity, which gives them an energy (directed towards the chamber wall) of $eT_e/2$, after which they are accelerated through the sheath. Equating the ion and electron fluxes at the chamber wall (which must be equal because a floating wall cannot draw any net current) allows the floating wall potential V_f to be determined as[3]:

$$V_f = -\frac{T_e}{2} \ln \frac{m_i}{2\pi m_e}. \tag{1.36}$$

Thus the total energy with which these ions strike the wall is given by the sum of the energy with which they enter the sheath ($\frac{T_e}{2}$) and the energy they gain accelerating across the sheath:

$$E_{ion} = e(V_p - V_f) = \frac{eT_e}{2} \left(\ln \frac{m_i}{2\pi m_e} + 1 \right). \tag{1.37}$$

And in a nitrogen plasma it is expected that a collisionless sheath next to a floating wall will accelerate diatomic cations to energies of $\approx 5eT_e$.

1.1.7 High-voltage sheaths

In industrial surface processing plasma applications it is often desirable to have control over the energies of the ions incident upon the surface. In particular, in semiconductor etching applications, the anisotropy of the etch is limited by the directional uniformity of the incident ions and can generally be improved by accelerating the ions across a large sheath voltage. To this end, many industrial plasma etching chambers mount the wafers which are being processed on a surface that can be supplied with a bias voltage (either radio-frequency (rf) or direct current (DC)) and this has a profound effect on the plasma sheath, modifying V_f and mitigating excessive charge build-up on the wafer.

DC sheath

If one supposes that a large constant negative voltage is applied to the wall, V_{DC}, such that $|e\Phi(x)| >> |\frac{1}{2} m_i v_B^2|$ throughout the sheath then equation 1.32 (with $v_{i,s} = v_B$) can be written as

$$n_i(x) = n_{i,s} v_B \left(-\frac{2e\Phi(x)}{m_i} \right)^{-\frac{1}{2}}, \tag{1.38}$$

whilst the electron density in the sheath is so small that it can be neglected ($n_e(x) \approx 0$). The Poisson equation thus becomes:

$$\frac{\mathrm{d}^2\Phi(x)}{\mathrm{d}x^2} = -\frac{en_{i,s}v_B}{\epsilon_0}\left(-\frac{2e\Phi(x)}{m_i}\right)^{-\frac{1}{2}}, \tag{1.39}$$

which can be solved with appropriate boundary conditions (see for example Lieberman and Lichtenberg[3]) to give:

$$\Phi(x) = -|V_{\mathrm{DC}}|\left(\frac{x}{s}\right)^{\frac{4}{3}}, \tag{1.40}$$

where s is the sheath thickness given by:

$$s = \frac{\sqrt{2}}{3}\lambda_{D,s}\left(\frac{2|V_{\mathrm{DC}}|}{T_e}\right)^{\frac{3}{4}}, \tag{1.41}$$

and $\lambda_{D,s}$ is the Debye length at the sheath edge ($\lambda_{D,s} = \left(\frac{\epsilon_0 T_e}{en_{e,s}}\right)^{\frac{1}{2}}$). This also allows the ion density as a function of position in the sheath to be expressed as

$$n_i(x) = \frac{4}{9}\frac{\epsilon_0}{e}\frac{|V_{\mathrm{DC}}|}{s^2}\left(\frac{x}{s}\right)^{-\frac{2}{3}}, \tag{1.42}$$

and is the well known Child's law plasma sheath (or Child-Langmuir sheath)[3,13,14]. Figure 1.5a shows the variation of sheath thickness, s, as a function of $|V_{DC}|$ for a plasma with $T_e = 2$ eV and $n_{e,s} = 10^9$ and 10^{10} cm^{-3} whilst figure 1.5b shows the variation in potential and ion density as a function of position in a DC Child's law sheath with $T_e = 2$ eV, $n_{e,s} = 10^{10}$ cm^{-3} and $V_{\mathrm{DC}} = -250$ V.

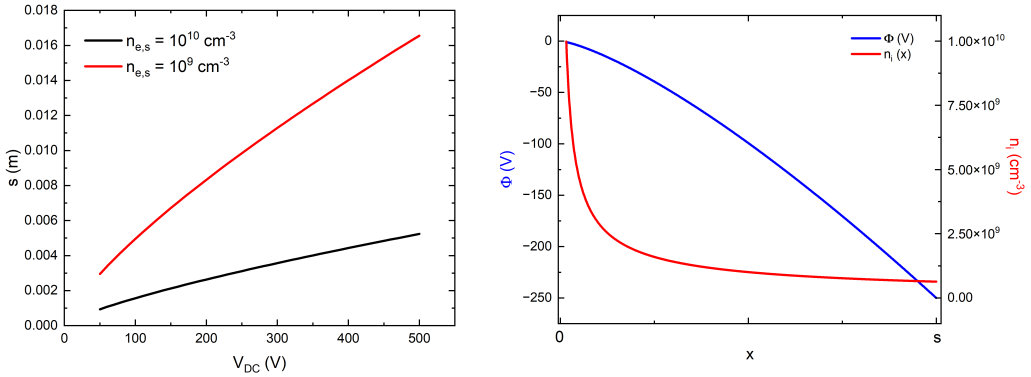

(a) **(b)**

Figure 1.5: (a) The variation of sheath thickness with DC voltage for a sheath described by the Child-Langmuir law. Also shown is how sheath thickness varies with the electron density at the sheath edge. (b) The variation of ion density and potential in a Child-Langmuir sheath. Note that electron density is not shown because the Child-Langmuir sheath model assumes that electrons are entirely absent from the sheath.

rf sheath

The sheath that forms next to an electrode biased with a rf potential is significantly more complicated than a DC sheath. This complexity arises chiefly because both the electrons and ions respond to the time varying voltage. Both electrons and ions in a plasma have characteristic plasma frequencies, given by:

$$\omega_e = \sqrt{\frac{e^2 n_e}{\epsilon_0 m_e}} \quad \text{and} \quad \omega_i = \sqrt{\frac{q_i^2 n_i}{\epsilon_0 m_i}}, \tag{1.43}$$

where q_j is the charge and n_j is the density of species j. It should be noted that, with the above definition, the Debye length can be written as

$$\lambda_D = \left(\frac{\epsilon_0 T_e}{e n_e}\right)^{\frac{1}{2}} = \frac{v_e}{\omega_e}, \tag{1.44}$$

where v_e is the electron thermal speed in one dimension defined as $v_e = \sqrt{\frac{eT_e}{m_e}}$. In other words the Debye length is defined by the speed with which electrons travel and their ability to respond to an electromagnetic field.

If the plasma frequencies (equation 1.43) exceed the plasma driving frequency then the species in question is able to respond virtually instantaneously to the oscillating rf potential. This is invariably the case for electrons in industrial plasma (when $n_e = 10^{10}$ cm^{-3} $\omega_e \approx 5$ GHz $>> \omega_{\text{rf}}$) where radio frequencies of 13.56 MHz are usually used to avoid interference with radio frequency telecommunications ($\omega_{\text{rf}} = 2\pi \times 13.56 = 85.2$ MHz). This means that the electron sheath thickness varies as a function of phase angle within the rf cycle, and the rapidly varying electron sheath is a significant source of plasma heating known as stochastic heating[3]. On the other hand, ions often have a plasma frequency less than or comparable to the driving frequency (for example when $n_i = 10^{10}$ cm^{-3} for N_2^+ cations $\omega_i \approx 25$ MHz) and the ions are not able to respond instantaneously to the applied potential but will instead exhibit time averaged behaviour, with the ion sheath being either entirely static or varying only slightly with the rf field depending on the size of $\omega_i/\omega_{\text{rf}}$. The different abilities of the ions and electrons to respond to the plasma field is the origin of the disequilibirium between electrons and ions within non-equilibrium plasmas. In a plasma where electrons may respond to the rf field instantaneously but ions cannot, the ion current to the surface is expected to be constant whilst the electron current will vary; over one rf cycle however, the net current drawn by a floating wall should be zero.

The rf biasing is usually applied to the substrate electrode via a blocking capacitor which prevents DC whilst allowing AC power to be transmitted from the power supply to the electrode. As a result, a self-bias builds up on the electrode which, even if the ions see only an averaged field, is sufficient to accelerate ions entering the sheath to high velocities. Thus the potential drop across the sheath can be approximated as

$$V(t) = V_{\mathrm{DC}} + V_{\mathrm{rf}} \sin(\omega_{\mathrm{rf}} t), \tag{1.45}$$

where V_{DC} is the self-bias potential (which will be negative) and V_{rf} is the amplitude of the applied rf potential. In the limit where $\omega_i/\omega_{rf} << 1$ and the ions don't respond to the rf field, then the effective potential experienced by ions crossing the sheath is simply V_{DC} which can be found by equating the time averaged ion and electron fluxes to give[3,15,16]:

$$V_{\mathrm{DC}} = -V_{\mathrm{rf}} - \frac{T_e}{2}\left(\ln\frac{m_i}{2\pi m_e} - \ln\frac{2\pi V_{\mathrm{rf}}}{T_e}\right), \tag{1.46}$$

and thus in the limit of high rf voltage $V_{\mathrm{DC}} \approx -V_{\mathrm{rf}}$. Note that in equation 1.46 the first term within the bracket is the same term that arose for a floating wall due to the different temperatures and mobilities of ions and electrons[3]. Still working within the limit of $\omega_i/\omega_{rf} << 1$, the ion sheath thickness next to an rf driven electrode can be expressed by an adjusted Child-Langmuir sheath according to[3]:

$$s = \frac{10\sqrt{3}}{27}\lambda_{D,s}\left(\frac{2|V_{\mathrm{DC}}|}{T_e}\right)^{\frac{3}{4}}. \tag{1.47}$$

The rf case shows a sheath that is ≈ 1.36 times thicker than the DC sheath for the same voltage as a result of the reduced space charge within the sheath caused by the non-zero electron density present for some of the rf cycle. In the case when the ions can respond to the rf potential (*i.e.* $\omega_i/\omega_{rf} >> 1$), the ion sheath will change thickness through the rf cycle and when the ions can only partially respond (*i.e.* $\omega_i/\omega_{rf} \approx 1$), then their motion can be described by an effective potential that is a damped version of equation 1.45[17].

Collisional sheaths

All of the above discussion regarding both DC and rf sheaths assumes a collisionless sheath (*i.e.* the sheath thickness is less than the ion mean free path such that ions traverse the sheath without undergoing collision). Such sheaths exist in low pressure plasmas (typically a few mTorr), but it is likely that some of the conditions studied in this thesis (up to 100 mTorr) will have weakly collisional sheaths. When sheaths

are collisional, the Child-Langmuir description no longer holds. However, there are two limiting cases of the highly collisional sheath for which power law solutions exist, similar to those discussed above for the Child-Langmuir case[3,16]. These are the so called Mott-Gurney sheath (whose name arises because of its origin in semiconductor physics), which assumes a constant ion mobility through the sheath (μ_i), and the Warren sheath, which assumes a constant ion mean free path through the sheath (λ_i). The power law solutions for the different types of sheath are summarised in table 1.1.

Table 1.1: The dependence of sheath potential on distance from the chamber wall and of sheath thickness on sheath voltage drop for the collisionless Child-Langmuir sheath and the collisional Mott-Gurney and Warren sheaths.

Sheath Model	$\Phi \propto$	$s \propto$
Child-Langmuir[13,14]	$x^{\frac{4}{3}}$	$\lvert V_{\mathrm{DC}}\rvert^{\frac{3}{4}}$
Mott-Gurney[18]	$x^{\frac{3}{2}}$	$\lvert V_{\mathrm{DC}}\rvert^{\frac{2}{3}}\mu_i^{\frac{1}{3}}$
Warren[19]	$x^{\frac{5}{3}}$	$\lvert V_{\mathrm{DC}}\rvert^{\frac{3}{5}}\lambda_i^{\frac{1}{5}}$

Recently several efforts have been made to link the collisionless and collisional sheath limits, in particular, the work of Benilov[20] bridged the gap between Child-Langmuir and Mott-Gurney type behaviour, whilst the work of Naggary *et al.*[21] did the same for the Child-Langmuir and Warren cases. Whichever collisional model is used, it is found that, as pressure increases, the plasma sheath decreases in thickness as collisions become increasingly important, concomitant with a reduction in the mobility/mean free path. This has been observed experimentally (see for example Mutsukura *et al.*[22] who made measurements in H_2, N_2 and Ar CCPs by observing spatially resolved optical emission and making electrical probe measurements (see later) and Schleitzer *et al.*[23] who used the force acting on a charged optically-trapped microparticle as it moves through the electric field associated with the plasma sheath to quantify the sheath thickness of an argon CCP.

1.1.8 Langmuir probes

Spectroscopic studies of plasma are the focus of this thesis but it is important to remember that their are diagnostic techniques other than spectroscopy. The interactions of charged species in plasmas with surfaces are not only important for sheath formation, they also form the basis of one of the most important and widely used non-spectroscopic plasma diagnostic techniques, the Langmuir probe[3,24–32]. Use of

such a probe involves the introduction of a conducting electrode into the plasma, which is then biased in order to obtain information about the flux of charged species. Naturally the flux of electrons and ions is controlled by the sheath formation around the probe, which is dictated by the applied bias voltage. If the probe is held at a large negative voltage, then the current through the probe is entirely due to ions (the ion saturation current), whilst if the probe is held at a large positive voltage, the current is instead due to the electrons (the electron saturation current). At intermediate voltages, some electrons will have sufficient energy to overcome the probe voltage and others will not, thus the I-V characteristics in this region are dictated by the distribution of electron energies. Classical probe theory then suggests that the EEDF, $f(E)$, of the plasma is directly related to the second derivative of the probe I-V curve (with the ion current accounted for) according to

$$f(E) = \frac{2m_e}{e^2 A}\left(\frac{2E}{m_e}\right)^{\frac{1}{2}} \frac{\mathrm{d}^2 I}{\mathrm{d}V^2}, \tag{1.48}$$

where A is the collecting area of the probe[29].

Although they are very widely used, Langmuir probes have a number of drawbacks[3]. Fundamentally, introducing a piece of metal into the plasma changes the plasma characteristics; attempts are usually made to minimise these perturbing effects by constructing the probe from a thin piece of wire, but there will always be some perturbation. Secondly, the probe necessarily collects charged species from the sheath which forms around it; the extent of this sheath, and thus the effective collection area of the probe, changes as a function of applied voltage. This can make interpreting I-V data considerably more complicated. Finally, Langmuir probes show no specificity for particular charged species, this means that their application is made significantly more complicated if several different positive ions (with different Bohm velocities and mobilities) are present in significant quantities in the plasma. Additionally, this makes the I-V characteristics of electronegative plasmas difficult to interpret[31,32]. For this reason Langmuir probes find significantly less use in electronegative plasmas than they do in electropositive ones. When Languir probes are used in electronegative plasmas they are often accompanied by independent methods of quantifying negative ion densities in order to help distinguish the electron contribution to the saturation current.

1.2 Radio frequency discharges

The generation of plasmas for industrial processing is most often achieved through the application of a radio frequency field to a low pressure gas sample. These fields are capable of ionising a few molecules (typically impurities in the chamber which have particularly low ionisation energies) and the resulting electrons are subsequently accelerated by the field, allowing the production of more electrons and the instigation of plasma chemistry by some of the processes mentioned previously. This section will give a brief overview of the two most common ways of coupling power into an rf plasma. The two types of rf discharge described here are the Capacitively Coupled Plasma (CCP) and the Inductively Coupled Plasma (ICP). Other types of rf plasma also exist (for example the helicon plasma in which strong magnetic fields are used to enable resonant energy transfer between the rf antenna and helicon waves within the plasma)[3] but these are less relevant to this thesis.

1.2.1 The CCP

A diagram of a typical CCP discharge is depicted in figure 1.6. The normal CCP geometry is that of a parallel plate reactor with one electrode driven at a radio frequency and the other grounded. rf power is delivered via an impedance matching box (shown by a dotted red line) consisting of two adjustable capacitors, one arranged in series with the plasma chamber and the other in parallel to ensure efficient coupling of power into the discharge (as opposed to power being reflected back to the source). High voltage rf sheaths form around each electrode in a CCP, with the in series matching capacitor acting as a blocking capacitor, allowing the driven electrode to accumulate charge and hence a self-biased potential. Ions are accelerated towards this electrode and by mounting a substrate onto this electrode efficient reactive ion etching can be achieved.

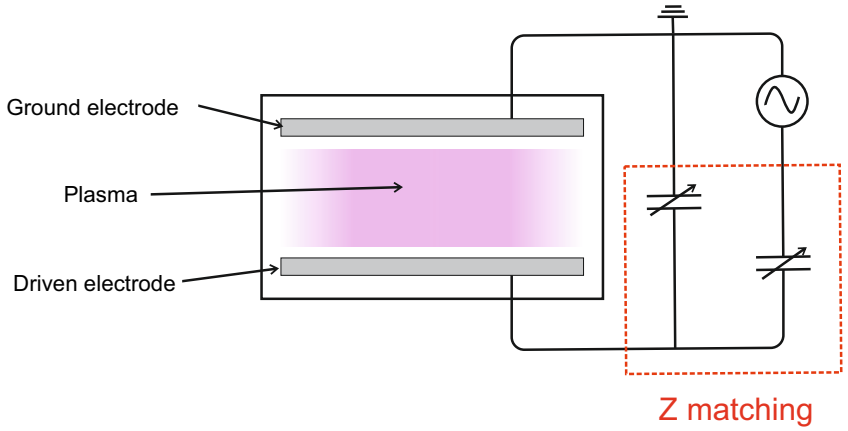

Figure 1.6: Schematic of a capacitively coupled plasma chamber including a basic, two capacitor, impedance matching arrangement.

Alternatively, to offer more control over the incident ion energies, the two electrodes can be powered independently, with one typically driven by a high frequency and high power rf supply to sustain the plasma and the other driven (via a blocking capacitor) with a lower frequency and tunable bias voltage to control the energies of incident ions. As a result, the rate of the desired process can be optimised whilst avoiding potential damage to the substrate that could result from very high energy ions.

1.2.2 The ICP

Inductively coupled plasma, as the name suggests, relies on electromagnetic induction in order to couple energy into the plasma. This is achieved by applying the rf power via a coiled antenna. The AC current within the coil produces a time varying magnetic field which, according to Faraday's law, results in an electromotive force on charged species within the magnetic field. The electromagnetic waves which drive an ICP can only penetrate some limited distance into the plasma before they are absorbed. This distance is referred to as the *skin depth*, δ. Just as the Debye length defines the distance over which electrostatic perturbations to the plasma can exist, the skin depth defines the distance over which electromagnetic waves can propagate. For a collisionless plasma (*i.e.* very low pressure), the skin depth is given by:

$$\delta = \frac{c}{\omega_e} \tag{1.49}$$

which has clear similarities to equation 1.44. For typical ICP electron densities of 10^{10} cm^{-3} a collisionless skin depth of 5 cm is expected. This means the power is typically deposited into the gas that is within $\approx$ 5 cm of the coiled antenna to generate the plasma which then spreads to the rest of the chamber by (ambipolar) diffusion[3,15]. Ambipolar diffusion occurs when oppositely charged species with different mobilities diffuse from a region of high density, with the faster species (the electrons) slowed down by electrostatic interaction with the slower species (the ions)[3]. Conversely, the slower species (ions) diffuse more rapidly than if the fast species (electrons) were not present.

Figure 1.7 shows the two most common arrangements for generating inductively coupled plasma (ICP): 1.7(a) shows a planar (or stove top) coil arrangement, whilst 1.7(b) shows the cylindrical coil alternative.

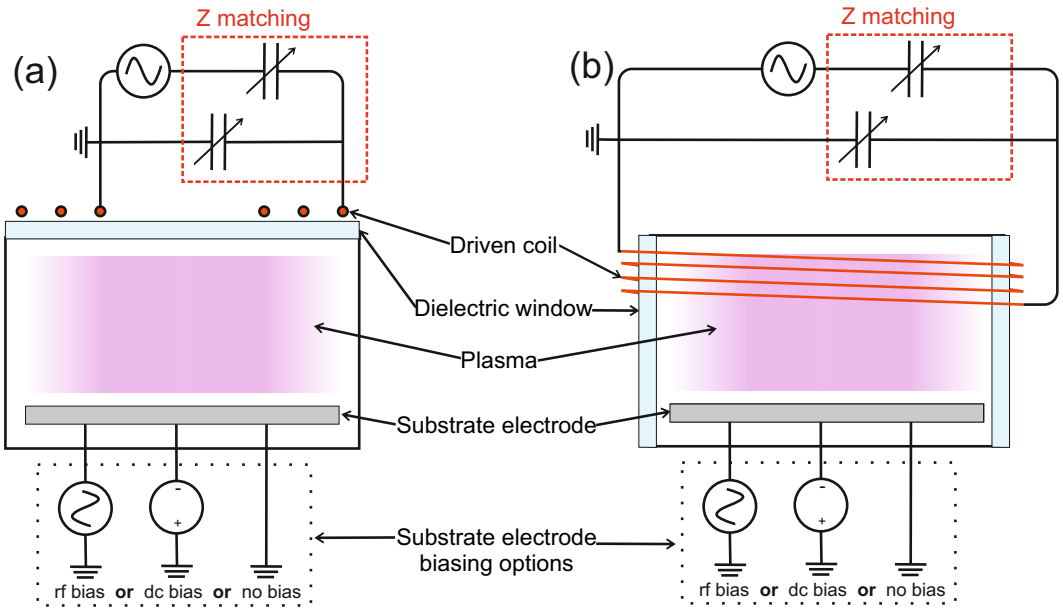

Figure 1.7: (a) A schematic of an inductively coupled plasma (ICP) chamber with a planar (or stove top) driven coil. Also shown are the options available for biasing the substrate electrode, a technique of technological importance. (b) A schematic of an ICP chamber with the alternative cylindrical driven coil.

In both cases, as for the CCP, the energy is coupled into the plasma via impedance matching electronics, and through a dielectric window forming part of the chamber. The use of a dielectric window, in contrast to the CCP, ensures that no conductive material that is in direct contact with the plasma is driven to high voltage, and thus,

all the sheaths in an ICP chamber are relatively low voltage sheaths. The low sheath voltages in an ICP chamber mean that a pure inductively coupled plasma cannot produce the fast ions needed for high quality etching. Instead, as shown in figure 1.7, the substrate electrode can be independently biased (either with an rf or DC potential) in order to carefully control the energies of incident ions. The rf biasing would, once again, typically employ impedance matching and a blocking capacitor, neither of which are shown in the figure. As well as the prospect of fine control of the ion velocities, ICPs also provide the advantage of quicker etching because they typically have plasma densities an order of magnitude higher than CCPs of the same power. The absence of high voltage electrodes from the discharge (other than the biasing which can be carefully controlled) also reduces the rate of sputtering (*i.e.* the ballistic degradation of the electrode surface by fast ions), which can be a significant source of plasma impurities in CCP chambers. The ICP with a biased substrate electrode is a common choice for Reactive Ion Etching (RIE) because the rf coil power can provide control over ion densities whilst the bias voltage can independently provide control over ion energies. The rate and quality of the etch can thus be optimised as a function of both of these parameters.

One notable feature of the ICP discharge is a change in mode of operation that occurs as the applied rf power is increased. At low powers, the inductive coupling is rather inefficient, and thus, capacitive coupling dominates; the driven end of the antenna can sustain potentials of $10^2 - 10^3$ V, and this can be sufficient to drive a capacitive rf current, even through a dielectric window. This capacitive mode of operation is referred to as the E-mode. As power increases, the electron density also increases. Increasing electron density makes the capacitive coupling less efficient[16] and the inductive coupling more efficient, such that the plasma switches mode to the high power, truly inductive, H-mode. This mode switch is accompanied by an order of magnitude increase in electron density and a visible increase in the plasmas optical emission intensity. The mode switch will be investigated in detail for an oxygen ICP in the experimental sections.

1.3 Processing with rf discharges

Several surface processes that utilise non-equilibrium rf plasma have been referred to thus far. This section will provide a little more detail on some of the most industrially important uses of capacitively and inductively coupled rf plasma.

Plasma etching is a process by which fast ions accelerated through a plasma sheath bombard the surface of a substrate and thereby remove material. Plasma etching has found great use in semiconductor microfabrication where, by applying an etch resistant mask, material can be selectively removed from a microchip. The most widely used such process is Reactive Ion Etching (RIE)[33,34] usually utilising an ICP and a biased substrate electrode, whilst the latest emerging technique is Atomic Layer Etching (ALE)[35,36] which, by chemical modification of the substrate surface (*e.g.* chlorination of a silicon wafer[35,36]), can enable control of etching on an atomic length scale.

Plasma based deposition processes go hand-in-hand with etching processes in microfabrication of layered semiconductors. Once a channel has been etched, new surface layers can be synthesised and modified by plasma based deposition of material, and thus, over several etch-deposition cycles, semiconducting chips can be constructed[37,38]. The main plasma enhanced technique used industrially is Plasma-Enhanced Chemical Vapour Deposition (PECVD)[39–41]. One particular type of PECVD, known as Plasma Assisted Atomic Layer Deposition (PAALD), enables the thickness of the deposited layers to be controlled on the atomic scale[38,42]. This is achieved by subjecting the wafer to a surface modifying precursor (typically producing a chemisorbed monolayer) and then oxidising, nitriding or hydriding the precursor with an oxygen, nitrogen or hydrogen containing ICP, respectively[42]. For example an additional SiO_2 layer can be deposited on an SiO_2 surface using PAALD by first exposing the surface to the precursor silanamine (SiH_3NH_2) and then to an oxygen ICP[42]. Where etching processes are dependent on fast ions, deposition processes utilising plasmas often make use of atomic radicals instead[42]. Given their industrial importance it is highly desirable to be able to quantify ion and atom densities with ICP plasmas and this aim provides the motivation for much of the work presented in this thesis.

1.4 The ICP chamber

The measurements detailed in this thesis are made in an ICP device in the style of figure 1.7(a) which was designed and constructed in house. A schematic of the chamber is shown in figure 1.8 and it comprises (a) the main body of the reactor vessel, (b) the rf coil and impedance matching arrangement and (c) the pumping and gas handling region. Each of these sections is described in turn here.

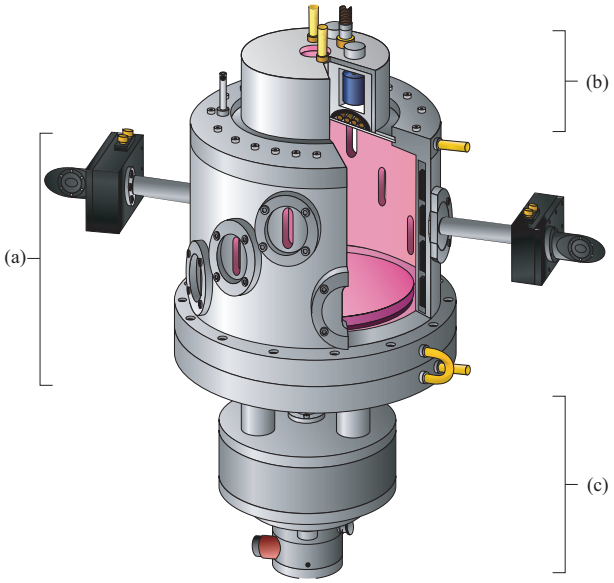

Figure 1.8: A diagram of the planar coil driven ICP chamber used throughout this work. Part (a) depicts the body of the chamber, part (b) the driven coil and impedance matching arrangement, and part (c) part of the gas handling system.

The body of the chamber is cylindrical and constructed from aluminium and is depicted in a scale drawing in figure 1.9. It has an internal diameter of 350 mm and an average height of 210 mm. Optical access to the plasma is provided by 12 ports situated at various heights in the chamber wall and arranged in pairs diametrically opposite one another. One pair of ports has a pair of narrow baffle arms (10 mm internal diameter), each 200 mm in length, at the end of which sit vacuum mirror boxes which contain gimbal mirror mounts. The mounts hold the high reflectivity mirrors which create the optical cavity used for various spectroscopic techniques discussed in the next chapter, with a total cavity length of 770 mm. The details of the custom mirror boxes are depicted in figure 1.10 including the piezo-electric transducer used to ensure regular cavity resonance excitations during ringdown experiments (see later). The purpose of the arms is to provide physical separation between the mirrors and the plasma to protect them from damage that may reduce the mirror reflectivity. The plasma is weakly magnetically confined by 128 high flux magnets placed in the walls of the chamber ($\tilde{\mathbf{B}}$ is 500 G at the walls) and the body and base of the chamber are water-cooled (yellow pipes in figure 1.8). In the bottom of the chamber sits a circular aluminium electrode with a diameter of 225 mm which is earthed. The lower electrode assembly is replaced for some of the later experiments in this thesis and details of the changes are given in the relevant chapters.

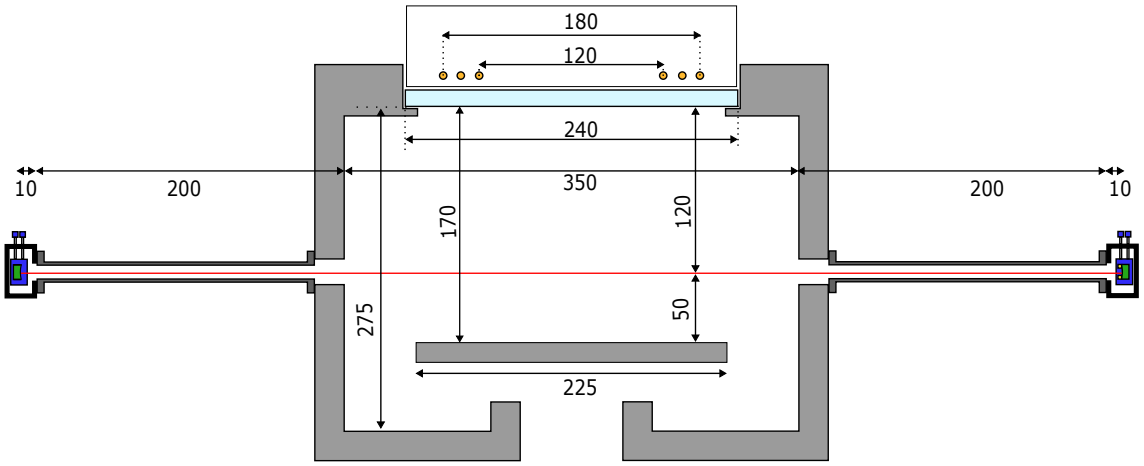

Figure 1.9: A scale cross section of the ICP chamber used in this work. All measurements are in mm. The total cavity length is 770 mm whilst the CRDS measurement position is 50 mm above the lower electrode and 120 mm below the upper window (other measurements are explained in the text). Note that the components in this chamber are essentially the same as those in the schematic (figure 1.7 (a) except for the addition of the arms and mirror mounts to enable CRDS experiments.)

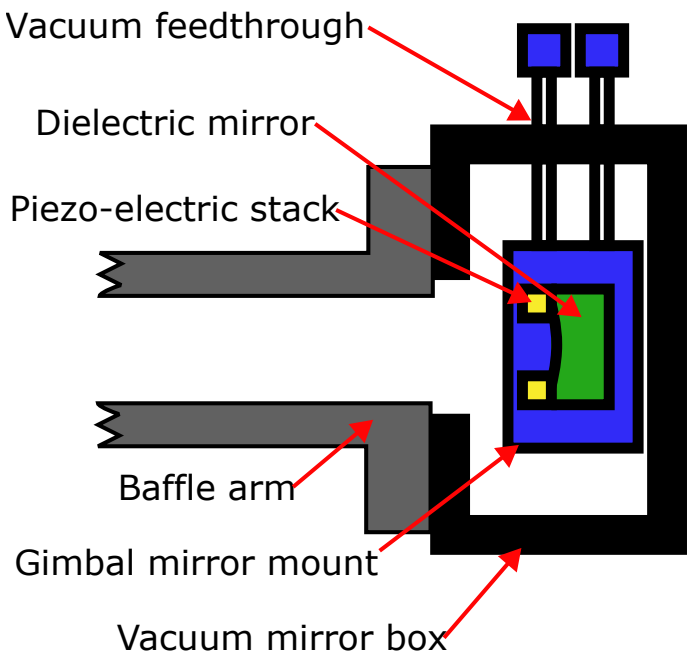

Figure 1.10: A close up of the mirror box arrangements employed in this thesis. The mirror and the gimbal mount sit entirely within the vacuum with feedthroughs allowing fine control of the mirror orientation for the purpose of optical cavity alignment. The piezo-electric stack modulates the mirror position to ensure the regular excitation of resonant cavity modes required for CRDS.

The rf coil which drives the plasma sits on top of the chamber. This consists of a 6 mm diameter copper pipe wound into a $1\frac{1}{2}$ turn, double-spiral antenna with an internal coil diameter of 120 mm and an external diameter of 180 mm. The use of copper pipe allows cooling water to flow through the coil whilst it operates. This coil is separated from the vacuum by a dielectric window of fused silica, 12 mm thick and 240 mm in diameter. The impedance matching network is built into the coil drive assembly and consists of two vacuum variable capacitors, one in series with the coil and the other in parallel. These enable the impedance of the load (coil and plasma) to be matched to that of the rf power supply and thus maximise power coupling into the plasma. Radio frequency power of up to 600 W at 13.56 MHz is provided by a solid state rf generator (Coaxial Power Systems) not pictured in figure 1.8.

The gas handling system sits beneath the chamber and consists of several pumps and valves. The two stage vacuum system (not shown in the figure) consists of a rotary vane pump (Edwards) which acts as a roughing pump and is capable of evacuating the chamber to pressures ≈ 10 mTorr. High vacuum (in this case $< 10^{-5}$ Torr) is achieved by an air cooled turbomolecular pump (Leybold). The pressure within the chamber is monitored by three pressure gauges: a high pressure capacitance manometer (Leybold Ceravac: 1-1000 Torr); a low pressure capacitance manometer (Baratron: $10^{-3} - 10^{-1}$ Torr); and a Penning gauge (Leybold Penningvac: $10^{-8} - 10^{-3}$ Torr). Two valves separate the pumping system and the chamber: the first is a gate valve capable of isolating the chamber, whilst the second is a butterfly valve which throttles the pumping speed to control the pressure in the chamber. For plasma operation, gas is introduced into the chamber along pipes attached to the mirror boxes. The flow of gas along the baffle arms helps to protect the mirrors and the flow rate is controlled by a temperature stabilised mass flow controller (Sierra) which is always set to 10 sccm for the purposes of experiments in this thesis. By adjusting the angle of the butterfly valve the pressure in the chamber can be precisely controlled and maintained at any value from 10 to 100 mTorr. An automatic feedback system utilises the output of the low pressure capacitance manometer to control the butterfly valve and thus automatically maintain a selected pressure.

1.5 Outline of Thesis

This thesis is divided into three sections. In this, the first section, an introduction is given both to the fundamental physics and chemistry of plasma (chapter 1) and to the

spectroscopic theory and optical principles relevant to the experimental techniques employed throughout the rest of the work (chapter 2).

The following two sections detail experimental and modelling results divided according to the plasma feedstock gas. The second section introduces the specifics of oxygen ICPs and methods used to probe them (chapter 3); the new experimental measurements made on an oxygen ICP (chapter 4); volume averaged chemical kinetic model results used to support and interpret the experimental observations (chapter 5) and finally some observations and modelling that provide evidence of plasma inhomogeneity (chapter 6). The section concludes with a summary of the findings for experiments on oxygen plasma.

The third and final section focuses on nitrogen ICPs. The most important techniques used to probe nitrogen ICPs are introduced (chapter 7) and extensive experimental measurements (chapter 8) and kinetic modelling (chapter 9) are detailed, including the consideration of optical saturation in the measurements. The spatial variation of ions and metastable species within the plasma are measured using a novel chamber modification that allows densities to be determined directly (< 1 mm) above the lower electrode surface, an important parameter for plasma processing (chapter 10). Finally, the widths of the Lamb dips that arise from saturated experimental spectra are considered in detail (chapter 11), and the main broadening mechanisms identified. As with the previous section on oxygen plasma, this section concludes with a summary of the findings in the preceding chapters. The thesis closes with a brief discussion of the general conclusions and outlook of the work.

Chapter 2

Introduction II: Spectroscopy and Optics

This chapter introduces the concepts of linear and non-linear spectroscopy pertinent to the experimental work presented in this thesis. In particular the chapter will detail the relationships between the various quantities which quantify transition strengths, namely, absorption cross sections, Einstein coefficients and transition moment matrix elements. These relationships are of particular relevance for studies of $O_2(a^1\Delta_g)$ and an example calculation pertinent to that species is also presented. In addition, the most important experimental technique in the context of this thesis, cavity ringdown spectroscopy, is introduced as are the spectroscopic lineshapes expected to arise under both saturated and unsaturated conditions. Finally, the energy level hierarchy of the species most pertinent to the spectroscopic measurements of this thesis are presented, and includes the effects of spin-orbit coupling, Λ-doubling and nuclear spin statistics.

2.1 Resonant light-matter interactions

The strongest interactions between electromagnetic radiation and atoms (or molecules)[i] occur when the radiation frequency, ν, is related to the difference in energy, $\Delta E = E_2 - E_1$ between a lower energy level $|1\rangle$ (with degeneracy g_1) and a higher energy level $|2\rangle$ (with degeneracy g_2) by $\Delta E = h\nu$. When this condition is met the radiation is said to be on resonance and it is able to perturb the atomic Hamiltonian and hence induce transitions between the two levels. Einstein proposed that, in a two-level system subject to resonant radiation and with population densities N_1 and N_2, three processes may occur.

[i]For brevity, in the remainder of this section "atoms" will be referred to, although the physics applies equally well to molecules. This will continue until section 2.2 when the distinction becomes important.

First, the photon may be absorbed by an atom in level $|1\rangle$ which becomes excited to level $|2\rangle$ in a process known as absorption and quantified by:[43]

$$\frac{\mathrm{d}N_1}{\mathrm{d}t} = -N_1 B_{12} \rho(\nu). \tag{2.1}$$

Secondly, the photon may interact with an atom in level $|2\rangle$ causing it to drop to level $|1\rangle$ with the emission of a photon in a process known as stimulated emission and quantified by:[43]

$$\frac{\mathrm{d}N_1}{\mathrm{d}t} = N_2 B_{21} \rho(\nu). \tag{2.2}$$

Finally, an atom in level $|2\rangle$ may drop to level $|1\rangle$ spontaneously, again with the emission of a photon, in a process known as spontaneous emission, quantified by:[43]

$$\frac{\mathrm{d}N_1}{\mathrm{d}t} = N_2 A_{21}. \tag{2.3}$$

In the above equations $\rho(\nu)$ is the spectral energy density of the radiation per unit frequency [J m^{-3} Hz^{-1}] and B_{12} [m^3 J^{-1} s^{-2}], B_{21} [m^3 J^{-1} s^{-2}] and A_{21} [s^{-1}] are referred to as Einstein coefficients and are related as follows:[43]

$$A_{21} = \frac{8\pi h\nu^3}{c^3} B_{21} = \frac{g_1}{g_2} \frac{8\pi h\nu^3}{c^3} B_{12}. \tag{2.4}$$

Overall the rate of change of population of $|1\rangle$ due to radiative transitions may be written:

$$\frac{\mathrm{d}N_1}{\mathrm{d}t} = -\left(N_1 - \frac{g_1}{g_2} N_2\right) B_{12} \rho(\nu) + N_2 A_{21}, \tag{2.5}$$

and this change in population is directly related to a change in intensity of the electromagnetic field. It is worth noting that spontaneously emitted photons are incoherent (they can be emitted in any direction and with any phase), whilst stimulated emission is a coherent process, and the emitted photon has a wavevector and phase identical to that of the incident photon.

Consider a monochromatic beam of frequency, ν, and intensity, I, passing through a sample of atoms and on resonance with a transition. As the beam traverses some length of sample, L, the photons within the beam have some non-zero probability of being absorbed (thus decreasing I) and some non-zero probability of stimulating emission (increasing I). In principal spontaneous emission may also increase the intensity of the beam, however the vast majority of spontaneously emitted photons will not be emitted in the beam direction and hence this effect can be neglected. From equation 2.5 it is evident that the change in intensity of the beam as it traverses the sample will be proportional to $-\left(N_1 - \frac{g_1}{g_2} N_2\right)$. Additionally, a more intense beam

will lead to more photons being absorbed and thus a faster change in beam intensity. Combining these statements yields:[43]

$$\frac{\mathrm{d}I}{\mathrm{d}L} \propto -\left(N_1 - \frac{g_1}{g_2}N_2\right) I. \tag{2.6}$$

Introducing a proportionality constant, $\sigma(\nu)$, known as the absorption cross section and solving the differential equation (2.6) gives:[43]

$$I = I_0 \exp\left(-\left(N_1 - \frac{g_1}{g_2}N_2\right)\sigma(\nu)L\right), \tag{2.7}$$

which reduces to the well known Beer-Lambert law[43]

$$I = I_0 \exp\left(-N_1\sigma(\nu)L\right) = I_0 \exp\left(-\alpha(\nu)L\right), \tag{2.8}$$

when $N_1 >> N_2$ as is common if $\Delta E >> k_B T$. The Beer-Lambert law describes the attenuation of light as it traverses an absorbing sample, which is the basis of laser absorption spectroscopy and the determination of the absorption coefficient $\alpha(\nu)$. The cross section, $\sigma(\nu)$, depends on various broadening mechanisms that operate in the system being probed (*e.g.* the Doppler effect, *vide infra*). A more convenient broadening-independent quantity is the integrated cross section, σ_{INT}, defined as[43]

$$\sigma_{INT} = \int_{\nu_1}^{\nu_2} \sigma(\nu)\mathrm{d}\nu \tag{2.9}$$

where the limits of integration are chosen to include the full profile of the broadened transition. σ_{INT} is directly related to population densities, N_1 and N_2 and the integrated area under an absorption spectrum α_{INT} by the following:[43]

$$\alpha_{INT} = \int_{\nu_1}^{\nu_2} \alpha(\nu)\mathrm{d}\nu = \left(N_1 - \frac{g_1}{g_2}N_2\right)\sigma_{INT} \approx N_1\sigma_{INT}. \tag{2.10}$$

2.2 Quantifying the strength of optical transitions

Just as the Einstein coefficients quantify the probability of transitions occurring, so σ_{INT} quantifies that same probability in equation 2.10. It follows therefore that the Einstein coefficients and σ_{INT} are intrinsically linked. If we recall that the electromagnetic field that causes transitions may be thought of as a perturbation to the atomic Hamiltonian then it becomes clear that the matrix elements of this perturbation must also be directly related to the transition probability. Where a known

density of atoms can be prepared and their spectrum measured (for example by laser absorption) then integrated cross sections are straightforward to measure (using equation 2.8) and use to quantify unknown atom densities. However, species that are of interest in plasmas are often internally excited and short-lived making preparation of known concentrations (and hence cross section measurements) difficult or impossible. It is often possible however to calculate transition probabilities quantum mechanically or to measure Einstein coefficients from emission spectra. It is important therefore to understand how these quantities are related in order that accurate cross sections can be found and used in absorption experiments.

2.2.1 Transitions in atoms

Electric dipole transitions - 'allowed'

To a first approximation the perturbing interaction between the electromagnetic field and an atom can be thought of as an interaction between the oscillating electric field of the radiation and the electric dipole moment of the atom. The relevant matrix element is the transition dipole moment given by:[43]

$$\int \psi_2^* \hat{\boldsymbol{\mu}} \psi_1 d\tau = \langle 2|\hat{\boldsymbol{\mu}}|1\rangle, \tag{2.11}$$

where $\hat{\boldsymbol{\mu}} = -e\sum_i \boldsymbol{r}_i$ is the electric dipole moment operator[44]. The square of this matrix element is sometimes referred to as the line strength. Transitions that have a non-zero transition electric dipole moment are referred to as 'allowed' because they are much stronger than other transitions (which are referred to as 'forbidden' even though they can occur). The electric dipole moment matrix element is related to the other quantities already mentioned as follows:[43]

$$A_{21} = \frac{1}{g_2}\frac{16\pi^3\nu^3}{3\epsilon_0 hc^3}|\langle 2|\hat{\boldsymbol{\mu}}|1\rangle|^2 = \frac{g_1}{g_2}\frac{8\pi\nu^2}{c^2}\sigma_{INT}. \tag{2.12}$$

Thus if A_{21} or $\langle 2|\hat{\boldsymbol{\mu}}|1\rangle$ is known, σ_{INT} may be deduced. The transition dipole moment matrix elements also prove useful because they are the basis of the selection rules that govern whether or not a transition is allowed. Selection rules for specific cases will be discussed later in this chapter.

Magnetic dipole transitions - 'forbidden'

When the electric dipole transition moment is zero then the magnetic dipole moment of the atom becomes the most important cause of transitions between levels. In this

case, equation 2.12 must be modified by the replacement of the electric dipole moment operator with the magnetic dipole moment operator,[44] $\hat{\boldsymbol{M}} = -\frac{e}{2m_e c}\sum_i(\boldsymbol{L}_i + 2\boldsymbol{S}_i)$ and an adjustment of some constants which effectively correct for the fact that electric dipole and magnetic dipole moments have different units:[43,45]

$$A_{21} = \frac{1}{g_2}\frac{16\mu_0\pi^3\nu^3}{3hc^3}|\langle 2|\hat{\boldsymbol{M}}|1\rangle|^2 = \frac{g_1}{g_2}\frac{8\pi\nu^2}{c^2}\sigma_{INT}. \tag{2.13}$$

Note in the above equation that the relationship between Einstein coefficients and integrated cross sections is identical to equation 2.12.

Electric quadrupole transitions- 'forbidden'

When neither type of dipole transition is possible then high order multipoles of the charge distribution become relevant and can lead to very weak transitions. The most important such multipole is the electric quadrupole. In the case where the quadrupole moment mediates the transition the operator is[44] $\hat{\boldsymbol{Q}} = -e\sum_{i,j}\boldsymbol{r}_i\boldsymbol{r}_j$ and equation 2.12 becomes:[43,45]

$$A_{21} = \frac{1}{g_2}\frac{8\pi^5\nu^5}{5\epsilon_0 hc^5}|\langle 2|\hat{\boldsymbol{Q}}|1\rangle|^2 = \frac{g_1}{g_2}\frac{8\pi\nu^2}{c^2}\sigma_{INT}. \tag{2.14}$$

2.2.2 Transitions in molecules

Molecules are significantly more complex than atoms, they have internal structure which leads to much more complicated spectra. Here we restrict ourselves to the case of diatomic molecules. An electronic transition in such a molecule may in general be accompanied by a change in both vibrational and rotational state of the molecule, leading to a highly structured spectrum, and it is important to understand this structure in order to make quantitative use of spectra.

Electric dipole transitions

The spatial wavefunctions may be denoted $|n, v, J\rangle$ where n, v and J represent the electronic, vibrational and rotational states of the diatom, respectively. Thus the square of the electric dipole transition moment can be written (applying the Born-Oppenheimer approximation):[46]

$$|\langle 2|\hat{\boldsymbol{\mu}}|1\rangle|^2 = |\langle n', v', J'|\hat{\boldsymbol{\mu}}|n'', v'', J''\rangle|^2 = |\langle n', v'|\hat{\boldsymbol{\mu}}|n'', v''\rangle|^2\mathscr{S}_{J',J''} = \boldsymbol{R_e}(\bar{r})^2 q_{v',v''}\mathscr{S}_{J',J''}, \tag{2.15}$$

where $\boldsymbol{R_e}(\bar{r})$ is the electronic transition dipole moment evaluated at nuclear separation $\bar{r}$ (known as the r-centroid), $q_{v',v''}$ is the Franck-Condon factor accounting for

the square of the overlap between the final and initial vibrational states, $\mathscr{S}_{J',J''}$ is the Hönl-London factor which accounts for the square of the rotational overlap between final and initial states and the single or double primes refer to the upper and lower energy level, respectively. An important convention exists dictating the values to which Franck-Condon factors[47] and Hönl-London factors[46,48] should sum, these conventions are as follows:

$$\sum_{v''} q_{v',v''} = 1 \tag{2.16}$$

and

$$\sum_{J''} \mathscr{S}_{J',J''} = (2 - \delta_{0,\Lambda'+\Lambda''})(2S'+1)(2J'+1). \tag{2.17}$$

In 2.17 δ is the Kronecker delta and Λ is the quantum number for the magnitude of the projection of the electronic orbital angular momentum onto the internuclear axis (taking values $0, 1, 2...$ for electronic states $\Sigma, \Pi, \Delta...$ respectively). Provided these requirements are met, the vibronic part of the transition dipole moment is related to the Einstein A coefficient for the whole vibrational band by:[46,48]

$$A_{v',v''} = \frac{16\pi^3\nu^3}{3\epsilon_0 hc^3}\frac{(2 - \delta_{0,\Lambda'+\Lambda''})}{(2 - \delta_{0,\Lambda'})}\boldsymbol{R_e}(\bar{r})^2 q_{v',v''}, \tag{2.18}$$

and the full rovibronic electric dipole transition moment is related to the cross section for that rovibronic transition by a rearrangement of equation 2.12:

$$\sigma_{INT} = \frac{1}{g''}\frac{2\pi^2\nu}{3\epsilon_0 hc}|\langle n', v', J'|\hat{\boldsymbol{\mu}}|n'', v'', J''\rangle|^2. \tag{2.19}$$

Magnetic dipole and electric quadrupole transitions

Once again the electric dipole equations 2.18 and 2.19 can be adjusted for other types of transitions to produce:[45,49]

$$A_{v',v''} = \frac{16\mu_0\pi^3\nu^3}{3hc^3}\frac{(2 - \delta_{0,\Lambda'+\Lambda''})}{(2 - \delta_{0,\Lambda'})}|\langle n', v'|\hat{\boldsymbol{M}}|n'', v''\rangle|^2, \tag{2.20}$$

and

$$\sigma_{INT} = \frac{1}{g''}\frac{2\mu_0\pi^2\nu}{3hc}|\langle n', v', J'|\hat{\boldsymbol{M}}|n'', v'', J''\rangle|^2 \tag{2.21}$$

for magnetic dipole transitions, and

$$A_{v',v''} = \frac{8\pi^5\nu^5}{5\epsilon_0 hc^5}\frac{(2 - \delta_{0,\Lambda'+\Lambda''})}{(2 - \delta_{0,\Lambda'})}|\langle n', v'|\hat{\boldsymbol{Q}}|n'', v''\rangle|^2, \tag{2.22}$$

and

$$\sigma_{INT} = \frac{1}{g''}\frac{\pi^4\nu^3}{5\epsilon_0 hc^3}|\langle n', v', J'|\hat{\boldsymbol{Q}}|n'', v'', J''\rangle|^2 \tag{2.23}$$

for electric quadrupole transitions.

An example calculation: The O_2 Noxon system

The Noxon system of O_2 is the name given to the transition between the two lowest lying excited states $O_2(b^1\Sigma_g^+) \leftarrow O_2(a^1\Delta_g)$[50]. Probed in absorption this transition has $\Delta\Lambda = -2$ and both its electric and magnetic transition dipole moments are zero (see selection rules later in this chapter). The electric quadrupole moment is therefore responsible for the observation of this transition and as a result the transition is very weak. The only available data quantifying the strength of the transition are Einstein A coefficients for the (0, 0) vibrational band, either measured from atmospheric emission or calculated. The correct conversion of this $A_{0,0}$ value to absorption cross sections has proved a stumbling block in several previous publications[51,52], with the most common error involving a factor of 2 arising due to incorrect normalisation of Hönl-London factors. Starting from the literature value[52] ($A_{0,0} = 1.26 \times 10^{-3}\,\mathrm{s}^{-1}$) equation 2.22 allows the vibronic quadrupole transition moment for this band to be calculated. Noting that $\Lambda' = 0$ and $\Lambda'' = 2$ and therefore the ratio involving Kronecker deltas in equation 2.22 is equal to 2 (accounting for the fact that the Δ state will be Λ-doubled whilst the Σ state will not) a vibronic transition quadrupole moment of $\langle n', v'|\hat{\boldsymbol{Q}}|n'', v''\rangle = 4.374 \times 10^{-40}\,\mathrm{C\ m^2}$ is found.

Many Hönl-London factors are tabulated by Kovacs[53], however the tabulated values are not scaled so as to obey the sum rule (2.17) which in this case requires the sum of Hönl-London factors to be equal to $2(2J' + 1)$. The values for this transition appear in table 3.5 of Kovacs. These tabulated values sum to $\frac{4}{3}(2J' + 1)$ and must therefore be scaled by a factor of $\frac{3}{2}$ to obey the sum rule.[54] The corrected factors for the Noxon transition are given in table 2.1.

Table 2.1: Hönl-London factors for the Noxon band.

Branch	$\mathscr{S}_{J',J''}$
O(J'')	$\frac{(J''+1)(J''+2)}{2(2J''-1)}$
P(J'')	$J'' + 2$
Q(J'')	$\frac{3(2J''+1)(J''-1)(J''+2)}{(2J''-1)(2J''+3)}$
R(J'')	$J'' - 1$
S(J'')	$\frac{J''(J''-1)}{2(2J''+3)}$

Due to Pauli constraints (nuclear spin statistics) on the permissible J' levels in the $O_2(b^1\Sigma_g^+)$ state the O-, Q- and S- branches of the spectrum only show lines from even

J'' whilst the P- and R- branches show only odd J'' lines (all J'' levels are permissible in the $O_2(a^1\Delta_g)$ state due to Λ-doubling). However, the appearance of the lines in the spectrum (or not) does not affect the way in which Hönl-London factors are summed (all five factors must be included in the sum, regardless of Pauli constraints on the spectrum).

In order to calculate integrated cross sections for individual rovibronic transitions the rovibronic transition quadrupole moment is calculated according to:

$$|\langle n', v', J'|\hat{\boldsymbol{Q}}|n'', v'', J''\rangle|^2 = |\langle n', v'|\hat{\boldsymbol{Q}}|n'', v''\rangle|^2 \mathscr{S}_{J',J''}, \tag{2.24}$$

and is then inserted into equation (2.23) with $g'' = 2J'' + 1$ to yield integrated cross sections. Such cross sections for several Q-branch lines are given in table 2.2.

Table 2.2: Calculated cross section for Noxon (0, 0) band Q-branch lines.

Transition	$\mathscr{S}_{J',J''}$	$\sigma_{INT}/\mathrm{m^2Hz}$	$\sigma_{INT}/\mathrm{cm^2cm^{-1}}$
Q(2)	2.857	5.21797×10^{-17}	1.74053×10^{-23}
Q(4)	6.312	6.40315×10^{-17}	2.13586×10^{-23}
Q(6)	9.455	6.63807×10^{-17}	2.21422×10^{-23}
Q(8)	12.526	6.72185×10^{-17}	2.24217×10^{-23}
Q(10)	15.570	6.75994×10^{-17}	2.25487×10^{-23}
Q(12)	18.599	6.77827×10^{-17}	2.26099×10^{-23}

These cross sections (which are temperature independent), when used with equation (2.10), return number densities in the particular rotational level being probed. The application of statistical mechanics to these rotational state densities can then allow the total densities of $O_2(a^1\Delta_g)$ to be calculated provided that rotational and vibrational temperatures are known.

An alternative approach is to apply the statistical mechanics one stage earlier in order to derive a temperature dependent cross section which already includes the effect that changing temperature has on rotational state populations. Using this cross section in equation 2.10 would then yield the total density of $O_2(a^1\Delta_g)$ directly. Temperature dependent cross sections of this type are the ones usually included in databases and calculated by simulation software[55,56] (discussed in the next section).

Spectral databases and simulation software

It is not always necessary to go through the laborious process of calculating cross sections from scratch. For many important species integrated cross sections are tabulated in openly accessible databases. The most commonly used database is HITRAN,[56] which contains spectral information for molecules primarily of importance in atmospheric chemistry. Unfortunately HITRAN does not, in general, have information on the cross sections for absorption by electronically excited molecules, nor does it include many of the species of interest to the plasma community, making it of limited use.

A more versatile tool capable of calculating line positions and rotational line strengths for any diatomic molecule (provided the molecular constants are known) is the spectral simulation program PGOPHER.[55] PGOPHER is capable of including many rotational constants (including several centrifugal distortion terms) and angular momentum coupling constants in order to accurately produce model spectra. For electric and magnetic dipole transitions, if the transition dipole moment is known (or can be calculated) then PGOPHER is capable of finding absolute cross sections for each rotational line (including the influence of Hönl-London factors and nuclear spin statistics). PGOPHER can also calculate line positions for electric quadrupole transitions, however calculating absolute line strengths for such transitions is not currently within the capabilities of the program (hence the need for the calculation in the previous section). These capabilities make PGOPHER an extremely useful tool for selecting absorption lines to probe and extracting number densities from absorption spectra.

The program is also capable of carrying out spectral fitting, with the user able to select which variables will be allowed to float to optimise the fit. This facility was originally designed to allow the extraction of molecular constants from experimental spectra, but in the context of studying plasma it is useful for finding rotational and vibrational temperatures from spectra of species for which molecular constants are already known.

2.3 The broadening of spectral lines

When discussing integrated cross sections, an allusion was made to broadening mechanisms as a motivation for introducing the integrated cross section. This section will give more details on the origins of line broadening.

The model of resonant light-matter interactions introduced in section 2.1 essentially assumed that the atoms or molecules have levels with precisely defined energies such that incident radiation should have zero probability of being absorbed unless it meets the resonance condition ($\Delta E = h\nu$). Such a system would show arbitrarily narrow spectral transitions. In reality such spectra are never observed. High resolution experimental absorption spectra show a distribution of absorbed radiation frequencies around each resonant transition frequency. The shape of this distribution is observed to change with changing sample conditions (for example becoming broader as temperature or pressure increase), this makes it clear that the broadening is not instrumental but instead relates directly to the fundamental physics of the absorption process. Physical causes of spectral line broadening can be divided into two categories:[43] homogeneous broadening mechanisms affect all atoms or molecules equally whilst inhomogeneous mechanisms affect different absorbers in different ways (usually dependent upon their velocity), both are discussed here.

2.3.1 Homogeneous broadening

Natural broadening[57]

The wavefunction of an arbitrarily long lived atomic state may be described by a stationary state of the Schrödinger equation whose time dependence is:

$$\Psi(x,t) = \psi(x)T(t) = \psi(x)\exp\left(\frac{-iE_0t}{\hbar}\right), \tag{2.25}$$

and whose energy, E_0, is precisely defined. If however the state is not arbitrarily long lived, but instead may decay (*e.g.* by spontaneous emission) to a different state with a lifetime, τ, then the corresponding wavefunction is

$$\Psi(x,t) = \psi(x)T(t) = \psi(x)\exp\left(\frac{-iE_0t}{\hbar}\right)\exp\left(\frac{-t}{2\tau}\right). \tag{2.26}$$

While this wavefunction no longer has a precisely defined energy, it can be expressed as a superposition of states with a distribution of energies, $g(E)$, about the central energy E_0 according to[57]

$$T(t) = \exp\left(\frac{-iE_0t}{\hbar}\right)\exp\left(\frac{-t}{2\tau}\right) = \int_0^\infty g(E)\exp\left(\frac{-iEt}{\hbar}\right)\mathrm{d}E, \tag{2.27}$$

where $g(E)$ takes the form[57]

$$g(E)\mathrm{d}E = \frac{\left(\frac{\hbar}{2\pi\tau}\right)}{(E-E_0)^2 + \left(\frac{\hbar}{2\tau}\right)^2}\mathrm{d}E. \tag{2.28}$$

This state therefore has some uncertainty as to its energy and $g(E)$ shows that the shorter the lifetime τ, the wider the energy distribution and hence the greater this uncertainty.

Naturally, this uncertainty in the energy of atomic and molecular states leads to a broadening of the transitions associated with these states. This is known as natural broadening because it is inherent to all spectroscopic systems. The spectral profile that arises due to this broadening mechanism, $L(\nu)$, is known as a Lorentzian profile, follows directly from equation 2.28 and can be expressed as:

$$L(\nu)\mathrm{d}\nu = \frac{1}{\pi}\frac{\frac{\Delta\nu_N}{2}}{(\nu-\nu_0)^2+(\frac{\Delta\nu_N}{2})^2}\mathrm{d}\nu \tag{2.29}$$

where $\Delta\nu_N = \frac{1}{2\pi\tau}$ is the full width at half maximum (FWHM) of the profile and the expression is area normalised. When both initial and final levels in a transition have lifetimes short enough to cause significant uncertainty in their energy then the linewidth is given by

$$\Delta\nu_N = \frac{1}{2\pi}\sqrt{\frac{1}{\tau_i^2}+\frac{1}{\tau_f^2}} \tag{2.30}$$

Any other mechanism that shortens the lifetime of absorbing or emitting species also contributes to the linewidth and in most experiments natural broadening (arising from the lifetime against spontaneous emission) is dominated by other line broadening processes.

Collisional or pressure broadening

Collisional processes can clearly perturb an absorbing or emitting species and can be elastic or inelastic in nature. Inelastic collisions change the state of the absorbing or emitted species and thus directly influence its lifetime whilst elastic collisions that occur during a radiative process have a dephasing effect on the transition, leading to an uncertainty in the transition frequency and thus line broadening. Pressure broadening[43] also leads to a Lorentzian profile described by equation (2.29) but now with the natural linewidth $\Delta\nu_N$ augmented by the pressure broadening to give a FWHM linewidth $\Delta\nu_p$. It is found that this linewidth scales linearly with gas pressure such that, for a mixture of gases

$$\Delta\nu_p = 2\tilde{c}\sum_i \gamma_i p_i, \tag{2.31}$$

where γ_i is the broadening parameter for species i and is expressed in $\mathrm{cm}^{-1}\mathrm{atm}^{-1}$, p_i is the partial pressure of species i in atm and $\tilde{c}$ is the speed of light in $\mathrm{cm\,s}^{-1}$.

Typical broadening parameters are of the order of 0.05 $cm^{-1}atm^{-1}$ leading to pressure broadening FWHM at pressures of $10-100$ mTorr relevant to our chamber of $20-200$ kHz.

2.3.2 Inhomogeneous broadening

Doppler broadening

Doppler broadening[43] arises due to the thermal motion of absorbing or emitting molecules. As the molecules move, either towards or away from a radiation source or detector, the frequency of light that they experience or emit is Doppler shifted. In absorption, the resonance condition for each molecule depends on the frequency of light it experiences and so a distribution of molecular velocities results in a distribution of absorbed frequencies in the laboratory reference frame. The apparent resonant frequency of a moving molecule, ν, is given by:

$$\nu = \nu_0 \left(1 + \frac{v_z}{c}\right), \tag{2.32}$$

where ν_0 is the resonant frequency of a stationary molecule and v_z is the component of the molecular velocity in the direction of propagation of the radiation. The distribution of speeds $f(v_z)$ in one dimension for a thermally equilibrated gas sample is given by a Maxwellian distribution:

$$G(v_z)\mathrm{d}v_z = \left(\frac{m}{2\pi k_B T}\right)^{\frac{1}{2}} \exp\left(\frac{-mv_z^2}{2k_B T}\right) \mathrm{d}v_z. \tag{2.33}$$

Combining equations (2.32) and (2.33) yields a distribution of absorbed frequencies for the gas sample, the Doppler profile:

$$G(\nu)\mathrm{d}\nu = \left(\frac{mc^2}{2\pi k_B T \nu_o^2}\right)^{\frac{1}{2}} \exp\left(\frac{-mc^2(\nu-\nu_0)^2}{2k_B T \nu_0^2}\right) \mathrm{d}\nu, \tag{2.34}$$

the FWHM, $\Delta\nu_D$, of which is directly related to sample temperature by:

$$\Delta\nu_D = \left(\frac{8\ln 2 k_B T \nu_0^2}{mc^2}\right)^{\frac{1}{2}}. \tag{2.35}$$

For small molecules such as O_2 and N_2 at temperatures of a few hundred Kelvin Doppler widths of ≈ 1 GHz are expected for visible/near infrared wavelengths and Doppler broadening is expected to be the dominant broadening process under the low pressure conditions in the plasma chamber used here.

Transit time broadening

A final type of broadening that can sometimes be important in absorption experiments is transit time broadening[58]. This occurs when the time it takes a molecule to traverse the probe beam is short compared to the natural lifetime of the species. In such situations the timescale of the coherent interaction between the molecule and beam is limited by the transit time and this can lead to additional broadening. This is usually only observed with tightly focused beams and fast moving molecules (e.g. in molecular beams where narrow velocity distributions make Doppler broadening small) and in the case of non-linear spectroscopy where Doppler free spectra can be obtained (see later in this chapter).

2.3.3 The Voigt profile

In most gas sensing applications pressure broadening and Doppler broadening are the dominant broadening mechanisms under higher pressure and low pressure conditions, respectively (for a given temperature). Under certain conditions of temperature and pressure however, both mechanisms are significant and the resultant spectrum is a convolution of the two lineshapes[43] resulting in a Voigt profile. Since pressure broadening is insignificant in the applications described in this thesis, the Doppler profile will suffice for the bulk of the work herein. However, in the case of Lamb dip spectroscopy (*vide infra*) the linewidth is Doppler free and a Lorentzian profile is more appropriate. Hence the need to discuss other potential broadening processes here.

2.4 Absorption spectroscopy on forbidden transitions (or for detection of low density species)

As eluded to in section 2.1, the simplest laser absorption experiment consists of a laser, a sample and a detector. The laser beam of negligible linewidth is passed through the sample and the transmitted intensity is measured by the detector as the laser wavelength is tuned over a resonant transition. Equation 2.8 then allows absorption coefficients $\alpha(\nu)$ to be determined and if cross sections are known then number densities can be found according to equation 2.10. This technique is simple and generally highly effective in detection using electric dipole allowed transitions. However, if one wishes to use forbidden transitions as targets for absorption spectroscopy (for example if there are no alternative allowed transitions at convenient wavelengths) or to

detect a species that is very low in number density, then the small absorption signal, which has to be measured in a large (and often varying) background with resulting poor signal to noise ratio, can be prohibitive.

Several techniques exist to improve the sensitivity of absorption spectroscopy in this situation. One approach is to reduce the noise, this is most simply achieved by averaging many measurements in order to reduce the effect of white noise (noise that is equally intense at all signal frequencies) but is of limited usefulness in systems that exhibit long term drift or instability, and can be problematic in high resolution spectroscopy experiments. Another common type of noise is pink noise or $1/f$ noise the intensity of which (as the name indicates) is inversely proportional to signal frequency. The deleterious effect of this type of noise can be reduced by the techniques of wavelength and frequency modulation; in essence these techniques encode the absorption signal at a high frequency (where $1/f$ noise is small) by using modulation techniques. Demodulation then allows retrieval of the absorption signal without the effects of low frequency noise.[59,60]

Another, perhaps more obvious, approach is to increase the size of the signal. Equation 2.8 suggests that this can be done in three ways: selecting the line with the largest cross section, increasing the density of the species under investigation or increasing the interaction pathlength between the radiation and the absorbing medium. The first of these is of no use if all the accessible transitions are weak (the case for numerous plasma species detailed later). The second is of limited use because any method one uses to increase excited species densities in plasma (e.g. increasing power or pressure) leads to a fundamentally different plasma. Additionally it is often impossible to increase densities sufficiently to make direct single pass measurement possible. By far the most common solution therefore is to increase the pathlength of the radiation through the absorbing medium. The simplest way of achieving this is using a multipass cell (e.g. a White cell[61] or Herriott cell[62]). Such cells consist of two (or more) mirrors whose radius of curvature and separation are chosen such that radiation introduced into the cell passes back and forth several times (without retracing its own path, thus avoiding interference) and eventually escapes the cell through a small aperture for detection. Multipass cells are capable of providing path lengths of 10s or even 100s of metres, however this is not always sufficient for detection of very low density species, and in these cases optical cavities may be employed to further enhance the absorption pathlength. Basic details of passive optical cavities are given in appendix A; a description of their application to spectroscopy is given in the next sections.

2.5 Optical cavities applied to spectroscopy

Two techniques have predominated in the use of optical cavities to enhance absorption spectroscopy signals, these are cavity ringdown spectroscopy (CRDS) and cavity enhanced absorption spectroscopy (CEAS). Both of these techniques have been used to probe plasma chemistry[63–66] and they are summarised here.

2.5.1 Cavity ringdown spectroscopy (CRDS)

During a CRDS experiment an optical cavity is constructed around the absorbing medium of interest. A laser beam is launched into this cavity and, when resonance is achieved (typically ensured by dithering one cavity mirror back and forth using a piezoelectric transducer), the intracavity power builds up. The intracavity power is monitored by a detector positioned behind one of the cavity mirrors and when it reaches a preset threshold value a fast optical switch (typically an acousto-optic modulator (AOM), see appendix C) is triggered which prevents the laser from entering the cavity. The intracavity field (and hence the signal at the detector) then decays exponentially and the lifetime of this decay (the ringdown time) is indicative of the cavity losses (*i.e.* mirror losses and absorption losses). When no absorber is present the change of cavity intensity with time, $I(t)$, is given by:

$$\frac{\mathrm{d}I(t)}{\mathrm{d}t} = -\frac{I(t)}{\tau_0} \Longrightarrow I(t) = I_0 \exp\left(\frac{-t}{\tau_0}\right), \tag{2.36}$$

with the ringdown time, τ_0, simply determined by the mirror reflectivity and cavity length according to

$$\tau_0 = \frac{-L}{c \ln R}, \tag{2.37}$$

whilst with an absorber inside the cavity

$$\frac{\mathrm{d}I(t)}{\mathrm{d}t} = -\frac{I(t)}{\tau_0} - c\alpha(\nu)I(t) \Longrightarrow I(t) = I_0 \exp\left(\frac{-t}{\tau}\right), \tag{2.38}$$

with

$$\tau = \frac{-L}{c(\ln R - \alpha(\nu)L)}. \tag{2.39}$$

Thus by measuring ringdown times with and without an absorber present a spectrum can be determined according to:[67]

$$\alpha(\nu) = \frac{1}{c}\left(\frac{1}{\tau} - \frac{1}{\tau_0}\right). \tag{2.40}$$

Knowledge of absorption coefficient as a function of laser frequency allows information about the probed species (*e.g.* densities from integrated absorption coefficients and temperatures from Doppler widths) to be retrieved just as it is for direct absorption spectra.

Mode matching

When a laser beam enters an optical cavity its power couples into several transverse cavity modes. Different transverse cavity modes in general can have different ringdown times (different modes utilise different areas of the cavity mirrors, they have different diffraction losses and undergo different Guoy phase shifts when they pass through the cavity focus)[68,69]. It is generally desirable therefore to excite only a single mode (preferably the TEM_{00}) in order to ensure a consistent ringdown time and maximise the signal to noise ratio. In order to selectively couple laser radiation into the TEM_{00} mode it is necessary to manipulate the laser beam such that, when it is injected into the cavity, it resembles the TEM_{00} mode as closely as possible (both in terms of beam diameter and radius of curvature of the wavefront). This is achieved through the use of one or more lenses in the beam path and this manipulation of the beam shape to ensure efficient coupling is referred to as mode matching.

The appropriate mode matching arrangement for a given CRDS system can be calculated using the beam parameter/ABCD matrix formalism described in Appendix A. The beam parameter of the radiation produced by a laser source (which is usually approximately Gaussian in cross section) can be straightforwardly estimated for visible and near IR lasers by imaging the laser spot with an appropriate camera. The effect of passing this beam through a series of lenses can then be calculated and the positions and focal lengths of the lenses varied so as to ensure that the beam that enters the cavity couples efficiently into the TEM_{00} mode. Mode matching lenses are used in the CRDS experiment in this thesis along with careful cavity alignment in order to ensure that the TEM_{00} is preferentially excited.

The clipping of cavity modes

Later in this thesis (chapter 10) CRDS spectra will be reported for the case where the laser beam propagates close to a surface. As the surface, the plane of which lies parallel to the cavity axis, is introduced into the optical cavity it will begin to clip the cavity modes and thereby cause an extra loss of photons upon each cavity round trip. This clipping of the intracavity field leads to a reduction in the ringdown time and provided the intracavity spot size is known, can be used to calibrate the distance

between the surface and the centre of the beam. The lowest order cavity mode will have a Gaussian intensity distribution:

$$I = I_0 \exp\left(-\frac{2(x^2+y^2)}{w^2}\right) \tag{2.41}$$

where x and y are the two orthogonal dimensions perpendicular to the cavity axis and w is the beam spot size. If the surface approaches to a distance d from the negative x-direction then the fraction of the laser that is not clipped by the surface, f, can be calculated as:

$$f = \frac{P_{unclipped}}{P_{total}} = \frac{\int_{x=-d}^{\infty}\int_{y=-\infty}^{\infty} I_0 \exp\left(-\frac{2(x^2+y^2)}{w^2}\right) \mathrm{d}x\mathrm{d}y}{\int_{x=-\infty}^{\infty}\int_{y=-\infty}^{\infty} I_0 \exp\left(-\frac{2(x^2+y^2)}{w^2}\right) \mathrm{d}x\mathrm{d}y} \tag{2.42}$$

This can be simplified using the following standard integrals:

$$\int_{-\infty}^{\infty} \exp(-ax^2)\mathrm{d}x = \sqrt{\frac{\pi}{a}} \tag{2.43}$$

and

$$\int_{-d}^{\infty} \exp(-ax^2)\mathrm{d}x = \frac{1}{2}\sqrt{\frac{\pi}{a}}(1+\mathrm{erf}(d\sqrt{a})), \tag{2.44}$$

where erf is the error function defined as

$$\mathrm{erf}(z) = \frac{2}{\sqrt{\pi}}\int_0^z \exp(-t^2)\mathrm{d}t \tag{2.45}$$

to give

$$f = \frac{1}{2}\left(1+\mathrm{erf}\left(\frac{d\sqrt{2}}{w}\right)\right). \tag{2.46}$$

The losses on each pass through the cavity are directly related to the ringdown time. When the losses are only due to losses from the mirrors the ringdown time is given by equation 2.37, when losses due to clipping are also included then the appropriate equation is

$$\tau_{clip} = \frac{-L}{c\ln R + c\ln f}. \tag{2.47}$$

It is convenient to determine the ratio of the unclipped and clipped ringdown times,

$$\frac{\tau_0}{\tau_{clip}} = 1 + \frac{\ln f}{\ln R}. \tag{2.48}$$

An example in which this equation is utilised to find the separation of the cavity mode and the surface will be presented in chapter 10.

2.5.2 Cavity enhanced absorption spectroscopy (CEAS)

CEAS removes the need for an optical switch and for careful mode matching, and is often easier to realise experimentally than CRDS. CEAS relies on laser radiation coupling accidentally into (usually high order) modes of the cavity. The laser is scanned repeatedly and rapidly over the region of interest such that it excites many high order cavity modes in turn. During the laser scan each cavity mode will be excited by the laser for approximately an equal time after which the intensity of radiation within this cavity mode will decay exponentially. The transmission of the cavity is measured by a detector and includes contributions from many cavity modes each excited and then decaying in turn. The transmitted intensity therefore depends on the reflectivity of the mirrors and importantly on the absorption taking place in the cavity. Crucially, the cavity should be aligned such that low order modes are avoided, because excitation of these modes can lead to undesirable sharp residual mode structure in the cavity transmission signal. Typically the signal from several hundred laser scans are averaged and CEAS signals are obtained both without an absorber ($I_0(\nu)$) and with an absorber ($I(\nu)$).

The CEAS signals are then related to the absorption coefficient according to:

$$\frac{I_0(\nu) - I(\nu)}{I(\nu)} = \frac{\alpha(\nu)L}{1-R}, \tag{2.49}$$

where L is the cavity length and R is the apparent mirror reflectivity, which is often found using equation 2.37 with one of the low order cavity modes used to measure the ringdown time. This can be a source of error in CEAS results however, because the apparent R value for the low order mode is typically greater than that for the high order modes used for CEAS (the high order modes typically have other cavity losses that contribute to the apparent value of R). An alternative is to use a known pressure of a calibrant gas to define the pathlength enhancement factor, $(1-R)^{-1}$.

2.6 Saturation in spectroscopy

In section 2.1 the assumption that $N_1 >> N_2$ was inherent in deriving the Beer-Lambert law, equation (2.8). This implies that care must be taken if there is any reason to believe that the upper state of a transition might have a significant population. This could be the case, for example, if the plasma produces a significant amount

of the upper state accessed in the transition (this is relevant to the oxygen Noxon band). Another possible reason for significant upper state population density, N_2, is the effect of optical pumping due to the probe laser. This is particularly relevant in this thesis when CRDS is used to probe allowed transitions (for an example see chapter 8) and where the intracavity field can be of very high intensity (of the order $10^8\,\mathrm{Wm}^{-2}$). In this scenario the rate of excitation to the upper state of the transition due to the intense field can be significantly greater than the rate of its depopulation (for example by collisional de-excitation or spontaneous emission). This leads to a build up of excited state population and (according to equation 2.7) a reduction in the absorption coefficient. The reduction of absorption coefficients due to pumping by an intense laser is called optical saturation and is an effect that needs to be quantified and accounted for in order to extract meaningful densities from saturated spectra. The precise implications of saturation for spectral lineshapes depends on the dominant broadening mechanism[43,70] and these are now discussed.

2.6.1 Homogeneously broadened lines

The homogeneous lineshape for an absorption transition in the absence of saturation is given by equation 2.29 with a scaled normalisation factor such that the absorption coefficient at the line centre $\alpha_0(\nu_0)$ is returned when $\nu = \nu_0$[43]:

$$\alpha_0(\nu) = \alpha_0(\nu_0)\frac{(\frac{\Delta\nu_L}{2})^2}{(\nu-\nu_0)^2+(\frac{\Delta\nu_L}{2})^2} \tag{2.50}$$

where $\Delta\nu_L$ is the unsaturated Lorentzian FWHM. The effects of saturation are conveniently quantified by the saturation parameter, S, which is the ratio of the pumping rate, P, to the average relaxation rate of the excited state, $\bar{R}$:

$$S = \frac{P}{\bar{R}}. \tag{2.51}$$

This means that, if relaxation is fast or the pumping rate low then $S \approx 0$ and the unsaturated case is recovered. For homogeneously broadened transitions, all the absorbing atoms or molecules contribute to the entire lineshape and this means that in the wings of the Lorentzian profile the pumping rate must be less than at the line centre (because the same number of absorbers are being addressed, but the absorption is smaller). Thus the saturation parameter for homogeneously broadened lines varies as a function of frequency across the lineshape according to:

$$S(\nu) = S(\nu_0)\frac{(\frac{\Delta\nu_L}{2})^2}{(\nu-\nu_0)^2+(\frac{\Delta\nu_L}{2})^2}, \tag{2.52}$$

where $S(\nu_0)$ is the saturation parameter at the line centre. The saturation leads to a reduced absorption coefficient, $\alpha_S(\nu)$, given by:

$$\alpha_S(\nu) = \frac{\alpha_0(\nu)}{1+S(\nu)} = \alpha_0(\nu_0)\frac{(\frac{\Delta\nu_L}{2})^2}{(\nu-\nu_0)^2 + \left(\frac{\Delta\nu_L\sqrt{1+S(\nu_0)}}{2}\right)^2}. \tag{2.53}$$

Power broadening

One important effect of saturating a homogeneously broadened transition is the additional line broadening that results, known as power broadening[43,58]. Equation 2.53 takes the form of a Lorentzian but instead of the usual FWHM ($\Delta\nu_L$) that is observed in an unsaturated spectrum, the width of the saturated line, $\Delta\nu_{L,S}$ is instead given by

$$\Delta\nu_{L,S} = \Delta\nu_L\sqrt{1+S(\nu_0)}. \tag{2.54}$$

This broadening of the Lorentzian profile arises because of the variation in the degree of saturation across the absorption profile, the line centre is more saturated than the wings, thus its absorption coefficient is reduced more significantly and the absorption profile becomes smaller in amplitude and wider. A series of simulated spectra with increasing saturation parameter and plotted according to equation 2.53 are shown in figure 2.1.

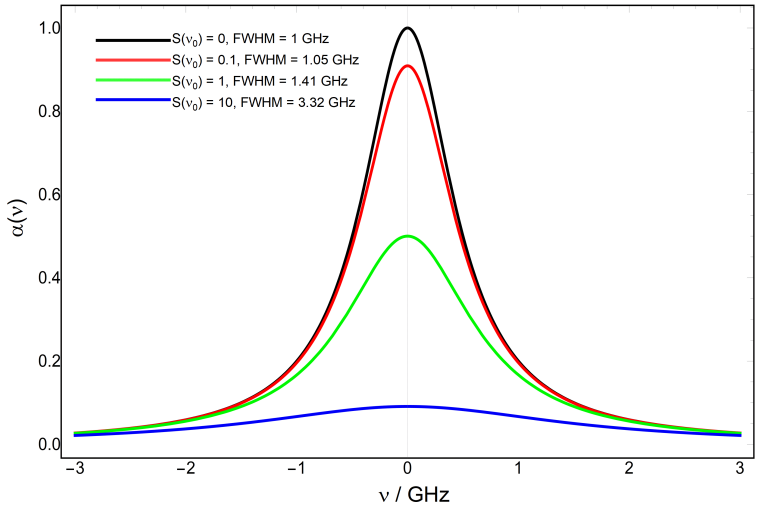

Figure 2.1: A series of simulations of increasingly saturated homogeneously broadened spectra. In this case the saturation both decreases the apparent absorption coefficient and leads to a broadening of the line (by so called power broadening).

2.6.2 Inhomogeneously broadened lines

The unsaturated lineshape for an inhomogeneously broadened transition can be written:[70]

$$\alpha_0(\nu) = \alpha_0(\nu_0) \exp\left(-\frac{4\ln 2}{\Delta\nu_D^2}(\nu - \nu_0)^2\right), \tag{2.55}$$

where $\Delta\nu_D$ is again the FWHM for the Doppler profile. When taking the spectrum of an inhomogeneously (Doppler) broadened transition the laser now only addresses a small subset of absorbers at any particular frequency (the group that has the appropriate velocity component in the beam direction to experience the laser frequency in resonance, known as a velocity group). The absorption coefficient in the wings of the line in this case is reduced, not because the pumping rate is any different amongst the molecules being addressed, but because there are fewer molecules with the required velocity to be addressed by the laser. The probability of excitation per molecule is the same across the whole transition lineshape, and so is the saturation parameter, in stark contrast to the case of homogeneously broadened lines. Thus, in a saturated absorption experiment on a Doppler broadened line, as the laser scans across the transition it depletes each velocity group of the absorbing molecule in turn in a process called *hole burning*, producing a so called *Bennett hole*[71]. A schematic of hole burning is shown in figure 2.2 with the Bennett hole in the lower state population and an excess for the same velocity component in the upper state of the transition.

Importantly, for a single pass experiment hole burning reduces $\alpha_0(\nu)$ by the same proportion at each frequency and the resulting absorption lineshape, $\alpha_S(\nu)$ shows no holes but is simply a scaled version of the unsaturated lineshape given by[70]

$$\alpha_S(\nu) = \frac{\alpha_0(\nu)}{\sqrt{1+S}} = \frac{\alpha_0(\nu_0)}{\sqrt{1+S}} \exp\left(-\frac{4\ln 2}{\Delta\nu_D^2}(\nu - \nu_0)^2\right), \tag{2.56}$$

where S is now independent of frequency.

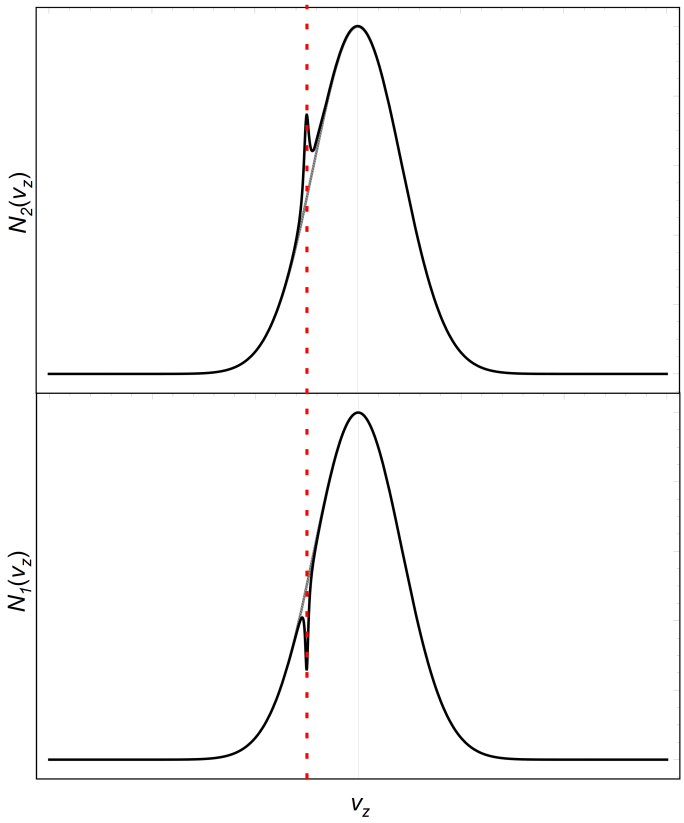

Figure 2.2: A schematic of the depletion in the population density of lower state molecules N_1 and the accompanying increase in population of the same velocity group in the excited state N_2. The depletion in population is known as hole burning and results in a so called Bennett hole.

Simulated saturated spectra, plotted according to equation 2.56 are shown in figure 2.3, note that due to the square root in equation 2.56 the reduction in peak absorption coefficient is less significant in the inhomogeneous case than in the homogeneous case (figure 2.1) for the same value of S. Also note that, for transitions that only experience inhomogeneous broadening, the FWHM is unchanged by saturation, although in practice all transitions have some homogeneous linewidth contribution which could, in principle, become dominant as saturation parameters become very large.

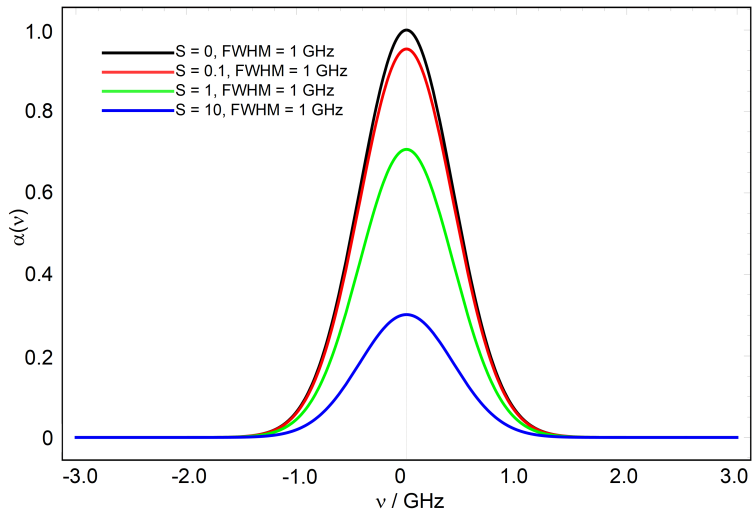

Figure 2.3: A series of simulations of increasingly saturated inhomogeneously broadened spectra. The saturation decreases the apparent absorption coefficient but less so than in the homogeneous case. Purely inhomogeneously broadened spectra do not exhibit power broadening.

Lamb dips

Hole burning cannot be observed by single pass absorption, because it affects all velocity groups equally. It can be observed, however, by taking the output of a single laser source and splitting it into an intense pump beam and a weak probe beam. If these two beams are passed through a sample in opposite directions then they interact with different velocity groups. Specifically, if the pump beam interacts with molecules with velocity in the z-direction, v_z, then the probe beam interacts with the group of molecules with velocity component $-v_z$. The intense pump beam will burn a hole in the velocity distribution at v_z whilst the probe beam (which is too weak to cause saturation) will measure the unsaturated spectrum of the molecules with velocity component $-v_z$. Thus the probe spectrum will largely appear unsaturated with one important exception. When the laser source is tuned to the line centre the two counter propagating beams address the same molecules (those with $v_z = 0$). The strong pump will burn a hole in the population and thus the probe beam will experience a smaller absorption coefficient. This will lead to the formation of a dip in the middle of the probe beam spectrum, known as a Lamb dip[72]. When the laser linewidth is sufficiently narrow the width of the Lamb dip is dictated by the homogeneous broadening mechanisms acting on the system (Lamb dips are Doppler free because they are only formed by the subset of molecules with $v_z = 0$). The

spectrum produced by monitoring the intensity of the probe beam as the frequency is scanned over a transition has the form:[70]

$$\alpha_S(\nu) = \alpha_0(\nu)\left(1 - \frac{S}{\sqrt{1+S}}\frac{\left(\frac{\Delta\nu_L}{2}\right)^2}{(\nu-\nu_0)^2 + \left(\frac{\Delta\nu_L + \Delta\nu_{L,S}}{4}\right)^2}\right) \tag{2.57}$$

where S is the saturation parameter associated with the pump beam (the probe beam is assumed to cause no saturation). By definition under conditions where inhomogeneous broadening dominates $\Delta\nu_D >> \Delta\nu_L$ and the observed lineshape is then an unsaturated Doppler profile away from the Lamb dip. The Lamb dip itself is a Lorenztian with a width (FWHM) equal to $(\Delta\nu_L + \Delta\nu_{L,S})/2$, *i.e.* the average of the power broadened homogeneous width of the Bennett hole burnt by the pump beam ($\Delta\nu_{L,S}$) and the homogeneous width associated with the weak probe beam ($\Delta\nu_L$).

Figure 2.4 shows example Lamb dip spectra for several values of the (pump beam) saturation parameter. Note that all spectra are identical (and unsaturated) in the wings because the pump and probe beams do not probe the same velocity group in these regions so the probe beam sees no saturation effects from the pump beam. Additionally the Lamb dip width increases with increasing saturation parameter due to the power broadening of the Bennett hole burnt by the intense pump beam.

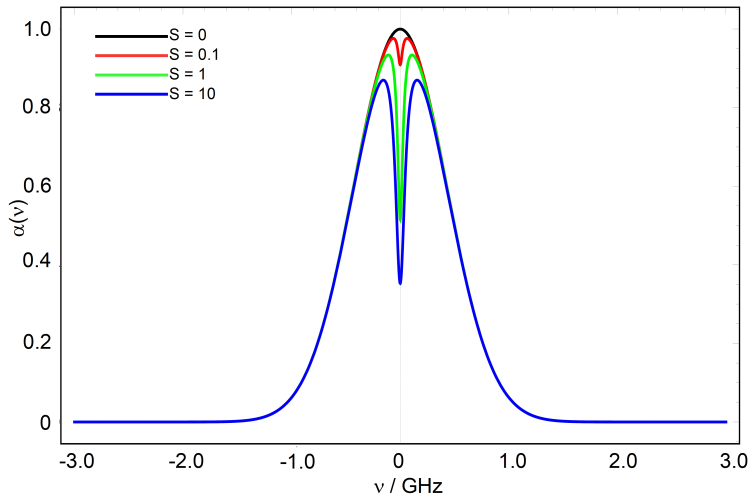

Figure 2.4: A series of simulations of the spectra expected when an intense pump beam and a weak probe beam are passed through a saturable sample and the spectrum is measured using the weak beam. Here S represents the level of saturation caused by the intense beam. Away from resonance the two beams address different velocity groups and the absorption appear unsaturated. On resonance the same velocity group is addresses by both beams and the a Lamb dip is observed. Lamb dips represent only one velocity group of molecules and are thus free from Doppler broadening.

Saturation in an optical cavity

A more complex case of Lamb dip spectroscopy arises when the two counter-propagating beams are both equally intense and both can therefore cause optical saturation. This situation occurs within an optical cavity, where the standing wave cavity modes can be thought of as a linear combination of two equally intense beams propagating in opposite directions. Here it would be expected that, away from the line centre, the absorption coefficient is given by:[58,70]

$$\alpha_S(\nu) = \frac{\alpha_0(\nu)}{\sqrt{1+S}}, \tag{2.58}$$

and at the line centre by

$$\alpha_S(\nu) = \frac{\alpha_0(\nu)}{\sqrt{1+2S}}, \tag{2.59}$$

where S is the saturation parameter for *one* of the two counter-propagating beams and the degree of saturation doubles at the line centre relative to the wings. The full lineshape that meets these requirements and is therefore appropriate for the saturated CRDS spectra presented in this thesis is given by[58,70]

$$\alpha_S(\nu) = \alpha_0(\nu)\frac{\frac{\Delta\nu_L}{2}}{B\left(1-\left(\frac{2(v-v_0)}{A+B}\right)^2\right)^{\frac{1}{2}}}, \tag{2.60}$$

where

$$A = \left((\nu-\nu_0)^2 + \left(\frac{\Delta\nu_L}{2}\right)^2\right)^{\frac{1}{2}} \tag{2.61}$$

and

$$B = \left((\nu-\nu_0)^2 + \left(\frac{\Delta\nu_L}{2}\right)^2(1+2S)\right)^{\frac{1}{2}}. \tag{2.62}$$

Figure 2.5 shows a series of spectra with different saturation parameters plotted according to equation 2.60. Note that these spectra show an overall decrease in absorption coefficient with increasing S as observed in figure 2.3 and also Lorentzian Lamb dips which broaden with increasing saturation parameter. The Lamb dips in this case are expected to have widths given by[58,70]

$$\Delta\nu_{L,S} \approx \Delta\nu_L\sqrt{1+S}, \tag{2.63}$$

in other words these Lamb dips are power broadened.

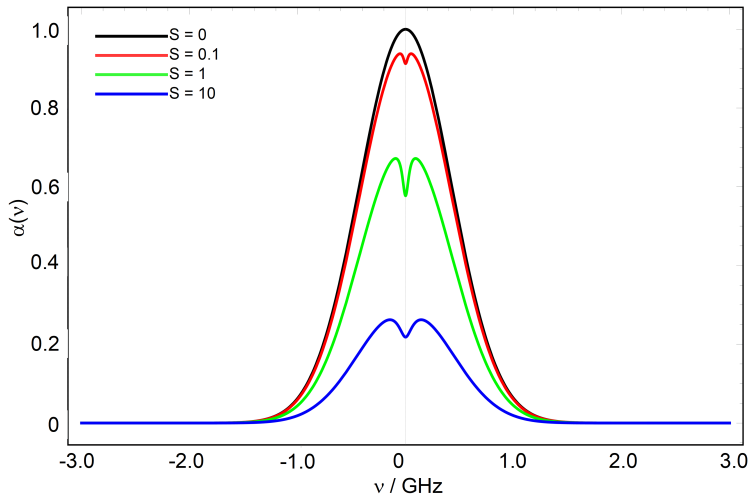

Figure 2.5: A series of simulations of the spectra expected when two equally intense beams are passed through a saturable sample. Here S represents the level of saturation caused by one of the two beams. Away from resonance the saturation is caused by a single beam and the spectra are identical to those in figure 2.3. On resonance the same velocity group is addresses by both beams and a Lamb dip is observed due to the doubling of the saturation parameter. The Lamb dips are Doppler free but exhibit power broadening.

2.7 Electronic and rotational structure of atoms and diatomic molecules

The spectroscopic experiments discussed in the remainder of this thesis utilise electronic transitions within atoms and molecules found within the plasma chamber, it is therefore pertinent to describe the energy level structure of these species.

2.7.1 Atomic terms and selection rules

The pertinent example for this thesis is that of atomic oxygen whose ground state electronic configuration is $1s^2 2s^2 2p^4$. In symmetry terms this configuration (with two holes in the unfilled subshell) is equivalent to having two electrons in this subshell (the hole formalism) and gives rise to three Pauli allowed atomic terms: ^{3}P, ^{1}D and ^{1}S (see appendix B for an explanation of atomic terms). The energy ordering of these terms is predicted by Hund's rules[73]. The lowest ^{3}P term is split into three levels by spin orbit coupling ($^3P_2$, $^3P_1$ and $^3P_0$) leading to the energy level diagram shown in figure 2.6.

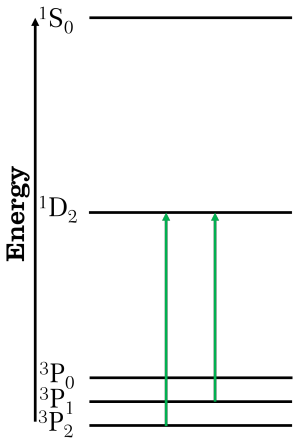

Figure 2.6: Energy level diagram of the low lying states of atomic oxygen.

The selection rules for atomic transitions (arising from the requirement that the transition moment matrix element must be non-zero in order for a transition to be allowed) are shown in table 2.3[44].

Table 2.3: Selection rules for electronic transitions in atoms within the Russell-Saunders coupling regime. The rules for ΔL and ΔS hold only within Russell-Saunders coupling and can be relaxed when spin-orbit coupling becomes large.

Selection rule	Electric Dipole	Magnetic Dipole	Electric Quadrupole
Δn	anything	0	anything
Δl	± 1	0	$0, \pm 2$
parity	changed	unchanged	unchanged
ΔJ	$0, \pm 1$ (not $0 \leftrightarrow 0$)	$0, \pm 1$ (not $0 \leftrightarrow 0$)	$0, \pm 1, \pm 2$ (not $0 \leftrightarrow 0$, $\frac{1}{2} \leftrightarrow \frac{1}{2}$ or $0 \leftrightarrow 1$)
ΔL	$0, \pm 1$ (not $0 \leftrightarrow 0$)	0	$0, \pm 1, \pm 2$ (not $0 \leftrightarrow 0$ or $0 \leftrightarrow 1$)
ΔS	0	0	0

Since all the levels depicted in figure 2.6 arise from the same electron configuration, any transitions between them necessarily have $\Delta l = 0$ and are thus electric dipole forbidden. Several of the transitions however have non-zero magnetic dipole or electric quadrupole moments and occur with low probability. Two such transitions

are depicted in the figure and are those used in this thesis. These transitions occur at ≈ 630 nm and are used to detect O(^{3}P) because the lowest energy allowed transitions of this species only occur at difficult to handle wavelengths < 130 nm. Both of these transitions rely on the break down of Russell-Saunders coupling (i.e. large spin-orbit coupling) such that the spin selection rule ($\Delta S = 0$) is relaxed. Spin-orbit coupling can also relax the ΔL selection rule and thereby make the magnetic dipole moment for these transitions non-zero[74]. Each transition also has a small contribution ($< 0.5\%$ of total line strength) from being electric quadrupole allowed[74].

2.7.2 Molecular terms for diatomic molecules

The three diatomic species relevant to the work in this thesis are: O_2, N_2 and N_2^+, and the low lying configurations and resulting molecular terms (see appendix B) for these species are as follows.

O_2 electronic terms

The ground state configuration for O_2 is $(1\sigma_g)^2(1\sigma_u)^2(2\sigma_g)^2(2\sigma_u)^2(3\sigma_g)^2(1\pi_u)^4(1\pi_g)^2$. Like the atomic case, this configuration has two unpaired electrons and leads to three Pauli allowed terms; in order of increasing energy these are $O_2(X^3\Sigma_g^-)$, $O_2(a^1\Delta_g)$ and $O_2(b^1\Sigma_g^+)$. Figure 2.7 shows the potential energy curves for the lowest energy states of O_2, the three states arising from the ground state configuration are highlighted in red ($O_2(X^3\Sigma_g^-)$), blue ($O_2(a^1\Delta_g)$) and green ($O_2(b^1\Sigma_g^+)$).

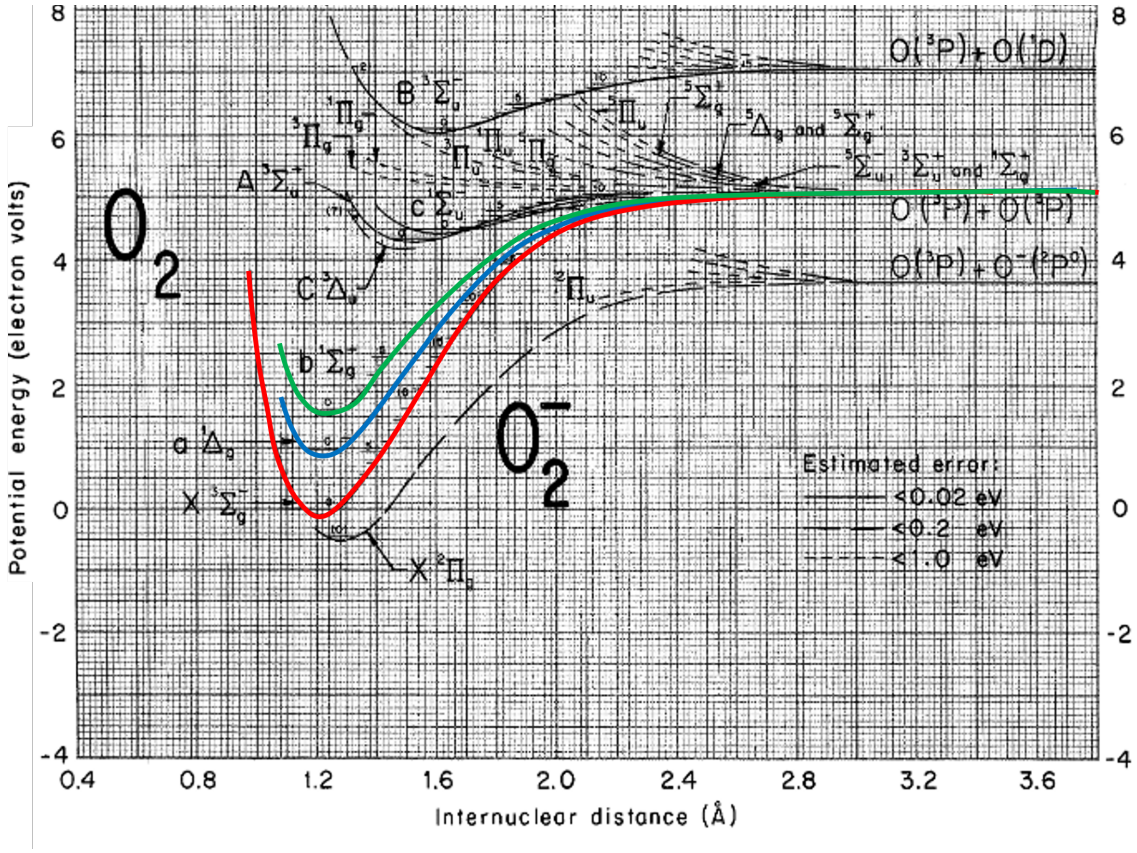

Figure 2.7: Potential energy curves for the low lying states of O_2 with the three states of interest in this thesis highlighted as described in the text. This figure is adapted from Gilmore[75].

N_2 electronic terms

The ground state configuration for N_2 is $(1\sigma_g)^2(1\sigma_u)^2(2\sigma_g)^2(2\sigma_u)^2(1\pi_u)^4(3\sigma_g)^2$. This configuration is closed shell and gives rise to only the totally symmetric $N_2(X^1\Sigma_g^+)$ ground state term. The first and second excited states of N_2 arise from different configurations, the first excited $N_2(A^3\Sigma_u^+)$ term arises (along with other higher energy terms) from the $(1\sigma_g)^2(1\sigma_u)^2(2\sigma_g)^2(2\sigma_u)^2(1\pi_u)^3(3\sigma_g)^2(1\pi_g)^1$ configuration whilst the second most important excited $N_2(B^3\Pi_g)$ term arises (again with other higher energy terms) from the $(1\sigma_g)^2(1\sigma_u)^2(2\sigma_g)^2(2\sigma_u)^2(1\pi_u)^4(3\sigma_g)^1(1\pi_g)^1$ configuration. These three states are depicted in the lower half of figure 2.8 highlighted in red ($N_2(X^1\Sigma_g^+)$), blue ($N_2(A^3\Sigma_u^+)$) and green ($N_2(B^3\Pi_g)$).

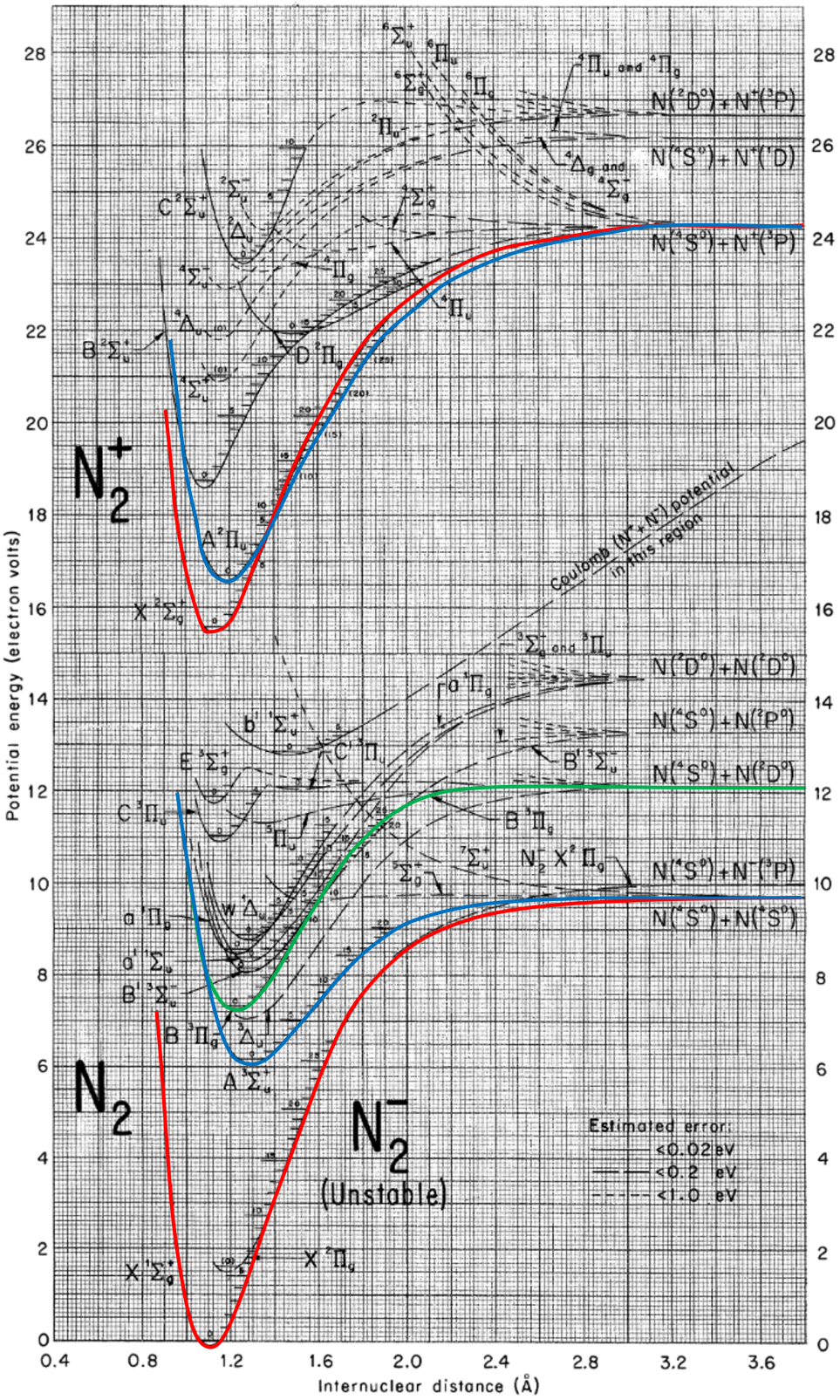

Figure 2.8: Potential energy curves for the electronic states of N_2 and N_2^+ with the states of interest in this thesis highlighted as described in the text. This figure is adapted from Gilmore[75].

N_2^+ electronic terms

The ground state configuration for N_2^+ is $(1\sigma_g)^2(1\sigma_u)^2(2\sigma_g)^2(2\sigma_u)^2(1\pi_u)^4(3\sigma_g)^1$. This configuration gives rise to only the spin doublet $N_2^+(X^2\Sigma_g^+)$ ground state term. The first excited state of N_2^+ arises from the $(1\sigma_g)^2(1\sigma_u)^2(2\sigma_g)^2(2\sigma_u)^2(1\pi_u)^3(3\sigma_g)^2$ configuration which also gives rise to one term; $N_2^+(A^2\Pi_u)$. The potential energy curves for these two states are shown in the top half of figure 2.8 highlighted in red ($N_2^+(X^2\Sigma_g^+)$) and blue ($N_2^+(A^2\Pi_u)$).

2.7.3 Vibrational structure

Unlike atoms, molecules can both vibrate and rotate and these degrees of freedom add structure to molecular energy levels and spectra. The vibrational structure of diatomic molecules is, in general, simple, with each electronic state having a stack of non-degenerate vibrational levels. During an electronic transition the change in vibrational state is unrestricted and thus an electronic absorption system consists of a series of vibrational bands. The relative intensities of these vibrational bands depends on their Franck-Condon factors and populations of the initial vibrational states.

2.7.4 Rotational structure

Rotational structure in diatomic spectra can be much more complicated. In order to understand the rotational energy levels it is important to know how the various sources of angular momentum possessed by the molecule couple to one another. Hund established how coupling occurs for a series of limiting cases whereby some couplings are much stronger than others[76–78]. Details of the relevant Hund's cases ((a) and (b)) and the good quantum numbers in each case are given in appendix B.

The selection rules for electronic transitions in diatomic molecules that obey Hund's cases (a) and (b) are given in table 2.4[78]. In the table the first two rows provide selection rules relating to the electronic states whilst the next three rules restrict the specific rotational transitions that can occur. Changes in vibrational state during electronic transitions are unrestricted but with intensities governed by Franck-Condon factors. Additionally, all transitions are subject to the approximate selection rule $\Delta S = 0$ however transitions that violate this rule can become allowed due to spin-orbit coupling, in analogy with the atomic case.

Table 2.4: Selection rules for electronic transitions in diatomic molecules (note that $\Delta\Lambda = 0$ transitions are only magnetic dipole allowed when the spin selection rule is broken (i.e. $\Delta S \neq 0$) see page 277 of Herzberg[78]).

Selection rule	Electric Dipole	Magnetic Dipole	Electric Quadrupole
$\Delta\Lambda$	$0, \pm 1$	$(0), \pm 1$	$0, \pm 1, \pm 2$
g/u	$g \leftrightarrow u$	$g \leftrightarrow g$ / $u \leftrightarrow u$	$g \leftrightarrow g$ / $u \leftrightarrow u$
ΔJ	$(0), \pm 1$ (not $0 \leftrightarrow 0$)	$(0), \pm 1$ (not $0 \leftrightarrow 0$)	$(0), \pm 1, \pm 2$ (not $0 \leftrightarrow 0$, $\frac{1}{2} \leftrightarrow \frac{1}{2}$ or $0 \leftrightarrow 1$)
$\oplus/\ominus$	$\oplus \leftrightarrow \ominus$	$\oplus \leftrightarrow \oplus/\ominus \leftrightarrow \ominus$	$\oplus \leftrightarrow \oplus/\ominus \leftrightarrow \ominus$
s/a	$s \leftrightarrow s/a \leftrightarrow a$	$s \leftrightarrow s/a \leftrightarrow a$	$s \leftrightarrow s/a \leftrightarrow a$
ΔS	0	0	0

Rotational structure of O_2

The ground state, $O_2(X^3\Sigma_g^-)$ is well described by Hund's case (b). The projection of the *electronic orbital angular momentum* on the internuclear axis is zero ($\Lambda = 0$) and the *electronic spin angular momentum quantum number* $S = 1$. Hence the *total angular momentum quantum number excluding spin*, N, is simply equal to the *molecular rotation quantum number*, R, and the possible values of the *total angular momentum quantum number* J are $J = N + 1$ (labelled F_1), $J = N$ (labelled F_2) and $J = N - 1$ (labelled F_3). The first excited state, $O_2(a^1\Delta_g)$, has $\Lambda = 2$ but no spin angular momentum ($S = 0$) such that there is no distinction between Hund's cases (a) and (b) and $J = N = 2 + R$ for this state. Each level in this state is also doubly degenerate due to the two possible electronic angular momentum vectors $\mathbf{L}$ that each have the same projection magnitude, $|\Lambda|\hbar$. This is referred to as Λ-doubling because it is present in all states with $\Lambda > 0$ and this degeneracy may be lifted if the coupling of $\mathbf{L}$ to $\mathbf{R}$ is accounted for. This coupling is neglected in Hund's cases (a) and (b) and indeed is so small in $O_2(a^1\Delta_g)$ that it has no effect on the spectrum. Finally, the second excited state, $O_2(b^1\Sigma_g^+)$, has no electronic angular momentum at all and so Hund's cases are not wholly necessary ($J = R$). The rotational structure that results from these angular momentum couplings for each of the three lowest lying electronic states is shown in figure 2.9. The Pauli principle dictates that the total wavefunction (product of space and spin wavefunctions) must be symmetric (s) with respect to the exchange of Bosons (^{16}O in this case). For ^{16}O the nuclear spin quantum number, $I = 0$, and hence the nuclear spin wavefunction can only have s

symmetry. Therefore the only allowed spatial wavefunctions are those that also have s symmetry, the rotational levels with a symmetry do not exist for O_2 and only one of each pair of Λ-doubled levels exist in the $O_2(a^1\Delta_g)$ state. The Pauli forbidden levels are shown as dashed lines in figure 2.9.

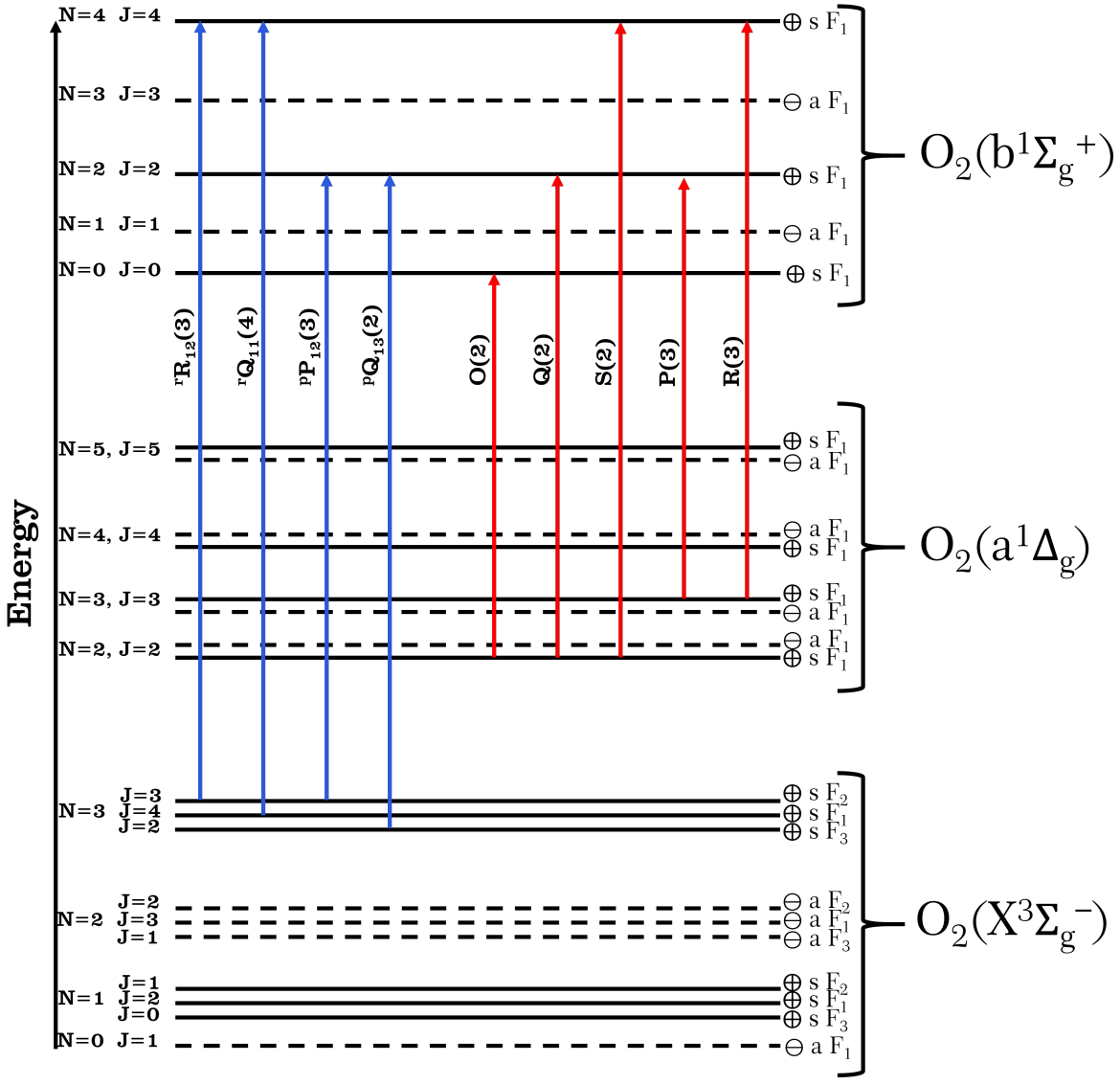

Figure 2.9: Rotational energy level diagram of the first three electronic states of O_2 along with the symmetry labels of each level (see text). Also shown are rotational transitions (one from each of the possible rotational branch) in each of the two systems which are investigated by CRDS in this chapter (the $O_2(b^1\Sigma_g^+) \leftarrow O_2(X^3\Sigma_g^-)$ system in blue and the $O_2(b^1\Sigma_g^+) \leftarrow O_2(a^1\Delta_g)$ Noxon system[50] in red)

From the selection rules (table 2.4) and figure 2.9 it is clear that none of the possible transitions between the three low lying states of O_2 are electric dipole allowed. The $O_2(b^1\Sigma_g^+) - O_2(X^3\Sigma_g^-)$ system is spin forbidden but magnetic dipole allowed; the $O_2(b^1\Sigma_g^+) - O_2(a^1\Delta_g)$ Noxon system[50] is electric quadrupole allowed and the $O_2(a^1\Delta_g) - O_2(X^3\Sigma_g^-)$ system is spin forbidden and electric quadrupole allowed. For this reason all of these bands are very weakly absorbing (particularly those systems that are magnetic dipole forbidden) and they require large pathlengths in order to be observed in absorption, for example through use of cavity enhanced absorption techniques (see section 2.5).

In this thesis measurements are reported on two of these systems, both shown in figure 2.9. The first, shown in blue, is the $O_2(b^1\Sigma_g^+) - O_2(X^3\Sigma_g^-)$ system which is first measured in emission in chapter 4 (giving information on $O_2(b^1\Sigma_g^+)$) and later in absorption as a probe for $O_2(X^3\Sigma_g^-)$ in chapter 6. The (0, 0) vibrational band of this transition is commonly known as the oxygen A-band[79]. The branches of this transition are labelled according to the following scheme ${}^{\Delta N}\Delta J_{F'F''}(J'')$, hence, for example, the transition from $N'' = 3, J'' = 4, (F_1)$ to $N' = 4, J' = 4, (F_1)$ has $\Delta N = +1 \rightarrow r$, $\Delta J = 0 \rightarrow Q$, $F' = F_1 \rightarrow 1$, $F'' = F_1 \rightarrow 1$ and $J'' = 4$ and therefore has the overall assignment ${}^rQ_{11}(4)$. The four branches that appear in the spectrum of O_2 are shown in the diagram. Notably, three other branches (${}^qQ_{12}$,${}^q R_{13}$ and ${}^qP_{11}$) can appear for such electronic transitions but are absent from the spectrum of O_2 due to nuclear spin statistics.

The second group of transitions shown in red are those of the Noxon system and this is measured in absorption to quantify temperatures and densities of $O_2(a^1\Delta_g)$ in chapter 4. Calculations of line strengths for this band were given in detail in section 2.2.2. Assignment of the lines of the Noxon band is straightforward because $N = J$ in both the electronic states involved. The transitions are therefore simply denoted $\Delta J(J'')$. For an electric quadrupole transition this leads to five branches, O-, P-, Q-, R- and S- corresponding to $\Delta J = -2, -1, 0, 1$ and 2 respectively. Due to nuclear spin statistics the O-, Q- and S- branches are missing the lines with odd J'' whilst the P- and R- branches are missing the lines with even J''.

Rotational structure of N_2

Figure 2.10 shows the rotational energy levels for the first and second excited states of N_2. The first excited state $N_2(A^3\Sigma_u^+)$ is well described by Hund's case (b) and hence has rotational structure very similar to $O_2(X^3\Sigma_g^-)$ except for the fact that each rotational state has the opposite $\oplus/\ominus$ symmetry. The second excited state, $N_2(B^3\Pi_g)$,

obeys (to a good approximation) Hund's case (a) with $|\Lambda| = 1$ and the *electron spin angular momentum projection quantum number*, $\Sigma = 1$, giving rise to three spin orbit manifolds: the lowest in energy has the *total electronic angular momentum projection quantum number*, $\Omega = 0$, and is labelled F_1, followed by $\Omega = 1$ labelled F_2 and $\Omega = 2$ labelled F_3. Within each manifold the minimum value of J is Ω and each state is Λ-doubled (the extent of Λ-doubling is greatly exaggerated in figure 2.10).

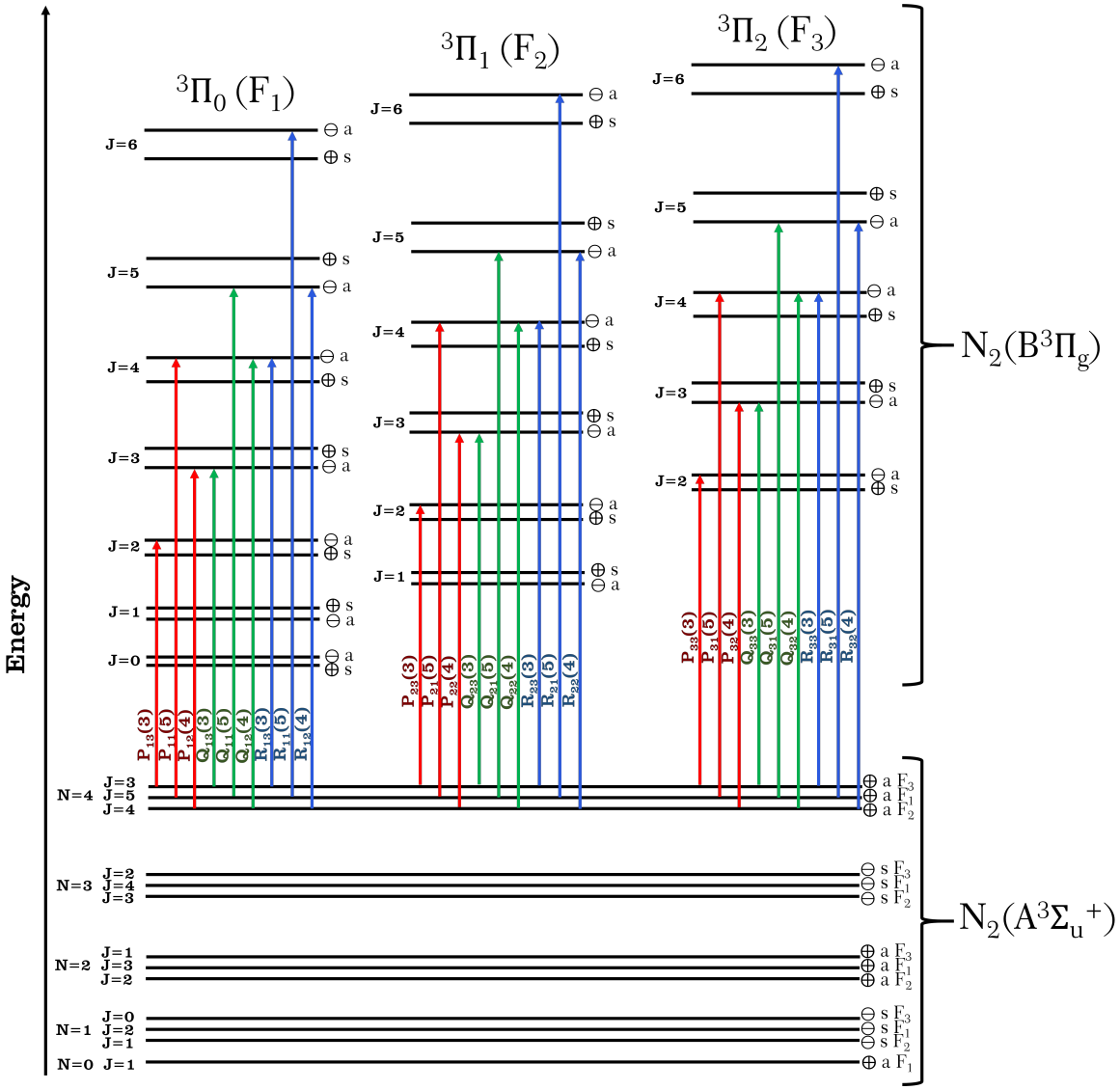

Figure 2.10: A rotational energy level diagram of the first two electronically excited states of molecular nitrogen. Also depicted are the rotational transitions (one from each possible branch) of the first positive system of nitrogen ($N_2(B^3\Pi_g) \leftarrow N_2(A^3\Sigma_u^+)$).

For ^{14}N the nuclear spin quantum number, I, is equal to 1, and leads to an alternation in population of the rotational states, with the s symmetry states having twice the population of the a symmetry states. Transitions between the first and second excited states of molecular nitrogen are fully allowed and constitute what is known as the first positive system of N_2. The complex rotational structure of the two states means that each vibrational band of the first positive system shows 27 rotational branches as shown in figure 2.10 where P-branch lines are depicted in red, Q-branch lines in green and R-branch lines in blue. Rotational lines are labelled very similarly to those of the oxygen A-band but without the superscript denoting the change in N (because N is not well defined for Hund's case(a)).

Rotational structure of $\mathbf{N_2^+}$

Figure 2.11 shows the rotational structure of the two lowest lying electronic states of N_2^+. The ground term of the nitrogen molecular cation, $N_2^+(X^2\Sigma_g^+)$, is well described by Hund's case (b) and has no orbital angular momentum, it is thus similar in rotational structure to $N_2(A^3\Sigma_u^+)$ and $O_2(X^3\Sigma_g^-)$ except that each N state is here split into a spin doublet rather than a triplet. Because the electronic term is of both g and $+$ symmetry the even N levels have $\oplus$ and s symmetry whilst the odd N levels have $\ominus$ and a symmetry (see appendix B). The first excited state $N_2^+(A^2\Pi_u)$ follows Hund's case (a) and hence has two spin-orbit manifolds ($\Omega = 3/2$ and $\Omega = 1/2$) where once again the minimum J value in each manifold is equal to Ω. As for N_2 the levels with s symmetry have twice the population of those with a symmetry due to nuclear spin statistics and each state is Λ-doubled. The transition between the two lowest lying electronic states is fully allowed and is referred to as the Meinel system of N_2^+[80]. Each vibrational band of the Meinel system shows 12 rotational branches as depicted in figure 2.11. The rotational lines are assigned is a way completely analogous to the assignments for the first positive system of N_2 and again P-, Q- and R- branch transitions are depicted in red, green and blue respectively.

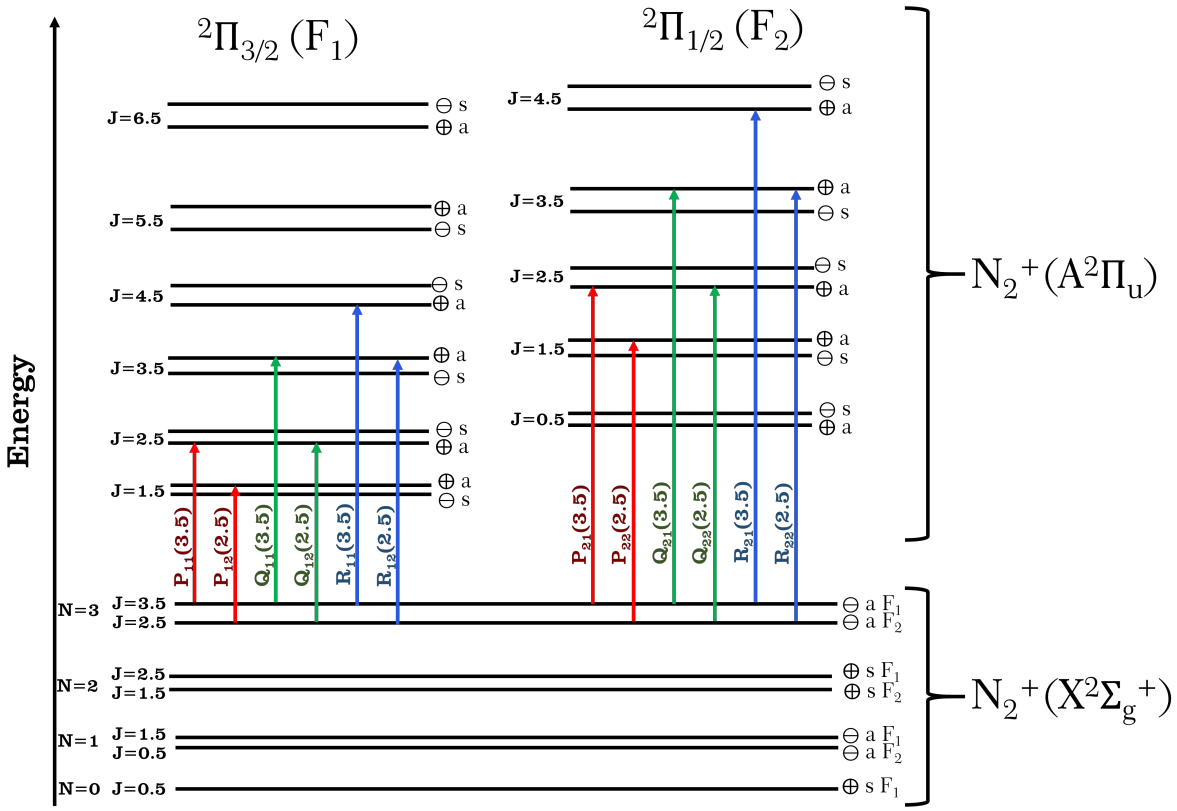

Figure 2.11: A rotational energy level diagram of the two lowest lying electronic states of the molecular nitrogen cation. Also depicted are the rotational transitions (one from each possible branch) of the Meinel system of the molecular nitrogen cation ($N_2^+(A^2\Pi_u) \leftarrow N_2^+(X^2\Sigma_g^+)$).

2.8 Summary

The foundations of optical spectroscopy have been described in this chapter, from the fundamentals (*e.g.* Einstein coefficients, rates of absorption and emission) to the more practical elements (*e.g.* cross sections and line broadening mechanisms). Cavity ringdown spectroscopy, from which minimum detectable absorption coefficients $\approx 10^{-10}$ cm^{-1} are achieved in this work, is explained in detail. Finally a detailed description of the energy levels in the key atomic and molecular species, O, O_2, N_2 and N_2^+ is given, from which the spectroscopy can be understood. Other pertinent information on the properties of passive optical cavities relevant here; on atomic and molecular terms and Hund's coupling cases (a) and (b); on the hardware required for CRDS measurements (lasers, detectors and acousto-optic modulators); and a line list

of all the transitions probed in this work and the lasers used to probe them can be found in appendices A, B, C and D, respectively.

Part II

Oxygen Plasma

Chapter 3

Introduction to oxygen plasma

3.1 Key species in oxygen plasma

Oxygen based plasmas are of fundamental interest[11,81,82] as they constitute a prime example of an electronegative plasma (a plasma in which negative ions play a significant role). They are also of industrial importance as oxygen-containing plasmas have been widely used in many fields, including plasma enhanced chemical vapour deposition (for example, of metal oxide films[83]), surface treatment/oxidation[84–86], chamber cleaning and etching of silicon dioxide layers[87], and plasma sterilisation of medical devices[88]. As a result of this interest from both academia and industry there has been much work, both experimental and theoretical[30,89,90], aimed at understanding these complex systems including analysis of the switch from the capacitive E-mode observed at low power to the technologically important, higher electron density, inductive H-mode seen at higher powers[91]. The chemistry and physics of these plasmas is heavily influenced not only by the presence of negative ions, but also high densities of ground state atoms, $O(^3P)$, and electronically excited molecules, particularly the low-lying metastable state, $O_2(a^1\Delta_g)$. Such is the importance of these species that accurate knowledge of their absolute densities is key to testing and refining models of both the gas-phase chemistry and the gas-surface interactions occurring in these complex systems, leading to for example, improvements in the quality of films produced by atomic layer deposition plasmas[42]. This chapter outlines the optical methods that have been used to detect $O(^3P)$ and $O_2(a^1\Delta_g)$ in plasma environments.

3.2 Techniques for $O(^3P)$ and $O_2(a^1\Delta_g)$ detection

A range of techniques have been developed to determine atomic and molecular metastable concentrations in O_2 plasmas, and the principles behind the most important tech-

niques, as well as their advantages and drawbacks are detailed here.

Optical emission and actinometry

Perhaps the simplest indication of the presence of atomic species in oxygen plasmas are the strong atomic emission lines (triplets at 777 nm ($1s^2 2s^2 2p^3 3p^1 (^5P) \rightarrow 1s^2 2s^2 2p^3 3s^1$ (^5S)) and 844 nm ($1s^2 2s^2 2p^3 3p^1 (^3P) \rightarrow 1s^2 2s^2 2p^3 3s^1$ (^3S)) being most prominent)[92]. The atomic states responsible for this emission are, by definition, excited and thus the intensity of the emission depends both on the density of ground state atoms and on the rate of excitation of these atoms to the emitting state. If this excitation is predominantly via electron impact excitation of ground state atoms then the emission intensity, I_O, increases with both atom and electron densities, $I_O = k_O[\mathrm{O}(^3P)][e]$, where k_O is a proportionality constant that accounts for both the rate coefficient for electron impact excitation and the probability that the excited state undergoes radiative decay.

In order to use this emission to quantify ground state atom densities it is necessary to quantify the excitation rate which, in principal, requires knowledge of electron impact cross sections as well as the electron density and energy distribution. These electron properties are in general difficult to determine but the need to know them can be partially bypassed by the addition to the plasma of a chemical actinometer (usually argon is chosen)[93–95]. The intensity of emission from excited states of this actinometer, I_{Ar} , also depend on its ground state density (which is known) and the electron density, such that $I_{Ar} = k_{Ar}[Ar][e]$. Thus the ratio between the O emission intensity and that of Ar should be independent of electron density and may be determined according to:

$$[\mathrm{O}(^3P)] = [Ar]\frac{k_{Ar} I_O}{k_O I_{Ar}}. \tag{3.1}$$

Thus, if the electron excitation cross sections are known for both species and their excitation threshold energies are similar (such that the section of the EEDF for excitation is the same for both species) then the ratio of proportionality constants, k_{Ar}/k_O can be determined and the density of ground state atoms $[\mathrm{O}(^3P)]$ can be deduced.

Actinometric measurements of this sort are practically easy to perform however they have several limitations. First, electron impact cross sections must be known in order to determine absolute number densities, such cross sections for O(^{3}P) are particularly difficult to measure because it is difficult to prepare a known concentration of atoms and as such semi-empirical or *ab initio* values which lack experimental

verification must be used[96]. Secondly, the technique requires the addition of Ar to the plasma and thus, although it can be of great use in probing oxygen-argon mixtures, the technique is inapplicable in pure oxygen plasmas. This is significant because even the addition of a small amount of argon can change the plasma properties[90,97]. Finally the technique assumes that all of the emitting state is formed by electron impact on $O(^3P)$. In reality oxygen plasma can contain a small but significant amount of $O(^1D)$ which may be excited to the emitting state by electron impact (with a different cross section to $O(^3P)$). Even more importantly it is also possible for the emitting atomic state to be formed directly by electron impact excitation/dissociation of molecular species, and although this pathway can be accounted for in more sophisticated actinometry schemes[98], this too requires knowledge of electron impact cross sections.

The presence of $O_2(a^1\Delta_g)$ may be confirmed directly by emission spectroscopy[96]. The only state to which $O_2(a^1\Delta_g)$ can emit is the molecular ground state $O_2(X^3\Sigma_g^-)$. This emission is weak due to its dipole and spin forbidden nature, with an Einstein A-factor of just 2.256×10^{-4} s^{-1} for the (0, 0) vibrational band[99]. Finding absolute densities from emission spectra is also very difficult requiring precise knowledge of the emitting volume being imaged onto the detector as well as the solid angle that the light collection optics image onto the detector[100]. Actinometric schemes for $O_2(a^1\Delta_g)$ are more or less impossible because whichever emitting state was chosen the majority of its population would originate from electron impact excitation of the more abundant molecular ground state $O_2(X^3\Sigma_g^-)$.

Two-photon laser induced fluorescence (TALIF)

A more sophisticated technique for $O(^3P)$ detection is that of two-photon laser induced fluorescence (TALIF)[101–105]. In a TALIF experiment a pulsed laser is used to excite a ground state atom to an excited state by the simultaneous absorption of two photons (a non-linear optical process). The excited state then emits (fluoresces) at 844 nm and the intensity of the fluorescence is directly proportional to the initial ground state atom density. A two photon pathway is chosen in order to avoid the need for deep ultraviolet photons ($\approx$ 113 nm) that would be required to undertake conventional LIF on atomic oxygen.

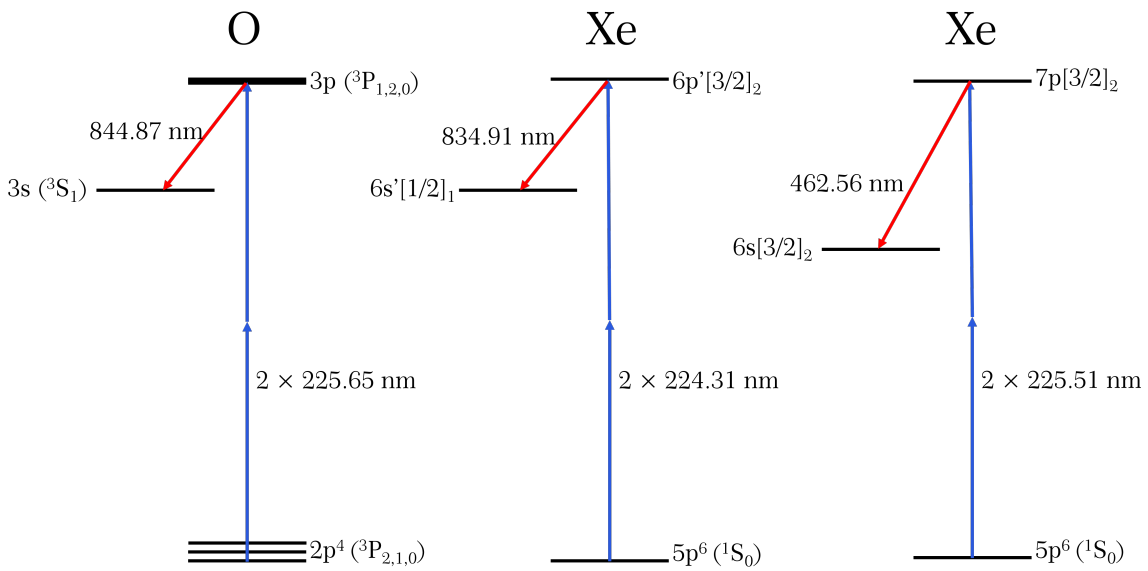

Figure 3.1: TALIF schemes for O and Xe. Either of the two possible Xe schemes can be used as a reference for calibration of the O TALIF signal. This figure is adapted from Peverall and Ritchie[106].

In order to achieve a calibration of the TALIF signal, to provide absolute atom number densities, once again a reference signal is required. O(^{3}P) TALIF typically uses the TALIF signal of Xenon as a reference[107]. Xenon is chosen because it is straightforward to introduce a known concentration into the chamber and because it has a two-photon excitation transition very close in wavelength to that of O(^{3}P). The oxygen atom TALIF scheme along with the two possible Xe TALIF calibration schemes are shown in figure 3.1. Even with this Xe reference signal, several further steps are required before absolute O(^{3}P) densities can be determined from TALIF. The most important of these are accounting for the two photon absorption cross sections for both Xe and O(^{3}P) and the branching ratio of the fluorescence emission into the observed transition if other possible transitions exist. This calibration process is so complex and fraught with difficulty that the resulting densities are only typically reliable to within a factor of ≈ 2 [(96)].

Despite these difficulties in putting TALIF on an absolute footing it is extremely powerful and sensitive as a technique for measuring relative atom densities. In particular, by careful focusing of the pump beam and imaging of the florescence into the detector TALIF is capable of very high spatial resolution (<100 μm), particularly useful in small inhomogeneous discharges. Additionally, because TALIF utilises ps

or fs pulsed lasers it can also provide excellent temporal resolution (limited by the fluorescence lifetime of the emitting state, typically ≈ ns) and can also be applied at high pressure, for example to atmospheric pressure plasma jets[108].

TALIF on $O_2(a^1\Delta_g)$ is not inconceivable, for example one could try exciting on the $O_2(e^1\Delta_u) - O_2(a^1\Delta_g)$ system (2 × ∼290 nm) and measure near infrared fluorescence on the $O_2(e^1\Delta_u) - O_2(d^1\Pi_g)$ system (∼1650 nm). Making quantitative use of such a measurement however would be extremely difficult due to the need to know two photon absorption cross sections (even one photon cross sections have only been measured a couple of times for the $O_2(e^1\Delta_u) - O_2(a^1\Delta_g)$ system[109]) and the need to find an appropriate reference molecule with which a LIF signal could be compared. In addition, the near infrared emission is from a system which, although electric dipole allowed, has not been observed previously. Finally, detection would have to utilise a photodiode because the fluorescence wavelength is too far into the near infrared for photomultiplier tubes to be sensitive. For these reasons LIF on $O_2(a^1\Delta_g)$ is not a practical detection technique and has never been demonstrated.

Vacuum ultraviolet (VUV) absorption spectroscopy

Optical absorption methods are preferable to the aforementioned 'indirect' methods, since the absolute number density is returned directly (using the Beer-Lambert law 2.8) and the accuracy of the measurement depends only on the accuracy to which the transition line strength/ cross section is known. For $O(^3P)$ atoms the lowest energy fully allowed optical transitions occur in the vacuum ultraviolet (VUV), at 130 nm and correspond to excitation of a 2p electron into the 3s orbital. The VUV is technically difficult to access with narrow linewidth tunable lasers and is also inconvenient to handle due to its absorption by air.

The most common laboratory VUV sources are discharge lamps[95,110–112], however, absorption measurements with such sources present two difficulties. First, the light from lamps is not narrow linewidth and cannot therefore be treated as monochromatic, thus both the source and absorber's lineshapes contribute to the observed spectrum and the source lineshape must be estimated or measured in order to deconvolute these and obtain an absorption spectrum. Secondly, broadband plasma light sources usually require substantial effort to ensure negligible self-absorption within the source. Yang *et al.*[110] have recently reported on a self-absorption calibration method for a compact microwave plasma used in VUV absorption spectroscopy measurements. There the self-absorption calibration was performed by spectral analysis of the emission line profile, taking into account the optical escape factor, such that a

low-resolution monochromator could be used. These researchers demonstrated oxygen atomic density measurements in a mixed nitrogen and oxygen surface-wave plasma; the atomic oxygen density varied from $\approx 1.3 \times 10^{12}$ cm^{-3} to $\approx 4 \times 10^{12}$ cm^{-3} as a function of N_2:O_2 gas mixture ratio.

A more sophisticated alternative to UV lamps is the use of synchrotron radiation. An example of the method can be found in the work of Niemi *et al.*[113] who carried out VUV absorption measurements of atomic oxygen produced in a radio-frequency driven atmospheric pressure plasma using the broad continuum spectral output from the VUV beamline at the SOLEIL synchrotron facility coupled to a unique high resolution Fourier-transform spectrometer. Clearly the need for synchrotron radiation and a specially built spectrometer mean that this method is extremely expensive and technologically challenging to carry out. Some work also exists utilising harmonics of dye lasers.[114] Importantly, whatever the light source, the large absorption cross sections for the O(^{3}P) transitions (the Einstein A factors for the spin–orbit resolved transitions range from 0.676 to $3.41 \times 10^8\,\mathrm{s}^{-1}$)[74], mean that such VUV absorption measurements occur under optically thick conditions unless they are limited to situations with very low atomic densities (e.g. low pressure discharges) so that VUV absorption is not a universally applicable technique for O(^{3}P) detection.

The lowest energy allowed optical transitions of $O_2(a^1\Delta_g)$ also occur in the VUV meaning that similar technological restrictions are placed on direct absorption measurements of this species and very few such measurements exist. Western *et al.*[109] have demonstrated the detection of $O_2(a^1\Delta_g)$ in a DC discharge, again using the SOLEIL synchrotron and its unique Fourier-transform spectrometer, probing the $O_2(e^1\Delta_u) - O_2(a^1\Delta_g)$ system at ∼145 nm (amongst others) in absorption. These measurements were combined with *ab initio* calculations to find molecular constants for the electronic states involved and transition dipole moments for the measured transitions.

Much of the work to measure VUV absorption by atomic and metastable species in oxygen plasmas is complicated by the strong Schumann-Runge continuum absorption of $O_2(X^3\Sigma_g^-)$ between ∼130 and ∼170 nm. This continuum however has recently found use as a tool to quantify the densities of both atoms and metastable molecules. By modulating the plasma on and off and monitoring the Schumann-Runge absorption (again using SOLEIL) Booth *et al.*[96] were able to quantify the recovery dynamics of $O_2(X^3\Sigma_g^-)$. The recovery was observed to take place with two temporal components. The faster component was assigned to atom recombination to form $O_2(X^3\Sigma_g^-)$ whilst the slow component was due to the loss of $O_2(a^1\Delta_g)$. In this way the densities and

loss dynamics of the two species could be deduced. This technique is reliant on the fact that the two species have significantly different lifetimes in the system under investigation (which is not always true). It is also limited by the fact that the cross section of the Schumann-Runge continuum is temperature dependent in a way that has not been comprehensively measured and thus measurements are limited to the late afterglow (when temperatures are ambient and cross sections well known).

Visible and near-infrared absorption spectroscopy

Given the technical maturity of laser and optical technology in the visible and near-infrared regions and the drawbacks associated with the VUV (for example the difficult calibration processes and/or need for synchrotron radiation) it is unsurprising that several research groups have resorted to using absorption on forbidden transitions within optical cavities for atomic and metastable detection.

Harris and Weiner[115] demonstrated the first observation of O(^{3}P) in absorption using the technique of intra-cavity laser absorption spectroscopy (ICLAS) on the O($^1D_2$)-O($^3P_2$) and O($^1D_2$)-O($^3P_1$) transitions at 630.205 and 636.554 nm respectively (shown in figure 2.6), with oxygen atoms generated in a discharge flow tube. These were followed by measurements by Teslja and Dagdigian[116] using pulsed laser cavity ringdown spectroscopy (CRDS) at 630.205 nm to detect ground state oxygen atoms in a microwave discharge of either pure O_2 or Ar/N_2O. This set-up enabled the concentration of oxygen atoms in the 10^{14} cm^{-3} regime to be detected, and comparison with NO_2 titration yielded an experimental accuracy of within 20%. Subsequently, Gupta *et al.*[117] reported on the absolute O($^3P_1$) concentration generated in a high finesse optical cavity by an inductively coupled discharge arrangement at 10–40 Torr total pressure of a 10% O_2/He mix using the off-axis integrated cavity output spectroscopy (ICOS) technique, reporting a minimum detectable concentration of $\sim 10^{12}$ cm^{-3}. Finally, Hancock *et al.*[118] have used cavity enhanced absorption spectroscopy (CEAS) to determine O($^3P_2$) concentrations in the technically relevant low pressure environment of an inductively coupled plasma (ICP) chamber with pure oxygen as a precursor gas. At a pressure of 100 mTorr and 500 W plasma power the O(^{3}P$_2$) concentration was determined to be $(4.8 \pm 0.6)\times10^{14}$ cm^{-3}.

$O_2(a^1\Delta_g)$ measurements have utilised the $O_2(b^1\Sigma_g^+)$-$O_2(a^1\Delta_g)$ Noxon system, so called because it was first observed by Noxon in 1961[50] in the emission from an O_2/He discharge. Noxon based absorption measurements are usually made on the (0, 0) and (1, 0) bands at ∼1900 nm and ∼1500 nm, respectively, the former band is preferable because of its superior Franck-Condon factor whilst the latter band is much more

convenient in terms of the availability of tunable lasers and high reflectivity mirrors. The first absorption measurements of this species were made by ICLAS in a flow tube (1.9 Torr) on the (0, 0) band[119] and detected singlet oxygen densities of $\approx 1.5 \times 10^{15}$ cm^{-3} with a detection limit of $\approx 2 \times 10^{14}$ cm^{-3}. Later measurements, utilising off-axis ICOS[52], were the first to observe the (1, 0) band[51], this time in the afterglow of an ICP (Helium with $5 - 10\%$ O_2) with densities of around 10^{15} cm^{-3} determined and detection limits improved by an order of magnitude to $\approx 2.5 \times 10^{13}$ cm^{-3}. The same technique was later used to probe a $15 - 30$ Torr microwave plasma (He with $1 - 10\%$ O_2) with similar detection limits achieved[120]. Földes *et al.*[121] demonstrated detection on the (1, 0) band using cw-CRDS in a 2.25 Torr microwave plasma of pure oxygen, this was the first measurement in a pure oxygen plasma and the first to utilise CRDS but had a poorer minimum detectable concentration of $\approx 4 \times 10^{14}$ cm^{-3}. All of these previous measurements represent conversion efficiencies of between 3 and 6% for excitation of O_2 to the first excited metastable state.

3.3 Outlook of Section

The limitations of absorption spectroscopy are: uncertainty in absorption cross sections (often the target bands' cross sections are known only from calculations), its limited sensitivity in comparison to other techniques (*e.g.* LIF) and the fact that it is line of sight integrated and so provides limited spatial resolution. This latter point can be particularly important in plasmas where temperature and number density inhomogeneity across the plasma can be significant. Despite these constraints laser absorption is a powerful, practical and absolute technique which avoids the need for calibration. The utility of the technique will be demonstrated in the next three chapters where experiments utilising cavity ringdown spectroscopy (CRDS) are used to quantify densities and temperatures of key plasma produced oxygen species within the chamber with the measurements being supported by a volume averaged kinetic model. Finally CRDS measurements of $O_2(X^3\Sigma_g^-)$ will be used to demonstrate that, although line of sight averaged, absorption spectra can contain enough information to probe spatial inhomogeneity within the plasma chamber.

Chapter 4

Oxygen plasma measurements

In this chapter CRDS measurements of $O(^3P)$ and $O_2(a^1\Delta_g)$ are presented across a range of plasma operating conditions to determine densities, temperatures and lifetimes with respect to loss at the chamber walls. These are complimented by optical emission studies of $O_2(b^1\Sigma_g^+)$, Additionally the density of the O^- anion is determined using cavity ringdown photodetachment as the plasma is slowly modulated.

4.1 Experimental arrangement

All the measurements in this thesis utilise the plasma chamber described in chapter 1. The measurements in the next three chapters are made on a plasma produced from a feedstock of pure O_2 (99.999 % BOC) delivered into the chamber via the baffle arms at a constant flow of 10 sccm. To undertake CRDS measurements on the plasma, high reflectivity mirrors are mounted in gimbal mirror mounts contained within home-made vacuum compatible mirror boxes which are attached to the chamber baffle arms. The flow of gas along these arms helps to protect the mirrors from the plasma. One mirror is also mounted upon a piezo-electric stack which is modulated at $\approx 10\,\text{Hz}$ in order to ensure the frequent occurrence of cavity resonances. A general optical set-up is depicted in figure 4.1 and the specific lasers and mirrors used to probe each species of interest are given in table 4.1. The CRDS arrangement follows closely that for cw-CRDS described in chapter 2 whilst the precise spatial arrangement of the plasma chamber and optical cavity were described in chapter 1 (figure 1.9). Laser radiation is directed into the chamber via an AOM, and when a cavity resonance occurs and is detected by a photomultiplier tube (in the case of the Toptica lasers) or an InGaAs photodiode (in the case of the Eblana laser), a trigger signal is generated that both switches off the AOM and starts the acquisition of a ringdown event.

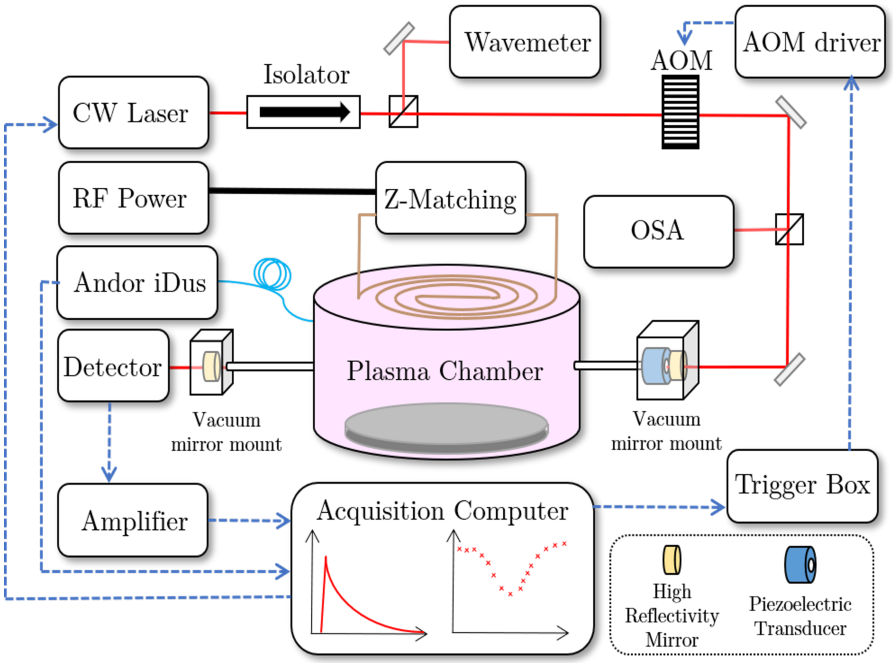

Figure 4.1: A schematic of the experimental arrangement. For cavity ringdown measurements cw laser radiation passes through an isolator and an AOM and is then coupled into the optical cavity. Detection and amplification allow ringdown signals to be recorded and spectra produced. The laser wavelength and stability are monitored by use of a wavemeter and an optical spectrum analyser (OSA), respectively. Optical emission spectra are recorded using an Andor Shamrock spectrograph with iDus CCD camera. Radio frequency power is provided to the plasma chamber via an impedance (Z) matching circuit.

Typically several hundred ringdown events are captured at one discrete wavelength before the acquisition and control software steps the laser either by adjusting the feedback grating of the ECDL or changing the temperature of the DFB laser. This process is repeated until a reasonable wavelength scan is achieved (usually over 3-10 GHz) such that the full lineshape of the transition being probed is covered. An absorption profile is then produced by fitting a baseline to the ringdown data in order to find τ_0 values and then using equation 2.40 to extract α (the absorption coefficient). This can then be fitted with a Gaussian (Doppler) lineshape and number densities and temperatures deduced according to equations 2.10 and 2.35, respectively. In the case of O^-, where detection is not on a discrete transition but on a photoionisation continuum, absorption measurements are made at a single wavelength (away from resonant atomic transitions) and densities deduced from the wavelength specific absorption coefficient, *vide infra*. In each case the scan and wavelength of the laser are carefully calibrated using an optical spectrum analyser, a wavemeter and, in the

Table 4.1: Lasers and mirrors used to probe oxygen plasma

Species	Laser	λ / nm	mirrors	reflectivity
$O(^3P)/O^-$	Toptica DL100 LD-0633-0100-1 (Littrow ECDL)	$629.0 - 636.5$	Layertec (coating: 137550)	$> 99.99\%$ @635 nm
$O_2(a^1\Delta_g)$	Eblana EP1909 DXT0250 (DFB diode)	$1907 - 1911$	Layertec (coating: 140981)	$> 99.99\%$ @1980 nm
$O_2(X^3\Sigma_g^-)$	Toptica DLPro LD-0780-0100-AR-1 (Littrow ECDL)	$747.6 - 792.1$	Layertec (coating: 140967)	$> 99.995\%$ @760 nm

cases of the 630 nm and 760 nm ECDL lasers, reference spectral lines from an iodine cell and from $O_2(X^3\Sigma_g^-)$, respectively. The broadband optical emission from the plasma was monitored by a silicon photodiode and by a photomultiplier tube, whilst wavelength-resolved emission spectra were obtained by imaging the plasma, via a large core multimode optical fibre, into a spectrograph (Andor Shamrock 303i) with a cooled CCD camera (Andor iDus). Optical emission measurements provide a quick and convenient way to monitor the plasma and provide information complementary to that provided by CRDS. Optical emission measurements also have the advantage of being applicable over a very wide range of plasma conditions which is useful because the CRDS measurements here are made across a range of plasma powers ($0 - 300$ W) and pressures ($10 - 100$ mTorr) for $O(^3P)$. O^- density is investigated as a function of gas pressure at 300 W power (at lower powers it was increasingly difficult to distinguish the absorption signal from the change in baseline ringdown time). $O_2(a^1\Delta_g)$ meanwhile is probed as a function of plasma power at 100 mTorr, the extremely small absorption signals in this case lead to very long experimental times and mean that measurements at low power or low pressure are possible, but not both simultaneously. The density variation with power was deemed more pertinent to measure because of the interest in the E to H mode switchover and probing this mode change was the main purpose of the $O_2(X^3\Sigma_g^-)$ measurements.

4.1.1 Density measurements

The number densities derived from absorption spectra according to equation 2.10 are line of sight averaged densities, $\bar{N}$. In general the reactive species under investigation are lost quickly in the baffle arms and as such only penetrate a short distance, l, into each arm[65,66]. This being the case, the average density of absorber in the plasma itself, N, is related to the line of sight averaged value, $\bar{N}$, by a simple length adjustment:

$$N = \bar{N}\frac{L}{2(R+l)}, \tag{4.1}$$

where L is the total cavity length (chamber plus arms) and R is the chamber radius.

Diffusion into baffle arms

Assuming that the predominant source of reactive species in the baffle arms is diffusion from the bulk plasma and that the predominant loss process is loss at the arm walls (a good assumption for the species considered in this chapter) then the penetration depth, l, of such species into the baffle arms can be calculated using Fick's second law (with a loss term) given by:[66]

$$\frac{dN(x)}{dt} = D\frac{d^2N(x)}{dx^2} - k_w N(x) = 0, \tag{4.2}$$

where $N(x)$ is the species number density at a distance x along the baffle arm and k_w is the rate coefficient for wall loss. When the plasma is operating in a steady state an equilibrium is reached and equation 4.2 is equal to 0. The equation then has solutions:

$$N(x) = N(0)\exp\left(-\sqrt{\frac{k_w}{D}}x\right), \tag{4.3}$$

where $N(0)$ is the number density in the main chamber. The $1/e$ scale length for penetration into the baffle arms, l, is therefore given by:

$$l = \sqrt{\frac{D}{k_w}}. \tag{4.4}$$

The loss rate coefficient, k_w, can be estimated for wall loss in the arms by use of the equations detailed in the next section. The baffle arms have a narrow channel (≈ 10 mm diameter) and are made of stainless steel, for which the surface loss probability is usually substantially larger than for the aluminium chamber surfaces[122]. This means that the lifetimes of excited species that enter the baffle arms are significantly shorter than in the plasma bulk and therefore species in the baffle arms contribute little to the measurements.

4.1.2 Kinetic measurements

Loss of species at plasma chamber walls is one of the biggest sources of uncertainty in plasma modelling and makes direct measurement of wall loss rates very desirable. Under the operating conditions investigated in this work, it is expected that diffusion to and reaction at the chamber walls is a significant loss process for $O(^3P)$, $O_2(a^1\Delta_g)$ and $O_2(b^1\Sigma_g^+)$[91,123,124]. In order to characterise this process the plasma was modulated at ≈1 Hz with a symmetric square wave (on: 300 W and off: 0 W). The modulation rate was chosen to allow sufficient time for the plasma to equilibrate after being turned on and this was verified by measurement of the broadband optical emission from the plasma with a photodiode. Extinguishing the plasma takes just a few tens of μs as can be observed by measurement of the decay of broadband plasma emission using a silicon photodiode. Figure 4.2 shows the decay in the broadband emission intensity which comes predominantly from fully allowed atomic emission lines (e.g. atomic oxygen line at 777 nm and 844 nm often used for actinometry).

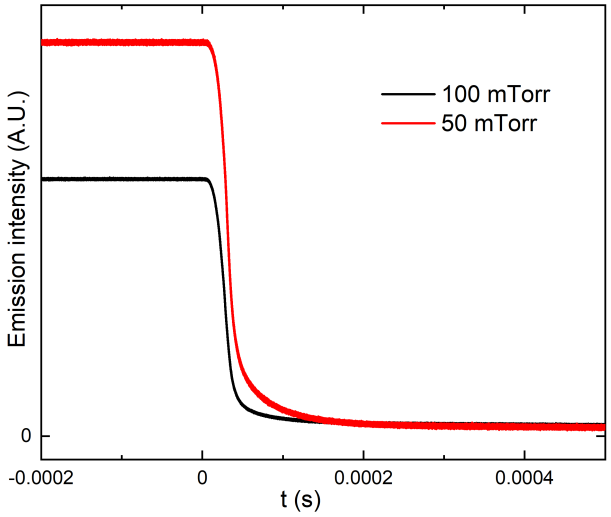

Figure 4.2: Temporal decay in the broadband emission from the plasma after the plasma is extinguished (power is rapidly reduced from 300 to 0 W). This data indicated that the plasma is extinguished on the time scale of tens of μs.

After the plasma is extinguished the production of the aforementioned species by electron impact stops as do all the important loss processes other than wall loss. The decay in density of the species is therefore dictated only by the rate of diffusion and wall reaction. In the cases of $O(^3P)$ and $O_2(a^1\Delta_g)$ it was possible to monitor the absorption coefficient (on the maxima of the respective transitions) as a function of time after the plasma was extinguished. Wall loss of $O_2(b^1\Sigma_g^+)$ was quantified by

observing the change in the intensity of emission from that species after the plasma was extinguished. In all cases the decay in signal was exponential and the decay time τ_w is related to the first order rate coefficient for wall loss k_w by $\tau_w = 1/k_w$.

Wall loss coefficients

The rate of wall loss is influenced by surface material, chamber dimensions, temperature and diffusion coefficients for a particular species. The relationship between these factors and k_w was discussed by Chantry[125] and is given approximately by:

$$\frac{1}{k_w} = \tau_w = \frac{\Lambda_0^2}{D} + \frac{V}{A}\frac{2(2-\gamma)}{\bar{v}\gamma}, \tag{4.5}$$

where D is the diffusion coefficient for the species being lost at the wall, V/A is the chamber volume to surface area ratio, $\bar{v}$ is the mean speed of the diffusing species of mass, m, given by:

$$\bar{v} = \left(\frac{8k_BT}{\pi m}\right)^{\frac{1}{2}}, \tag{4.6}$$

and Λ_0 is the geometric diffusion length given by:

$$\frac{1}{\Lambda_0^2} = \left(\frac{\pi}{H}\right)^2 + \left(\frac{\chi_{01}}{R}\right)^2, \tag{4.7}$$

where H and R are the chamber height and radius and $\chi_{01} = 2.4048$ is a radial scale factor given by the first zero of the zeroth order Bessel function of the first kind, appropriate for solutions of fundamental mode diffusion in geometries with radial elements. For the chamber used throughout this work $(V/A) = 0.048\,\mathrm{m}$ and $\Lambda_0 = 0.049\,\mathrm{m}$. The first term on the right hand side of equation 4.5 effectively accounts for the time taken to diffuse to the wall whilst the second term corresponds to the time taken to react once the wall is reached. In this chapter diffusion coefficients are taken, with temperature dependences, from Winn for molecules[126] and from Morgan and Schiff for atoms[127]. It is also assumed that electronic excitation does not change the diffusion coefficient as has been observed for the lowest lying excited state of O_2[128]. The crucial variable in equation 4.5 is the so called sticking coefficient or wall loss coefficient, γ. If the sticking coefficient is known then wall loss rates can be calculated at a range of different conditions. This flexibility makes knowledge of γ extremely desirable for plasma modelling.

4.2 O(^{3}P) measurements

The ECDL used in these measurements can be coarse-scanned manually to access the desired wavelengths for both the O(^{1}D$_2$)← O(^{3}P$_2$) and O(^{1}D$_2$)← O(^{3}P$_1$) transitions

(at 630.205 and 636.554 nm, respectively). Baseline (vacuum) ringdown times of 35 μs are observed for this optical cavity, corresponding to a (geometric mean) experimental mirror reflectivity of 99.993%.

The $O(^1D_2) \leftarrow O(^3P_J)$ transitions in atomic oxygen have Einstein A factors calculated as 5.65×10^{-3} s^{-1} and 1.82×10^{-3} s^{-1} for J = 2 and J = 1, respectively. These can be converted into integrated cross sections for these transitions using equation 2.13, with $g_2 = 5$ and $g_1 = 5$ or 3 for $J = 2$ and 1, respectively. This calculation yields integrated absorption cross sections of 2.98×10^{-23} cm^2 cm^{-1} (8.93×10^{-22} cm^2 GHz) for the $O(^1D_2) \leftarrow O(^3P_2)$ transition and 1.63×10^{-23} cm^2 cm^{-1} (4.9×10^{-22} cm^2 GHz) for the $O(^1D_2) \leftarrow O(^3P_1)$ transition.

The appropriate length adjustment factor, in the case of oxygen atoms, was calculated using wall loss coefficients for stainless steel (from which the arms are constructed) and equation 4.4. A value of $\gamma_O = 0.1438 \exp(2.5069/p)$ taken from Gudmundsson[129] where p is in mTorr, yields scale lengths for baffle arm penetration, l, that range between 1.4 cm (10 mTorr) and 0.5 cm (100 mTorr) with corresponding absorption length adjustments (equation 4.1) of (77/37.8) and (77/36), respectively.

4.2.1 $O(^3P)$ variation with gas pressure

CRDS spectra of the $O(^1D_2) \leftarrow O(^3P_2)$ transition are shown in figure 4.3 at four different pressures and all with 300 W plasma power. Also shown are Gaussian fits to the data used to reveal the number density and temperature of the $O(^3P_2)$ state.

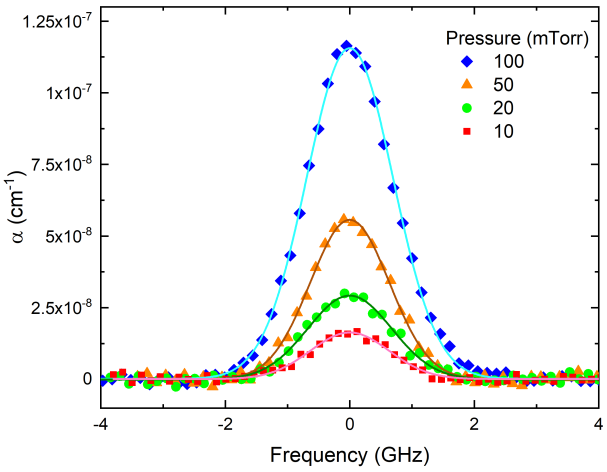

Figure 4.3: Cavity ringdown measurements of atomic oxygen ($O(^3P_2)$) at 630.205 nm (in vacuo) showing the variation in absorption at 300 W as a function of pressure and Gaussian fits to the data. From the scatter on the baseline in the figure ($\approx 3\times10^{-9}$ cm^{-1}) the minimal detectable atom concentration with this experimental protocol can be estimated as $\approx 10^{13}$ cm^{-3}.

The extracted translational temperatures of $O(^3P_2)$ are shown in figure 4.4 and are found to fall within the range $300-350$ K. The temperature shows no conclusive trend with pressure. Small signals at lower pressures lead to the large uncertainties in temperature indicated in the figure. For $O(^3P_1)$, absorption signals are smaller again because it has both a smaller population (lower degeneracy and higher energy) and a smaller absorption cross section. This makes temperature measurements of $O(^3P_1)$ even more uncertain and of very limited use. Another major source of uncertainty in these CRDS derived temperature values is the difficulty in fitting the baseline to the ringdown data that is used to find τ_0. During the course of acquiring a spectrum the baseline ringdown time typically shows a slow variation (varying by as much as 2 or 3 μs). This baseline must be fitted (usually with a polynomial) in order to find τ_0 and hence absorption spectra. The baseline that is used subtly alters the area and width of the absorption profile and results in uncertainty in number densities and translation temperatures. Uncertainties in temperatures are also large because $T_{trans} \propto (\Delta\nu)^2$ (equation 2.35) and hence any uncertainty in the FWHM is magnified when temperatures are calculated.

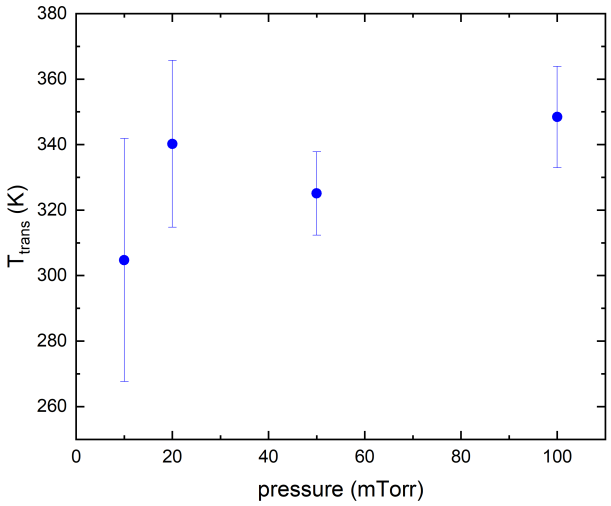

Figure 4.4: Pressure dependence of atomic translational temperatures, T_{Trans} at 300 W power, determined from the Doppler widths of the profiles in figure 4.3 .

Results of density measurements of $O(^3P_2)$ and $O(^3P_1)$ (length corrected according to equation 4.1) are presented in figure 4.5. Number densities range from low 10^{13} cm^{-3} to 5×10^{14} cm^{-3} over the pressure range studied; at 10 mTorr pressure the number density of $O(^3P_1)$ was too small to obtain reliable data. The ratio of populations of $O(^3P_1)$ to $O(^3P_2)$ was found to be in keeping with that expected from thermodynamic equilibrium given the measured translational temperatures (figure 4.4):

$$\frac{[O(^3P_1)]}{[O(^3P_2)]} = \frac{g_1 \exp\left(\frac{-E_1}{k_B T}\right)}{g_2 \exp\left(\frac{-E_2}{k_B T}\right)} \tag{4.8}$$

where E_J is the absolute energy of the spin orbit level and g_J is its degeneracy given by $g_J = 2J + 1$. This equation allows the total atomic concentrations $[O(^3P_{tot})]$ to be calculated from the $O(^3P_2)$ number densities (chosen because they are the most significant data) using:

$$\frac{[O(^3P_2)]}{[O(^3P_{tot})]} = \frac{g_2 \exp\left(\frac{-E_2}{k_B T}\right)}{\sum_{J=0}^{2} (2J+1) \exp\left(\frac{-E_J}{k_B T}\right)}. \tag{4.9}$$

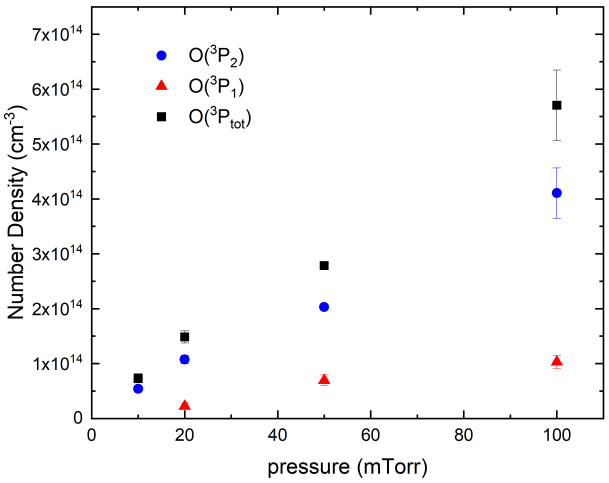

Figure 4.5: Pressure dependence of atomic densities in the plasma at 300 W. Densities for each spin orbit level were determined from the integrated area of the absorption profiles (e.g. those in figure 4.3), whilst the total density (black squares) was determined using statistical mechanics as detailed in the text. All values are adjusted to account for the baffle arms and the diffusion of atoms into them.

Ground state atom density shows a clear linear increase with increasing gas pressure. Combining knowledge of densities with temperature and pressure allows the calculation of the dissociation fraction, δ, according to:

$$\delta = \frac{[\mathrm{O}(^3\mathrm{P}_{tot})]}{2[\mathrm{O}_2]} \tag{4.10}$$

where $[\mathrm{O}_2]$ is the density of oxygen molecules that would exist at the plasma temperature if all the atoms were to spontaneously recombine. Dissociation fractions as a function of gas pressure are shown in figure 4.6 and, given only 300 W of power is being applied, are consistently high (above 0.1) across the pressure range investigated; there is also evidence of an increase in dissociation fraction towards lower pressures.

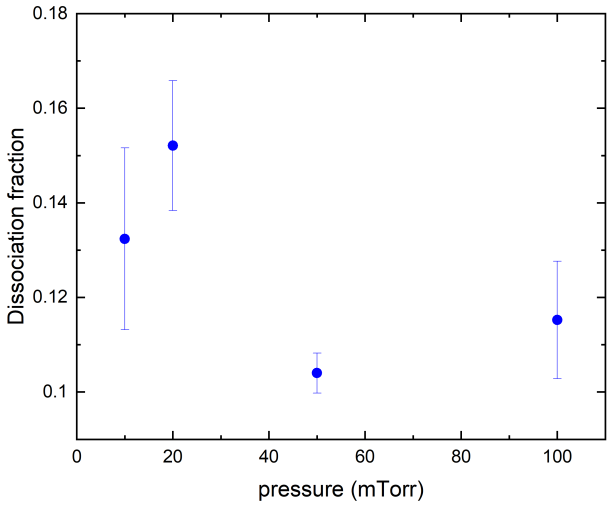

Figure 4.6: Pressure dependence of the dissociation fraction of the 300 W oxygen plasma, δ, determined from the total atom densities (black points in figure 4.5).

4.2.2 Wall loss kinetics

Kinetics of wall recombination of oxygen atoms can be measured using the plasma modulation scheme described earlier. Around 630 nm it is found that the baseline ringdown time (i.e. away from the atomic resonance) changes when the plasma is switched on and off, this variation is attributed to absorption by O^- (amongst other things, discussed later). In order to account for this and thereby to measure $O(^3P)$ kinetics the ringdown time was measured in 10 ms windows after the plasma was extinguished both on the maximum of the absorption and away from the absorption (to quantify baseline changes). These on and off resonance ringdown times, in conjunction with equation 2.40, allow the maximum absorption coefficient (due to $O(^3P)$) as a function of time after the plasma is extinguished, to be determined. This absorption coefficient is proportional to atom density (provided that the temperature is fairly constant). The results from this experiment are shown in figure 4.7 for gas pressures of 50 and 100 mTorr; fitting a single exponential function to the data yields decay times of 70 ± 12 ms and 110 ± 17 ms, respectively. These lifetimes against wall loss indicate that diffusion to the wall is relatively fast and τ_w is dominated by the time it takes to react at the wall (i.e. the second term in equation 4.5 dominates). Measurements at lower pressures are prevented by the smaller absorption signal and the significantly larger baseline variation during plasma modulation.

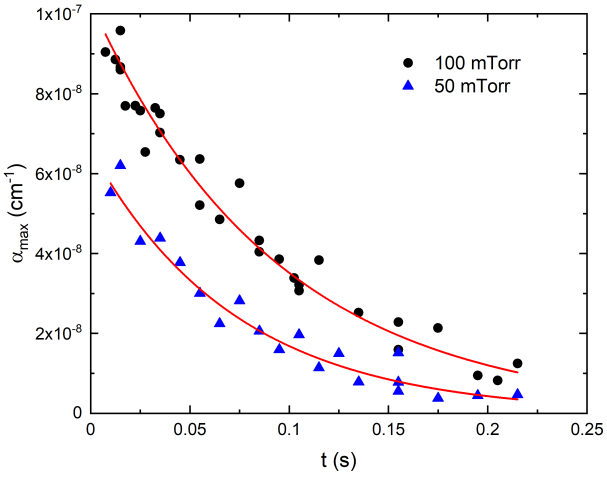

Figure 4.7: The decay of atomic oxygen measured after the 300 W plasma is extinguished at 50 mTorr (red triangles) and 100 mTorr (black circles). Each data point was calculated using the average of 20 on and off resonance ringdown events. At the lower pressures investigated in this work (10 and 20 mTorr) the smaller O(^{3}P) concentrations precluded the accurate measurement of α_{max} values beyond $t \approx 30$ ms and hence make reliable lifetime measurements very challenging.

The diffusion coefficient, D, for atomic oxygen diffusing through an environment of O_2 (required for wall loss coefficient calculations) has been both measured experimentally[127,130] and calculated from theory[131]. Theoretical calculations and values derived from beam scattering experiments are limited to the high temperature regime ($T > 1000$ K). Of the low temperature measurements, those reported by Morgan and Schiff[127] are considered to be most reliable[132] and are widely used[133–135]. In general the diffusion coefficient depends on both temperature and pressure, $D(T, p)$, and has units cm^2 s^{-1}. It is convenient to introduce a reference pressure, here 1 Pa, and to define the diffusion coefficient at that pressure $\tilde{D}(T)$ with units cm^2 s^{-1} Pa. The diffusion coefficient at a given pressure is then found using:

$$D(T, P) = \frac{\tilde{D}(T)}{p}, \tag{4.11}$$

where p is the pressure in Pa. The temperature dependence of the diffusion coefficient is expected to be of the form

$$\tilde{D}(T) = aT^b \tag{4.12}$$

with $b = 1.5$ from a hard sphere model but closer to $b = 1.75 - 1.80$ empirically[136].

Experimental diffusion coefficients at 1 Pa found from Morgan and Schiff are shown in figure 4.8a and the fitting according to 4.12 is the basis (along with equation 4.11) for the diffusion calculations used for atomic oxygen throughout the rest of this

thesis. The diffusion coefficient, $\tilde{D}$, is 4.21×10^4 cm^2 s^{-1} Pa at 340 K[127]. Using this value, together with equations 4.5 and 4.11 yields surface loss probabilities, γ, of $(4.3 \pm 0.8)\times10^{-3}$ and $(2.8 \pm 0.5)\times10^{-3}$ at pressures of 50 mTorr and 100 mTorr, respectively. Shown in figure 4.8b are the self diffusion coefficients for O_2 measured by Winn[126], also fitted according to equation 4.12. Vidaud *et al.*[128] found that the diffusion coefficients of $O_2(X^3\Sigma_g^-)$ and $O_2(a^1\Delta_g)$ are identical and Winn's data are therefore used in this thesis to describe the diffusion of $O_2(a^1\Delta_g)$. Both sets of diffusion data are used in the next chapter for the purposes of kinetic modelling.

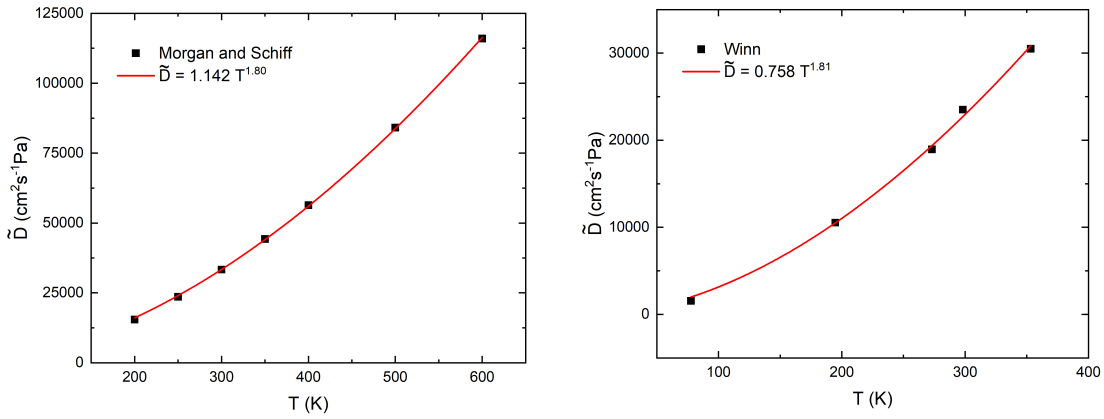

Figure 4.8: Diffusion coefficient data for (a) O(^{3}P) taken from Morgan and Schiff[127] and for (b) $O_2(a^1\Delta_g)$ taken from Winn[126]. Also shown for each data set is a fit according to equation 4.12. Values from these fits are used to find wall loss coefficients and also later for the purposes of volume averaged modelling.

4.2.3 O(^{3}P) variation with plasma power

Measurements of [O(^{3}P)] as a function of plasma power are desirable because they provide a method to probe the E/H mode switchover in the chamber (see section 1.2.2) and to quantify how this switchover effects the density of this industrially relevant species. In ICP chambers the E/H switchover is often identifiable by an increase in the intensity of plasma emission. Figure 4.9a shows the atomic oxygen emission line at ≈777 nm as a function of plasma power (at 100 mTorr) as measured using the Andor spectrometer whilst figure 4.9b shows the integrated area under the 777 nm line as a function of power and the broadband emission intensity as measured by the silicon photodiode. The agreement between these methods supports the idea that the majority of the plasma emission comes from strongly allowed atomic emission lines

and also shows clearly that the E/H switchover for a 100 mTorr pure oxygen plasma in this chamber occurs at $\approx 120 - 140$ W.

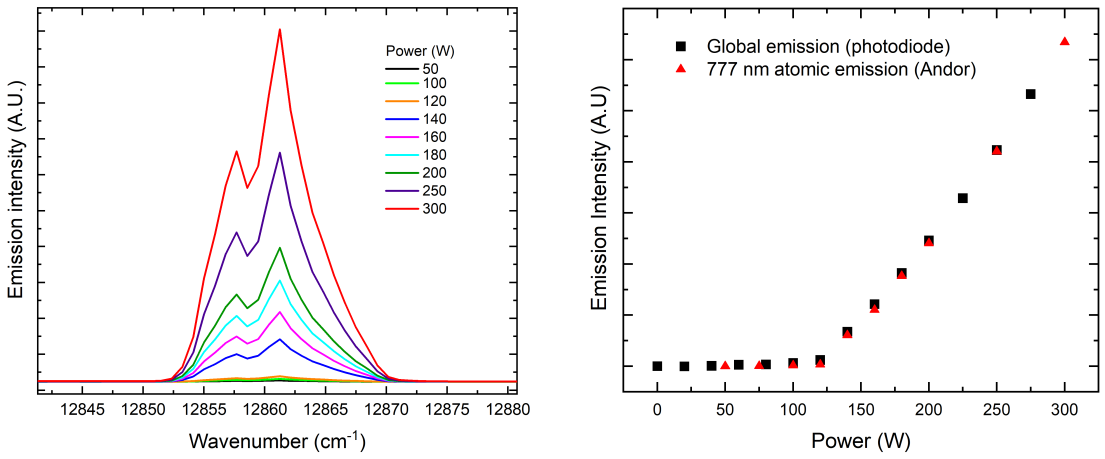

Figure 4.9: (a)The variation in the $(^5P) \rightarrow (^5S)$ atomic oxygen emission spectrum around 777 nm with plasma power at 100 mTorr gas pressure and (b) the integrated area under the spectra in (a) compared to the global plasma emission measured by a photodiode showing clearly the E/H switchover between 120-140W for a 100 mTorr oxygen plasma.

Cavity ringdown spectra, as a function of plasma power at 100 mTorr pressure, are shown in figure 4.10. The spectra show a significant increase in absorption with increasing plasma power. As before, Gaussian fitting enables the extraction of translational temperatures (figure 4.11) which show a marked increase from values that are approximately ambient at ≈300 K in the E-mode to those that are significantly hotter ≈450 K at the highest powers studied. The temperature shows a marked increase between powers of 100 and 140 W suggesting that this is where the E/H transition occurs. Also shown in figure 4.11 is a spline fitting to the data which is utilised in plasma modelling and will be explained in more detail later.

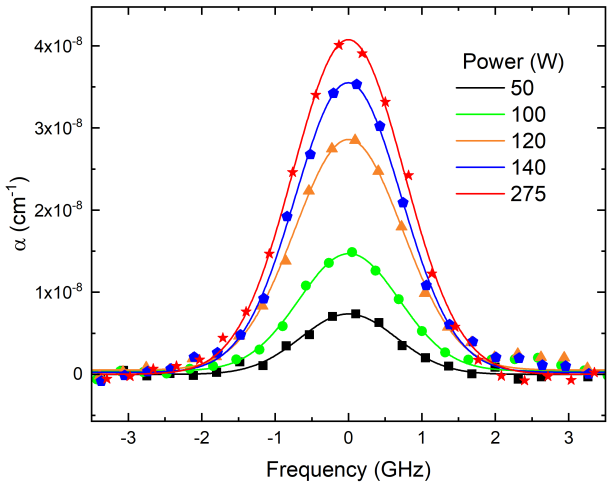

Figure 4.10: Cavity ringdown measurements of atomic oxygen ($O(^3P_2)$) at 630.205 nm (*in vacuo*) showing the variation in absorption as a function of plasma power and Gaussian fits to the data which were taken at 100 mTorr gas pressure.

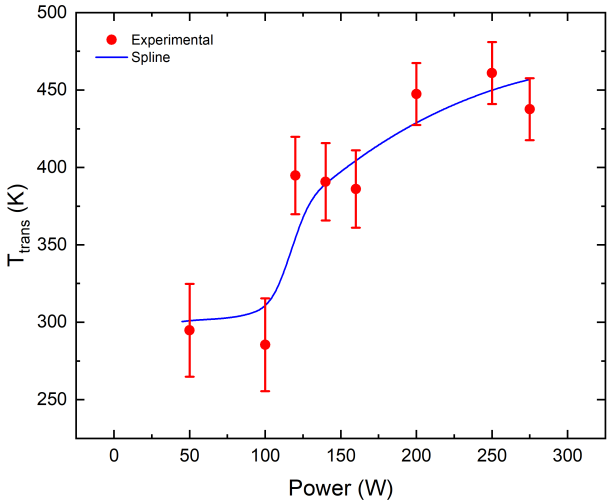

Figure 4.11: Translational temperatures of atomic oxygen as a function of plasma power (at 100 mTorr pressure) determined from Doppler widths of fits to the spectra. Also included is a smoothed spline which is used to estimate temperatures used in volume averaged modelling (see later).

Number densities, both of the spin orbit level being probed and of total $O(^3P)$ are shown in figure 4.12a, with the latter calculated according to an equilibration between the spin orbit levels (equation 4.9). All density values in this figure are adjusted by

the factor of 77/36 which accounts for the length of the baffle arms and for diffusion of atoms into the arms (equation 4.1). Shown in figure 4.12b are the dissociation fractions, calculated as before, as a function of plasma power. It should be noted that the much greater uncertainties on the total number densities and dissociation fractions in figure 4.12 arise because the calculations of these values utilise the (relatively uncertain) temperature values (figure 4.11) whilst the number density of $O(^3P_2)$ doesn't rely on the temperature measurement and is more certain as a result. Once again the major sources of uncertainty in the temperature measurement are the uncertainty in fitting the baseline ringdown times and the fact that $T_{trans} \propto (\Delta\nu)^2$.

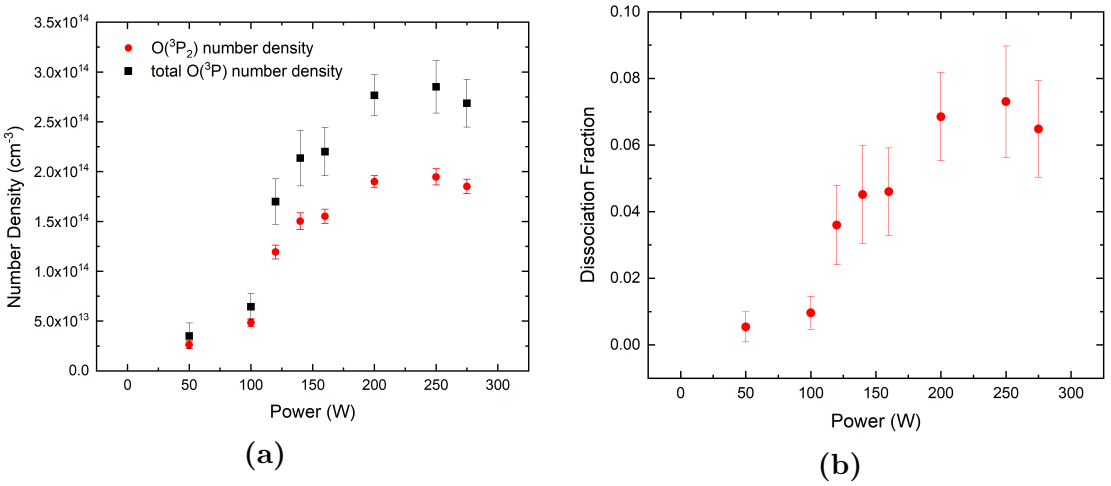

Figure 4.12: (a) Densities of $O(^3P_2)$ (red) as a function of plasma power (at 100 mTorr) calculated from the absorption spectra and adjusted for the baffle arms and total atomic densities calculated using statistical mechanics (see text) (b) dissociation fraction of the plasma as a function of plasma power.

The measured number densities and dissociation fractions, δ, both show a similar trend to the translational temperature, with a rapid increase between 100 and 120 W and a more gradual increase within the H-mode before eventually plateauing at the highest powers. δ in the E-mode is <0.01 and increases by nearly an order of magnitude as the power is increased to 300 W. The E/H-mode switchover power measured by CRDS agrees well with that observed by emission from highly excited states (figure 4.9).

It is remarkable to note that, for conditions of 100 mTorr and 275/300 W, this experiment finds an atomic density that is smaller by a factor of ≈2 than was found in the pressure variation experiments for the same plasma conditions (see section 4.2.1). Additionally the temperature is around 25% hotter than was previously observed. The only major change made between these two sets of experiments that could explain

these remarkable differences was the cleaning of the interior walls of the chamber following a vacuum system failure. Both before and after the cleaning the results were consistent and reproducible and this leads to the conclusion that the measurements are truly representative of a significant change in atom density and temperature within the plasma caused by cleaning the chamber walls. The likelihood is that the wall cleaning altered either the wall's thermal accommodation coefficient, α, the atom's wall loss coefficient, γ, or both. These possibilities will be discussed at length in the next section.

4.2.4 Discussion

The pressure variation studies presented above were conducted over a technologically important pressure range (10–100 mTorr) and at all pressures the equilibrium concentration of ground state atomic oxygen found in this plasma device is considerable; under certain conditions contributing up to 30% of the total number density within the plasma. This conclusion is consistent with a previous measurement, made under limited conditions in the same plasma chamber, recorded using CEAS[118].

Such are the high concentrations of atomic oxygen in this plasma system, that conspicuous changes in pressure are observed when the plasma is ignited (usually controlled by the plasma chamber automatic pressure regulation feedback system). With the chamber completely sealed and containing 60 mTorr of pure O_2, ignition of the plasma causes the measured pressure to increase to 75 mTorr. Taking into account the increase in gas temperature this leads to an estimate for the atomic oxygen concentration corresponding to a dissociation fraction of $11\pm 4\%$, in keeping with the spectroscopic measurements. High equilibrium levels of a plasma borne product species must have significant ramifications on the electrical characteristics of the plasma (i.e. electron number densities and energies) and in this case are intrinsically related to the nature and material of the plasma vessel.

The measured lifetime of atomic oxygen firmly supports the perception (as expected) that the loss process for this species is dominated by recombination at the chamber walls. The wall recombination probability inferred from these data is small ($\gamma < 10^{-2}$), but not unrealistic for aluminium (by far the largest constituent of the plasma chamber)[137] with γ taking values of $(4.3 \pm 0.8)\times10^{-3}$ and $(2.8 \pm 0.5)\times10^{-3}$ at pressures of 50 mTorr and 100 mTorr, respectively. The trend for γ to decrease with increasing pressure has been observed before and has been rationalised by invoking both Eley–Rideal and Langmuir–Hinshelwood wall recombination mechanisms[138]. These observations are also congruent with the hypothesis that at lower pressures,

incident ions with higher energies can bombard the surface to provide more adsorption sites[134,139,140], an effect that is further enhanced in the work reported here, by the increase in ion density at lower pressures which are reported in the next section of this chapter.

The power variation experiments show an increase in [O(^{3}P)] by an order of magnitude in switching from the E- to the H-mode, this is in good agreement with a number of previous workers. However, the absolute densities are significantly higher than those found by others[91,141]. This is directly attributable to the significantly smaller wall loss coefficient for the chamber used in this work. Kiehlbauch and Graves[82] modelled and measured hot, gas-phase temperatures and cooler wall temperatures for a chamber similar to the one used here. The temperatures presented in figure 4.11 (440 ± 25 K at 300 W) are intermediate between the gas phase temperature ($\approx$ 600 K at 300 W) of Kiehlbauch and Graves and the temperature they calculate close to the chamber wall ($\approx$ 375 K at 300 W). This observation can be attributed to the fact that CRDS provides a line of sight average temperature over a thermally inhomogeneous plasma. We will return to the topic of inhomogeneity both later in this chapter and in chapter 6

The effect of cleaning the chamber

As alluded to in the previous section the CRDS studies under conditions of varying power show two differences compared to the pressure variation results taken under the same conditions (300 W 100 mTorr), namely, the lower number density (by a factor of $\approx$ 2) but higher temperature (450 K here compared to 350 K previously) of the atoms. The only potentially significant change in the plasma chamber between the two sets of measurements was the cleaning of the chamber's internal surfaces. Thus, a potential explanation of the discrepancies between previous measurements and those presented here is that the cleaning significantly changed the thermal accommodation properties of the surfaces or indeed the probability of atom recombination, for example by removing or reducing the thickness of the oxide layer that tends to exist on such walls. This could have a significant impact on the plasma temperature and atom temperature and density, as discussed by Gibson *et al.*[142]. Their modelling showed that an increase in atom density upon changing either the recombination coefficient or thermal accommodation coefficient is always accompanied by a decrease in temperature and visa versa, this conclusion is consistent with the observations in this chapter. The observed temperature increase would be expected to result in a $\approx$30% increase in the rate of wall loss of O(^{3}P), by increasing both the diffusion rate and

mean thermal velocity (and assuming an unchanged wall loss coefficient of 0.003). The increase in temperature would also lead to a depletion of $O_2(X^3\Sigma_g^-)$ by ≈30% simply following the ideal gas law and this would cause a corresponding drop in the production rate of $O(^3P)$ (because $O_2(X^3\Sigma_g^-)$ is the main precursor to atomic oxygen, see modelling later). The combination of slower production and faster destruction would be expected to reduce $[O(^3P)]$ by ≈50%, in very good agreement with the observed reduction in density. Thus the reduced number density can be rationalised entirely by the temperature change (caused by a change in thermal accommodation coefficient) without the need to invoke a change in the atomic wall loss coefficient. Attempts were made to verify this conclusion by measuring the wall loss of $O(^3P)$ post-cleaning, however the combination of the reduced $O(^3P)$ signal and the faster decay in the signal (due to faster wall loss) made the extraction of reliable lifetimes impossible.

4.3 O^- measurements

Conveniently, the O^- ion has an absorption (photodetachment) continuum at wavelengths shorter than 830 nm and at 630 nm the photodetachment cross section is large enough to be observed by CRDS ($\sigma(\nu) = 7 \times 10^{-18}$ cm^2 at 630 nm)[143]. The presence of O^- will therefore cause a measurable change in baseline cavity ringdown time at 630 nm when the plasma chamber is operating. Indeed, it is expected that the dominant negative ion under the plasma conditions investigated in this work is O^-[11], essentially because the stabilisation of O_2^- requires a third body, whereas O^- is generated by dissociative electron attachment (DEA) for electron - O_2 collision energies >3.7 eV. Additionally, the photodetachment cross section of O_2^- is small (1.2×10^{-18} cm^2 at 630 nm)[144]. Other gas phase species with potential to cause a plasma dependent baseline effect are of no consequence; e.g. ozone is thought to exist only in very small quantities (≈ 10^{10} cm^{-3} at operating pressures of 10–100 mTorr[124]), and the ozone absorption cross section around 630 nm is small (4×10^{-21} cm^2)[145]. Accordingly, the number density of oxygen anions, O^-, was determined in a similar modulated plasma arrangement as described for the $O(^3P)$ lifetime measurements, but with the laser always tuned off of the atom resonance (and also avoiding transitions on the (2, 0) band of the $O_2(b^1\Sigma_g^+) - O_2(X^3\Sigma_g^-)$ system). It is found that there is a difference in the baseline cavity ringdown time between on- and off-plasma states, which can be as large as a few μs; furthermore, these changes in baseline after the plasma is extinguished have both a fast and slow component (both resulting in an

increase in ringdown time on plasma extinction). The slow component takes place on a timescale of a few seconds (at 10 mTorr) to several tens of seconds (at 100 mTorr), this change is far too slow to be the result of O^- kinetics and is instead attributed to a temporary alteration (decrease) of mirror reflectivity when the plasma is on either as a result of subtle temperature changes or by the plasma itself (some reactive species could survive long enough to reach the mirrors). The fast change in ringdown time occurs on a timescale of <1 ms. This change is on the correct timescale to be attributed to absorption by O^- and it is this quick change that is used to determine ion concentrations.

To ascertain the O^- concentration, the ringdown time was measured during 5 ms windows immediately before and 500 μs after the plasma was turned off, when the effects of slowly changing mirror reflectivity can be neglected. O^- lifetimes are of the order of μs[124] and so a delay of 500 μs is sufficient to ensure that all O^- is lost. It can also be assumed that O^- is restricted to the bulk of the discharge by the combined effects of the positive plasma potential[123] and the relatively fast wall loss rate within the narrow baffle arms such that the relevant length adjustment factor is 77/35. The density of O^-, can then be inferred using equation 2.40 and the fact that $\alpha(\nu) = \sigma(\nu)[O^-]$. The measured O^- number density in the discharge as a function of total gas pressure is shown in figure 4.13.

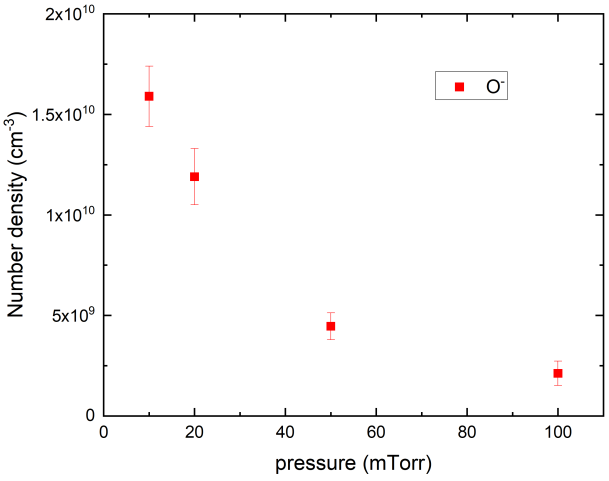

Figure 4.13: The variation of O^- number density as a function of total pressure at 300 W as measured by photodetachment at a wavelength of 630 nm. Error bars reflect the reproducibility in the measurement over several datasets.

Over this pressure range the O^- number density is a monotonically decreasing function of total pressure showing a maximum of 1.6×10^{10} cm^{-3} at 10 mTorr falling eightfold to 2×10^9 cm^{-3} at 100 mTorr. At the lower end of the pressure range it becomes more difficult to distinguish the O^- signal from other factors changing the ringdown time. In particular, at the lower pressures the slow component of the changing ringdown time becomes larger in magnitude and closer in timescale to the fast O^- signal and thereby masks it.

4.3.1 Discussion

It has been previously reported in work on both capacitively (10 W and $10 - 200$ mTorr[146]) and inductively coupled plasma (220 W and $5 - 40$ mTorr[89]) that the number density of O^- increases with increasing pressure at low pressures (below ≈20 mTorr) before decreasing as the pressure increases further. This has been widely justified by considering the relative importance of O^- loss processes under different pressure regimes. At low pressure, O^- loss is thought to be dominated by ion-ion recombination and by electron detachment: referred to as a recombination-dominated plasma. At high pressures the losses are dominated instead by associative detachment with $O(^3P)$ and reactions with other neutral species, $O_2(X^3\Sigma_g^-)$, $O_2(a^1\Delta_g)$ and $O_2(b^1\Sigma_g^+)$ states have all been reported to be important, referred to as a detachment-dominated plasma[11,89,123,124,146]. It has been noted by Lieberman and Lichtenberg[3] that the maximum in O^- number density corresponds to the recombination–detachment transition for a given plasma power, and this has been previously found from experimental data to occur at around 20 mTorr[89,146]. It is evident from the data that the transition pressure for this chamber is significantly lower. This can be attributed to the aluminium chamber employed in this work as opposed to the stainless steel chambers used in most experimental and modelling work. As measured previously, the surface recombination probability of oxygen atoms, γ, for this chamber is significantly smaller than those reported for stainless steel ($\gamma \approx 0.151$)[94,129]. The critical pressure at which the recombination–detachment transition occurs was found by Gudmundsson[123] to decrease with decreasing γ. This is because decreasing γ increases the equilibrium atomic oxygen number density and hence associative detachment with $O(^3P)$ continues to be a dominant O^- loss process down to lower pressures compared to a situation with higher recombination probability. For a power of 300 W and a recombination probability of 0.5, Gudmundsson[123] predicted that the critical transition pressure was in the range 4–7 mTorr; from this it would be expected that the chamber used here (with $\gamma < 10^{-2}$) would undergo the recombination–detachment transition below 4

mTorr, and so it is not observed. This assertion is supported by kinetic modelling detailed later.

4.4 $O_2(a^1\Delta_g)$ measurements

The DFB diode laser used to perform these measurements operates at around 1900 nm and can be temperature tuned over a range of wavelengths that includes five rotation lines of the (0, 0) band of the Noxon system ($Q(4), Q(6), Q(8), Q(10)$ and $Q(12)$). The $Q(8)$ line is coincident with a strongly allowed water transition and is hence obscured by trace water within the chamber, the other four lines however can be probed by CRDS. The baseline ringdown for the set up at this wavelength was ≈43 μs corresponding to a mean mirror reflectivity of 99.994%, whilst the appropriate length adjustment factor is 77/45 (using γ= 0.007 measured for iron but often used for steel[122]). Cavity ringdown spectra of the four Q branch lines are shown in figure 4.14, each set of data (blue) is derived using equation 2.40.

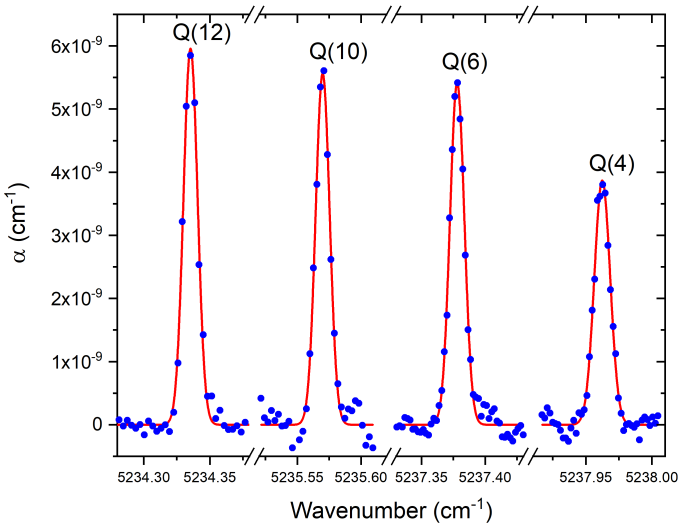

Figure 4.14: CRD spectra of $Q(12), Q(10), Q(6)$ and $Q(4)$ lines of the $O_2(b^1\Sigma_g^+) \leftarrow O_2(a^1\Delta_g)$ (0, 0) vibrational band recorded at 100 mTorr total pressure and 300 W power. Gaussian fits to the data are shown in red.

The data are the averages of multiple individual CRD spectra for each line (between three and six depending on the signal to noise ratio) collected at a pressure of 100 mTorr and a plasma power of 300 W. As for the atomic measurements, data are fitted with a Gaussian function (pressure broadening is again negligible) to reveal the line of sight integrated absorption coefficient (α_{INT}) and average translational temperature, T_{trans} (determined from the Gaussian FWHM according to equation 2.35).

For $Q(12)$, the transition with the highest signal to noise ratio, the width of the averaged spectrum corresponds to a value of T_{trans} of (359 ± 16) K. To confirm this, each of the four individual $Q(12)$ spectra were also fitted with Gaussian functions and the FWHM of each found. The average temperature from this process was (370 ± 23) K, in good agreement with that from the averaged spectrum.

The calculation of absorption cross sections for these transitions is detailed in chapter 2 and line positions were found and lines assigned using a PGOPHER simulation with the molecular constants taken from Drouin *et al.*[147]. The cross sections in table 2.2 can be used alongside α_{INT} and equation 2.10 to find the line of sight averaged number density in the specific rotational state being probed. The value is then length adjusted to account for the baffle arms (and diffusion into them) to find the number density of each rotational state in the plasma (here denoted either as $[O_2(a^1\Delta_g, v = 0, J'')]$ for clarity or simply $N_{J''}$ for convenience). These values can then be used to find the total number density in the lowest vibrational level, $[O_2(a^1\Delta_g, v = 0)] \equiv N_{v=0}$, if the rotational temperature, T_{rot}, is known. The most straightforward way to find both T_{rot} and $N_{v=0}$ when the densities of several rotational states are known is the construction of a Boltzmann plot according to:

$$N_{J''} = N_{v=0} \frac{(2J''+1)\exp\left(\frac{-E_{rot,J''}}{k_B T_{rot}}\right)}{q_{rot}}. \tag{4.13}$$

Equation 4.13 can be rearranged to give

$$\ln\left(\frac{N_{J''}}{2J''+1}\right) = \ln\left(\frac{N_{v=0}}{q_{rot}}\right) - \frac{E_{rot,J''}}{k_B T_{rot}}. \tag{4.14}$$

Hence a plot of $\ln\left(\frac{N_{J''}}{2J''+1}\right)$ against $E_{rot,J''}$ (which can be taken directly from PGOPHER[55]) yields a straight line whose gradient provides T_{rot} and whose intercept provides $N_{v=0}$. Calculation of $N_{v=0}$ requires knowledge of the rotational partition function but once again this can be calculated using PGOPHER using T_{rot} derived from the plot gradient. Figure 4.15 shows such a plot for the rotationally resolved number densities determined from the data in figure 4.14. The gradient of this plot yields $T_{rot} = (346 \pm 38)$ K, in good agreement with the translational temperature determined from the FWHM of the individual spectral lines. The intercept in figure 4.15, along with this temperature, gives $N_{v=0} = (9.5 \pm 1.3) \times 10^{13}$ cm^{-3}. Thus, at a total pressure of 100 mTorr, the apparent proportion of the sample that is $O_2(a^1\Delta_g, v = 0)$ is $(3.5 \pm 0.45)\%$. It should be noted that, formally, the absorption measurements depend on the population of both the lower and upper states of the probed transitions (see equation 2.10).

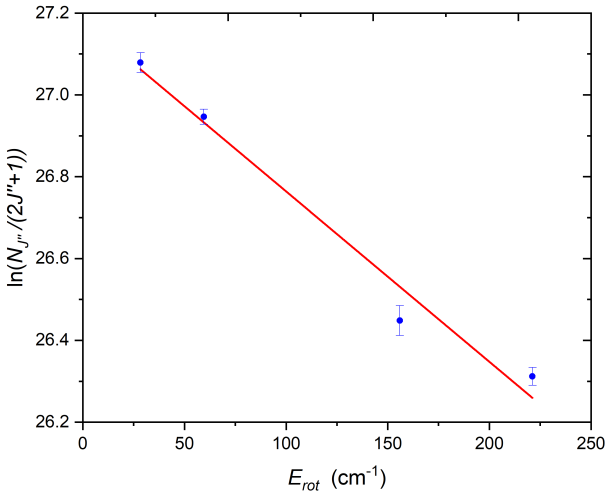

Figure 4.15: Boltzmann plot to determine T_{rot} and $N_{v=0}$ for $O_2(a^1\Delta_g)$ at 100 mTorr and 300 W.

For the transitions probed here the degeneracies of the upper and lower states are identical ($2J' + 1 = 2J'' + 1$) because they are Q-branch lines and because one of each Λ-doubled pair of levels in the $O_2(a^1\Delta_g)$ state is forbidden by nuclear spin statistics. This means that the absorption measurement directly measures the population difference between the two states. Usually the upper state population can be neglected as it is much smaller, but that is not necessarily the case here. The $b^1\Sigma_g^+$ state of molecular oxygen is also metastable and has been predicted to have significant concentrations under certain circumstances. However, equilibrium kinetic considerations (presented in detail later) based on the relative electron impact production and loss rates of the $O_2(a^1\Delta_g)$ and $O_2(b^1\Sigma_g^+)$ states, which includes contributions from the $O(^3P)$ chemistry and wall loss rates recorded here for $O_2(a^1\Delta_g)$ and later in this chapter for $O_2(b^1\Sigma_g^+)$, indicate that the $O_2(b^1\Sigma_g^+)$ state has a concentration ≈15% of that of the $O_2(a^1\Delta_g)$ state. These considerations yield a corrected $O_2(a^1\Delta_g, v = 0)$ contribution of $(4.1 \pm 0.5)\%$. Emission measurements (presented later) also show vibrational temperatures for $O_2(b^1\Sigma_g^+)$ of the order of 900 K and it would be expected that the vibrational temperature of $O_2(a^1\Delta_g)$ should be similar to this. Taking account of a probable upper limit of the $O_2(a^1\Delta_g)$ vibrational temperature of 1300 K (low v) and the effects of a non-thermal distribution (high v), which has been reported recently for slightly different conditions (500 W, 80 mTorr)[141] increases the total $O_2(a^1\Delta_g)$ contribution by 25% to an upper bound of $(5.15 \pm 0.7)\%$.

Thus, with reasonable confidence it can be estimated that the total contribution of $O_2(a^1\Delta_g)$ lies between the bounds of 3.6%-5.85%, corresponding to a concentration

of between 1×10^{14} cm^{-3} and 1.63×10^{14} cm^{-3}. Further $Q(12)$ spectra were gathered at plasma powers between 50 and 300 W to study how the $O_2(a^1\Delta_g)$ density varies across the E/H (capacitive/inductive) switchover region. Across the power range an increase in the translational temperature from ≈310 K (50 W) to ≈360 K (300 W) is observed. By assuming that T_{trans} is equilibrated with T_{rot} (as was indicated by the Boltzmann plot in figure 4.15) and accounting for estimated $O_2(b^1\Sigma_g^+)$ densities the total number density, $N_{v=0}$, in the ground vibrational level of $O_2(a^1\Delta_g)$ is inferred. The variation in density with plasma power is shown in figure 4.16 and show a marked increase (by a factor of 5) through the E-mode before reaching a peak at $\approx 1.5 \times 10^{14}$ cm^{-3} at 150 W and then decreasing gradually with increasing power in the H-mode.

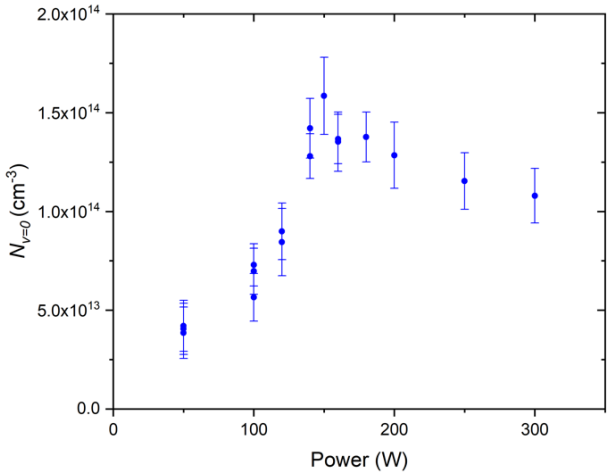

Figure 4.16: The measured $O_2(a^1\Delta_g, v = 0)$ number density as a function of power at 100 mTorr pressure, clearly illustrating the E/H switch-over region. Densities are corrected for estimated $O_2(b^1\Sigma_g^+, v = 0)$ populations.

4.4.1 Wall loss kinetics

Wall loss to form ground state molecules is an important process for the destruction of $O_2(a^1\Delta_g)$[123,124]. Once again the wall loss was quantified by modulating the plasma (at 0.5 Hz). The laser was set at the line centre for the $Q(12)$ transition and the ringdown time recorded for 2 hours. Ringdown events were sorted according to the time in the modulation cycle at which they occurred and a 3 ms rolling average was then applied. At this wavelength it was found that the baseline ringdown time was unaffected by the plasma (1900 nm is too long a wavelength to cause photodetachment in O^- or O_2^-) which made off resonance measurements unnecessary. The temporal decay in α_{max} (and hence $O_2(a^1\Delta_g)$ concentration) was fitted with an exponential

decay as shown in figure 4.17 and yields lifetimes (1/e) for $O_2(a^1\Delta_g)$ of (152 ± 17) ms at 100 mTorr and (128 ± 7) ms at 75 mTorr.

The diffusion coefficient for $O_2(a^1\Delta_g)$ is known to be the same as for ground state O_2 [128] and is taken (with its temperature dependence) from the work of Winn [126] as shown in figure 4.8b. The measured lifetimes and diffusion coefficient of $\tilde{D} = 3.05\times10^4$ cm^2 s^{-1} Pa (at 359 K) correspond to $\gamma = (2.8 \pm 0.3)\times10^{-3}$ and $(3.3 \pm 0.2)\times10^{-3}$ at 100 and 75 mTorr, respectively.

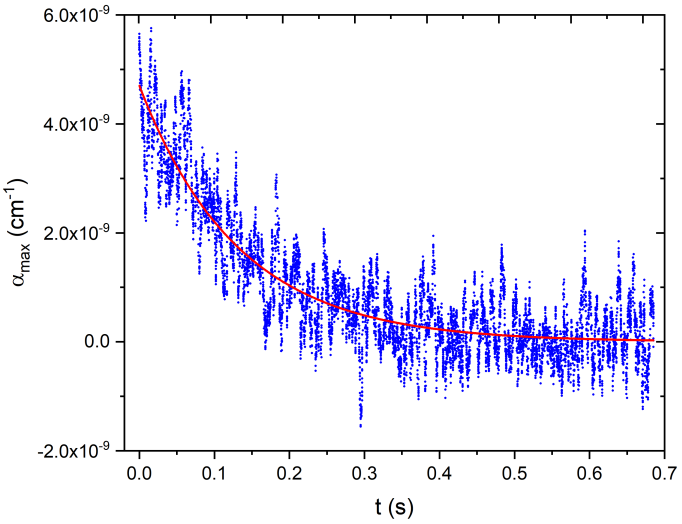

Figure 4.17: Value of the maximum absorption coefficient for the $Q(12)$ line as a function of time after the 100 mTorr 300 W plasma is extinguished. The lifetime (1/e) for the first order decay of $O_2(a^1\Delta_g, v = 0)$ is (152 ± 17) ms.

4.4.2 Detection limit

The maximum absorption coefficient observed here is very small ($\approx 6\times10^{-9}$ cm^{-1} see figure 4.14) and measurements with a high signal to noise ratio require an optimised CRD system. The performance of the system can be quantified by the well-known Allan variance [148]. In such an analysis, a series of measurements of some quantity, $y(t)$, where t is the time of the measurement, is made. The data set, arranged in order of the time the measurements were made is split into a series of time bins of length Γ each containing n data points, these two being simply related by the time it takes to measure each data point, Γ_0, by $\Gamma = n\Gamma_0$. If the average value of y within the k^{th} bin is denoted $\bar{y}_k$ then the Allan variance, $\sigma_y^2(\Gamma)$, is defined as:

$$\sigma_y^2(\Gamma) \equiv \sigma_y^2(n) = \frac{\sum_{k=1}^{P_0} \left(\bar{y}_{k+1} - \bar{y}_k\right)^2}{2P_0} \tag{4.15}$$

where P_0 is the number of groups or bins that the data set is distributed over. The Allan variance is effectively a measure of the mean square difference in the average value of $y(t)$ from one bin to the next. If Γ is small then there will be few measurements of $y(t)$ in each bin and the difference in the average value of $y(t)$ between one bin and the next will be dominated by the noise on the measurements. If, on the other hand, Γ is large then each bin will contain many measurements of $y(t)$ and the difference between the average value from one bin to the next will be dominated by the long term drift of the system. Between these two extremes there exists an optimum bin size whereby Γ is large enough to benefit from the extra certainty associated with averaging more measurements but not so large that the system drift will have a large effect, this is the point with the minimum Allan variance. In this case the variable is the ringdown time $\tau(t)$ and by varying the bin sizes (or equivalently the number of data points in each bin) and finding the bin size which minimises the Allan variance one can find the optimum number of ringdown events to average for the most sensitive possible CRDS measurement with this set up. Ringdown times were recorded over several thousand events and $\sigma_\tau^2(n)$ calculated for the possible values of n. This was done with the laser tuned to the maxima of the $Q(4)$ and $Q(6)$ lines, and exemplar data for the former case is shown in figure 4.18.

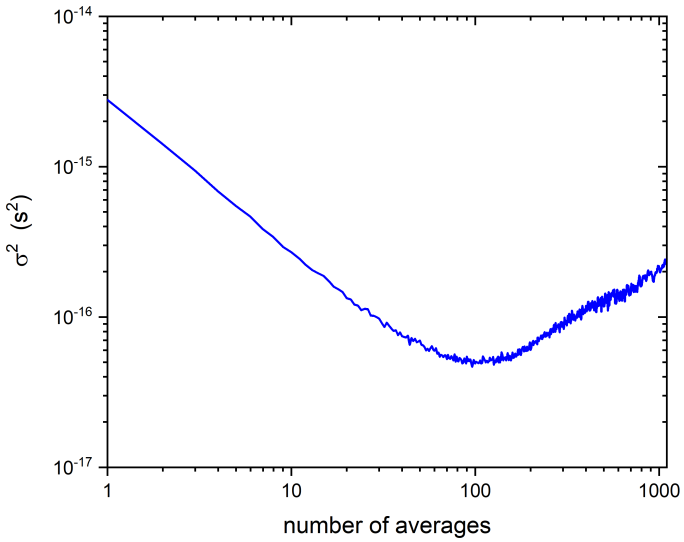

Figure 4.18: An Allan variance plot to find the minimum detectable amount of $O_2(a^1\Delta_g, v = 0)$ with the laser tuned to the $Q(4)$ line. α_{min} was found to be 1.3×10^{-10} cm^{-1}.

The number of ringdown events that must be averaged for minimum variance is ≈100 and corresponds to an Allan variance of 5×10^{-17}s^2 and a corresponding Allan deviation of 7×10^{-9}s. The Allan deviation represents the smallest change in ringdown time, from one point to the next, that this system could possibly detect and corresponds to a minimum detectable absorption coefficient, $\alpha_{min}(\nu)$, of $1.3{\times}10^{-10}$ cm^{-1}. Using the integrated cross section derived for the $Q(12)$ line $\sigma_{INT} = 2.26{\times}10^{-23}$ cm^2 cm^{-1} this corresponds to a minimum detectable line of sight averaged density in the $J'' = 12$ state of $8{\times}10^{10}$ cm^{-3} and at a rotational temperature of 346 K, a minimum detectable line of sight averaged density of $O_2(a^1\Delta_g, v = 0)$ of $1.1{\times}10^{12}$ cm^{-3} (i.e. an order of magnitude improvement over the previous absorption measurements of $O_2(a^1\Delta_g, v = 0)$)[51,52].

4.4.3 Lower pressures

Spectra were also obtained at lower pressures (50, 20 and 10 mTorr) with 300 W of plasma power. Examples of the $Q(6)$ spectra are shown in figure 4.19a along with one of the several 100 mTorr spectra that were averaged to produce the $Q(6)$ data in figure 4.14. Figure 4.19b shows the same but for the $Q(10)$ line.

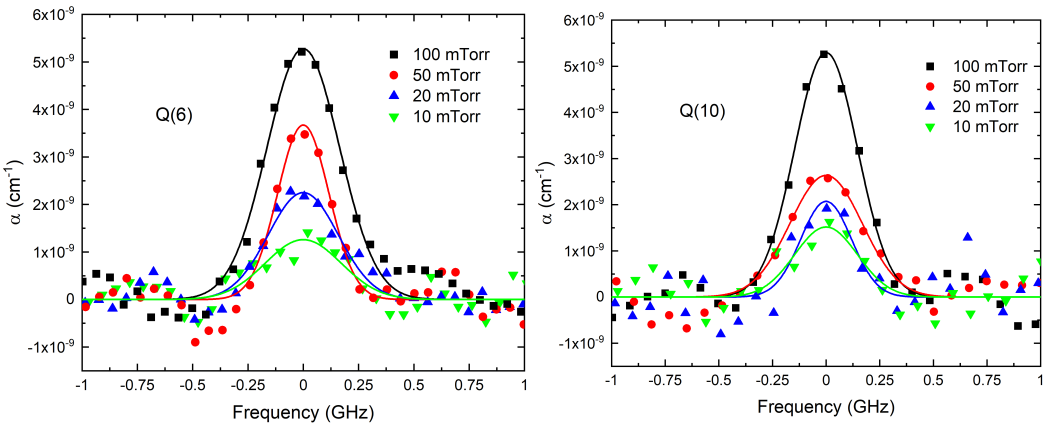

Figure 4.19: CRD spectra of the (a) $Q(6)$ and (b) $Q(10)$ rotational lines of the (0,0) Noxon band as a function of gas pressure at 300 W plasma power.

Both rotational lines show integrated areas that scale approximately linearly with pressure, as expected from previous work[123,124] and even at 10 mTorr there is discernable absorption and the ringdown system is capable of detecting $O_2(a^1\Delta_g)$. Given that the lowest pressures previously probed by absorption on the Noxon system are $>$ 1 Torr[121] this represents a significant expansion of the scope of this technique.

Unfortunately, the poor signal to noise ratio precludes a more detailed analysis of this lower pressure data and also make it impossible to observe $O_2(a^1\Delta_g)$ densities in the E-mode at 20 or 10 mTorr. The Gaussian fits shown for the various lines return temperature values of the order of 400 K but with typical uncertainties (at 10 and 20 mTorr) of ±200 K. This uncertainty is visible in the fits, for example, the 50 mTorr $Q(6)$ spectrum is markedly narrower that the lower pressure spectra whilst the 50 mTorr $Q(10)$ spectrum is much wider than its lower pressure counterparts. This inconsistency is purely a result of the poor signal to noise ratio making good fitting extremely difficult. For the 100 mTorr case this problem was overcome by taking several spectra (typically 6) and averaging them to produce reliable results as detailed above, but as the signal becomes smaller the number of spectra that must be averaged to produce reliable results becomes prohibitively large (10s or even 100s of spectra at the lowest pressures).

Given that the E/H switchover cannot be probed for $O_2(a^1\Delta_g)$ at the lower pressures (because of the small signals); that the $O(^3P)$ data shows that plasma temperature varies little with pressure; and the fact that the spectra in figure 4.19 already suggest, consistent with the literature, that $O_2(a^1\Delta_g)$ varies linearly with pressure, it was decided that taking the many spectra that would be required to confirm this unequivocally was not worthwhile. Instead the focus was on measuring the power variation of the $O_2(a^1\Delta_g)$ density at 100 mTorr where the E/H transition can be observed.

4.4.4 Discussion

Densities

Figure 4.16 illustrates that the $O_2(a^1\Delta_g)$ density increases markedly between 130 and 150 W in good agreement with the E/H switchover power determined by $O(^3P)$ CRDS and emission measurements. Meichsner and Wegner[91] report similar changes in the $O_2(a^1\Delta_g)$ number density with power at 38 and 75 mTorr. The trend in number density as a function of power can be qualitatively explained by considering the important production and loss processes for $O_2(a^1\Delta_g)$ in the E-mode and H-mode of the plasma[124]. Production of $O_2(a^1\Delta_g)$ is dominated by electron impact excitation of $O_2(X^3\Sigma_g^-)$ whilst the loss is dominated by wall quenching to form $O_2(X^3\Sigma_g^-)$. As power is increased in the E-mode the increasing electron density leads to increased $O_2(a^1\Delta_g)$ production while the rate of destruction at the walls is approximately constant; this explains the rapid increase in $O_2(a^1\Delta_g)$ density in this mode of operation

as power increases. In the H-mode the electron density increases much more modestly as power increases[149]. In this mode the increasing electron density is outweighed by the effects of increasing temperature. As the plasma heats the total number density in the chamber decreases (simply due to the ideal gas law) leading to a depletion of $O_2(X^3\Sigma_g^-)$ and a corresponding drop in the rate of $O_2(a^1\Delta_g)$ production. Additionally, heating of the plasma increases the rate of diffusion to, and loss at, the chamber walls. These two processes outweigh any electron density increases resulting in the observed decrease in $O_2(a^1\Delta_g)$ density with power in the H-mode. A more quantitative treatment of these kinetic considerations will be given in the next chapter.

Wall loss

The value of γ measured here is $\approx 3 \times 10^{-3}$, in good agreement with previous observations by Derzsi *et al.*[150] who deduced a γ value of 6×10^{-3} in a chamber constructed from aluminium which had been exposed to a pure oxygen plasma at 100 mTorr. Under such conditions aluminium surfaces exist with an oxidised layer, leading to the low wall loss coefficient. This is in contrast to metals such as Ag, Pt and Ni where the lack of such an oxidised layer leads to a wall loss coefficient an order of magnitude higher[122]. Small values for this wall loss coefficient have also been measured on a variety of other surfaces as summarised by Wayne.[151]

Comparison with atom measurements

The temperatures measured in these experiments ($T_{rot} = 346 \pm 38$ K at 300 W) should, in principle, be comparable to those measured for $O(^3P)$ in the power variation experiments (440 ± 25 K at 300 W) because both give line of sight average temperatures across the chamber. The significant difference between these values is therefore somewhat surprising, but it can be explained by the spatial inhomogeneity of the plasma temperature and the stability of the two species against wall loss on the steel baffle arms. $O_2(a^1\Delta_g)$ has a wall loss coefficient on steel of $\gamma \approx 0.007$[122] and is able to penetrate ≈5 cm into each baffle arm. Species present within the arms are thermally equilibrated with the chamber walls and hence the gas temperature is likely to be close to room temperature and absorption from gas in the arms brings down the line of sight average temperature. By way of comparison $O(^3P)$ has a wall loss coefficient on steel of ≈ 0.15[129] and thus penetrates ≈ 0.5 cm into the baffle arms leading to the much higher line of sight average temperature. It is of significance that the complementary data for the two species provides insight into their spatial distributions even though the CRDS technique itself is line of sight averaged.

4.5 $O_2(b^1\Sigma_g^+)$ measurements

$O_2(b^1\Sigma_g^+)$ (being the uppermost of the two low lying excited electronic states of molecular oxygen) cannot be probed by visible or near infrared absorption spectroscopy. Useful information can still be provided however by the near infrared emission of this state on the magnetic dipole allowed $O_2(b^1\Sigma_g^+) - O_2(X^3\Sigma_g^-)$ system. Wavelength resolved emission on the (0, 0) and (1, 1) bands of this system were collected using the Andor spectrometer described in section 4.1.

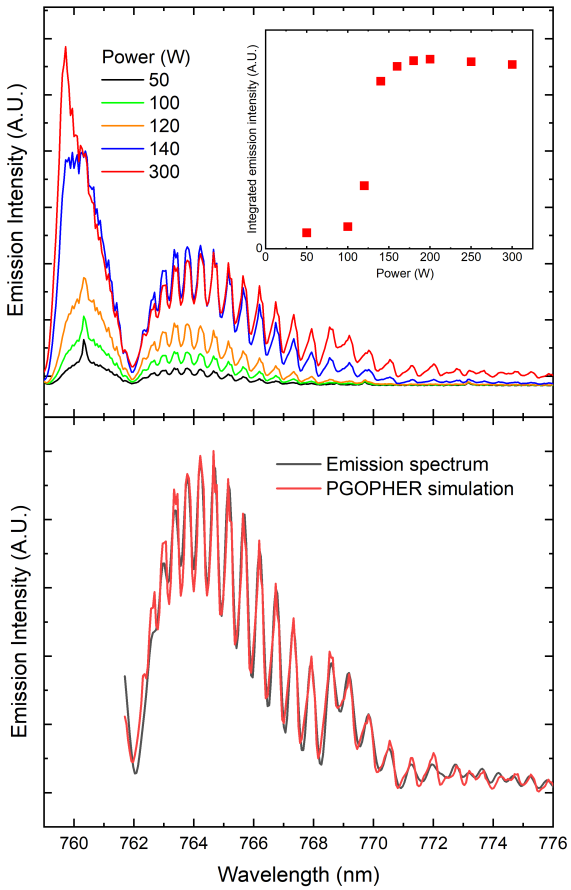

Figure 4.20: Upper panel: Emission on the oxygen A-band ($O_2(b^1\Sigma_g^+, v = 0) - O_2(X^3\Sigma_g^-, v = 0)$) as a function of plasma power (and at 100 mTorr gas pressure) showing evidence of E-H mode switchover and rotational and vibrational heating. Inset: Integrated area of the A-band emission as a function of power, indicating the trend in $[O_2(b^1\Sigma_g^+)]$. Lower panel: PGOPHER fit to the 300 W data (adjusted for spectrometer efficiency) yielding $T_{rot} = 629 \pm 10$ K and $T_{vib} = 905 \pm 40$ K

The upper panel of figure 4.20 shows a sample of raw emission data gathered at 100 mTorr pressure and operating powers between 50 and 300 W. The dominant feature in all the spectra is the (0,0) vibrational band. The increase in emission intensity

(which is also visible to the naked eye) between 120 W and 140 W provides strong evidence of the E/H switchover and corroborates the observation of this switchover by broadband emission and CRD spectroscopy. Although emission spectra are limited in their ability to provide absolute number densities it is expected that the integrated area under the emission band is proportional to the $O_2(b^1\Sigma_g^+)$ density. The results of numerical integration of the emission spectra are shown in the inset to figure 4.20. It is notable that from 140 W up to 300 W the total emission changes little, indicating an approximately constant $[O_2(b^1\Sigma_g^+)]$. However, over this power range, emission from higher rotational states ($\approx$ 768 nm) increases in intensity whilst that from lower rotational states ($\approx$ 763 nm) becomes less intense providing evidence of rotational heating. Likewise the increasing emission on the (1,1) band (above 768 nm) is also evidence of internal heating, in this case, in the vibrational mode.

Extraction of a reliable temperatures from these spectra can be achieved via a contour fit with a PGOPHER[55] simulation (with molecular constants and Franck-Condon factors from Yu *et al.*[152] and the magnetic dipole moment from Drouin *et al.*[79]). Before such a fit can be performed the raw spectra must be scaled in order to account for the wavelength dependence of the spectrometer diffraction grating efficiency and the quantum efficiency of the CCD, both of which are taken from the spectrometer's manual. The lower panel of figure 4.20 shows an example fit to the scaled emission spectrum taken at 300 W and returns a rotational temperature $T_{rot} = 629 \pm 10$ K and a vibrational temperature of $T_{vib} = 905 \pm 40$ K (errors are estimated by repeatedly fitting the spectrum with different initial parameters to establish the reproducibility of the optimised fit). Usefully, because the $O_2(b^1\Sigma_g^+)$ state is metastable it is likely to be in vibrational equilibrium with $O_2(a^1\Delta_g)$ and $O_2(X^3\Sigma_g^-)$ (because V-V energy transfer between the different electronic states is likely to be faster than their production and loss rates[141]) meaning that these emission spectra can provide a reasonable guide as to the vibrational temperature of other species in the plasma. Fits to spectra at other powers produced the rotational temperatures displayed in figure 4.21.

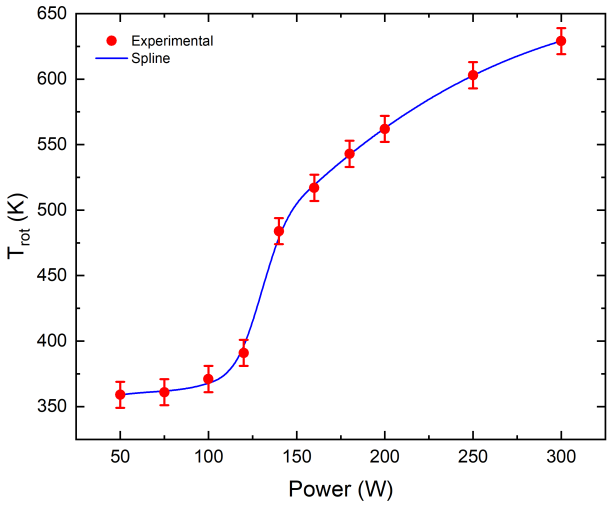

Figure 4.21: Rotational temperature as a function of plasma power (at 100 mTorr pressure) as determined by contour fitting using PGOPHER to emission data shown in figure 4.20. Also shown is a spline interpolation (shown in blue) used later for volume averaged modelling.

The temperatures show a smooth trend of increasing T_{rot} with increasing power from ≈350 K in the CCP regime up to ≈630 K in the ICP regime. The E/H mode transition is clearly present, as a sharp rise in temperature, again between 120 and 140 W. Also shown on the plot is a spline (blue) which is used for kinetic modelling purposes (see later). The low intensity of the (1,1) emission for powers below 300 W precluded the accurate determination of T_{vib} under these conditions. It should be noted that these emission derived temperatures should be treated with caution because the data are necessarily weighted towards the hottest (and brightest) regions of the plasma, this is the reason for the significant difference between these emission derived temperatures and those found using CRDS (which are line of sight averaged). The difference in temperature is ≈ 50 K in the E-mode, increasing to ≈ 150 K in the H-mode and is a strong indication that different regions of the plasma exhibit different translational temperatures. Such spatial inhomogeneity is well known in ICPs and is discussed at length below. As a result of this inhomogeneity, temperatures derived from emission are not representative of the bulk but instead indicate a lower bound on the maximum temperature within the plasma.[82] Additional uncertainty is introduced by the need to correct the raw data for the wavelength dependence of the spectrograph and the CCD quantum efficiencies. Nevertheless, the data do provide a good qualitative guide to trends in internal excitation within the plasma.

4.5.1 Wall loss kinetics

As for $O(^3P)$ and $O_2(a^1\Delta_g)$ reaction at the chamber walls is also an important loss process for $O_2(b^1\Sigma_g^+)$. Temporally resolved observation of the $O_2(b^1\Sigma_g^+) - O_2(X^3\Sigma_g^-)$ emission taken whilst the plasma was modulated can provided a measurement of the wall loss coefficient for $O_2(b^1\Sigma_g^+)$. A 760 nm optical filter (FWHM = 10 nm) was placed in front of a photomultiplier tube, chosen for its high sensitivity and fast response time (≈1 ns), to restrict the emission incident on the detector to that arising from the $O_2(b^1\Sigma_g^+) - O_2(X^3\Sigma_g^-)$ system. The plasma was then modulated on and off (between 0 and 200 W) and the decay in emission intensity from $O_2(b^1\Sigma_g^+)$ measured, as shown in figure 4.22.

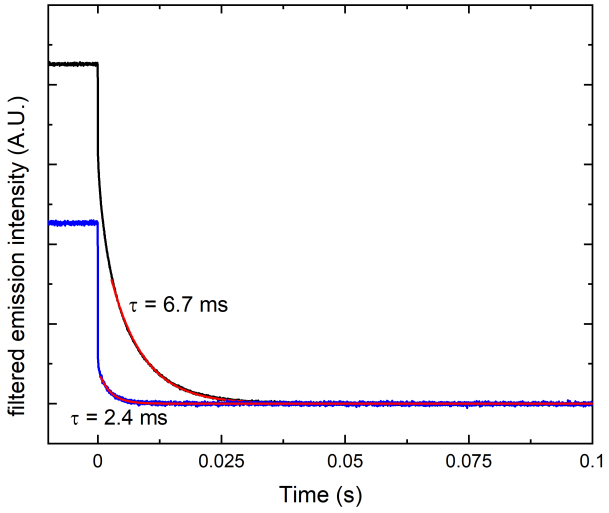

Figure 4.22: Temporal decay in the emission intensity of the oxygen A-band as a function of time after plasma is extinguished (from 300 W to 0 W) at 100 mTorr (black) and 10 mTorr (blue) each fitted with an exponential. This measurement was made by filtering the emission from the plasma and then detecting with a photomultiplier.

Loss at the chamber walls is the only important loss process that persists for more than a few μs after the plasma is extinguished. Lifetimes of 6.7 ± 0.5 ms and 2.4 ± 0.3 ms were determined at 100 mTorr and 10 mTorr, respectively, from single exponential fits to the time-resolved data. For the purposes of fitting, the first few ms of data were excluded to ensure that the loss being measured was only due to wall reaction. The resulting lifetimes (< 7 ms) are significantly shorter than those measured for $O(^3P)$ and $O_2(a^1\Delta_g)$ (both ≈100 ms), indicating that $O_2(b^1\Sigma_g^+)$ wall loss lies much closer to the diffusion dominated regime, whereby the first term in equation 4.5 dominates.

In principle equation 4.5 allows wall loss measurements under one set of conditions to be reasonably extrapolated to other operating conditions. It should be noted, however, that this equation is an approximation, and strictly applies only when the plasma is well described by a single temperature. In this case, the different emission and CRDS temperature measurements result from the spatial inhomogeneity of the plasma temperature, and so equation 4.5 must be used with caution. For both $O(^3P)$ and $O_2(a^1\Delta_g)$ the second term in equation 4.5 dominates, and as this term is only weakly temperature dependent, $v \propto \sqrt{T}$, the approximation works reasonably well despite temperature inhomogeneity. For $O_2(b^1\Sigma_g^+)$ however, the first term in equation 4.5 is significant and has a much stronger temperature dependence (from kinetic theory $D \propto T^{\frac{3}{2}}$). This means that at 100 mTorr, the temperature inhomogeneity leads to significant spatial variation in the rate at which $O_2(b^1\Sigma_g^+)$ diffuses and this impacts the wall loss rate. Specifically, much of the $O_2(b^1\Sigma_g^+)$ will exist in the hot centre of the chamber and will be at a temperature above the average and therefore diffuse out of this region more rapidly than equation 4.5 predicts. Indeed using the $O(^3P)$ CRDS derived average temperature (429K at 200 W) and diffusion coefficients from Winn, equation 4.5 predicts a minimum wall loss lifetime (i.e. with $\gamma = 1$) of 7.5 ms at 100 mTorr. This value is longer than the observed lifetime of 6.7 ms and indicates the breakdown of the approximations inherent in equation 4.5. This difficulty can be overcome by moving into a regime where the plasma is more spatially uniform and diffusion to chamber walls is faster (so that the first term in equation 4.5 becomes less significant). This can be achieved by operating at a lower pressure, and a temporal decay in $O_2(b^1\Sigma_g^+)$ emission at 10 mTorr yields a lifetime of 2.4 ms and allows extraction of a more reasonable wall loss coefficient of $\gamma = 0.2$. Further measurements at 20 mTorr yield the same value, suggesting there is little variation of γ with pressure and hence that $\gamma = 0.2$ is likely to be a realistic value for wall loss of $O_2(b^1\Sigma_g^+)$.

4.5.2 Discussion

The majority of previous work utilising emission from O_2 plasmas as a diagnostic tool has focused on strong atomic emission (e.g at 777 and 844 nm). Such emission has been used in particular for actinometric[93–95], and TALIF based determination of atom densities (via non-trivial calibration processes)[101–105]. Molecular emission bands can yield useful quantitative information, namely temperatures T_{rot} and T_{vib}, with the former expected to be in equilibrium with the translational temperature T_{trans}, as well as relative density information (although absolute concentrations cannot be easily

determined). Plasma emission comes predominantly from the regions of the plasma where electron impact excitation is largest (i.e. in the centre of the chamber); these regions are also expected to have the highest gas temperature, such that temperatures derived from emission data are more representative of the temperature at the centre of the chamber. It is therefore significant that the emission based T_{rot} values (629 ± 10 K at 300 W) agree well with that from Kiehlbauch and Graves[82] for the gas phase neutral temperature (≈ 600 K for 300 W) away from the chamber walls. The emission derived temperatures are also in good agreement with other previous work utilising emission spectroscopy[149]. Vibrational temperatures, T_{vib}, in oxygen ICPs are expected to be higher than T_{trans} and T_{rot} due to the more efficient transfer of energy from electrons into vibrational modes[141]. They are however expected to be lower than the T_{vib} values observed in N_2 plasmas (where resonant vibrational excitation via the $N_2^-(X^2\Pi_g)$ state makes electron to vibration energy transfer extremely efficient)[153]. The measured value of 905 ± 40 K at 100 mTorr and 300 W sits in this regime, between ≈460 K for T_{trans} (based on $O(^3P)$ CRDS), and ≈ 3500 K measured for N_2 plasma under similar conditions in the same chamber[63,153]. This value also compares favourably with effective T_{vib} values that can be estimated (for low vibrational levels) from the vibrational distribution function of Annusova *et al.*[141]. At 80 mTorr and 500 W these researchers predict a ratio of v = 0 to v = 1 populations to be approximately 10, corresponding to a T_{vib} ≈ 1000 K. Annusova *et al.*[141] also report significantly non-thermal vibrational population distributions which indicates that the measured vibrational temperature is likely to underestimate the populations of higher lying vibrational levels. However, given that these high lying states are predominantly lost by V-T energy transfer with $O(^3P)$ and the observed atom densities are significantly higher than those modelled by Annusova *et al.*[141], it is likely that these vibrationally excited molecules account for a very small proportion of the total molecular density and thus ignoring this higher vibrational excitation (and its non-thermal nature) makes little difference to any conclusions based on treating the vibrational energy distribution as a Boltzmann distribution.

Wall loss

The fact that the plasma exhibits thermal inhomogeneity is also manifest in the inapplicability of the Chantry model[125] of wall loss (equation 4.5) to the time resolved observations at 100 mTorr, resulting in the need to reduce the gas pressure in order to obtain physically reasonable wall loss coefficients for $O_2(b^1\Sigma_g^+)$. It is of interest to compare the measured wall loss coefficient for $O_2(b^1\Sigma_g^+)$, $\gamma = 0.2$, with previous

literature values. Wayne[151] reported that γ lies between 0.002 and 0.04 for a variety of surfaces (none of them aluminium) whilst the more recent work of Perram *et al.*[154] found a value of 0.007 for aluminium (although in that work it was assumed that $O_2(a^1\Delta_g)$ was formed by loss of $O_2(b^1\Sigma_g^+)$ at the walls where most literature assumes that $O_2(X^3\Sigma_g^-)$ is the product). Meichsner and Wegner[91] found that a value of $\gamma = 0.007$ for $O_2(b^1\Sigma_g^+)$ wall loss was self consistent, within a volume averaged model, reproducing experimentally measured $[O_2(a^1\Delta_g)]$ determined in a stainless steel chamber. However, they also found that $[O_2(b^1\Sigma_g^+)]$ was expected to exceed the $[O_2(a^1\Delta_g)]$ in the H-mode, something which simply does not occur in the plasma investigated here - if it did there would be evidence of stimulated emission on the Noxon band rather than the absorption actually observed. In this way the measurements of $O_2(a^1\Delta_g)$ corroborate that 0.007 is far too low a value of γ for $O_2(b^1\Sigma_g^+)$ in the chamber used here. Several other modellers have used the significantly higher value of 0.1.[124,155] This is in much better agreement with the current observations and with the recent work of Booth *et al.*[156] who found a value of 0.135. The value of 0.1 originates from an assertion that wall loss of $O_2(b^1\Sigma_g^+)$ ought to be between 10 and 100 times faster than the same process for $O_2(a^1\Delta_g)$[128,157]. The measurements of sticking coefficients for both species presented here are in agreement with this assertion, with the ratio between the two coefficients for the current chamber found to be $\approx$66.

Measurements of key physiochemical parameters associated with the most important species present in a low pressure inductively coupled oxygen plasma, including number densities, temperatures and wall loss coefficients have been presented in this chapter. In the next chapter a volume averaged model is developed to help interpret these observations.

Chapter 5

Volume averaged kinetic modelling of oxygen plasma

This chapter presents the details of a volume averaged kinetic model which has been developed to interpret the optical measurements from chapter 4. In particular the model seeks to understand the variation in densities of $O(^3P)$ and $O_2(a^1\Delta_g)$ as plasma power is varied across the E/H transition. Much prior work exists on the modelling of oxygen ICPs at a range of pressures[11,30,90,91,123,124,149,155], and the reliability of such models relies heavily on the accuracy of rate coefficients available in the literature. Additionally, judging which reactions are most important and need to be included depends on the plasma conditions, e.g. termolecular reactions can be neglected at low pressure but can become important at high pressure. As the name suggests, inherent to a volume averaged model is the assumption that the plasma is spatially uniform throughout its volume (≈20 L for this chamber). Although this assumption is never strictly true, and chemistry can vary spatially, particularly near the chamber walls, such models can still prove quantitatively and qualitatively useful. The aim here is to select a reaction set capable of providing a reasonable quantitative agreement with experimental observations while retaining minimal complexity. To that end, excited molecular states above the $O_2(b^1\Sigma_g^+)$ state are excluded, as are the second excited state of the atom $O(^1S)$[158] and the ions O^+, O_3^+, O_2^- and O_3^- (which are less important than O_2^+[124] and O^-[91]). Ozone (O_3) is also excluded, because its formation generally involves a termolecular reaction and such reactions are slow at the low pressures investigated here.

5.1 Reaction set

Electron impact rate coefficients

Rate coefficients, $k(T_e)$, for electron impact processes are given in table 5.1 and for computational convenience are expressed in the form:

$$k(T_e) = aT_e^b \exp\left(\frac{-c}{T_e}\right), \tag{5.1}$$

where T_e is the electron temperature (in eV) and a, b and c are constants. Rate coefficients in this form were either deduced from the reported T_e dependence of literature rate coefficient values or determined from literature cross sections, in order to find the values of a, b and c that provided the best fit for $T_e < 4$ eV (i.e. the electron temperatures likely to be present in the plasma). When only collision cross sections, $\sigma(E)$, are available the rate coefficients may be calculated according to:

$$k = \sqrt{\frac{2}{m_e}} \int_0^\infty E^{\frac{1}{2}} \sigma(E) f(E) \mathrm{d}E, \tag{5.2}$$

where $f(E)$ is the EEDF and is here assumed to be Maxwellian. The dependence of the rate coefficient on electron temperature can then be well approximated by equation 5.1 with optimised parameters. Efforts are made to use the latest available rate coefficient and cross section data, particularly the calculations of Laporta *et al.*[159] and Tashiro *et al.*[160]. Sometimes, particularly for electronically excited species, electron impact cross sections are unknown. In such cases a couple of techniques of approximation exist in order to estimate the relevant rate coefficients.[161] The first of these techniques is threshold adjustment which estimates the rate coefficient for electron impact on an electronically excited state, k_{ex}, by multiplying the rate coefficient for the same electron impact process on the ground state, k_{gr}, by an Arrhenius factor. The Arrhenius factor accounts for the fact that less electron energy is required for reaction if the atom or molecule starts in an excited state. The threshold adjustment can be expressed as:[161]

$$k_{ex} \approx k_{gr} \exp\left(\frac{\Delta E}{T_e}\right), \tag{5.3}$$

where ΔE is the difference in energy between the ground and excited state expressed in eV. In O_2 the $O_2(a^1\Delta_g)$ state is 0.98 eV above the ground state whilst $O_2(b^1\Sigma_g^+)$ is 1.63 eV above the ground state. Threshold adjustment is used to estimate the rates of reactions 11 and 12 from the rate of reaction 10 by multiplication by factors of $\exp(0.98/T_e)$ and $\exp(1.63/T_e)$, respectively.

Table 5.1: Electron impact reactions and corresponding rate coefficients (T_e in eV).

#	Reaction	Rate Coefficient / $\mathrm{cm^3\,s^{-1}}$	ref.
1	$e^- + O_2(X^3\Sigma_g^-) \rightarrow e^- + 2O(^3P)$	$1.74\times10^{-8}T_e^{-0.71}\exp(-7.19/T_e)$	162
2	$e^- + O_2(a^1\Delta_g) \rightarrow e^- + 2O(^3P)$	$1.42\times10^{-8}T_e^{-0.65}\exp(-6.12/T_e)$	162
3	$e^- + O_2(b^1\Sigma_g^+) \rightarrow e^- + 2O(^3P)$	$1.22\times10^{-8}T_e^{-0.6}\exp(-5.37/T_e)$	162
4	$e^- + O_2(X^3\Sigma_g^-) \rightarrow e^- + O(^3P) + O(^1D)$	$1.08\times10^{-7}T_e^{-0.64}\exp(-9.45/T_e)$	162
5	$e^- + O_2(a^1\Delta_g) \rightarrow e^- + O(^3P) + O(^1D)$	$8.26\times10^{-8}T_e^{-0.51}\exp(-8.27/T_e)$	162
6	$e^- + O_2(b^1\Sigma_g^+) \rightarrow e^- + O(^3P) + O(^1D)$	$6.83\times10^{-8}T_e^{-0.42}\exp(-7.45/T_e)$	162
7	$e^- + O_2(X^3\Sigma_g^-) \rightarrow O^- + O(^3P)$	$8.01\times10^{-10}T_e^{-1.17}\exp(-5.57/T_e)$	159
8	$e^- + O_2(a^1\Delta_g) \rightarrow O^- + O(^3P)$	$2.34\times10^{-9}T_e^{-1.13}\exp(-4.52/T_e)$	159
9	$e^- + O_2(b^1\Sigma_g^+) \rightarrow O^- + O(^3P)$	$1.98\times10^{-9}T_e^{-1.1}\exp(-3.88/T_e)$	159
10	$e^- + O_2(X^3\Sigma_g^-) \rightarrow 2e^- + O_2^+$	$2.34\times10^{-9}T_e^{1.03}\exp(-12.29/T_e)$	161
11	$e^- + O_2(a^1\Delta_g) \rightarrow 2e^- + O_2^+$	$2.34\times10^{-9}T_e^{1.03}\exp(-11.31/T_e)$	161†
12	$e^- + O_2(b^1\Sigma_g^+) \rightarrow 2e^- + O_2^+$	$2.34\times10^{-9}T_e^{1.03}\exp(-10.66/T_e)$	161†
13	$e^- + O_2(X^3\Sigma_g^-) \rightarrow e^- + O_2(a^1\Delta_g)$	$1.02\times10^{-9}T_e^{0.12}\exp(-2.03/T_e)$	160
14	$e^- + O_2(a^1\Delta_g) \rightarrow e^- + O_2(X^3\Sigma_g^-)$	$1.53\times10^{-9}T_e^{0.12}\exp(-1.05/T_e)$	160‡
15	$e^- + O_2(X^3\Sigma_g^-) \rightarrow e^- + O_2(b^1\Sigma_g^+)$	$4.23\times10^{-10}T_e^{-0.04}\exp(-2.78/T_e)$	160
16	$e^- + O_2(b^1\Sigma_g^+) \rightarrow e^- + O_2(X^3\Sigma_g^-)$	$1.27\times10^{-9}T_e^{-0.04}\exp(-1.153/T_e)$	160‡
17	$e^- + O_2(a^1\Delta_g) \rightarrow e^- + O_2(b^1\Sigma_g^+)$	$2.75\times10^{-9}T_e^{-0.01}\exp(-0.82/T_e)$	160
18	$e^- + O_2(b^1\Sigma_g^+) \rightarrow e^- + O_2(a^1\Delta_g)$	$5.50\times10^{-9}T_e^{-0.01}\exp(-0.17/T_e)$	160‡
19	$e^- + O(^3P) \rightarrow e^- + O(^1D)$	$4.54\times10^{-9}\exp(-2.36/T_e)$	161
20	$e^- + O(^1D) \rightarrow e^- + O(^3P)$	$8.17\times10^{-9}\exp(-0.4/T_e)$	161
21	$e^- + O^- \rightarrow 2e^- + O(^3P)$	$5.47\times10^{-8}T_e^{0.324}\exp(-2.98/T_e)$	161
22	$e^- + O_2^+ \rightarrow O(^3P) + O(^1D)$	$1.47\times10^{-8}T_e^{-0.9}$	163
† Estimated by threshold adjustment of reaction 10 (see text) ‡ Estimated by detailed balancing (see text)			

The second approximate method is detailed balancing. Detailed balancing seeks to estimate the rate coefficient of superelastic processes (also known as electron impact de-excitation), k', from the rate of the corresponding excitation process, k

$$e^- + A \underset{k'}{\overset{k}{\rightleftharpoons}} e^- + A^*. \tag{5.4}$$

Detailed balancing suggests that

$$k' \approx k\frac{g_A}{g_{A*}}\exp\left(\frac{\Delta E}{T_e}\right), \tag{5.5}$$

where g_A and g_{A*} are degeneracies and ΔE is the energy difference between A and A* in eV.[161] In this way, detailed balancing effectively ensures that, if A and A* are only interconverted by electron impact processes, they will be in equilibrium. It neglects other processes that interconvert A and A* and is thus only a rough approximation but, in the absence of better alternatives, it is a method often utilised in plasma modelling. Detailed balancing is used to calculate the rate coefficients for reactions 14, 16, 18 and 20. The degeneracies for the low lying states of molecular oxygen depend on the number of available rotational states, for $O_2(X^3\Sigma_g^-)$, $O_2(a^1\Delta_g)$ and $O_2(b^1\Sigma_g^+)$ rotational states are in the approximate ratios 3:2:1 (due to the spin triplet ground state and the Λ-doubled first excited state). Hence, for example,

$$k_{14} \approx k_{13}\frac{3}{2}\exp\left(\frac{0.98}{T_e}\right). \tag{5.6}$$

Heavy species rate coefficients

Rate coefficients for reactions between heavy species are given in table 5.2 in terms of their translational temperature, T_{trans}. Over the entire temperature range modelled ($300-460$ K), the rate coefficients of the processes in table 5.2 vary by no more than 18%; they are thus approximately constant for all modelled conditions.

Table 5.2: Heavy species reactions and corresponding rate coefficients (T_{trans} in Kelvin).

#	Reaction	Rate Coefficient / $cm^3\,s^{-1}$	ref
23	$O^- + O_2^+ \rightarrow O(^3P) + O_2(X^3\Sigma_g^-)$	$3.2\times10^{-7}T_{trans}^{-0.44}$	161
24	$O^- + O_2^+ \rightarrow 3O(^3P)$	$3.2\times10^{-7}T_{trans}^{-0.44}$	161
25	$O^- + O_2(a^1\Delta_g) \rightarrow e^- + O_3$	3.3×10^{-11}	161
26	$O^- + O_2(b^1\Sigma_g^+) \rightarrow e^- + O(^3P) + O_2(X^3\Sigma_g^-)$	6.9×10^{-10}	161
27	$O^- + O(^3P) \rightarrow e^- + O_2(X^3\Sigma_g^-)$	1.6×10^{-10}	161
28	$O(^1D) + O_2(X^3\Sigma_g^-) \rightarrow O(^3P) + O_2(a^1\Delta_g)$	$1.6\times10^{-12}\exp(67/T_{trans})$	164,165
29	$O(^1D) + O_2(X^3\Sigma_g^-) \rightarrow O(^3P) + O_2(b^1\Sigma_g^+)$	$2.56\times10^{-11}\exp(67/T_{trans})$	164,165
30	$O(^1D) + O_2(X^3\Sigma_g^-) \rightarrow O(^3P) + O_2(X^3\Sigma_g^-)$	$4.8\times10^{-12}\exp(67/T_{trans})$	164,165

Some recent work has suggested that reactive quenching by $O(^3P)$ may be an important loss process for metastable oxygen molecules at high temperatures.[156,166] For the highest atom density ($\approx 3\times10^{14}$ cm^{-3} for power variation data) and temperature (≈ 450 K) the rate coefficients reported previously suggest lifetimes against this quenching process of ≈6000 s for $O_2(a^1\Delta_g)$ and ≈124 ms for $O_2(b^1\Sigma_g^+)$. The observed

lifetimes for both these species (from CRDS or emission) are significantly shorter than these calculations suggest and so these quenching processes are not important under the conditions investigated here. Additionally, many termolecular reactions, which could be important at high pressure are insignificant because the low pressures used here make three body collision processes extremely unlikely, these reactions are also excluded from the reaction set.

Wall loss coefficients

Rate coefficients for wall loss are calculated using equation 4.5 with wall loss coefficients for $O(^3P)$, $O_2(a^1\Delta_g)$ and $O_2(b^1\Sigma_g^+)$ measured (see previous chapter) and the coefficient for $O(^1D)$ assumed to be unity, as is common in the literature[91,124].

Table 5.3: Wall loss reactions and corresponding loss coefficients.

#	Reaction	Wall loss coefficient (γ)	ref.
31	$O_2(a^1\Delta_g)$ + wall $\rightarrow O_2(X^3\Sigma_g^-)$	0.003	This work
32	$O_2(b^1\Sigma_g^+)$ + wall $\rightarrow O_2(X^3\Sigma_g^-)$	0.2	This work
33	$O(^3P)$ + wall $\rightarrow \frac{1}{2}\ O_2(X^3\Sigma_g^-)$	0.003	This work
34	$O(^1D)$ + wall $\rightarrow O(^3P)$	1	[91,124]

5.2 Model inputs and outputs

Using this reaction set, and taking T_{trans}, T_e and $[e^-]$ as inputs, a series of kinetic balances are established whereby the rates of production and destruction of each species must be equal at equilibrium. Balances are constructed for $O_2(a^1\Delta_g)$, $O_2(b^1\Sigma_g^+)$, $O(^3P)$, $O(^1D)$ and O^-. Also included are a pressure balance (i.e. the sum of partial pressures of the important species equals the total pressure) and a charge balance ($[e^-] + [O^-] = [O_2^+]$). This set of seven simultaneous equations is then solved (for a given T_{trans}, T_e and $[e^-]$) for the seven variables: $[O_2(X^3\Sigma_g^-)]$, $[O_2(a^1\Delta_g)]$, $[O_2(b^1\Sigma_g^+)]$, $[O(^3P)]$, $[O(^1D)]$, $[O^-]$ and $[O_2^+]$. By taking experimental T_{trans} values and varying T_e and $[e^-]$ the values that best reproduce experimental measurements of $[O_2(a^1\Delta_g)]$ and $[O(^3P)]$ can be found and likely densities of other species inferred. It is worth noting that the threshold energy for producing $O_2(a^1\Delta_g)$ (via reaction 13) is 0.98 eV whilst the threshold for atom production (reaction 1) is $\approx$ 5 eV. The different threshold energies mean that the densities of these species are sensitive to different regions of the EEDF and the optimised model values of T_e and $[e^-]$ must reflect this.

Choice of translation temperature

The measurements presented so far ($O(^3P)$ (before and after chamber cleaning), $O_2(a^1\Delta_g)$ and $O_2(b^1\Sigma_g^+)$) all show different translational temperatures because of the cleaning of the chamber walls and because of the inhomogeneity of the plasma (as discussed previously). The question therefore arises as to which T_{trans} values ought to be used as inputs for the kinetic model. The model is primarily aimed at understanding the E/H switchover and all the data pertaining to this switchover were taken after the chamber cleaning, hence the $O(^3P)$ data from before the cleaning is not used for modelling. The emission data are expected to be weighted towards the brightest regions of the plasma and the $O_2(a^1\Delta_g)$ data (which is less certain anyway due to small signal to noise) weighted towards the cooler regions due to the extra penetration of this stable species into the baffle arms, for these reasons neither of these data sets are chosen. This leaves the $O(^3P)$ data from after the chamber cleaning which is deemed most representative of the mean temperature across the chamber diameter without undue weighting toward the hotter or cooler parts of the plasma.

These values have one disadvantage, compared to the values derived from emission spectra the CRDS derived values for T_{trans} have much greater uncertainties (compare figure 4.11 and figure 4.21). In an attempt to minimise the influence of this uncertainty on the model results a spline is fitted to the emission derived temperatures (figure 4.21 in blue) and scaled so as to best fit the CRDS data (figure 4.11 in blue). This allows an estimate of a smoothly varying line of sight averaged temperature using the CRDS measurements but taking advantage of the better signal to noise ratio offered by the emission data.

The EEDF

Throughout the modelling, for the sake of simplicity, a Maxwellian distribution of electron energies is assumed and this could influence the electron temperature that the model returns. In particular a Maxwellian distribution typically overestimates the relative density of higher energy electrons and to compensate this it is possible that the model may underestimate the effective electron temperature[167]. The assumption of a Maxwellian EEDF has been shown to be a good approximation for the plasma H-mode[149] with just a small depletion of electrons at high energies (> 15 eV[89]). In the E-mode however, the Maxwellian approximation is less realistic (bi-Maxwellian and Druyvesteyn EEDFs being more realistic[89,149]) and so the modelling is likely to be less reliable, although still qualitatively informative, in this regime.

5.3 Model results - varying power and the E/H switchover

Electron densities and temperatures

The modelled values for T_e and [e$^-$] that were found to best reproduce the measured [O(^{3}P)] and [$O_2(a^1\Sigma_g^+)$, v = 0)] are shown in figure 5.1. Both quantities show a sharp rise during the E/H switchover, with [e$^-$] increasing by approximately an order of magnitude (up to $\approx 4.2 \times 10^9$ cm^{-3}) over the power range. T_e undergoes a more modest increase (from ≈1.23 to ≈1.42 eV). Within the H-mode, [e$^-$] and T_e continue to increase only gradually.

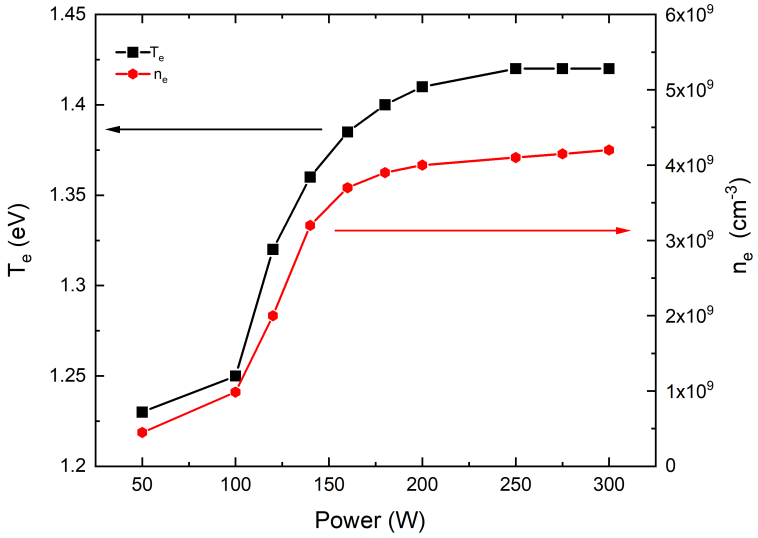

Figure 5.1: Electron densities and temperatures as predicted by the kinetic model as a function of plasma power at 100 mTorr gas pressure.

5.4 Neutral species

Figure 5.2 shows the variation in densities predicted by the kinetic model for all the species (note the logarithmic ordinate scale). By far the most abundant species are the three lowest lying molecular states (X, a and b) and the ground state atoms, all of which are more than two orders of magnitude more abundant than the next most abundant species (O(^{1}D)).

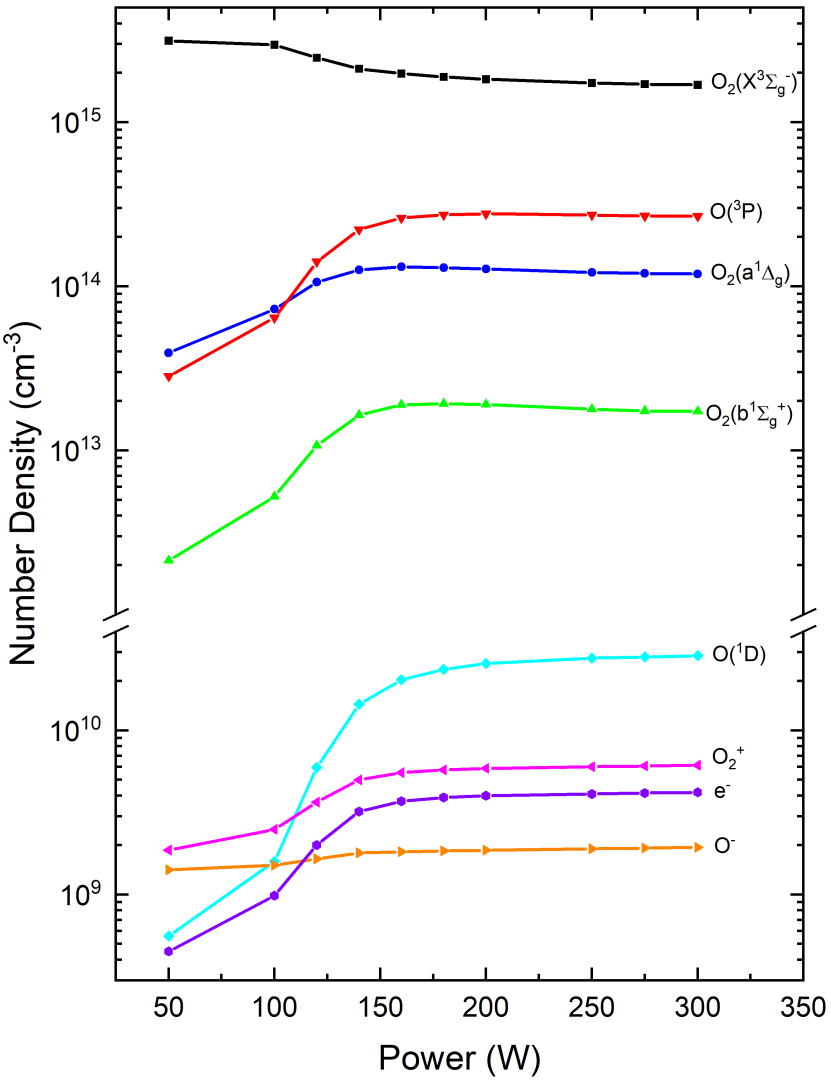

Figure 5.2: Number densities of all modelled species as a function of plasma power at 100 mTorr gas pressure.

Figure 5.3 shows a comparison of the predicted $[O(^3P)]$, $[O_2(a^1\Delta_g)]$ and $[O_2(b^1\Sigma_g^+)]$ and their experimentally determined values. The experimental values are absolute (from CRDS) for $O(^3P)$ and $O_2(a^1\Delta_g)$ and relative for $O_2(b^1\Sigma_g^+)$ from emission spectra (see figure 4.20 inset). In order to better understand the kinetic processes controlling the equilibrium densities found by the model, the important processes of production and loss for each species are now considered in turn.

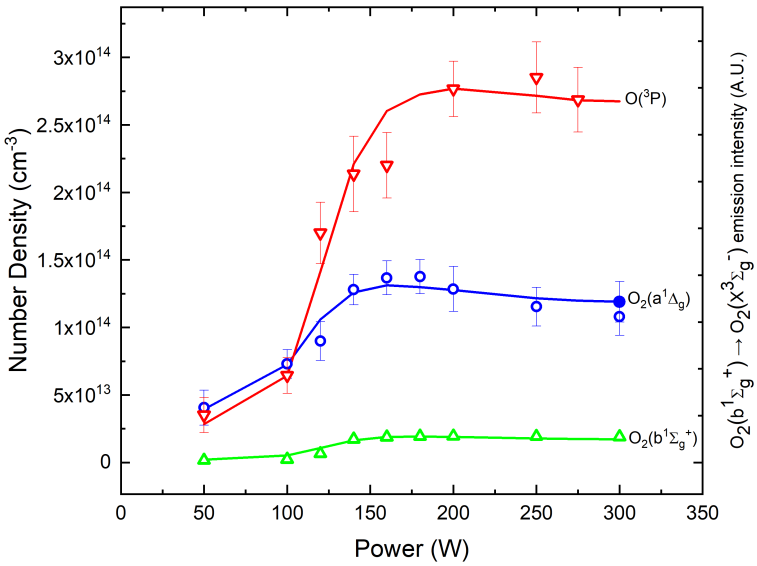

Figure 5.3: Number densities of $O(^3P)$ (red), $O_2(a^1\Delta_g)$ (blue) and $O_2(b^1\Sigma_g^+)$ (green) as a function of plasma power and at 100 mTorr gas pressure as predicted by the model (solid lines) and compared to values derived from experiments (unfilled points). For $O(^3P)$ and $O_2(a^1\Delta_g)$ experimental values are absolute measurements made by CRDS, for $O_2(b^1\Sigma_g^+)$ the values are scaled relative densities derived from emission spectra. The filled blue circle represents the density corrected for vibrational excitation, see text.

$O_2(X^3\Sigma_g^-)$

The ground state of O_2 is the only species whose density decreases monotonically with increasing power, see figure 5.2. Being the precursor to all other species formed within the plasma, $[O_2(X^3\Sigma_g^-)]$ necessarily decreases when the densities of other species increase. This is most notable during the E/H switchover where $[O_2(X^3\Sigma_g^-)]$ drops most rapidly as the rates of electron impact driven processes markedly increase. Within the H-mode, where excited state densities change relatively little compared to the switchover region, the depletion of $[O_2(X^3\Sigma_g^-)]$ is instead dominated by gas heating and resulting rarefaction as described by the ideal gas law.

$O_2(a^1\Delta_g)$

In the E-mode $O_2(a^1\Delta_g)$ is predominantly produced by electron impact excitation of $O_2(X^3\Sigma_g^-)$ (reaction 13), and lost at the chamber walls (reaction 31). As power increases (and $[e^-]$ rises) within the E-mode, production increases rapidly and wall loss remains approximately constant hence the rapid increase in $[O_2(a^1\Delta_g)]$. Within the H-mode however, electron impact de-excitation of $O_2(b^1\Sigma_g^+)$ (reaction 18), also

becomes a significant production process ($\approx 20\%$ of the total at 300 W) while electron impact excitation to $O_2(b^1\Sigma_g^+)$ (reaction 17), and de-excitation to $O_2(X^3\Sigma_g^-)$ (reaction 14) become significant loss processes ($\approx 36\%$ and $\approx 18\%$ of the total loss, respectively, at 300 W). Electron impact therefore becomes important for both production and destruction, thus $[O_2(a^1\Delta_g)]$ appears less dependent on $[e^-]$ in the H-mode than in E-mode. The reduction in $[O_2(a^1\Delta_g)]$ as power increases in the H-mode is therefore predominantly a result of gas heating decreasing $[O_2(X^3\Sigma_g^-)]$ (the main precursor to $O_2(a^1\Delta_g)$). As power increases, the measured density drops below that predicted by the model. This can be accounted for by noting that the measured values are only of $v = 0$ while the model does not discriminate vibrational levels; as power increases, so does T_{vib} and the discrepancy between the values also increases. Using a T_{vib} value of 905 K measured by emission spectroscopy at 300 W, the total density of $O_2(a^1\Delta_g)$ across all vibrational states can be estimated to be $(1.19 \pm 0.15)\times10^{14}$ cm^{-3}, in good agreement with the modelled value and shown by the filled blue circle in figure 5.3. This calculation suggests that, even at the highest power, more than 90% of the $O_2(a^1\Delta_g)$ in the plasma exists in the vibrational ground state. The decision not to include vibrational excitation in the volume averaged model therefore seems reasonable.

$O_2(b^1\Sigma_g^+)$

For $O_2(b^1\Sigma_g^+)$ in the E-mode, several production processes are important: electron impact excitation both from $O_2(X^3\Sigma_g^-)$ and $O_2(a^1\Delta_g)$(reactions 15 and 17 respectively) and the quenching of $O(^1D)$ by $O_2(X^3\Sigma_g^-)$ (reaction 29) which contribute in a $\approx 35 : 15 : 50$ ratio, respectively, at 50 W. As is the case for $O_2(a^1\Delta_g)$, loss is once again dominated by quenching at the chamber wall and so the same arguments hold for explaining the rapidly increasing $[O_2(b^1\Sigma_g^+)]$ in the switchover region (noting that both $[e^-]$ and $[O(^1D)]$ increase rapidly during the switchover, so all production processes increase markedly in rate). In the H-mode the same three production processes remain most important but now with respective relative rates $\approx 15 : 25 : 60$ at 300 W. Wall loss is still the predominant loss process, but electron impact de-excitation to $O_2(a^1\Delta_g)$ (reaction 18) now has a contribution of $\approx 15\%$. This means that the most important production and loss processes in the H-mode are not direct electron impact based reactions and $[O_2(b^1\Sigma_g^+)]$ in the H-mode is not greatly influenced by the small changes in $[e^-]$. Once again temperature effects dominate and the density decreases as power increases due to a depletion of the $O_2(X^3\Sigma_g^-)$ precursor .

$O(^3P)$

The predominant loss process for $O(^3P)$ is reaction at chamber walls (reaction 33) under all conditions. At the highest powers the rate of electron impact excitation to $O(^1D)$ (reaction 19) is competitive with wall loss, but as all $O(^1D)$ is subsequently quenched back to $O(^3P)$ this is not a net loss process for $O(^3P)$. In the E-mode, production of $O(^3P)$ is predominantly by electron impact dissociation (EID) of $O_2(X^3\Sigma_g^-)$ (reactions 1 and 4) and by dissociative electron attachment (DEA) to $O_2(X^3\Sigma_g^-)$ (reaction 7). All three play an important role with rates in the ratio 63:32:5. Production processes involving electronically excited molecules account for $< 3\%$ of the total production at 50 W. In the H-mode EID with $O_2(a^1\Delta_g)$ (reaction 2) and quenching of $O(^1D)$ by $O_2(X^3\Sigma_g^-)$ (reactions 28, 29 and 30) also become important production processes for $O(^3P)$. Note, although some of the $O(^1D)$ quenching simply offsets reaction 19, some of the $O(^1D)$ originates instead from reaction 4 and the net effect of the quenching reactions (28, 29 and 30) with reaction 4 is the production of $O(^3P)$. In the H-mode therefore, $[O(^3P)]$ becomes less dependent on $[e^-]$ and is once again influenced most strongly by gas heating.

$O(^1D)$

Modelled $[O(^1D)]$ are shown in figure 5.2. Across the power range $O(^1D)$ is predominantly lost through quenching by $O_2(X^3\Sigma_g^-)$ (reactions 28, 29 and 30) while its production is dominated by EID of $O_2(X^3\Sigma_g^-)$ (reaction 4) and electron impact excitation of $O(^3P)$ (reaction 19). In the E-mode these account for 88% and 12% of production, respectively. In the H-mode their importance is swapped, accounting for 44% and 54%, respectively (the remaining 2% is by EID of $O_2(a^1\Delta_g)$ and $O_2(b^1\Sigma_g^+)$ (reactions 5 and 6)). $O(^1D)$ is therefore produced exclusively by electron impact and destroyed without the need for electrons across the entire operating range. As a result of this $[O(^1D)]$ shows no maximum at high powers but instead continues to rise with $[e^-]$ across the whole range of powers modelled. Gas heating has little influence on $[O(^1D)]$ because $O_2(X^3\Sigma_g^-)$ acts not only as a precursor, but also as a quencher of $O(^1D)$.

5.5 Ions and electronegativity

The predicted behaviour of charged species with plasma power is shown in figure 5.4. Also shown is the change in electronegativity (the ratio of negative ion density

to electron density, $[O^-]/[e^-]$) and one experimental value for the $[O^-]$ taken from figure 4.13.

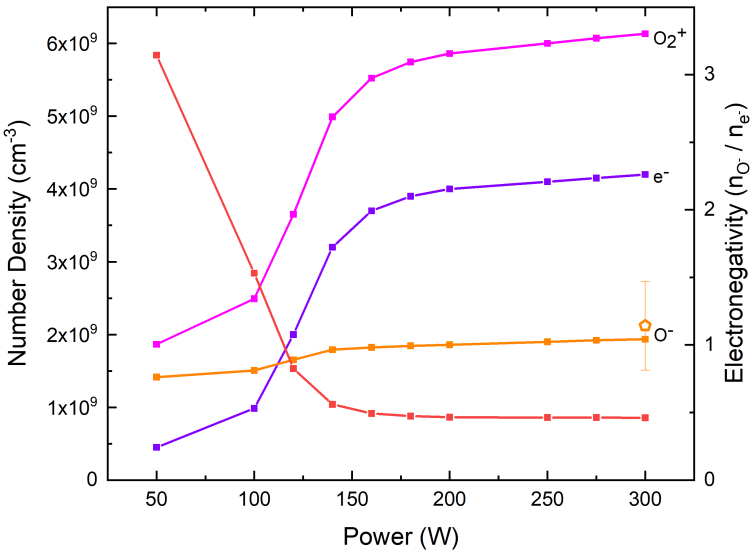

Figure 5.4: Densities of charged plasma species as a function of plasma power and at 100 mTorr gas pressure as predicted by the model, also shown in red is the electronegativity (ratio of negative ion to electron density). The pentagonal point is the experimental O^- density taken from figure 4.13.

O^- and electronegativity

At low power the major production route of O^- is DEA with $O_2(X^3\Sigma_g^-)$ (reaction 7) whilst it is predominantly lost by electron detachment with metastable molecules and $O(^3P)$ atoms (reactions 25, 26 and 27). Within the E-mode the densities of the quenching species are low, meaning that O^- is relatively long lived (compared to electrons) and is effectively a reservoir of negative charge. As power increases the densities of both electrons (responsible for producing O^-) and the excited species responsible for quenching O^- increase. And so while $[e^-]$ increases by an order of magnitude across the power range, $[O^-]$ undergoes a much more modest increase of ≈40%. The $[O^-]$ predicted by the model agrees well with the measurement of the species in this chamber under the same conditions. This behaviour is reflected in the predicted electronegativity. In the E-mode the electronegativity is high because O^- has a low quenching rate. As power increases the increasing $[e^-]$ is not mirrored in $[O^-]$ (despite faster O^- production) because the rate of quenching also increases, and leads to a lower electronegativity that shows much less variation with plasma power

in the H-mode than it does in the E-mode. Across all powers the electronegativity is significantly above zero indicating that ions are always a significant reservoir of negative charge, as would be expected for an oxygen system. The fall in electronegativity observed across the E/H-mode transition from 3 to 0.5 is consistent with previous work on oxygen plasma at similar pressures. Kiehlbauch and Graves model a drop in electronegativity from around 2.5 at 100 W to around 1.3 at 500 W at 100 mTorr[82]; Gudmundsson predicts changes in electronegativity from 1 at 300 W to 0.2 at 2000W for a 100 mTorr plasma[123], and for the typical electron densities inferred from the volume averaged model, Corr *et al.*[89] suggest a decrease by an order of magnitude on switching from the E to the H mode (from ≈ 10 at 27 W to ≈ 1 at 220 W at 25 mTorr).

Some more recent work[168–170] has suggested that the rate coefficient of electron detachment between O^- and $O_2(a^1\Delta_g)$ may be somewhat higher that the value used here (3.3×10^{-11} cm^3 s^{-1}). In particular, the most recent measurements of Midey *et al.*[170] find a temperature independent rate coefficient for reaction 25 of 6.1×10^{-11} cm^3 s^{-1} and, even more importantly, an additional reaction pathway (O^-+ $O_2(a^1\Delta_g)$ $\rightarrow$ O + O_2^-) whose rate coefficient is strongly temperature dependent and given by $7.3 \times 10^{-10} \exp\left(\frac{-890}{T_{trans}}\right)$ cm^3 s^{-1}.

The inclusion of the increased rate coefficient and the additional reaction pathway in the model would have no significant implications for $O_2(a^1\Delta_g)$, nor would it lead to the production of significant amounts of either O_3 or O_2^- both of which are rapidly destroyed at the pressures used here. It would, however, have some implications for the negative ion O^-. At the highest modelled temperatures (≈ 450 K) the total rate coefficient (via both reaction pathways) for O^- destruction by $O_2(a^1\Delta_g)$ would be $\approx 1.6 \times 10^{-10}$ cm^3 s^{-1}. Thus the work of Midey *et al.* indicates that, at 450 K, reaction of O^- with $O_2(a^1\Delta_g)$ occurs with the same rate coefficient as detachment with $O(^3P)$ (reaction 27). In the context of the relative densities of $O_2(a^1\Delta_g)$ and $O(^3P)$ present in the plasma at 300 W, the revised rate coefficients would correspond to a $\approx 25\%$ increase in the total rate of O^- destruction and thus a $\approx 25\%$ decrease in the O^- density predicted by the model.

For a lower power plasma, the lower temperature means that the increase in the O^-+ $O_2(a^1\Delta_g)$ reaction rate implied by the measurements of Midey *et al.* is more modest, however, at the lower powers the densities of $O_2(a^1\Delta_g)$ and $O(^3P)$ are much more similar. Thus, for the enhanced $O_2(a^1\Delta_g)$ reaction rate rate ($\approx 9.9 \times 10^{-11}$ cm^3 s^{-1} at 300 K) the total rate of destruction of O^- is increased by $\approx 35\%$ and the

density of O^- predicted by the model will decrease by $\approx 35\%$ at the lower plasma powers.

O_2^+

The model includes no kinetic balance for O_2^+ because its wall loss rate in the chamber is unknown (and is likely to be significant); instead its density is defined by quasi-neutrality. This makes detailed discussion of its kinetics difficult but the expectation is that O_2^+ is predominantly produced by electron impact ionisation of $O_2(X^3\Sigma_g^-)$ (reaction 10) with some additional contributions at higher powers from metastable molecules (reactions 11 and 12), and predominantly lost at the walls. This would correspond to a loss rate that is invariant with changing $[e^-]$ and a production rate directly proportional to $[e^-]$. This is in good agreement with the model's prediction that $[O_2^+]$ follows $[e^-]$ very closely.

5.6 Effects of gas temperature

The modelled results are calculated using the temperatures that are found using a spline fit to the CRDS data as described in section 5.2. It should be noted however, that the reaction set itself is actually only weakly dependent on gas temperature. Reactions in table 2 all have only weak temperature dependences whilst the wall loss rates for $O(^3P)$ and $O_2(a^1\Delta_g)$ vary by less than 20% for a temperature increase from 460 K to 630 K (the temperatures from $O(^3P)$ CRDS and emission experiments, respectively). Even the wall loss rates for $O_2(b^1\Sigma_g^+)$ and $O(^1D)$ which have the strongest temperature dependence only increase by $\approx 60\%$ as the temperature increases from 460 K to 630 K, and seeing as there are no absolute measurements of their densities with which to compare, this makes little difference to the conclusions that can be drawn from the model. In fact, by far the most important influence of using the elevated emission temperatures for modelling would be the resulting drop in the density of all species, reflecting the ideal gas law. It is found, across the modelled power range, that when the higher temperatures are used, good agreement between experimental and modelled number densities can still be achieved simply by increasing $[e^-]$. In the E-mode, where temperatures differ less between the two experiments, $[e^-]$ must be increased by $\approx 30\%$ to achieve good agreement, whilst in the H-mode an increase of $\approx 60\%$ in $[e^-]$ is required to achieve good agreement. In the context of the simplifying assumptions inherent in the volume averaged model these changes in $[e^-]$ represent a minor adjustment. Thus, the quantitative conclusions drawn from the model in the

cases of $O(^3P)$ and $O_2(a^1\Delta_g)$ are almost independent of the gas temperature that is used. Likewise, the more qualitative discussion as to the most important processes controlling densities of other species are also valid regardless of which T_{trans} values are used for modelling purposes.

5.7 Model results - varying pressure

Modelling of the pressure variation of plasma species is necessarily less certain because there are fewer experimental results with which to compare. Additionally the pressure variation data that is available (for $O(^3P)$ and O^-) was taken before chamber cleaning and is therefore less directly comparable with the power variation model results. Nevertheless, input parameters for the model can be estimated from those found in the power variation model and also utilising previous studies found in the literature for information on how electron temperatures and densities are expected to vary with pressure. The model input parameters used in this section that are different to those from the previous section are shown in table 5.4. Gas temperature is assumed to be 330 K (at 300 W) for all pressures (based on figure 4.4), electron density is assumed to be approximately constant at all pressures and is taken from the power variation modelling (some literature suggests n_e should increase with pressure[30], other literature that it should decrease[11,123] and yet other literature that it should vary relatively little with pressure[149,171]). Electron temperature is expected to be slightly higher at lower pressures[30,123,149], with the 100 mTorr value taken from the power variation modelling and T_e at lower pressures estimated from the ratios of T_e at different pressures as suggested by Gudmundsson[30,123]. Finally the change in wall loss coefficient of $O(^3P)$ is estimated based on measurements of the values at 100 and 50 mTorr presented above and extrapolated to lower pressures. All other model parameters are unchanged.

Table 5.4: Pressure variation modelling input parameters

Pressure (mTorr)	T_{trans} (K)	T_e (eV)	$[e^-]$ (cm^{-3})	γ_O
100	340	1.42	4.2×10^9	0.003
50	340	1.57	4.2×10^9	0.004
20	340	1.78	4.2×10^9	0.005
10	340	2	4.2×10^9	0.006

Figure 5.5 shows the modelled atomic oxygen densities in the chamber along with the experimental values which are reproduced from figure 4.5. The reasonably good agreement between the model and the experimental data supports the hypothesis that the change in atom density after the chamber cleaning is mainly a result of the change in plasma temperature and not to a change in atom wall loss coefficient.

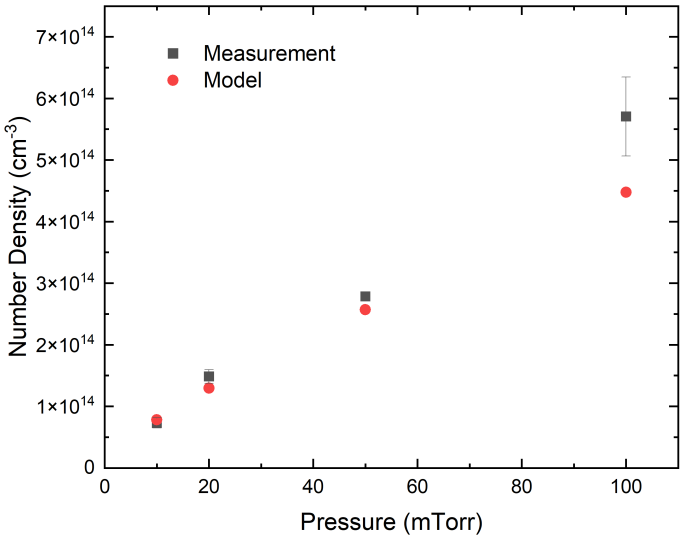

Figure 5.5: A comparison of the measured and modelled pressure variation of oxygen atom densities in the plasma at 300 W.

In terms of negative ions the model is, once again, successful at reproducing the density of O^- at 100 mTorr. The model however fails to predict the rapidly increasing negative ion density as pressure falls (in fact the model predicts that $[O^-] \approx 1.9 \times 10^9$ cm^{-3} at all pressures). One possible resolution of this discrepancy is to invoke some augmentation of the DEA production rate which is important at low pressures and not already included in the model. An augmented DEA rate has been invoked by others in order to explain large O^- concentrations in discharge systems. In particular, Ding *et al.*[172] required DEA to high lying Rydberg states of O_2 in order to explain the observed enhancement of negative ions in an oxygen discharge afterglow, a prerequisite being large DEA cross sections available to low energy electrons. Similarly, Wagner and Katsch[173] infer the presence of either Rydberg or metastable O_2 in their pulsed rf discharge and Kiehlbauch and Graves[82] also conclude the attachment to Rydberg states is an important production process for O^- production.

Despite its limitation in terms of O^- production processes the model can still give an indication as to whether the destruction of O^- is detachment or recombination dominated. The total quasi first order rate coefficient for detachment loss of O^-

(reactions 24, 25 and 26) is around 200 times great than that for recombination (reactions 23 and 24) at 100 mTorr and still at least an order of magnitude bigger at 10 mTorr even if it is assumed that the recombination partner O_2^+ has a density as high as $\approx 1.6 \times 10^{10}$ cm^{-3} (i.e. the density implied by the [O^-] measurement at 10 mTorr). Thus the model supports the hypothesis that the plasma is detachment dominated over the entire pressure range and that as pressure is lowered the system moves closer to the recombination dominated regime.

5.8 Modelling conclusions

The validity of quantitative conclusions arising from any kinetic plasma model is invariably limited by the certainty with which the plasma chemistry is understood. In the case of the model used here, the fact that electron temperatures and densities are adjustable model input parameters means that, to a degree, deficiency in the chemistry set can be compensated for by changes in electron temperature and density. Nevertheless, the validity of the model can be assessed by comparing the optimal electron temperatures and densities it requires to best reproduce the observations, against other measurements.

Many researchers have modelled or measured (*e.g.* by microwave interferometry[149]) values for T_e and [e^-] in O_2 plasmas under conditions similar or identical to those investigated here. Much of the literature work was carried out using (or modelling) chambers considerably smaller than that which was used in the current work, *i.e.* with electrode separations < 10 cm, and perhaps unsurprisingly much of this work results in [e^-] values somewhat higher than this model predicts for the same power. The highest literature values are $\approx 10^{11}$ cm^{-3} in chambers with small volumes operating at low pressures < 30 mTorr[89,155]. Slightly lower [e^-] values ($\approx$ a few $\times 10^{10}$ cm^{-3}) are found in chambers that are either smaller[82,91,149] or operate at lower pressures than the chamber used here[30,90]. Meanwhile the lowest literature values ($\approx 5 \times 10^9 - \approx 10^{10}$ cm^{-3}) most comparable with the value inferred here (4.2×10^9 cm^{-3} at 300 W) are found in a chamber much bigger than the one used here[171] and in plasmas that differ only in their volume[123] or power[124] from the one used here.

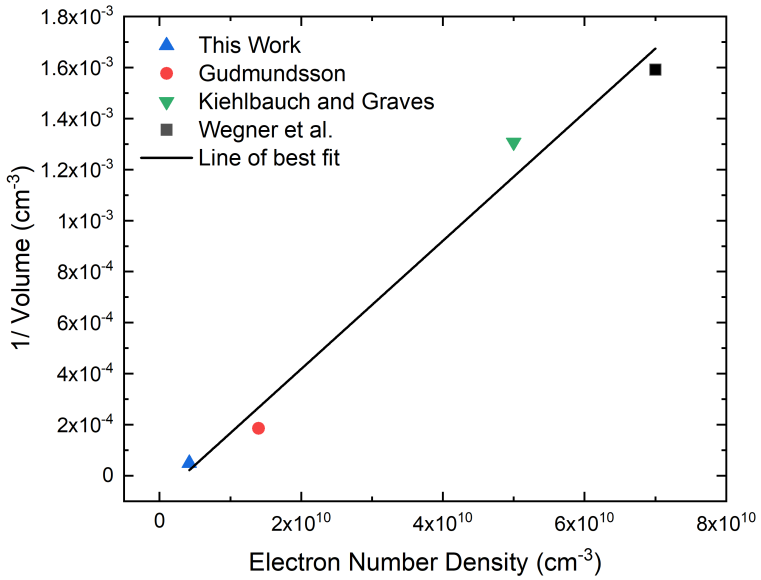

Figure 5.6: Plot demonstrating the linear relationship between modelled electron densities and the inverse of the plasma volume; all points are for a 100 mTorr 300 W plasma. Data points are taken from this work, Gudmundsson[123], Kiehlbauch and Graves[82] and Wegner *et al.*[149].

This comparison is exemplified by figure 5.6 which demonstrates how modelled or measured [e$^-$] changes with plasma volume (calculated simply as the chamber volume except in one case[149] where the chamber is significantly larger than the discharge volume and as such the volume between the two electrodes was used instead). Most notably, these literature data are chosen because they either present directly[82,123] or allow straightforward estimation of[149] [e$^-$] at 300 W power and 100 mTorr pressure. The results show quite convincingly that the [e$^-$] in an O_2 plasma scales inversely with plasma volume if power and pressure are kept constant and that, given this relationship, modelled [e$^-$] fall in line with those found in other chambers.

The electron temperatures derived from the model lie between 1.2 and 1.42 eV. These values are somewhat lower than those measured in similar pure oxygen discharges with values typically between 2 and 4 eV[89,149], albeit with higher power densities. Some previous work however, falls in line with the model values found here, in particular the work of Toneli *et al.*[167] which models an electron temperature (assuming a Maxwellian EEDF) of less than 2 eV for a 100 mTorr and 500 W plasma and the work of Seo and Chung[171] who measure an electron temperature of 1.4 eV in a 40 mTorr 400 W plasma (and might expect an even lower electron temperature at higher pressures). The electron temperatures found here are thus well within the

bounds of previous work and, most compellingly of all, they are in rather good agreement with measurements made using a planar electrical probe in the same chamber which found electron temperatures of 1.6 eV at 100 mTorr and 400 W and also found electron densities of a few 10^9 cm^{-3}, also in good agreement with the model results[64].

It is clear from the preceding discussion that a volume averaged kinetic model based upon a relatively small number of reactions (34) can describe the essential features of the plasma. The model returns realistic values of number densities of $O(^3P)$ and $O_2(a^1\Delta_g)$ and electron densities and temperatures commensurate with the physical properties of the plasma chamber. It should be noted however that the data presented in chapter 4 shows the signatures of spatial inhomogeneity. Experiments and models that investigate this inhomogeneity are the subject of the next chapter.

Chapter 6

Oxygen plasma inhomogeneity

While the volume averaged model was successful at reproducing line of sight averaged experimental number densities of several plasma species, the effects of inhomogeneity are readily apparent within the data previously presented. This chapter features more CRDS data, this time on the molecular ground state $O_2(X^3\Sigma_g^-)$, which shows unequivocally that the plasma is inhomogeneous. This inhomogeneity is then explored through a simple one dimension model.

6.1 $O_2(X^3\Sigma_g^-)$ measurements

The $O_2(b^1\Sigma_g^+)$-$O_2(X^3\Sigma_g^-)$ system of molecular oxygen that was previously observed in emission in order to probe $O_2(b^1\Sigma_g^+)$ can also be probed in absorption by CRDS. This measurement is significantly less challenging than those on $O(^3P)$ and $O_2(a^1\Delta_g)$ presented in chapter 4 because the density of the absorbing species ($O_2(X^3\Sigma_g^-)$) is higher and the cross sections for this transition are larger. This larger signal makes it possible to detect $O_2(X^3\Sigma_g^-)$ on both the (0, 0) and the (1, 1) vibronic bands giving some indication of the vibrational excitation present within the plasma which can be compared with the emission measurements. Furthermore, both vibrational bands can be reached by coarse tuning the ECDL used for the spectra in this section which has a coarse scanning range between 747 and 792 nm.

Despite the relative ease of the measurements any interpretation is made significantly more difficult (particularly for $v = 0$) because, where other species are, to a first approximation, absent from the baffle arms, $O_2(X^3\Sigma_g^-)$ fills the arms. Indeed, because the feedstock gas flows along the arms there is actually a pressure gradient along each arm. Thus, there exists high density of ground state molecular oxygen outside of the plasma zone which contributes significantly to absorption measurements and makes it very difficult to establish how much of the absorption originates from

$O_2(X^3\Sigma_g^-)$ within the plasma itself. On top of this there is also the issue of temperature inhomogeneity, when the plasma is on, the species in the central part of the chamber show a translational temperature approaching 600 K (from emission at 300 W), whilst most of the species in the arms are expected to be approximately ambient (300 K). This is a significant confounding influence when it comes to interpreting line of sight averaged CRDS data. Despite this difficulty the ability of this spectrometer to probe several rotational lines (in both the (0, 0) and (1, 1) vibrational bands) enables some insight to be obtained.

6.1.1 $O_2(X^3\Sigma_g^-,\ v = 0)$

CRDS spectra were obtained at 100 mTorr pressure and a range of plasma powers. In order to probe the expected change in $\bar{T}_{trans}$ with rotational energy several rotational lines of the (0, 0) vibrational band were probed, specifically: ${}^pP_{12}(1)$, ${}^rQ_{11}(18)$, ${}^rR_{12}(19)$, ${}^rQ_{11}(28)$, ${}^rQ_{11}(30)$ and ${}^pP_{12}(31)$ (see appendix D for line positions). These lines were selected based on the desire to probe a wide range of rotational energies and where possible were selected so that 2 lines could be probed in a single laser scan, this not only provides more data but also enables self calibration of the frequency scale because the line positions are known from a highly precise PGOPHER simulation (already utilised for fitting the emission data). This PGOPHER simulation is also able to calculate cross sections for these magnetic dipole allowed transitions. For the (0, 0) band the PGOPHER cross section values could be compared with the database HITRAN[56] and showed very good agreement. A small sample of the obtained spectra are shown in figure 6.1. Figure 6.1a shows spectra of the ${}^rQ_{11}(18)$ and ${}^rR_{12}(19)$ transitions with and without plasma whilst figure 6.1b shows the same for the ${}^rQ_{11}(28)$ and ${}^rQ_{11}(30)$ transitions. The strongest rotational lines have an absorption coefficient an order of magnitude bigger than those observed for $O(^3P)$ and two orders of magnitude higher than those observed for $O_2(a^1\Delta_g)$. As previously, the spectra can be used to find line of sight averaged densities and translational temperatures. Unfortunately, because (for a thermally inhomogeneous sample) the distribution of each rotational state along the beam path will be different no simple length adjustment can be made to determine the density of $O_2(X^3\Sigma_g^-)$ in the chamber specifically. The line of sight averaged values can nevertheless still be informative, and figure 6.2 shows line of sight averaged number densities for each rotational state as a function of plasma power.

The low J'' states, shown in figure 6.2a show a decrease with power. The reasons for this are three-fold: as power increases the gas in the chamber is heated and hence becomes less dense; as power increases, the mole fraction of $O_2(X^3\Sigma_g^-)$ in the chamber

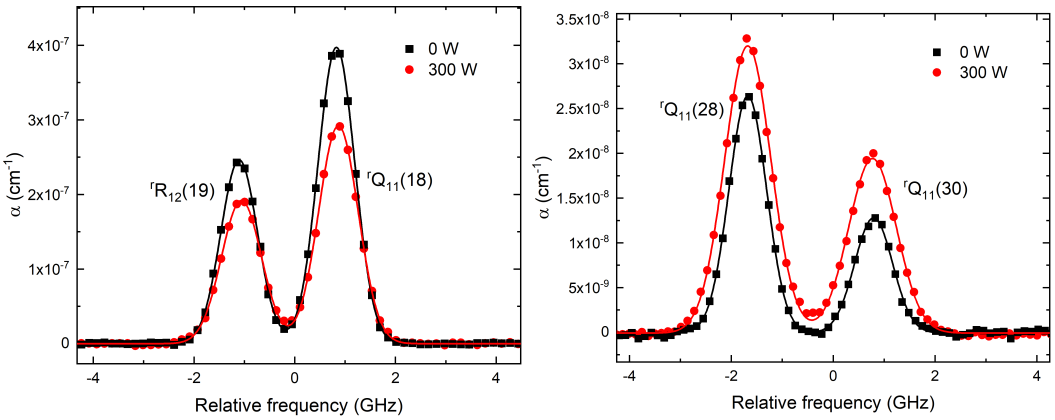

Figure 6.1: CRD spectra on the oxygen A-band for a 100 mTorr gas pressure showing (a) decreasing line of sight averaged absorption as power increases for low J'' and (b) increasing line of sight averaged absorption as power increases for high J''.

decreases; and as power increases, the fraction of $O_2(X^3\Sigma_g^-)$ which is partitioned into the lowest rotational states (particularly $J'' = 1$) decreases. For the high J'' states (figure 6.2b) the first two factors once again act to decrease density as power increases, they are however outweighed by the fact that as the gas heats, the fraction of $O_2(X^3\Sigma_g^-)$ partitioned into high J'' states increases significantly (for example at 300 K around 1 in every 3300 molecules would be in the $J'' = 31$ state but this increases to 1 in every 210 molecules at 600 K).

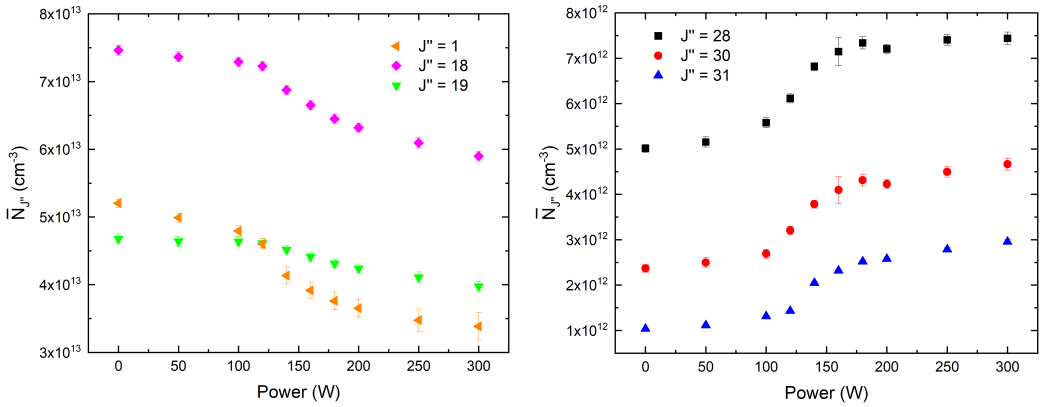

Figure 6.2: Line of sight averaged rotational state densities for a 100 mTorr gas pressure derived from CRD spectra for (a) low J'' lines and (b) high J'' lines. Both show the effect of rotational heating of the gas as power increases.

Figure 6.3 shows the line of sight average translational temperatures, $\bar{T}_{trans}$, for

each of the rotational states (extracted from the Doppler lineshapes) as a function of plasma power. At low powers, where the plasma temperature is close to ambient and thus the entire cavity length is of approximately uniform temperature, all the rotational states show the same translational temperature close to 300 K. As power increases however the averaged temperature shows, once again, a significant difference between the high J'' states and the lower J'' states. Indeed, the state specific average temperature increases monotonically with increasing rotational energy. This observation is entirely consistent with the densities in figure 6.2 and can once again be explained by the fact that the population of high J'' states in the colder baffle arms is small and their population in the hotter bulk of the plasma is much higher whilst the opposite is true of the lower J'' states.

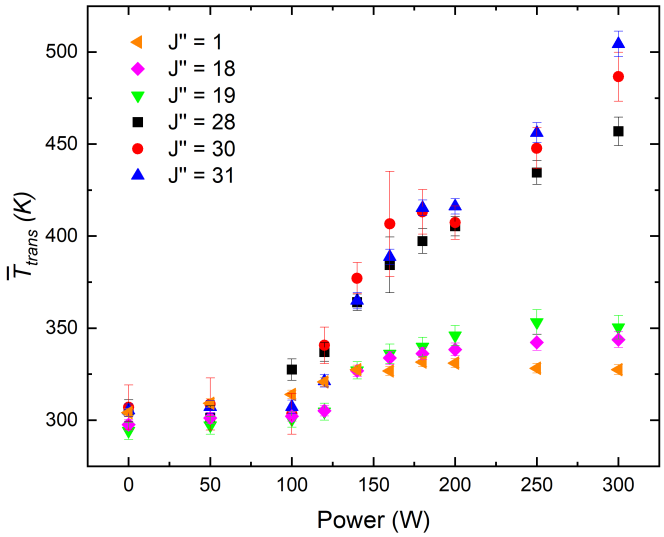

Figure 6.3: Line of sight averaged translational temperatures for the various rotational states of $O_2(X^3\Sigma_g^-)$ in a 100 mTorr plasma. The data show a clear increase in translational temperature with increasing rotational state in the H-mode resulting from the different spatial distributions of these states in the thermally inhomogeneous plasma.

When densities of several rotational states are known, a Boltzmann plot can be constructed (as it was previously for $O_2(a^1\Delta_g)$). The data in figure 6.2 was used to construct a Boltzmann plot at each plasma power. The plots for 0 and 300 W are shown in figure 6.4a (note that error bars are present but are significantly smaller than the data points in both cases).

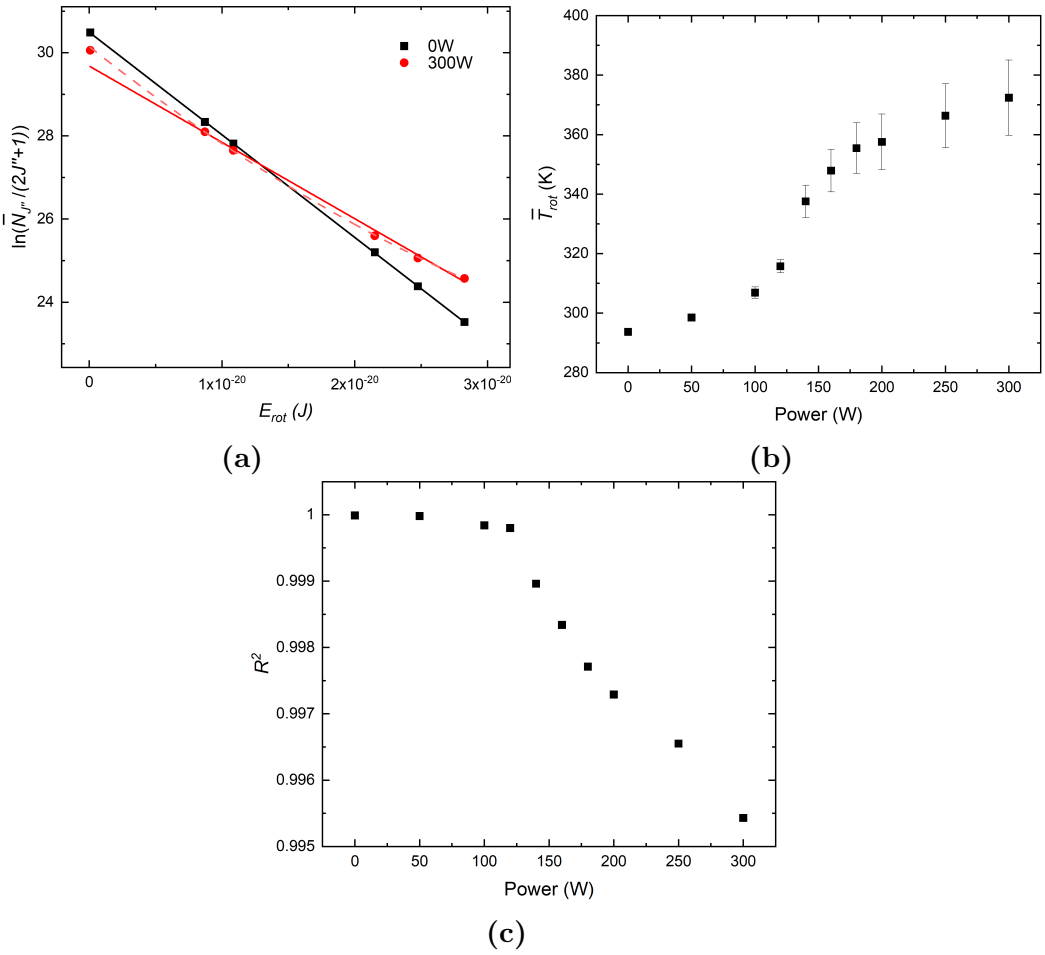

Figure 6.4: (a) Boltzmann plots for the 0 W, 100 mTorr (Black) and 300 W, 100 mTorr (Red) CRD data (in both cases the error bars are smaller than the points). Also shown are linear fits (solid lines) and a quadratic fit to the 300 W data (red dashed line) demonstrating the non-linearity of the Boltzmann plot. (b) Rotational temperature derived from the linear fits to Boltzmann plots, as the linear fit becomes less appropriate so the temperature becomes less certain. (c) The R^2 statistic for the linear fits as a function of power showing that the fits become markedly poorer when the plasma enters the H-mode (*i.e.* when the plasma is significantly hotter than the baffle arms).

The 0 W plot is truly linear (R^2 >0.99999) with a gradient corresponding to a rotational temperature of 293.7 ± 0.6 K (such accuracy is possible because at 0 W the temperature is entirely uniform along the CRDS line of sight) and an intercept corresponding to a line of sight average density of $O_2(X^3\Sigma_g^-,\ v\ =\ 0)$ of (3.70 ± 0.01)×10^{15} cm^{-3}. It should be noted that this density corresponds to a pressure greater than the 100 mTorr measured and maintained in the central chamber due to the flow of gas along the baffle arms; this flow is necessarily associated with a

pressure gradient and thus the pressure in the baffle arms is greater than that in the chamber. By subtracting the expected absorption from the 35 cm of 100 mTorr oxygen in the chamber itself from the total absorption coefficient one can determine the line of sight average pressure in the arms to be $\approx$ 123 mTorr. The precise spatial variation of pressure within the arms can be approximately modelled according to the Poiseuille equation (*vide infra*). Figure 6.4b shows the rotational temperatures, T_{rot}, derived from the Boltzmann plots for the other plasma powers. All such plots are influenced by the cool gas in the baffle arms but the temperatures still show a smooth increase with increasing power including a steeper increase at the expect E/H switchover. Noticeably in figure 6.4a the 300 W data shows a significant deviation from linearity, in fact a quadratic fit (dashed line) is much more successful at fitting the data, this non-linearity results in the much larger error bars in figure 6.4b at higher powers when a linear fit is used. This is again the result of thermal inhomogeneity in the plasma with the effect that the Boltzmann plot looks cooler (steeper) at low E_{rot} and hotter (shallower) at high E_{rot}. The deviation from linearity ought to be a good indicator of plasma inhomogeneity and thus it might be expected that this deviation should increase markedly over the E/H switchover. Figure 6.4c shows the R^2 statistic for the linear fits as a function of power and demonstrates the expected deviation from linearity when power is above $\approx$ 120 W in line with the prediction regarding the E/H switchover.

6.1.2 $O_2(X^3\Sigma_g^-,\ v = 1)$

CRD spectra as a function of plasma power were also obtained for the first vibrationally excited state of $O_2(X^3\Sigma_g^-)$ utilising the (1, 1) band of the $O_2(b^1\Sigma_g^+)$-$O_2(X^3\Sigma_g^-)$ system. CRDS is sufficiently sensitive that the small amount of $v = 1$ molecules present in a room temperature gas sample can also be detected. Figure 6.5 shows several spectra of the ${}^rQ_{11}(16)$, ${}^rR_{12}(17)$ and ${}^rQ_{11}(22)$ rotational transitions as a function of plasma power at 100 mTorr pressure. Spectra were also obtained for the ${}^rR_{12}(7)$ transition (see appendix D for line positions). Transitions from higher and lower J'' states were too weak to be observed at 0 W hence the more limited range of rotational states probed compared to the $v = 0$ data.

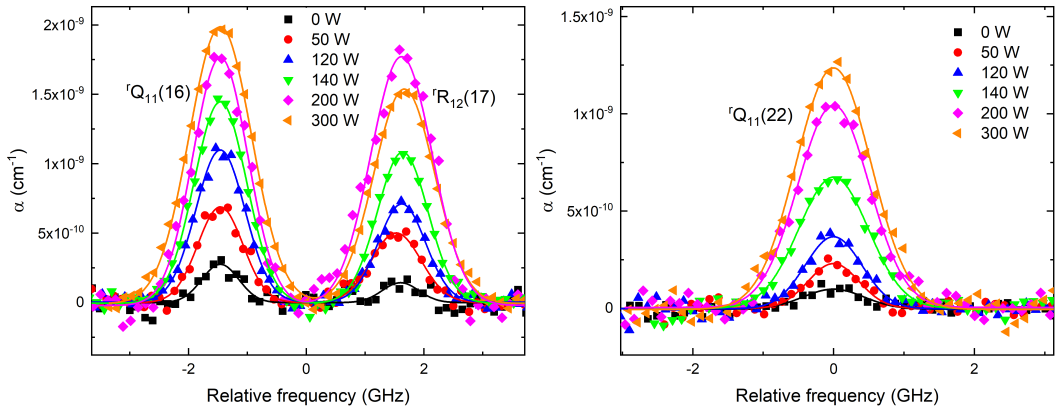

Figure 6.5: Example CRD spectra of several rotational lines in the (1, 1) band of the $O_2(b^1\Sigma_g^+)$-$O_2(X^3\Sigma_g^-)$ system in a 100 mTorr plasma. Panel (a) shows lines originating from $J'' = 16$ and 17 whilst (b) shows an absorption spectrum from $J'' = 22$.

Line of sight averaged number densities for each rotational state are shown in figure 6.6. The behaviour for $v = 1$ is very different to that seen for $v = 0$, with all rotational states showing a consistent increase in number density with power. This observation arises from the fact that (apart from the small density of $v = 1$ molecules present in the baffle arms) $v = 1$ is predominantly produced by the plasma discharge and hence as power increases so does the density of $v = 1$ regardless of rotational state.

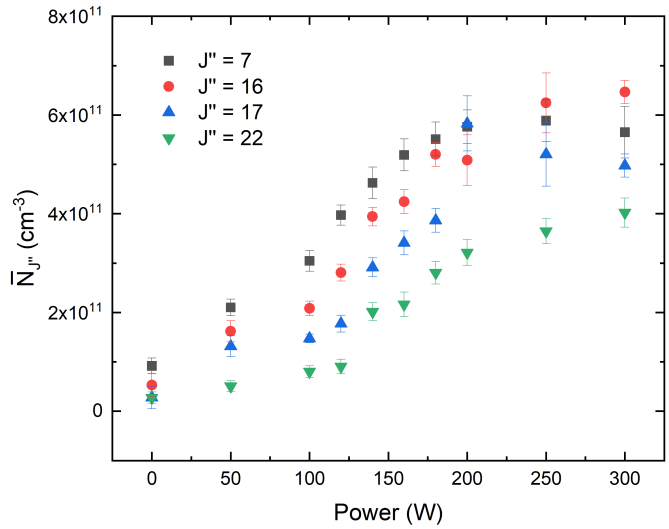

Figure 6.6: Variation in line of sight averaged rotational state specific number densities with plasma power at 100 mTorr gas pressure. In notable contrast to the vibrational ground state, the $v = 1$ densities all increase with increasing power.

The translations temperatures, T_{trans}, calculated from the Doppler widths of these transitions are shown in figure 6.7. All the measured rotational lines show similar increases from near ambient temperatures at low powers up to around 600 K at 300 W. These temperatures are elevated compared to those measured for $O(^3P)$ (450 K at 300 W) and are in fact closer to those measured by emission. This indicates that $v = 1$ molecules are largely confined to the hot central region of the plasma and that as they leave this region they are quickly quenched (the dominant loss process being V-T energy transfer with $O(^3P)$[141]). This means that $v = 1$ molecules fill, at most, 35 cm of the CRDS cavity (i.e. the full chamber diameter with no penetration into the arms) and probably less than 35 cm because they are likely not to be produced close to the chamber walls (where temperature and electron densities are expected to be lower than in the centre of the chamber).

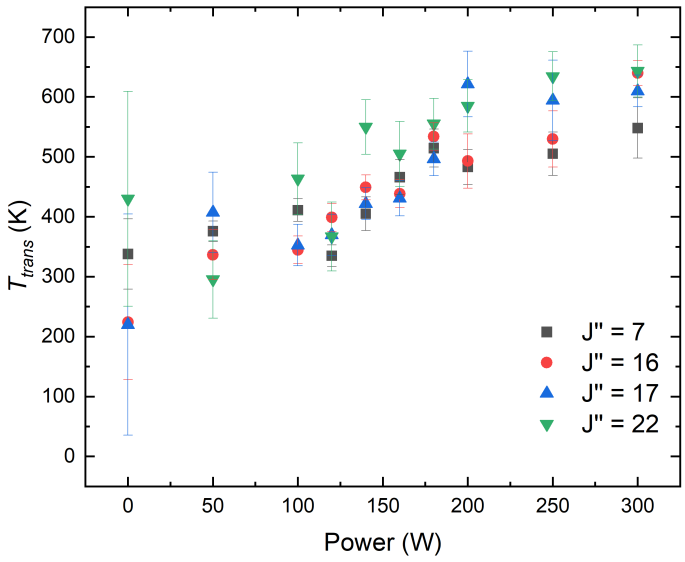

Figure 6.7: Line of sight averaged translational temperature for the various rotational states of $v = 1$ oxygen molecules in a 100 mTorr plasma. All rotational states show higher temperatures than were observed for $O(^3P)$ and display a significant increase in temperature with power which is broadly in line with the increase observed by emission measurements on the oxygen A-band. This indicates that $O_2(X^3\Sigma_g^-$, $v = 1)$ and $O_2(b^1\Sigma_g^+)$ molecules probably have similar spatial distributions and that both are largely absent from the cool baffle arms leading to elevated average temperatures in comparison to $O(^3P)$ and $O_2(a^1\Delta_g)$.

As before it is possible to construct Boltzmann plots at each plasma power and to calculate rotational temperatures, T_{rot} and total line of sight averaged $v = 1$ number densities, $\bar{N}_{v=1}$. Such plots with linear fits are shown in figure 6.8a, in this case there is no evidence of non-linearity, again because almost all the $v = 1$ molecules exist, not in the arms, but in the main chamber, where temperature is approximately constant. Rotational temperatures are shown in red in figure 6.8b along with the emission derived temperatures from figure 4.21 for comparison. The temperatures are similar and increase with power almost identically. The discrepancy in the two temperatures is likely to be a result of the significant influence of $v = 1$ molecules that are not produced by the plasma but are instead present in the arms at all plasma powers. Figure 6.8c shows line of sight averaged number densities of $v = 1$ molecules, this figure demonstrates a clear increase in vibrational excitation across the E/H switchover.

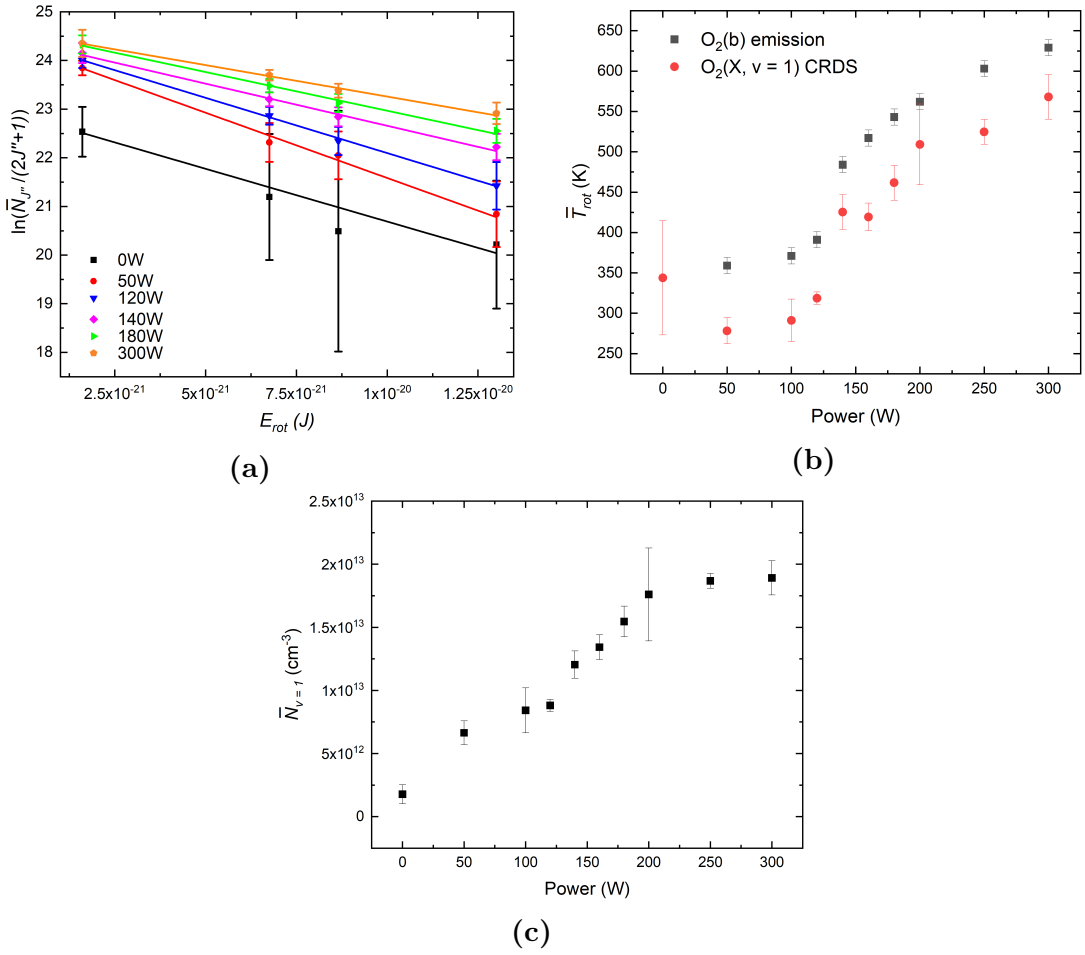

Figure 6.8: (a) Boltzmann plots for $O_2(X^3\Sigma_g^-,\ v = 1)$ as a function of plasma power at 100 mTorr gas pressure. There is no clear indication of non-linearity. (b) Rotational temperatures derived from the Boltzmann plots (red) and from the emission data (figure4.21) for comparison. (c) line of sight averaged $[O_2(X^3\Sigma_g^-,\ v = 1)]$ values calculated from the Boltzmann plot.

At low plasma powers the $O_2(X^3\Sigma_g^-,\ v = 1)$ densities shown in figure 6.8c will be strongly influenced by absorption in the arms. Conveniently, the 0 W absorption allows the absorption from the arms to be quantified, if it is then assumed that the temperature in the arms is always ambient and hence the density of $v = 1$ in the arms is approximately constant with plasma power, then this contribution to the absorption can be subtracted from the entire data set and thus the density of $v = 1$ in the 35 cm of the chamber itself can be estimated. The line of sight averaged number density $\bar{N}_{v=1}$ is simply the weighted mean of the average density in the arms, $\bar{N}_{v=1,\text{arms}}$, and the average density in the chamber, $\bar{N}_{v=1,\text{chamber}}$, where the weightings are the lengths of the two regions, $L_{\text{arms}} = 42\text{cm}$ and $L_{\text{chamber}} = 35\text{cm}$ respectively.

In mathematical terms

$$\bar{N}_{v=1}L = \bar{N}_{v=1,\text{arms}}L_{\text{arms}} + \bar{N}_{v=1,\text{chamber}}L_{\text{chamber}}. \tag{6.1}$$

The $v = 0$ data suggests that, if the chamber is held at 100 mTorr, the arms have line of sight average pressure of 123 mTorr. Given that, at 0 W, the temperature is entirely uniform (because the temperature change from the expansion down the arms is negligible) it can be deduced that $\bar{N}_{v=1,\text{arms}} = 1.23\bar{N}_{v=1,\text{chamber}}$ at 0 W power. Combined with equation 6.1 this allows the calculation of $\bar{N}_{v=1,\text{arms}} = 1.93 \times 10^{12}$ cm^{-3}. By assuming that this value of $\bar{N}_{v=1,\text{arms}}$ is the same for all plasma conditions, the effects of the arms can be subtracted from the data in figure 6.8c and the density of $v = 1$ across the 35 cm of the chamber, $\bar{N}_{v=1,\text{chamber}}$, as a function of plasma power can be estimated. These data are shown in figure 6.9a. It should be noted that this method inherently assumes that the vibrational heating by the plasma is uniform across the 35 cm diameter of the plasma chamber. If, as is suspected from the elevated $v = 1$ translational temperatures, the production of $v = 1$ is confined to a slightly smaller (and hotter) region in the centre of the chamber then the density of $v = 1$ molecules in this region would be higher. The values in figure 6.9a are thus lower bounds on the $v = 1$ density in the middle of the chamber. The $v = 1$ densities can be combined with the densities of $O_2(X^3\Sigma_g^-)$ from volume averaged modelling to estimate the vibrational temperature in the plasma as a function of power (noting that because $N_{v=0} >> N_{v=1}$ it can reasonably be approximated that the density of $O_2(X^3\Sigma_g^-)$ predicted by the model is equal to $N_{v=0}$). Vibrational temperatures, T_{vib}, calculated based on these assumptions are shown in figure 6.9b. It should be noted that, because the $v = 1$ densities are lower bounds, so too are the vibrational temperatures. At 300 W a vibrational temperature of 600 K is found as a lower bound. Previously emission measurements resulted in an upper bound of 900 K and thus it can be said with confidence that the line of sight average vibrational temperature across the 35 cm of the plasma chamber is 750 ± 150 K. It should also be noted that there is significant evidence that the population of vibrational states in oxygen plasmas are not well described by a Boltzmann distribution with a single vibrational temperature. In particular Annusova *et al.*[141] suggest that high vibrational levels can have populations much higher than would be expected based on the vibrational temperature apparent amongst the lower vibrational levels, thus the calculated vibrational temperatures are only applicable in defining the populations of lower vibrational levels (i.e. v $\leq\approx$ 2). As mentioned in section 4.5.2, the vibrational distribution function of Annusova *et al.* indicates a vibrational temperature (defined by the ratio of $v = 1$ and $v = 0$

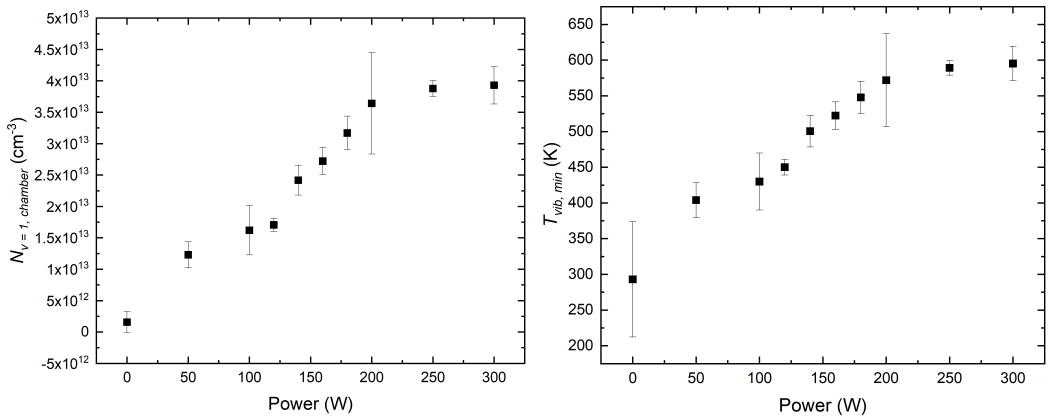

(a) **(b)**

Figure 6.9: (a) Estimated $[O_2(X^3\Sigma_g^-,\ v = 1)]$ in the 100 mTorr plasma, assuming that $O_2(X^3\Sigma_g^-,\ v = 1)$ produced by the plasma is evenly distributed across the entire 35 cm chamber diameter, but that the chamber arms contain the same amount of $O_2(X^3\Sigma_g^-,\ v = 1)$ as when the plasma is off. (b) Vibrational temperatures in the chamber calculated on the basis of the data in (a) and $O_2(X^3\Sigma_g^-,\ v = 0)$ taken from volume averaged modelling. The values in (a) and (b) should be considered as lower bounds on their respective values because in all likelihood $O_2(X^3\Sigma_g^-,\ v = 1)$ does not evenly fill the chamber but is in fact found in higher densities near the (translationally and rotationally hotter) chamber centre.

populations) of ≈ 1000 K for an 80 mTorr 500 W plasma and, bearing in mind the slightly different plasma conditions, this is in reasonable agreement with the value of 750 ± 150 K found here (100 mTorr 300 W).

6.2 A simple model of spatial inhomogeneity in the plasma

In order to further interpret the $O_2(X^3\Sigma_g^-,\ v = 0)$ data some level of spatially resolved modelling is required. The gold standard in such modelling would be a 3D computational fluid dynamics model of the chamber. In the absence of such a complex model a more simplistic model, presented below, can still provide some quantitatively useful results. The basis of the model is to approximate the variation in pressure, translational/rotational temperature and mole fractions as a function of position along the CRDS cavity. This then allows expected line of sight averaged temperatures and number densities of the various species (including different rotational states of molecules) to be predicted and compared with experiment.

Pressure

Feedstock gas entering the plasma chamber passes along the baffle arms and this flow is necessarily associated with a pressure gradient. The pressure change along a length of tube with a gas flow can be estimated using the Poiseuille equation for an ideal gas which can be expressed as:[174]

$$p(L) = \sqrt{p_0^2 + \frac{16\mu Q_0 p_0}{\pi R^4} L} \tag{6.2}$$

where $p(L)$ is the pressure at position L along the tube, p_0 is the pressure in the chamber, μ is the dynamic viscosity of the gas, Q_0 is the volumetric flow at $L = 0$ (*i.e.* the chamber/arm interface) and R is the baffle arm radius. Defining the origin as the centre of the chamber (such that the cavity mirrors are at ± 0.385 m) and using the Poiseuille equation it is then possible to define an approximate piecewise function that describes the line of sight pressure variation:

$$p(z) = \begin{cases} \sqrt{p_0^2 - AQ_0p_0(z + 0.175)} & \text{if } -0.385 \leq z < -0.175 \\ p_0 & \text{if } -0.175 \leq z \leq 0.175 \\ \sqrt{p_0^2 + AQ_0p_0(z - 0.175)} & \text{if } 0.175 < z \leq 0.385 \end{cases} \tag{6.3}$$

where $A = \frac{16\mu}{\pi R^4}$ and $P_0 = 100$ mTorr ($= 13.332$ Pa) in this case. For pure oxygen at 300 K $\mu = 2 \times 10^{-5}$ kg s^{-1} m^{-1} [175] and for a flow of 5 sccm along each arm flowing into a chamber held at 100 mTorr $Q_0 = 6.934 \times 10^{-4}$ m^3 s^{-1}, for the baffle arms, $R = 5 \times 10^{-3}$ m. The pressure variation along the CRDS cavity predicted by equation 6.3 is shown in figure 6.10

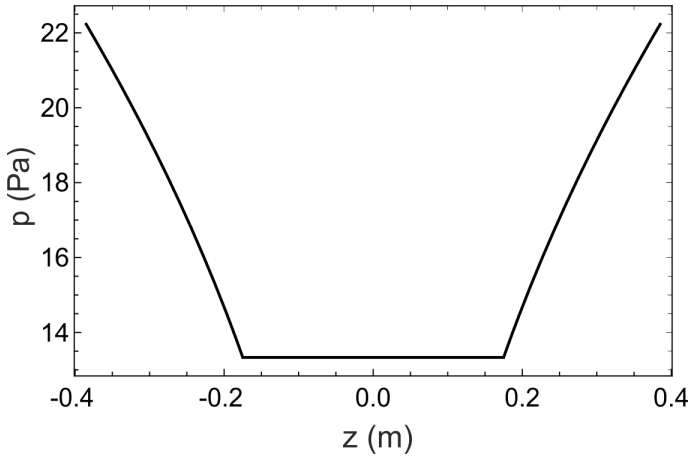

Figure 6.10: Variation of total pressure along the CRDS cavity, pressure in the centre is fixed at 100 mTorr (13.332 Pa) whilst pressure in the baffle arms increases according to the Poiseuille equation (6.3).

Temperature

For the purposes of this 1D model the temperature within the chamber is approximated by a flat topped Gaussian function (also known as a super-Gaussian[176]) of the form:

$$T(z) = T_0 + \Delta T \exp\left(-\left(\frac{z}{b}\right)^a\right) \tag{6.4}$$

where T_0 is the temperature in the baffle arms (taken as 300 K), ΔT is the difference in temperature between the arms and the centre of the chamber (taken as 300 K, in other words assuming the central chamber is at 600K based roughly on the emission data) and a and b are parameters that define how steeply the temperature drops from its maximum value and the extent of the hottest region, respectively. The temperature profile, used in calculating the expected line of sight integrated densities and temperatures for a 300 W plasma, uses values of $a = 4$ and $b = 0.018$ and is shown in figure 6.11. This profile is physically reasonable because its hottest region is approximately the same diameter as the driven coil and the temperature drops to 300 K at ± 0.175 m (*i.e.* where the plasma meets the cooled chamber wall).

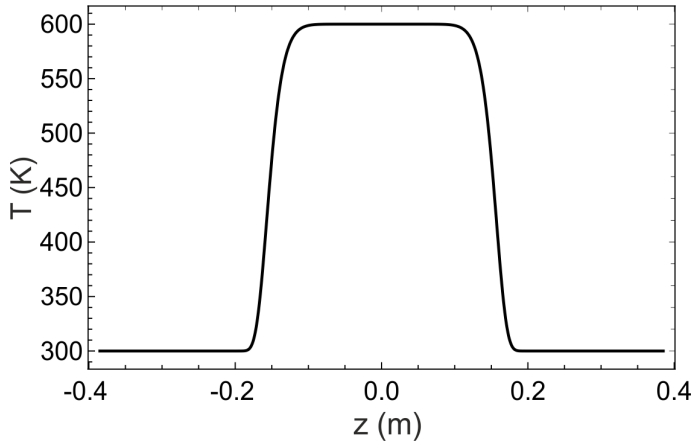

Figure 6.11: An estimate of the spatial variation of the rotational and translational temperature in the plasma. The profile is plotted according to equation 6.4 with parameters chosen as detailed in the text to give a physically reasonable approximation.

Mole fractions

The spatial variation in mole fractions of the various species in the plasma is also required for modelling calculation. The three species of interest are $O(^3P)$, $O_2(a^1\Delta_g)$ and $O_2(X^3\Sigma_g^-, v = 0)$ ($v = 1$ molecules show evidence of being confined to the hottest region of the plasma and are thus less interesting from the point of view of spatially resolved modelling). Mole fractions for the plasma borne species are calculated from the densities returned in the volume averaged model whilst mole fractions of these species in the baffle arms are found using the exponential decay lengths found using equation 4.4 (0.5 cm for $O(^3P)$ and 5 cm for $O_2(a^1\Delta_g)$). Thus the mole fraction of atomic oxygen, x_O is approximated as:

$$x_O(z) = \begin{cases} 0.12763 \exp\left(\frac{z+0.175}{0.005}\right) & \text{if } -0.385 \leq z < -0.175 \\ 0.12763 & \text{if } -0.175 \leq z \leq 0.175 \\ 0.12763 \exp\left(\frac{0.175-z}{0.005}\right) & \text{if } 0.175 < z \leq 0.385 \end{cases} \tag{6.5}$$

and for $O_2(a^1\Delta_g)$, the mole fraction, x_a, is approximated as:

$$x_a(z) = \begin{cases} 0.05679 \exp\left(\frac{z+0.175}{0.05}\right) & \text{if } -0.385 \leq z < -0.175 \\ 0.05679 & \text{if } -0.175 \leq z \leq 0.175 \\ 0.05679 \exp\left(\frac{0.175-z}{0.05}\right) & \text{if } 0.175 < z \leq 0.385 \end{cases} \tag{6.6}$$

Finally the mole fraction of $O_2(X^3\Sigma_g^-, v = 0)$, x_X, is approximated as

$$x_X = 1 - x_O - x_a. \tag{6.7}$$

Line of sight average temperature

The expected line of sight averaged translational temperature for species i, $\bar{T}_{trans,i}$, can then be calculated according to

$$\bar{T}_{trans,i} = \frac{\int T(z) N_i(z) dz}{\int N_i(z) dz} = \frac{\int p(z) x_i(z) dz}{\int \frac{p(z) x_i(z)}{T(z)} dz}, \tag{6.8}$$

and for each molecular species the line of sight averaged temperature expected for a particular rotational state can be calculated by noting that the mole fraction of the J''th rotational state of species i, $x_{J''}$, is given by

$$x_{J''}(z) = x_i(z) \frac{(2J''+1) \exp\left(\frac{-E_{rot}}{k_B T(z)}\right)}{q_{rot}}. \tag{6.9}$$

Since $q_{rot} \propto T(z)$ and also replacing, $x_i(z)$ in 6.8 with $x_{J''}$ given by equation 6.9 one finds the line of sight average temperature for a particular rotational state:

$$\bar{T}_{trans} = \frac{\int p(z) x_i(z) \frac{\exp\left(\frac{-E_{rot}}{k_B T(z)}\right)}{T(z)} dz}{\int p(z) x_i(z) \frac{\exp\left(\frac{-E_{rot}}{k_B T(z)}\right)}{T(z)^2} dz} \tag{6.10}$$

The model can therefore be used to predict line of sight averaged temperatures for each rotational state (and for $O(^3P)$) and these can be compared directly to the Doppler widths for each measured transition. For $O(^3P)$ the model predicts a line of sight averaged temperature of 476 K which compares very favourably with the observed temperatures in the H-mode $\approx 450 \pm 20$ K. The modelled and measured values for the rotational states of $O_2(X^3\Sigma_g^-, v = 0)$ and $O_2(a^1\Delta_g, v = 0)$ are shown in figure 6.12. The modelled translational temperatures for $O_2(X^3\Sigma_g^-)$ show a much

stronger rotational state dependence than those for $O_2(a^1\Delta_g)$ and this simply reflects the different distributions of the various rotational states along the line of sight of the cavity. Given the simplicity of the model and the many assumptions it makes, the agreement with the $O_2(X^3\Sigma_g^-, v = 0)$ data is good, with the model always within ≈ 40 K and much better than that for higher rotational states. The model also reproduces very well the variation of $\bar{T}_{trans}$ with rotational state energy and this strongly supports the explanation given previously that the Doppler widths vary due to the different spatial distributions of the various rotational states. The agreement for $O_2(a^1\Delta_g)$ is poorer but the data for this species are significantly less certain.

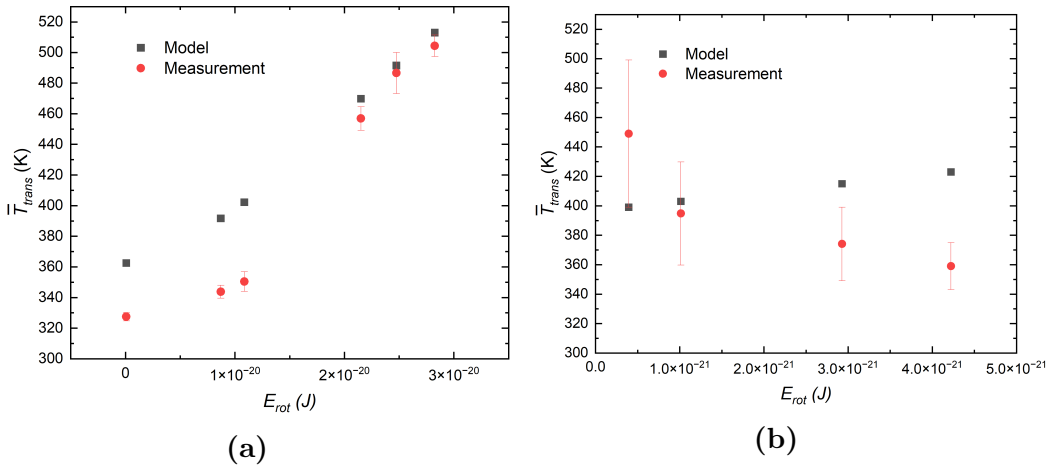

Figure 6.12: Modelled and measured line-of-sight averaged temperatures as a function of rotational energy for (a) $O_2(X^3\Sigma_g^-, v = 0)$ and (b) $O_2(a^1\Delta_g, v = 0)$ in a 100 mTorr, 300 W plasma..

Line of sight average number density

The line of sight averaged number density of a given species i can also be calculated for the modelled distributions using:

$$\bar{N}_i = \frac{1}{L}\int N_i(z)dz = \frac{1}{k_B L}\int \frac{p(z)x_i(z)}{T(z)}dz. \tag{6.11}$$

For individual rotational states of molecules equation 6.9 can be substituted into 6.11 to give:

$$\bar{N}_{J''} = \frac{(2J''+1)}{k_B L}\int p(z)x_i(z)\frac{\exp\left(\frac{-E_{rot}}{k_B T(z)}\right)}{q_{rot}(z)T(z)}dz, \tag{6.12}$$

and numerical solutions can be obtained using $q_{rot}(z) = 0.7215T(z)$ for $O_2(X^3\Sigma_g^-, v = 0)$ and $q_{rot}(z) = 0.481T(z)$ for $O_2(a^1\Delta_g, v = 0)$ (both obtained from linear fits to q_{rot} values calculated by PGOPHER and very close to the rigid rotor limits for

both molecules when spin multiplicities and Λ-doubling are accounted for). For O(^{3}P) the distributions described above predict a line of sight averaged number density of 1.21×10^{14} cm^{-3} in very good agreement with the line of sight averaged experimental value of 1.25×10^{14} cm^{-3}. Figure 6.13 shows the modelled and measured line of sight averaged densities in each rotational state of $O_2(X^3\Sigma_g^-, v = 0)$ and $O_2(a^1\Delta_g, v = 0)$. The agreement for ground state molecules is again remarkably good, whilst the agreement for the first metastable state is reasonable, and the modelled values demonstrate the correct trend with rotational energy.

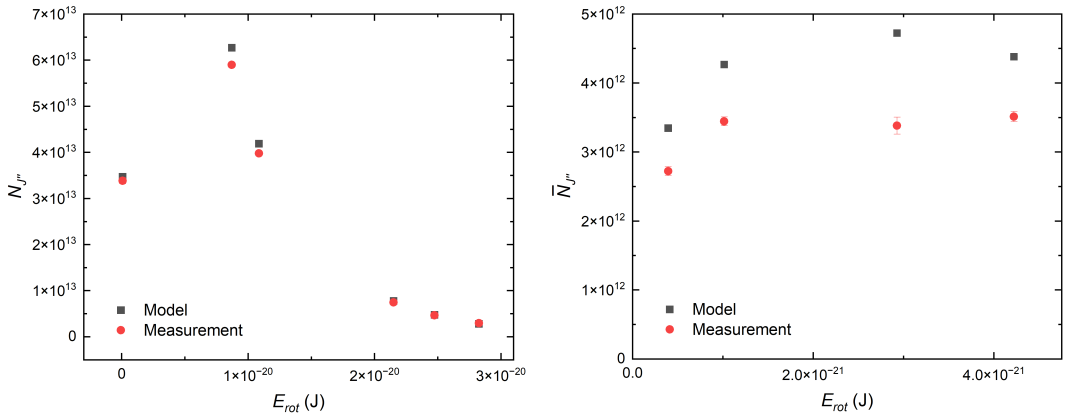

(a) **(b)**

Figure 6.13: Modelled and measured line of sight averaged number densities as a function of rotational energy for (a) $O_2(X^3\Sigma_g^-, v = 0)$ and (b) $O_2(a^1\Delta_g, v = 0)$ in a 100 mTorr, 300 W plasma.

In summary, this 1D model of the plasma is, given its simplicity, remarkably successful at reproducing the observed behaviour of several species within the plasma. This lends weight to the hypothesis that the plasma is not only thermally inhomogeneous in the H-mode but that this inhomogeneity plays a significant role in determining the average line of sight densities and temperatures not just of different species but also of different rotational states of the same species. The fact that resolving several rotational transitions allows spatial variations within the plasma to be inferred from line of sight averaged measurements is an extremely powerful result that could be of great utility in future work.

Oxygen plasma conclusions

This section of the thesis has detailed high resolution diode laser based cavity ring-down measurements of the most important species in a pure oxygen plasma. Ground state atomic oxygen ($O(^3P)$) has been probed, using the $O(^1D) \leftarrow O(^3P)$ transition at 630 nm, as a function of gas pressure and plasma power. Measurements include the observation of wall loss kinetics and of the switchover of the plasma from the capacitive E-mode of operation to the hotter and denser H-mode, indicated by an increase in atom density by an order of magnitude (from a few 10^{13} to a few 10^{14} cm^{-3}). The measured dissociation fractions ($\approx 10\%$ in the H-mode) are consistently high, predominantly as a result of the slow wall loss of atoms in the aluminium plasma chamber (as defined by the wall loss coefficient, $\gamma \approx 0.003$). Indeed the sensitivity of $[O(^3P)]$ to the condition of the chamber walls was exemplified by a reduction by a factor of 2 caused simply by cleaning. The significant photodetachment cross section of O^- has also made it possible to probe the anion density ($\approx 10^9 - 10^{10}$ cm^{-3}) and has produced results consistent with a detachment dominated plasma.

The first metastable state of molecular oxygen, $O_2(a^1\Delta_g)$, has also been measured by CRDS using the Noxon system at 1.9 μm and found to make up as much as 5% of the total plasma density; while it also shows a clear increase in density at the E/H switchover this increase isn't as marked as for $O(^3P)$. These are the first such direct measurements of $O_2(a^1\Delta_g)$ in a plasma operating at such low, technologically relevant, pressures ($\geq$ 10 mTorr) and through use of the calculations presented in chapter 2 are the first to unequivocally avoid errors in determining the electric quadrupole absorption cross sections[51,52]. The limit of detection achieved here ($[O_2(a^1\Delta_g, v = 0)]_{\min} = 1.1 \times 10^{12}$ cm^{-3}) represents an order of magnitude improvement on previous efforts to measure this species by absorption spectroscopy[51]. Time resolved measurements allowed the wall loss coefficient of this metastable species to be determined ($\gamma \approx 0.003$), a vital parameter for plasma kinetic modelling.

These CRDS results have been supported by observations of the plasma emission, in particular from atomic emission lines (*e.g.* at 777 nm) and from the $O_2(b^1\Sigma_g^+) \rightarrow O_2(X^3\Sigma_g^-)$ system. The fitting of molecular spectra to simulations enabled the extraction of both rotational ($350 - 630$ K) and vibrational (905 K) temperatures as well as giving an

indication of the relative density of $O_2(b^1\Sigma_g^+)$ as a function of plasma power. Time resolved emission measurements show that the wall loss lifetime of $O_2(b^1\Sigma_g^+)$ is $2-7$ ms (depending on pressure), and is significantly less than for either $O(^3P)$ or $O_2(a^1\Delta_g)$ (which have lifetimes ≈ 100 ms).

All of these experimental results are interpreted with the aid of a volume averaged kinetic model. This model, which includes 34 kinetic processes, is successful in reproducing experimental atom, ion and metastable molecule densities, and from it electron densities and temperatures are inferred. For a given gas pressure and power, the electron density is expected to scale with the inverse of the plasma volume and within this framework the electron densities inferred from the model were in line with other work reported in the literature.

Despite the success of the volume averaged model, several features of the CRDS data indicate that the plasma is not in fact homogeneous. In particular, different species tend to show different translational and rotational temperatures, with those that are longest lived ($O_2(a^1\Delta_g)$) showing lower temperatures compared to those with shorter lifetimes ($O_2(b^1\Sigma_g^+)$). This observation leads to the hypothesis that the plasma shows significant thermal inhomogeneity, with long lived species having sufficient lifetimes to thermally equilibrate with the cool chamber walls and also to penetrate a signifiant distance into the cold baffle arms and thereby exhibit a reduced line of sight averaged temperature.

In order to test this hypothesis CRDS measurements were performed on the $v = 0$ and $v = 1$ states of $O_2(X^3\Sigma_g^-)$. As expected, the $v = 0$ state which fills the majority of the arms shows cold (< 350 K) line of sight averaged translational temperatures unless very highly excited rotational states were probed. Such rotational states ($J'' = 28, 30, 31$) only exist in significant densities when the temperature is significantly above ambient and are hence largely confined to the plasma region and are not found in the baffle arms. $O_2(X^3\Sigma_g^-,\ v = 1)$ meanwhile is found to be translationally hot (≈ 550 K) across all rotational states as a result of it being produced only in the hot plasma and then lost rapidly (by V-T energy transfer) if it leaves this region. The hypothesis is also supported by a simple model of plasma inhomogeneity, whereby the pressure, temperature and mole fractions of the various species across the chamber (and arms) are approximated and the corresponding line of sight averaged densities and temperatures calculated. This basic model is reasonably successful at reproducing the observations for $O_2(X^3\Sigma_g^-,\ v = 0)$ and $O(^3P)$. Further detailed insights into spatial inhomogeneity will require computational fluid dynamics calculations and these are currently being undertaken.

Part III

Nitrogen plasma

Chapter 7

Introduction to nitrogen plasma

In this, the third part of this thesis, a nitrogen ICP will be investigated. This plasma will be produced in the same chamber as the oxygen plasma and will operate at a similar range of pressures ($10-100$ mTorr) and powers ($0-500$ W). This chapter will describe methods that have been used previously to quantify the densities of molecular cations and electronically excited molecules in various nitrogen plasmas. The following chapters will detail measurements, utilising CRDS, of the densities of both $N_2^+(X^2\Sigma_g^+)$ and $N_2(A^3\Sigma_u^+)$ first in the bulk of the plasma and then, with an experimental adjustment, close to the chamber's lower (non-driven) electrode. The major focus is on the measurements of the cations because these represent the first such CRDS measurements in a nitrogen ICP and because the density of cationic species is expected to change significantly in the plasma sheath and presheath. Finally, some discussion is given regarding the Lamb dips that are observed as a result of saturation in the CRDS spectra.

7.1 Key species in nitrogen plasma

Nitrogen plasmas, like oxygen plasma, are of both applied and fundamental interest. Many of the early observations on nitrogen discharges and nitrogen containing plasma in the earth's atmosphere provided some of the first observations of nitrogen's electronic and rotational structure[177–180]. In the laboratory and in industry, nitrogen plasma has found use in surface modification, in particular in nitriding processes, of importance to semiconductor manufacturing[42]. Nitrogen plasma is electropositive, meaning that electrons form by far the most important reservoir of negative charge whilst anions are unimportant and exist in insignificant quantities. It is therefore expected that the densities of electrons and cations will be equal and thus measuring the density of one allows the other be inferred. At the pressures investigated here

$(10-100$ mTorr) it is expected that $N_2^+(X^2\Sigma_g^+)$ will be the dominant cation (although at lower pressures N^+ can become important and at higher pressure N_3^+ and N_4^+ may also be found). The diatomic molecular cation is therefore of significant interest, not only because ion acceleration in the sheath could be responsible for the surface processing ability of nitrogen plasma, but also because, in the plasma bulk, the density of $N_2^+(X^2\Sigma_g^+)$ is likely to be a good indicator of the electron density. Apart from the cations, atomic and excited molecular species also play an important role in nitrogen plasma. Nitrogen atoms are expected to be an order of magnitude less abundant than $O(^3P)$ in oxygen plasmas, largely due to the strong N≡N triple bond which makes the threshold for electron impact dissociation of ground state molecules very high. Indeed the dominant mechanism for atom formation at the pressures investigated in this thesis is expected to be vibrational excitation (which reduces the dissociation threshold) followed by electron impact dissociation. Although the atomic content of nitrogen plasma is expected to be much less than that of oxygen the degree of vibrational excitation is expected to be much greater, this is because $N_2(X^1\Sigma_g^+, v=0)$ has unusually large cross sections for electron impact vibrational excitation (the reasons for which are discussed later in this chapter). As such, vibrationally excited molecules play an important role in the chemistry of nitrogen discharges (as already suggested in the case of atom formation) and measuring vibrational excitation is particularly important to understanding nitrogen discharges. Contrast this situation with that of O_2 where vibrationally excited molecules were sufficiently scarce that neglecting them made little difference to kinetic modelling (see chapter 5).

Another important group of molecules are the triplet excited electronic states, $N_2(A^3\Sigma_u^+)$, $N_2(B^3\Pi_g)$, $N_2(W^3\Delta_u)$, $N_2(B'^3\Sigma_u^-)$ and $N_2(C^3\Pi_u)$ (refer to the potential energy level diagram in figure 2.8 to see the relative energies of these states). The first four of these states constitute the four lowest lying excited states of N_2. The $N_2(A^3\Sigma_u^+)$ state is metastable and thus most important to plasma chemistry, with a radiative lifetime of 2 s it is an important reservoir of energy, lying around 6 eV above the ground state. The threshold energy for electron impact dissociation and ionisation of this metastable species is significantly smaller than that for $N_2(X^1\Sigma_g^+)$ and it can therefore have significant influence over the atom and ion content of the plasma. Its metastability can also make it an important source of higher excited states of N_2 which are formed via energy pooling reactions. The other triplet states are not metastable as each has an allowed radiative pathway (either direct or via $N_2(B^3\Pi_g)$) that produces the $N_2(A^3\Sigma_u^+)$ state. This radiative cascade mechanism means that the vast majority of the electronically excited molecules that are produced in the plasma

end up as $N_2(A^3\Sigma_u^+)$, thus further enhancing its importance to the overall chemistry of the plasma.

7.2 Techniques for the detection of $N_2^+(X^2\Sigma_g^+)$, $N_2(A^3\Sigma_u^+)$, $N_2(B^3\Pi_g)$ and $N_2(C^3\Pi_u)$

The range of techniques that have been used to probe nitrogen plasmas is vast, here an overview of the most important techniques is given with focus on those that are most relevant to this thesis.

7.2.1 Electrical probes and mass spectrometry

Much work exists which utilises Langmuir probes[24–26,28,181] and mass spectrometry[182,183] to investigate charged species in nitrogen plasma. The quasi-neutrality of such plasma means that a method that quantifies the electrons necessarily provides information about the ions as well. Using a Langmuir probe Zhu *et al.*[24,25] found that the electron density increased from 2×10^9 cm^{-3} at 100 W to 10^{10} cm^{-3} at 500 W in a 15 mTorr ICP with an electron temperature of ≈ 2 eV; Song *et al.*[26] saw a similar increase with power from $\approx 6 \times 10^9$ cm^{-3} at 200 W to $\approx 2 \times 10^{10}$ cm^{-3} at 600 W in a 5 mTorr nitrogen-argon mixture whilst Biloiu *et al.*[181] found electron densities of 8×10^{10} cm^{-3} at 600 W in their Helicon plasma with $T_e \approx 3$ eV.

An alternative to the typical Langmuir probe, which is usually constructed from a thin piece of wire, is a planar probe. The uniform sheath that forms around such a probe (which is usually surrounded by a guard ring to ensure sheath uniformity) can make analysis more straightforward. Bakowski[64] used such planar probes to investigate nitrogen plasma in the same chamber as used in this work and found electron temperatures of the order of 2 eV and electron densities (and thus N_2^+ densities) on the order of a few $\times 10^9$ cm^{-3} at 400 W and a range of pressures.

Some work also exists on the use of quadrupole mass spectrometry to detect positive ions produced in nitrogen plasma although these have mainly been used to find ion ratios[183] and ion energy distributions[182] as oppose to absolute densities (Mass spectrometry lends itself to ion flux measurements but measuring densities is more difficult[184]). The ability to measure the ion energy distribution[182] is an advantage of this techniques however the mass spectrometer generally has to be attached to the side of the chamber and thus measurements are not really *in situ* and nor are they absolute.

7.2.2 Optical emission spectroscopy

A great deal of work exists exploring the emission from nitrogen plasma. Plasma emission is a much more powerful and widely used diagnostic in nitrogen plasmas compared to oxygen because of the much wider range of molecular emission systems which are present. Each system also tends to show marked vibrational structure not only because they tend to involve states with rather different potential energy curves (and thus there are many significant Franck-Condon factors) but primarily because the degree of vibrational excitation in nitrogen plasma is significantly greater than in other simple molecular plasmas (T_{vib} is typically several thousand K in nitrogen). This vibrational excitation is important in determining the chemistry of the plasma and arises because of a shape resonance[185–187] whereby electrons with energy ≈ 2.3 eV can be captured particularly efficiently by $N_2(X^1\Sigma_g^+)$ to form the short lived $N_2^-(X^2\Pi_g)$ anion which can then decay to produce an electron and a vibrationally excited molecule:

$$N_2(X^1\Sigma_g^+, v) + e^- \rightarrow N_2^-(X^2\Pi_g) \rightarrow N_2(X^1\Sigma_g^+, v') + e^-. \tag{7.1}$$

The resulting vibrational excitation in the ground state can then be transferred (to some extent) to the electronically excited state species either during the electron impact production of the excited species or by V-V energy transfer.

Particularly prominent in the emission spectra of nitrogen plasmas are the first positive ($N_2(B^3\Pi_g) \rightarrow N_2(A^3\Sigma_u^+)$) and second positive ($N_2(C^3\Pi_u) \rightarrow N_2(B^3\Pi_g)$) systems as well as the first negative system of the molecular cation ($N_2^+(B^2\Sigma_u^+) \rightarrow N_2^+(X^2\Sigma_g^+)$)[25,188] (the systems are labelled positive or negative based on whether they appear in the positive column or the negative glow of a nitrogen containing glow discharge). These systems are all strongly allowed and produce a large number of vibrational bands. As an example an emission spectrum (300 W, 100 mTorr) taken using the Andor spectrometer (utilised previously for oxygen emission measurements) is shown in figure 7.1, this spectrum is scaled to account for the spectrometer efficiency and will be discussed in more detail later. For the time being the locations of the above systems are identified and a subset of the bands are assigned for illustrative purposes.

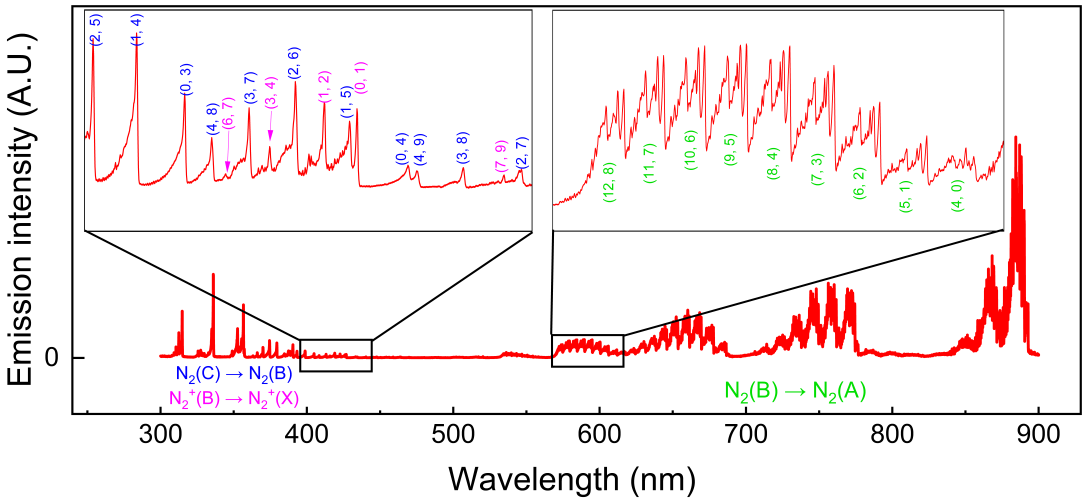

Figure 7.1: The emission spectrum of the nitrogen ICP operating at 300 W and 100 mTorr showing the second positive system labelled in blue; the first negative system labelled in pink and the first positive system labelled in green. Each band shows extensive vibrational structure indicative of the high degree of vibrational excitation present in the plasma. For the sake of illustration, two regions of the spectrum are enlarged and the vibrational bands assigned. These data are analysed in more detail in the next chapter.

The utility of emission spectra was exemplified in the previous chapter for oxygen, in particular for the extraction of rotational and vibrational temperatures. A great deal of work[181,188–192] exists in which the emission from first and second positive systems is utilised to find vibrational state distributions (also known as vibrational distribution functions, VDFs) which can deviate from a Boltzmann distribution. Where a Boltzmann distribution describes the vibrational population the VDF is described by the vibrational temperature T_{vib}.

The fitting of molecular emission bands typically yields a value for T_{vib}[181,189], however, the physical meaning of such temperatures must be considered carefully. This is because the vibrational temperature found in this way is strictly the vibrational temperature of the emitting state. If this state is long lived then it can undergo many V-V energy transfer collisions with the ground state molecules that make up the bulk of the plasma and thus the emission temperature will be representative of the vibrational temperature of all of the gas in the chamber (this was the case for the emission from the second metastable state of oxygen detailed in the previous chapter). However, both the first and second positive systems are the result of fully allowed transitions

and thus the radiative lifetimes of the emitting species are of the order of μs. This results in a situation whereby the VDF of the emitting species can be very different to that of ground state molecules and depends heavily on the rates of production and loss of the various vibrational states. This confounding factor was explored in depth in the recent work of Dilecce *et al.*[192] who found, from a collision radiative model for the second positive system, that the apparent temperatures measured in emission could routinely exceed those of the ground state molecules by a factor of 2 for pressures similar to those used in this study. Indeed, the relationship between the VDFs of the various electronic states of N_2 are found to be a very complex function of pressure, electron temperature and density, quenching rate coefficients, electron impact excitation rate coefficients and radiative lifetime (the last three of which are often strongly vibrational state dependent). It thus becomes extremely complicated to relate emission derived vibrational temperatures to those of the ground state molecules without detailed kinetic modelling. Despite this limitation the excited state VDFs can still be important, in their kinetic implications, for example and are thus worth measuring in their own right.

Several workers have demonstrated methods utilising the ratio of the intensities of the second positive and first negative system emission lines in order to estimate electron temperatures and densities[25,193] and also electric field strengths[191]. The basis of these methods is that, because the emitting species have different electron impact production threshold energies their emission intensities will be sensitive to different regions of the EEDF and thus their ratio will provide information on the EEDF. This work is dependent however on either a meticulous calibration approach (see for example[191]) or the construction of a complex collision radiative model (see for example[25]) in order to achieve quantitative results and thus depends on accurate knowledge of excitation and quenching rates in the plasma. For these reasons this line intensity ratio method shows the same drawback as many techniques involving the use of plasma emission, it requires many assumptions in order to extract meaningful results.

Although the first and second positive systems provide obvious approaches for probing the $N_2(B^3\Pi_g)$ and $N_2(C^3\Pi_u)$ states there is no equivalent allowed emission for the most important excited molecular state $N_2(A^3\Sigma_u^+)$. The only possible emission from this electronic state is on the spin forbidden Vegard-Kaplan system $N_2(A^3\Sigma_u^+) \rightarrow N_2(X^1\Sigma_g^+)$). This system, whose emission is at wavelengths shorter than 300 nm, has been utilised a few times to deduce densities and kinetics of $N_2(A^3\Sigma_u^+)$ both directly[194–197] and in the context of intensity ratio based methods[198]. As was

the case for the fully allowed transitions, any quantitative conclusions are heavily dependent on the knowledge of which kinetic processes are important and their rates, or else they require absolute calibration. As well as observations of the first negative system ($N_2^+(B^2\Sigma_u^+) \rightarrow N_2^+(X^2\Sigma_g^+)$) N_2^+ has also been observed using emission on the Meinel system[199] ($(N_2^+(A^2\Pi_u) \rightarrow N_2^+(X^2\Sigma_g^+))$). This work used a Fourier transform spectrometer for detection. Implementing this approach is made difficult by the fact the Meinel system is coincident with the first positive system of N_2, a problem that can be overcome by employing an alternative, ion specific, technique. One such technique is velocity modulation spectroscopy, discussed later in this chapter.

7.2.3 Laser induced fluorescence

There is a large body of research based on Laser Induced Fluorescence (LIF) on nitrogen plasmas. In particular, $N_2(A^3\Sigma_u^+)$ has been probed by LIF by several workers. For many years the LIF schemes typically involved exciting a selected vibrational band of the first positive system and then monitoring emission on a different vibration band of the same system[200–206]. More recently, a second scheme involving a double resonance (one excitation into the $N_2(B^3\Pi_g)$ state and then another into the $N_2(C^3\Pi_u)$ state) has been developed[207–209]. This so called optical-optical double resonance LIF (OODR-LIF) has practical challenges, requiring two synchronised lasers, but it has an advantage in terms of fluorescence detection because the $N_2(C^3\Pi_u)$ state has a very short radiative lifetime (with emission on the second positive system) and therefore always has a significant fluorescence yield even at atmospheric pressure; this is in contrast to the $N_2(B^3\Pi_g)$ state, the radiative lifetime of which is longer and which is therefore collisionally quenched at higher pressures making fluorescence too weak to detect. There has also been some work on probing $N_2(B^3\Pi_g)$ using LIF by excitation and detection on the second positive system[200,201].

Even without calibrating the LIF signals to find absolute concentrations the technique's excellent temporal resolution make it possible to determine kinetic parameters (for example for electronic quenching[202], vibrational relaxation[207] or electronic energy pooling reactions[200]). Crucially, the vibrational state dependence of all these kinetic parameters can be characterised by LIF. It is also possible to determine vibrational distribution functions for $N_2(A^3\Sigma_u^+)$ which are usually found to be approximately Boltzmann, but with some overlayed (non-Boltzmann) structure[202].

In terms of putting measurements on an absolute footing, several calibration techniques have been demonstrated including absolute calculation of the LIF system efficiency[205,206] which requires knowledge of the Einstein coefficients for both excitation

and fluorescence, of relaxation rates (i.e. quenching and unimolecular non-radiative processes), of laser pulse intensity and temporal width, of the volume of interaction between the pump laser and the plasma and of the absolute collection efficiency of the fluorescence detection system (including the solid angle covered by the detector and the efficiency of any filters and detectors). Clearly this absolute calibration approach has a large number of variables and is rather painstaking to implement. An alternative that has been utilised more recently is to compare LIF signals to those due to Rayleigh scattering of the excitation beam[200,201,204]. Provided the same collection optics are used for both experiments the ratio of the LIF and Rayleigh scattered signal will be independent of the solid angle occupied by the detection system. This method still requires detailed knowledge of excitation cross sections and of the rates of the various potential fates of the fluorescing state. It additionally requires that a Rayleigh scatterer of known number density and Rayleigh scattering cross section is chosen. Thus the Rayleigh scattering method is only slightly simpler than the absolute calibration and is still a significant challenge to perform.

LIF measurements have also been performed on the molecular cation $N_2^+(X^2\Sigma_g^+)$ produced in a variety of different plasmas[210–216] and usually utilising the First negative system for both excitation and fluorescence (one work by Miller *et al.*[215] instead uses the Meinel system but only for line position and molecular constant measurements). The oldest of these studies simply concerns itself with vibrational temperature measurements thus removing the need for absolute calibration[212]. The work of Gerassimou *et al.*[214] also sought information that could be obtained without the need for calibration: in that case relative concentrations (as a function of position in the plasma), rotational temperatures and lifetime of the cationic species. In addition Den Hartog *et al.*[213] utilised LIF to measure ion translational temperatures.

More recent works have sought to put the LIF signals from N_2^+ on an absolute footing and Woodcock *et al.*[210] achieved this in their measurement on a CCP chamber by considering the most important loss processes for N_2^+. One of these processes is dissociative recombination and, given quasi-neutrality ($[e^-]=[N_2^+]$), this process shows second order kinetics. If loss is dominated by this processes then providing that the rate constant is known the decay in $[N_2^+]$ after the plasma is extinguished can be analysed to yield the initial N_2^+ concentration. Other important loss processes (*e.g.* wall loss) show first order (or quasi first order) kinetics but it was still possible to find initial ion concentrations by including the effects of these reactions. An alternative calibration method was proposed by Konthasinghe *et al.*[211] who used the vibrational Raman scattering from N_2 (a process for which the cross section is well known) as a

calibrating signal. The Rayleigh scattering due to molecular nitrogen has also been used as a calibration signal for cation LIF by Visser *et al.*.[216]

Of particular interest are the spatially resolved measurements of Gerassimou *et al.*[214] and Woodcock *et al.*[210] who both attempt to quantify the behaviour of the ions as they approach the sheath of capacitively coupled rf plasmas, the former investigating ions close to a grounded metallic surface and the latter near to the driven rf electrode. Gerassimou *et al.* found that, close to the chamber walls, the density of ions drops by one to two orders of magnitude as is expected for a plasma sheath. Additionally they found that the lifetime of $N_2^+(B^2\Sigma_u^+)$ also decreased across the plasma sheath. This was tentatively attributed to acceleration through the sheath leading to increased collision frequencies and thus enhanced collisional quenching, although several other possibilities were considered. The work also probed the rotational temperature of molecular cations at different positions in the plasma using the LIF excitation spectrum, it was found that $N_2^+(X^2\Sigma_g^+)$ ions were rotationally equilibrated with the neutral gas (*i.e.* that translational acceleration by the sheath had no effect on the rotational populations) and that their rotational temperature decreased through the sheath such that ions near the wall had $T_{rot} = T_{wall}$. This is a result that would be expected if the sheath can be treated as collisionless and thus ions undergoing acceleration have no opportunity to participate in translational to rotational energy transfer with other molecules. As an alternative explanation of this observation, Gerassimou *et al.* posit an argument that charge exchange collisions between molecular ions and neutral molecules are important in the sheath and that this rapid conversion of neutrals into ions and visa versa necessarily means that these species end up in rotational equilibrium (particularly because the charge exchange process ought not to alter the rotational states of the species involved).

Woodcock *et al.*[210] were able not only to measure LIF spectra in the plasma sheath, but also to do so with sub-Doppler resolution and thereby resolve the (time averaged) ion velocity distributions in a direction perpendicular to the surface of the driven electrode. They observed a decrease in density by a factor of 50 across the sheath which they found to be $\approx$ 1 cm in thickness, both reasonable for a CCP. Far from the electrode (15 mm), ion velocities were found to be identical in both parallel and perpendicular directions and well described by a Boltzmann distribution corresponding to $T_{trans} = 355 \pm 15$ K. Close to the electrode however the perpendicular velocity distribution was found to be bimodal, with a group of fast ions, accelerated towards the driven electrode, and a group of ions close to the bulk temperature. Such bimodal distributions have also been observed and explained in several other

discharges[217–219] and are expected to arise when the rf period, τ_{rf}, is significantly longer than the time it takes for an ion to transit through the sheath, τ_{ion}[220]. This being the case, the accelerating voltage experienced by an ion will depend upon the point during the rf cycle that it enters the sheath and thus, when the signal is time averaged, the ions that experience the maximum drop in potential across the sheath contribute to the fast velocity component whilst those that experience the smallest drop will be closer to ambient temperatures leading to a bimodal distribution[15,221,222]. Even with this in mind, it is likely that the 13.56 MHz discharge investigated by Woodcock *et al.* is in the regime where $\tau_{rf} < \tau_{ion}$ and thus each ion would be expected to experience a time averaged drop in potential because it would experience many rf cycles during its transit through the sheath. In this case the two peaks in the bimodal ion energy distribution are expected to approach one another and eventually become indistinguishable (when $\tau_{rf} << \tau_{ion}$) - see for example Coburn and Kay[221].

This averaging (or not) of ion velocities with relation to the rf phase complicates the expected ion energy distribution. Even time resolved LIF studies under conditions where the ions should be able to respond to the instantaneous sheath potential[219] have shown that, at some points in the rf cycle, ions in the sheath can show a bimodal velocity distribution. Woodcock *et al.* as well as others[210,217,218] suggest that the slow velocity group arises due to charge transfer production of N_2^+ from N_2 in the sheath. The newly formed N_2^+ would be created with the velocity distribution of the neutral molecules (which is expected to be approximately the same as the bulk temperature) and would thus appear as a slow moving group of ions in LIF experiments. Despite this possible explanation, experiments aimed at detecting the fast neutrals that ought to be produced by such a charge transfer have not succeeded[217] and significant uncertainty still exists as to the origin of the slow group of ions.

7.2.4 Scattering techniques

As well as being used to calibrate LIF, scattering of light by the plasma can also be used to quantify the densities of plasma borne species. Of particular use are inelastic scattering from molecules (Raman scattering) and elastic scattering from electrons (Thomson scattering). Vibrational Raman scattering provides information about VDFs and has been utilised to detect $N_2(A^3\Sigma_u^+)$ with the scattering from ground state molecules removed by interference based optical filters[223].

Thomson scattered photons take on a Doppler frequency distribution indicative of the electron energies and the Thomson scattered photon frequency profile and intensity reveal the electron temperature and density, respectively. Thomson scattering

requires that the intense Rayleigh scattered radiation is filtered out and that any rotational Raman scattered signal is accounted for.

Both these scattering techniques suffer from the same requirement for absolute calibration as LIF. Additionally, Thomson scattering cross sections are invariably very small and thus Thomson scattering measurements are limited to high electron densities ($> 10^{11}$ cm^{-3}), and thus are typically carried out in noble gas discharges, with argon being by far the most common[224]. Despite this difficulty some work does exist utilising mixtures containing nitrogen[225].

7.2.5 Laser Optogalvanic Spectroscopy (LOGS)

Laser optogalvanic spectroscopy relies on the change in the impedance of a discharge that occurs when the discharge is irradiated by a laser that is on resonance with an allowed optical transition. The excited state that is produced naturally has a different ionization energy compared to the initial state and this change in electrical properties can be observed as a change in voltage across a resistor (where the supply voltage is held constant). This technique is sensitive and allows sub-Doppler spectral resolution but is not absolute or spatially resolved, the signal is also proportional to the ratio of the laser excitation volume to the total discharge volume and thus the technique is most applicable to small scale discharges. Nevertheless LOGS has been used to detect both $N_2(A^3\Sigma_u^+)$[226] and $N_2^+(X^2\Sigma_g^+)$[227] in nitrogen plasmas.

7.2.6 Velocity modulation spectroscopy

Velocity modulation spectroscopy (VMS) is a technique that utilises the acceleration of ions that occurs in each cycle of a low frequency discharge (typically kHz). As the electric field of the discharge alternates so does the velocity of the ions and thus the absorption features of ionic absorbers are Doppler shifted back and forth. By demodulating the signal using a lock-in amplifier the signals due to ionic absorption can be identified and those due to neutral species (which are not modulated) can be filtered out. The high level of discrimination between ions and neutrals makes this technique very useful in the detection of $N_2^+(X^2\Sigma_g^+)$ particularly because the Meinel system of N_2^+ is coincident in wavelength with the first positive system of N_2 which would otherwise interfere. As a result of these advantages VMS (or modifications thereof) has been the dominant technique for measuring line positions of the Meinel system and thus determining the molecular constants of the $N_2^+(X^2\Sigma_g^+)$ and $N_2^+(A^2\Pi_u)$ electronic states[228–233]. Of the many VMS studies that exist the most relevant to the

work presented here are those of Collet *et al.*[228] whose molecular constants are used to simulate the (2, 0) vibrational band using PGOPHER and the work from the group of McCall[229,230] which utilises a cavity enhanced version of VMS and was the first to observe Lamb dips in molecular ion spectra using a tunable laser absorption spectroscopic method, (similar observations are made later in this thesis). Despite its suitability for accurate line position determination, VMS has significant limitations. It is only applicable to plasmas which operate at a frequency low enough that the ions respond to each voltage cycle (likely not to be the case at 13.56 MHz). It is also extremely difficult to extract absolute absorption coefficients from a VMS spectrum[234] not least because the low frequency of the discharge leads to a modulation of the ion density but also because the fitting process for VMS signals involves several variables (modulation amplitude, linewidth and intensity) which show strong covariance.[234]

7.2.7 Direct absorption spectroscopy

Given that there are so many allowed optical transitions among the electronically excited states of both nitrogen molecules and cations it is no surprise that absorption spectroscopy has found widespread use as a detection technique for these species. Unlike oxygen, where transitions involving the electronic states of interest are either forbidden or in the difficult to access VUV, nitrogen has a number of allowed transitions at wavelengths that make direct absorption measurements possible. The first absorption measurements were made using light produced in a discharge tube and observing its attenuation as it passed through a second discharge tube[235–237]. This method was successful both in the quantitative detection of metastable molecules[235,236] and measurements of their vibrational distributions[237]. Later, as lasers became available that were capable of operating at the relevant wavelengths, the first positive system was observed by laser absorption spectroscopy[238], with Augustyniak and Borysow finding translational temperatures of 370 ± 20K and densities of the order of 10^{12} cm^{-3} in the $N_2(A^3\Sigma_u^+, v = 0)$ vibrational state in a pulsed DC discharge.

7.2.8 Cavity enhanced absorption techniques

$\mathbf{N_2(A^3\Sigma_u^+)}$

Although the transitions of interest are allowed, the fact that nitrogen metastables and cations are generally present in very low densities leads to weak absorption and thus cavity enhanced absorption techniques can be of great advantage in detecting these species. Early cavity based measurements used ICLAS whilst more recently

absorption techniques utilising optical cavities external to the laser source (e.g. CRDS and CEAS) have been favoured. Foissac *et al.*[239,240] made measurements using ICLAS on the (1, 0) band of the first positive system in a microwave driven flow tube at 440 Pa. They were able to quantify the density of $N_2(A^3\Sigma_u^+, v = 0)$ as 5×10^{11} cm^{-3} in the discharge region and an order of magnitude lower in the afterglow. The translational temperature was likewise found to decrease, from ≈1000 K in the discharge to ≈ 500 K in the afterglow. Stancu *et al.*[209] found $N_2(A^3\Sigma_u^+)$ densities of the order of $10^{14} - 10^{15}$ cm^{-3} in a ns pulsed discharge at atmospheric pressure using pulsed CRDS on the (2, 0) band of the first positive system. The extensive work of Bakowski and Thornton[63,64,153,241] also used the first positive system and was able to quantify $N_2(A^3\Sigma_u^+)$ densities and temperatures in the same chamber as is utilised in this work. The work of Bakowski[64] used cw-CEAS and found that the density of $N_2(A^3\Sigma_u^+, v = 0)$ rose by approximately an order of magnitude (from ≈ 10^{10} to ≈ 10^{11} cm^{-3}) as power was increased from 20 to 300 W and that the vibrational ground state has a maximum density at around 20 mTorr, with density decreasing sharply towards lower pressure and more gradually at higher pressures. This work also found that the rotational temperature increased from ≈300 K at 50 W up to around 500 K at 300 W, and it was also able to confirm that the rotational and translational degrees of freedom are in equilibrium at all pressures above 10 mTorr. The later work of Thornton[63] extended the CEAS work to include measurements of vibrationally excited molecules ($v = 1, 3$ and 6) and was thus able to estimate the vibrational temperature of $N_2(A^3\Sigma_u^+)$. The vibrational temperature was found to significantly exceed rotational and translational temperatures (which were found to be the same for the different vibrational states) as is expected for low pressure ICPs, increasing with power from ≈3000 K at 50 W up to ≈ 4000 K at 300 W.

$N_2^+(X^2\Sigma_g^+)$

Cavity enhanced absorption measurements of $N_2^+(X^2\Sigma_g^+)$ started with pulsed-CRDS measurements on microsecond pulsed discharges operating at low pressure (0.5-1 Torr) in mixtures of helium and nitrogen[242,243]. These early measurements used the (6, 0) band of the Meinel system and were able to detect ion densities of the order of 10^{11} cm^{-3}. Later Yalin *et al.*[244] detected densities of ≈ 10^{12} cm^{-3} in an atmospheric pressure glow discharge using the (0, 0) band of the first negative system again using pulsed-CRDS. In the work of Widicus Weaver *et al.*[245] cw-CRDS was used to make the first laboratory observation of the Meinel system (2, 1) band, although that study was concerned primarily with line positions rather than density measurements.

Of particular interest are the measurements of Gherman *et al.*[246] who were able to quantify $N_2^+(X^2\Sigma_g^+,\ v=0)$ densities in the same flowing microwave discharge as was used by Foissac *et al.*[239,240] for $N_2(A^3\Sigma_u^+)$ measurements. That work used a frequency doubled titanium sapphire laser to perform broadband CEAS measurements on the first negative system ((0, 0) band) and found densities of $N_2^+(X^2\Sigma_g^+,\ v=0)$ of $\approx 10^9$ cm^{-3}. Notably, the ions both in the discharge region and in the afterglow were found to have rotational temperatures that were $\approx$ 300 K hotter than those measured for the neutral metastable molecules. This discrepancy was ascribed to the ambipolar microfield of the plasma which could accelerate the ions and cause the heating. Thornton[63,153] was also able to measure absorption due to $N_2^+(X^2\Sigma_g^+)$ using cw-CEAS on the Meinel system in the same chamber that was used for the experiments presented here. The ion density was found to be of the order of 10^9 cm^{-3} at 10 mTorr and 400 W but the signal to noise ratio was particularly poor (≈3:1). Within the limits of this small signal it appeared that the ion had the same translational temperature as the neutral molecules. In order to increase the sensitivity of these measurements CEAS was combined with wavelength modulation spectroscopy and although this improved the detection limit by an order of magnitude the implementation of modulation techniques necessarily made the extraction of absolute number densities and translational temperature more difficult.

The next chapter will present measurements of both $N_2^+(X^2\Sigma_g^+)$ and $N_2(A^3\Sigma_u^+)$ in the bulk of the nitrogen plasma using saturated CRDS. The ways in which the effects of saturation are accounted for are described in detail. The CRDS measurements are supported by observations of the wavelength resolved plasma emission with particular focus on the first positive system, which is fitted with a spectral simulation to return rotational and vibrational temperatures for the emitting $N_2(B^3\Pi_g)$ state.

Chapter 8

Nitrogen plasma bulk measurements

In this chapter a cw-CRDS arrangement is used to probe several rovibronic lines of the Meinel and first positive systems of a nitrogen ICP. The effects of saturation inside the optical cavity are measured and accounted for and temperatures and densities are calculated. The experimental arrangement used to probe nitrogen plasma in this chapter is identical to that which was used previously to probe oxygen plasma. During the course of this chapter and those that follow it, it may prove useful to refer back to the potential energy diagrams for the various electronic states of N_2 and N_2^+ shown in figure 2.8.

8.1 Experimental arrangement

Emission measurements (such as that shown in figure 7.1) are once again performed by coupling light emitted from the plasma into an Andor iDus spectrometer via a wide core optical fibre. Cavity ringdown measurements are performed using the same optical arrangement as was utilised for measurements of $O_2(X^3\Sigma_g^-)$ with the toptica ECDL operating in the range 747-792 nm and cavity mirrors (Layertec GmbH) able to produce ringdown times of the order of 80 μs across the operating range of the laser. The laser scanning range is sufficient to reach several bands of both the first positive system of molecular nitrogen ($N_2(B^3\Pi_g) \leftarrow N_2(A^3\Sigma_u^+)$) and the Meinel system of the nitrogen cation ($N_2^+(A^2\Pi_u) \leftarrow N_2^+(X^2\Sigma_g^+)$) both of which are electric dipole allowed. Care must be taken when probing the Meinel system to avoid interference from the first positive system (which covers a huge range of wavelengths with a large number of rovibrational transitions). This system was successfully avoided by using the excellent PGOPHER simulation of various nitrogen systems published by Western *et al.*[247] and

comparing it to a custom built PGOPHER simulation for the Meinel system utilising the molecular constants found by Collet *et al.*[228] and the transition dipole moments and Franck-Condon factors tabulated by Gilmore *et al.*[248].

8.2 Analysis of emission on the first positive system

Figure 7.1 shows an emission spectrum of the nitrogen plasma scaled to account for the spectrometer efficiency. The part of the spectrum where the relative intensities of adjacent vibrational bands is most reliable is that where the spectrometer sensitivity is high and varies little with wavelength (approximately between 450 and 700 nm). In other regions, where the sensitivity varies a great deal over a relatively small wavelength range, any deviation in the sensitivity of our specific spectrometer from the nominal sensitivity published by the manufacturer is likely to lead to significant errors in the relative intensities of nearby vibrational bands. For this reason, it was decided that the best chance of extracting reliable temperature information from the emission spectra would be attained if the $\Delta\nu = \nu' - \nu'' = 3$ vibrational bands of the first positive system (between 610 and 700 nm) were used for fitting with the PGOPHER simulation from Western *et al.*[247]. Before such fitting could be carried out, it was observed that several vibrational bands that were predicted by the modelling of Western *et al.* were absent from the emission spectra of the plasma. This was most obvious in the $\Delta\nu = 4$ and $\Delta\nu = 5$ progressions, the data for which is shown, along with an (approximate) fit to the simulation of Western *et al.* in figure 8.1.

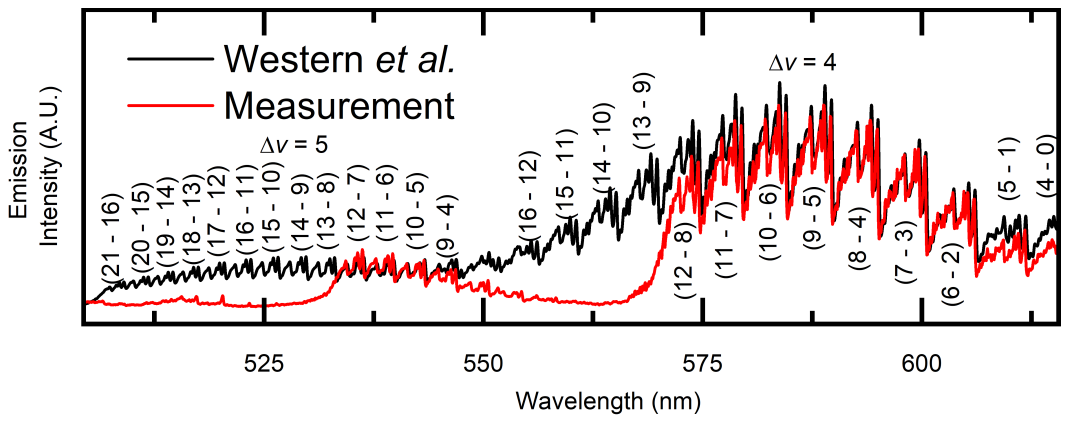

Figure 8.1: A comparison of the emission spectrum of the 500 W, 100 mTorr nitrogen plasma with an approximate fit using the simulation of Western *et al.*[247]. The comparison shows clearly that emission is not observed from vibrational states higher than $v = 12$ and this can be attributed to predissociation of these states.

In fact, no emission is observed from vibration states higher than $N_2(B^3\Pi_g, v = 12)$. The only possible explanation for such a discrepancy is that there is some rapid loss process for vibrational states with $v > 12$ such that the quantum yield for emission is very small for these states. Although reactions can have rates that are vibrational state dependent, it would not be expected that a normal collisional reaction would show such a strong dependence to explain the sharp decrease in emission seen here. Instead, previous work on the electronic structure of the nitrogen molecule has found that, provided it has sufficient energy, $N_2(B^3\Pi_g)$ is able to cross to the loosely bound $N_2(A'^5\Sigma_g^+)$ state and subsequently form a pair of ground state $N(^4S)$ atoms. $N_2(B^3\Pi_g, v > 12)$ molecules are thus predissociated. Shibusawa and Funatsu[249] observed this effect but found that the molecules with $v \leq 12$ had a vibrational distribution that was approximately Boltzmann like, whilst Geisen *et al.*[250] were able to measure the rate constant for predissociation from several vibration levels. They found that predissociation was fastest for $v = 13$ (with a first order rate coefficient $\approx 3 \times 10^8$ s^{-1}) and got progressively slower as v increased, reaching a value of $\approx 10^7$ s^{-1} for $v = 18$. For the $\Delta\nu = 4$ progression Einstein A factors are all of the order of $10^3 - 10^4$ s^{-1} [248] and thus emission is vastly slower than the predissociative pathway in all cases. Thus, in fitting the emission bands in the hope of finding vibrational and rotational temperatures (for the $N_2(B^3\Pi_g)$ molecules with $v \leq 12$) it is reasonable to adjust the simulation of Western *et al.*[247] by simply removing those vibrational states whose emission is not observed. This is an extreme example of the principle detailed in section 7.2.2 whereby the vibrational energy distribution of an excited electronic state is not necessarily representative of the distribution of the ground state. With the removal of higher vibrational states, the simulation of Western *et al.*[247] can be fitted very well to the emission data.

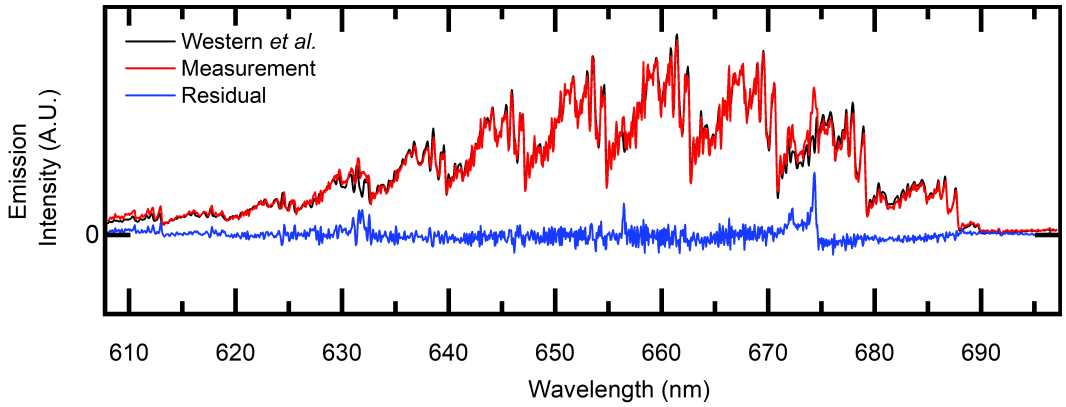

Figure 8.2: Contour fit to the experimental emission spectrum of the $\Delta\nu = 3$ progression of the first positive system utilising the spectral simulation of Western *et al.*[247] with vibrational states above $v = 12$ removed. The spectrum was taken at plasma power of 500 W and gas pressure of 100 mTorr. The residual (blue) shows the success of the fit.

An example fit to the $\Delta\nu = 3$ progression in the region $610 - 695$ nm is shown in figure 8.2 for a spectrum taken at 100 mTorr with 500 W power. For much of this region, the simulation and the experimental spectrum are coincident and the residual is thus largely a flat line. The few features that appear in the residual (at 630, 655 and 676 nm) are all due to species other than $N_2(B^3\Pi_g)$.

The rotational and vibrational temperatures that result from the fits are shown in figures 8.3a and 8.3b, respectively. 8.3a shows clearly a rise in rotational temperature from ambient at low powers to $800 - 1200$ K in the high power H-mode (500 W). It also shows higher rotational temperatures for higher pressures in the H-mode. Meanwhile, T_{vib} also shows a marked increase with power and again, in general, higher pressures show higher vibrational temperatures in the H-mode. Notably, the vibrational temperature of the emitting $N_2(B^3\Pi_g)$ state is hot (> 3000 K) even at powers as low as 10 W. It also shows a step-like increase at each pressure indicative of the E-H mode switchover. The switchover power is observed to increase with pressure from $25 - 100$ W at 10 mTorr to $150 - 250$ W at 100 mTorr.

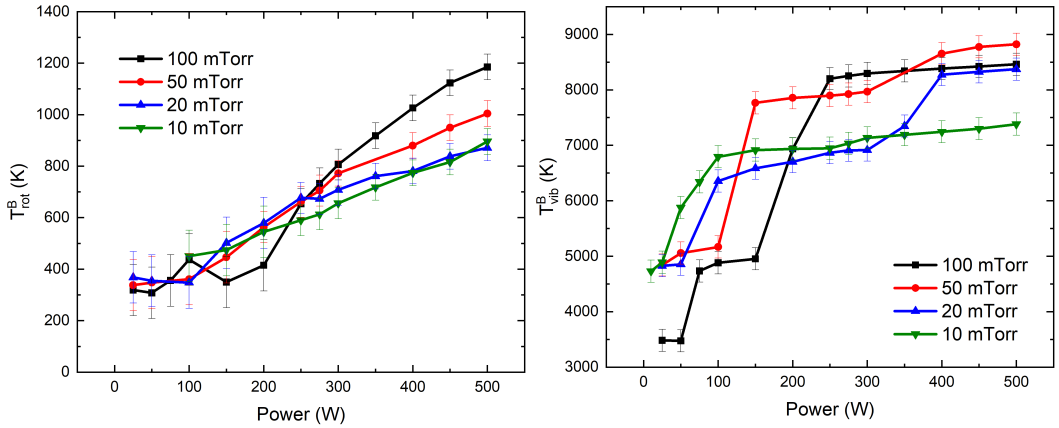

(a) **(b)**

Figure 8.3: (a) Rotational temperatures and (b) vibrational temperatures of $N_2(B^3\Pi_g)$ found by fitting the plasma emission spectra of the first positive system as a function of plasma power and pressure.

Additional confidence in the vibrational temperatures, found using this fit, is provided by the fact that fitting the $\Delta\nu = 4$ and $\Delta\nu = 5$ bands yields values that differ by less than 5% from the $\Delta\nu = 3$ band value. Rotational temperatures, meanwhile, have significantly larger relative uncertainties, this is because each vibrational band consists of 27 partially overlapping rotational branches (see figure 2.10) and the spectrometer resolution is too low to resolve these many rotational lines. As a result, it is found that the goodness of fit of the PGOPHER simulation to the data is insensitive to the rotational temperature such that the errors in these temperatures are significant (typically ±100 K from testing the reproducibility of fitting). Rotational temperatures are particularly uncertain at low powers, where the emission signal is smallest and the rotational structure becomes difficult to discern from the noise.

8.2.1 Discussion

Emission measurements demonstrate first and foremost that, for all the conditions investigated here, the nitrogen plasma shows significant disequilibrium between vibrational and rotational degrees of freedom, with vibrational temperatures being approximately an order of magnitude greater than the rotational temperatures. This high degree of vibrational excitation is expected for nitrogen plasma due to the shape resonance already mentioned and because electron impact excitation from ground state molecules forms excited states in a range of vibrational levels. The rotational temperatures are certainly within the expected range based on previous measurements in nitrogen plasma[181,189,190,251,252]; however, they are somewhat higher than

the previous measurements made by absorption on the first positive system in the same chamber (around 600 K at 10 mTorr and 500 W). This difference could be for a couple of reasons. First, as observed for O_2 plasma, emission measurements tend to be weighted towards hot regions of the plasma and thus give an upper bound on the average temperature in the chamber. Secondly, the previous measurements were made over a decade ago and in the intervening years the chamber has been used extensively for work involving oxygen plasma and has had its internal surfaces cleaned, both of which could have altered the chamber's thermal accommodation coefficient and thus altered the rotational temperature of the plasma. The observed increase in rotational temperature with increasing pressure has been observed before[189,251] and is quite straightforward to explain in terms of the increasing collision frequency that accompanies a rise in pressure. As collisions become more frequent, the opportunities for energy to be transferred from electrons, and highly excited vibrational degrees of freedom into rotations and translations also become more frequent. In this way, rotational and translational heating becomes more efficient at higher pressures.

Vibrational temperatures too are well within the realms of the expected values for nitrogen plasmas, measured previously using emission on the first[190,249,251–253] and second positive[26,189,193,251,254] systems. Once again, however, they significantly exceed the values measured by absorption previously in the same chamber (2900 K at 100 W and 3700 K at 300 W for a 25 mTorr plasma). This is, most probably, due to the fact that previous measurements probed the vibrational temperature of the metastable $N_2(A^3\Sigma_u^+)$, which is likely to be equilibrated with ground state molecules. The emission measurements here instead measure the vibrational temperature of the short lived $N_2(B^3\Pi_g)$ state. As discussed previously and modelled by Dilecce *et al.*[192], the vibrational temperature for radiative excited states can be significantly higher than those of the ground state and is determined by the kinetics of production and loss of the individual vibrational states. Indeed, one previous measurement on this chamber[255] of the second positive system determined a vibrational temperature for the $N_2(C^3\Pi_u)$ state, finding values of 7700 ± 600K for powers between 200 and 400 W and pressure of 10 mTorr. This temperature also significantly exceeds the temperature of the $N_2(A^3\Sigma_u^+)$ state, but is comparable to that measured for the $N_2(B^3\Pi_g)$ state here. The fact that vibrational temperature in the H-mode appears to go through a maximum value at around 50 mTorr has been observed previously in an ICP by Kang*et al.*[254]. They attributed this observation to the changing rates of vibrational excitation as electron temperatures and densities change with pressure. In reality, the full explanation will be more complex because the main source of vibrationally

excited $N_2(B^3\Pi_g)$ molecules is not vibrational excitation from $N_2(B^3\Pi_g, v = 0)$, but electronic excitation from the ground state (during the course of which vibrational state distributions in the ground state are not reproduced in the excited state). As pressure changes, not only will the vibrational distribution of the ground state change, but so will the electron temperatures and densities, thus a more complete collision radiative model would be required to fully understand the dependence of vibrational temperature of $N_2(B^3\Pi_g)$ on pressure.

The powers at which E/H switchover occurs are consistent with previous measurements (made by monitoring the reflected power as applied power was increased[241]). The switchover power shows a clear increase with gas pressure, and this too is consistent with previous observations in this chamber. This is in contrast to measurements on argon plasma in this chamber, where it was found that the switchover power decreased with gas pressure[241]. The explanation for this, given previously by Bakowski[64] and based on the work of El-Fayoumi[256], is that the current required to maintain the H-mode of the plasma goes through a minimum when the electron collision frequency for momentum transfer, ν, is equal to the angular frequency of the rf field, ω. ν depends on the pressure and the momentum transfer collision cross section for a given gas. Bakowski[64] found that, for argon, the momentum transfer cross section with electrons was small and in the pressure range $10 - 100$ mTorr $\nu < \omega$ thus as pressure (and hence ν) increased, the observed switchover power decreased as the system approached the minimum. For nitrogen the collision cross section is greater and thus at all pressures $10 - 100$ mTorr $\nu > \omega$, thus as pressure increases the system moves further from the minimum and the switchover power increases.

8.3 CRDS measurements of N_2^+

8.3.1 Effects of saturation on CRDS measurements

Optical saturation was introduced in chapter 2 of this thesis. So far it has not been an important effect because the transitions probed by CRDS in oxygen were forbidden and thus the pumping rate was insignificant. This is no longer the case for the transitions probed in this chapter. As discussed at the end of chapter 2, some of the transitions between low lying states of N_2 and N_2^+ are fully allowed, which means that saturation of these transitions occurs inside the high finesse optical cavity used here. The treatment of saturation given previously (section 2.6.2) relied on knowledge of the saturation parameter, S, which depends on the rates of pumping and relaxation in the system being probed. Both of these rates are difficult to calculate and depend

on several variables that are often poorly known (for example collisional quenching rates). An additional complicating factor from the stand point of utilising CRDS when there is saturation is the fact that the pumping rate varies as a function of intracavity power and thus the saturation parameter, S, varies during the course of a ringdown event. This means that, when the laser is tuned onto an optical transition, the beginning of the ringdown event is characterised by a high intracavity power, a correspondingly large S, and the absorption coefficient will be small (equation 2.54). On the other hand, towards the end of ringdown trace, the intracavity field will be smaller, S will likewise be small and the absorption coefficient will tend towards the larger value that would be observed if there was no saturation. With different parts of the ringdown trace being characterised by different absorption coefficients, it is unsurprising that the decay in intracavity intensity is no longer described by equation 2.38 and is no longer exponential. The decay is instead governed by:

$$\frac{\mathrm{d}I(t)}{\mathrm{d}t} = -\frac{I(t)}{\tau_0} - \frac{2c\alpha_0(\nu)I(t)}{1+\sqrt{1+\frac{I(t)}{I_{sat}}}} \tag{8.1}$$

where I_{sat} is the saturation intensity (a constant which depends on the strength of the transition) and is defined such that $I(t)/I_{sat}$ is equal to the saturation parameter $S(t)$ at a time, t, during the ringdown event. The intracavity intensity is directly proportional to the size of the detected signal with a proportionality constant that depends on the reflectivity of the cavity mirrors, the sensitivity of the detection system, and the gain of the amplifier that is used.

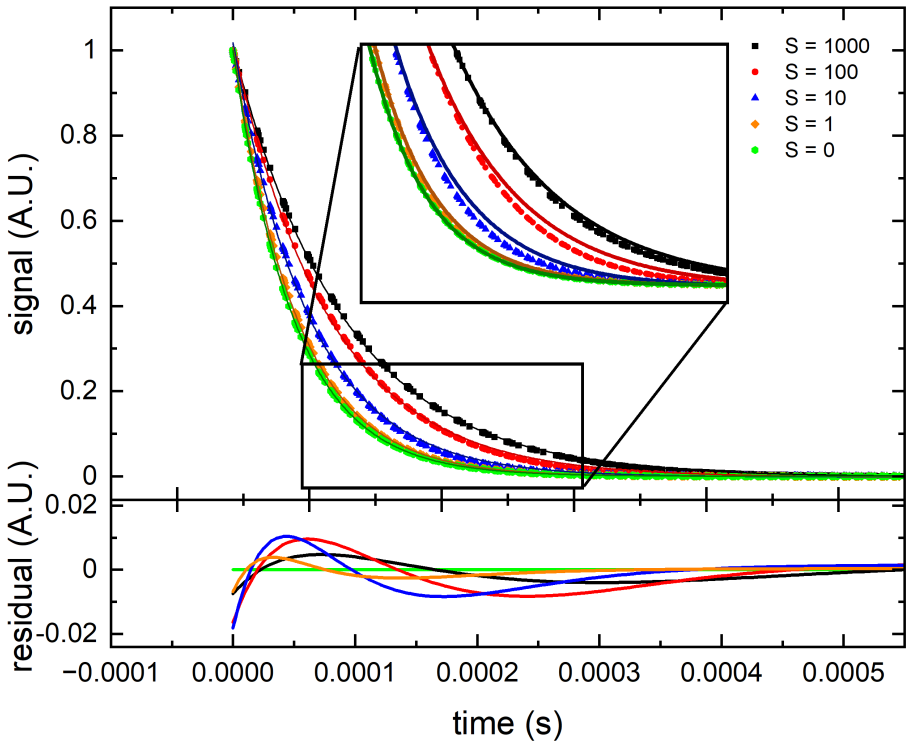

Figure 8.4: Numerical simulations of the non-exponential ringdown traces expected in a saturated CRDS experiments (here $S \equiv S(t=0) = I(t=0)/I_{sat}$). The simulations (shown by the points) are fitted with exponential decays (shown by lines) in order to demonstrate the deviation from exponential behaviour. The residual plots show how the deviation from exponential behaviour is most significant for intermediate saturation parameters ($S \approx 10 - 100$).

Equation 8.1 cannot be solved analytically, but numerical solutions can be calculated. The lack of analytical solutions makes the fitting of saturated ringdown traces on the fly computationally difficult, and hence real time extraction of unsaturated absorption coefficients ($\alpha(\nu)$) and saturation parameters is not easily possible. Instead the saturated ringdown traces are fitted with an exponential, this exponential will return a ringdown time concomitant with some sort of average degree of saturation during the course of the ringdown event, and hence the spectrum that results should be close in form to those shown in section 2.6.2 with an averaged saturation parameter. Some non-exponential ringdown events (simulated using mathematica according to equation 8.1) are shown in figure 8.4 along with exponential fits and residuals for a range of S values from $0 - 1000$. The possible error that fitting with an exponential introduces is discussed in section 8.3.3.

8.3.2 Finding saturation parameters experimentally

Provided the optical pumping rate and loss rate of the excited species (both emission and collisional) are known, then the saturation parameter for a given transition can be calculated theoretically. The rates of these processes are often difficult to measure and thus any calculated saturation parameter is likely to be approximate. The experimental determination of saturation parameters is certainly preferable in this case and can be achieved relatively straightforwardly.

The saturation parameter at the beginning of a ringdown event, $S(t = 0)$, depends on the intracavity intensity that is allowed to build up before the AOM is switched off and the ringdown trace recorded. This intensity can be carefully controlled by manipulation of the ringdown acquisition system, either by adjusting the trigger voltage at which the acquisition takes place or by changing the sensitivity of the detection set up. If, for example, the detection set-up were to become an order of magnitude more sensitive to laser intensity exiting the cavity, then an order of magnitude fewer photons would have to build up before a ringdown was triggered. This would mean that the saturation parameter at the beginning of the ringdown, $S(t = 0)$, would be reduced by an order of magnitude. This change in detection sensitivity is most easily achieved by changing the gain of the transimpedance amplifier that forms part of the acquisition arrangement (whilst also leaving the trigger level and the voltage applied to the photomultiplier unchanged). Figure 8.5 shows three spectra (found using equation 2.40) of the $P_{22}(7.5)$ rovibrational line of the (2, 0) band of the N_2^+ Meinel system each taken with exponential fits to the ringdown traces and a different transimpedance amplifier gain. These spectra were all taken with identical plasma conditions (10 mTorr of pure nitrogen and 400 W of power) and show clear indications of the changing saturation parameter both in their changing absorption coefficients and the appearance of Lamb dips. At the highest level of gain (10^7 V A^{-1}) the ringdown system is triggered by very small intracavity intensities and thus it becomes more difficult to achieve the desired discrimination between different TEM modes. The amplification also leads to a poorer signal to noise ratio on the ringdown traces and these two factors combined result in the greater scatter of the points for the least saturated (10^7 V A^{-1}) spectrum.

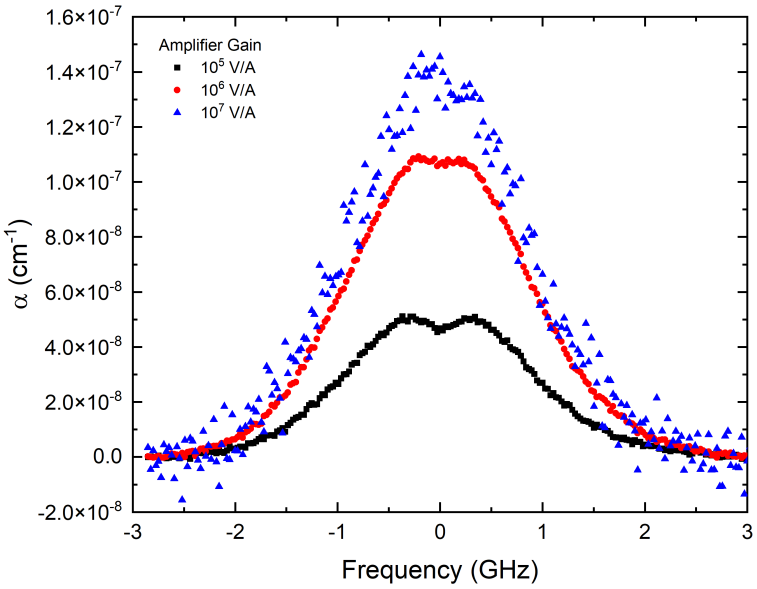

Figure 8.5: Three CRDS spectra of the $P_{22}(7.5)$ rovibrational line of the (2, 0) band of the N_2^+ Meinel system, taken with identical plasma conditions (10 mTorr 400 W) but varying the gain of the transimpedance amplifier. The changing gain alters the degree of saturation and leads to the expected reduction in absorption coefficient and the appearance of Lamb dips. The ringdown traced are fitted with exponentials during this experiment.

The utility of these measurements is that comparing the spectra allows the direct determination of saturation parameters without the need to calculate the rates of pumping or relaxation. Consider two spectra, with saturated absorption coefficients $\alpha_{S,1}(\nu)$ and $\alpha_{S,2}(\nu)$, whose ratio is $\xi = \alpha_{S,1}(\nu)/\alpha_{S,2}(\nu)$ and saturation parameters S_1 and S_2, whose ratio is $\eta = S_1/S_2$ (recall that, other than the Lamb dip, the saturation parameter is conserved across an inhomogeneously broadened line). Equation 2.54 will hold for both spectra, hence:

$$\alpha_{S,1}(\nu) = \frac{\alpha_0(\nu)}{\sqrt{1+S_1}} \quad \text{and} \quad \alpha_{S,2}(\nu) = \frac{\alpha_0(\nu)}{\sqrt{1+S_2}}. \tag{8.2}$$

Taking the ratio of equations 8.2 yields

$$\frac{\alpha_{S,1}}{\alpha_{S,2}} = \sqrt{\frac{1+S_2}{1+S_1}}, \tag{8.3}$$

which can be rearranged to give

$$S_2 = \frac{\xi^2 - 1}{1 - \eta\xi^2} \tag{8.4}$$

In the spectra in figure 8.5, if the spectrum with 10^6 VA^{-1} of amplification has saturation parameter S_1 and the spectrum with 10^5 VA^{-1} amplification has saturation parameter S_2 (which is 10 times larger than S_1), then $\eta = 0.1$ and saturation parameters can be found simply by taking the ratio of the absorption coefficients, ξ, and inserting these into equation 8.4. The saturation parameters found in this way using the data from the two most saturated spectra in figure 8.5 (10^5 and 10^6 VA^{-1} gain) are shown in figure 8.6 with a Lorentzian fitting. The scatter on the points is very large in the wings because the ratio of the absorption coefficients is dominated by noise when there is little or no absorption.

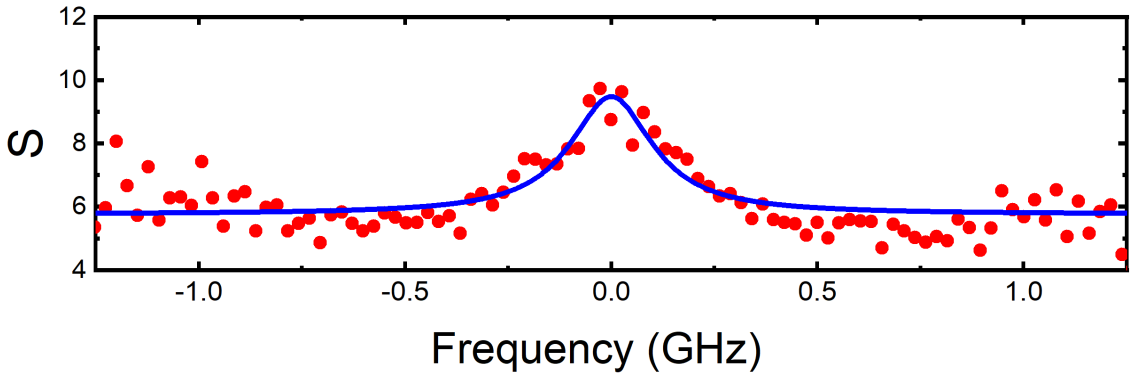

Figure 8.6: Saturation parameters calculated as a function of frequency using the ratio of the data from figure 8.5 and equation 8.4.

The validity of this method for determining saturation parameters is demonstrated by the fact that the saturation parameter is constant across most of the absorption profile (with $S = 5.6 \pm 0.2$ for the most saturated case) but approximately doubles over the Lamb dip (where both counter propagating beams within the cavity can interact with the same velocity group), as expected for an inhomogeneously broadened saturated absorption profile. A further demonstration of the success of this technique in finding saturation parameters is shown in figure 8.7, which depicts the same three spectra as figure 8.5 each adjusted by a factor of $\sqrt{1+S}$ in order to reproduce the unsaturated spectrum.

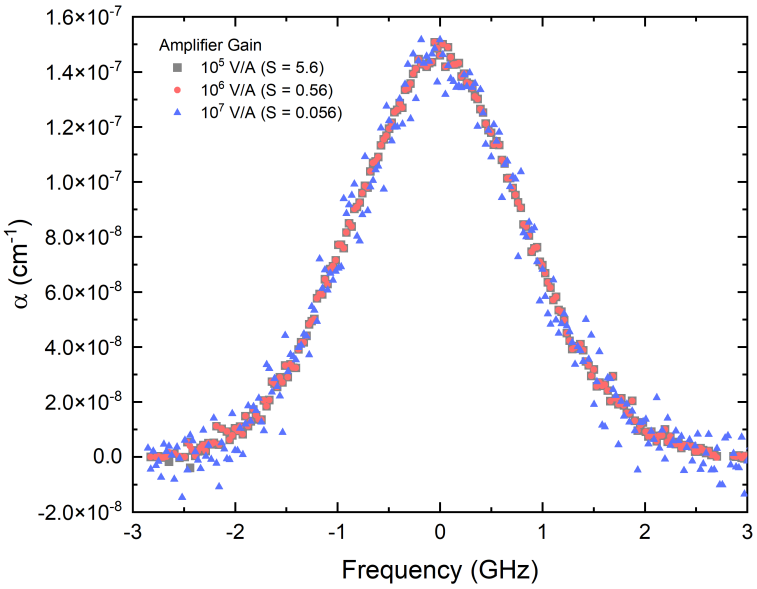

Figure 8.7: The three spectra from figure 8.5 each scaled according to equation 2.54 using the appropriate saturation parameters in order to infer the unsaturated spectrum. The good agreement between the three inferred spectra is indicative of the validity of the method described above used to find saturation parameters.

S is taken or inferred point by point from figure 8.6 and (away from the Lamb dips) is ≈ 5.6, 0.56 and 0.056 for the three spectra. The two most saturated spectra are bound to produce unsaturated spectra that concur, because of the method used to derive saturation parameters. However, the fact that they also find good agreement with the third, least saturated spectrum is a good indication that the saturation parameters found by this method are robust. In an ideal world, one might choose to operate in the unsaturated regime by increasing the amplifier gain further, however, as is demonstrated by the scatter on the least saturated spectrum in figures 8.5 and 8.7, when the gain is high, the signals required to trigger a ringdown event are so small that the signal to noise ratio of the ringdown trace becomes prohibitively poor. For this reason, it was decided that measuring saturated spectra and inferring the unsaturated values using experimentally determined saturation parameters was preferable, particularly when absorption signals are small (for example at low powers and in plasma sheaths).

8.3.3 The effects of fitting with an exponential

The decision to fit non-exponential ringdown traces with an exponential function necessarily introduces error into the results. Although this method has been used by

several workers[257,258] before, and the experiments in the previous section suggest that exponential fitting does not prevent accurate determination of unsaturated spectra, it is nonetheless important to explore the magnitude of the error that arises from exponential fitting. In particular, the question arises, based on the treatment of the experimental data in the previous section, if $S(t = 0)$ is changed by a factor of 10 (*e.g.* by altering the amplifier gain), is the average saturation parameter, S_{avg}, found by exponential fitting, also changed by a factor of 10? And, if not, how much influence does this have on the certainty with which saturation parameters and unsaturated spectra can be determined?

The theoretical treatment begins from equation 8.1. A series of simulations were carried out using this equation and each was fitted to determine an exponential best fit. Each simulated curve can be defined by three parameters: the empty cavity ringdown time, τ_0, chosen here as 100 μs for convenience; the ringdown time with an absorber present but assuming there is no saturation, τ, here given the value 50 μs (τ is related to the unsaturated absorption coefficient α_0 by equation 2.40); and the saturation parameter at the beginning of the ringdown event, $S(t = 0) = \frac{I(t=0)}{I_{sat}}$, which is varied across the simulations (for convenience, the boundary condition $I(t = 0) = 1$ is also imposed).

From the exponential fitting of each ringdown trace an effective absorption coefficient, α_{exp}, can be calculated using equation 2.40. This should correspond to the average absorption coefficient during the course of a given ringdown event and should therefore be close to α_0 when $S(t = 0)$ is small and close to 0 when $S(t = 0)$ is big (because in a very saturated medium there is effectively no absorption).

The interpretation of data fitted with an exponential function relies on the idea that the fitting will give an absorption coefficient that is well described by an "average" saturation parameter (where the averaging occurs over the course of a ringdown event). Given that only numerical solutions to equation 8.1 can be produced, the exact meaning of the "average" saturation parameter and how its meaning might vary with $S(t = 0)$ (which is experimentally controllable) is difficult to determine. The simplest situation would be the one that was assumed to be true in the previous section, in which $S(t = 0)$ and S_{avg} are proportional to one another. If this is the case then $S_{avg} \approx kS(t = 0)$ and from equation 2.58

$$\alpha_{exp} = \frac{\alpha_0}{\sqrt{1 + S_{avg}}} \approx \frac{\alpha_0}{\sqrt{1 + kS(t = 0)}}, \tag{8.5}$$

where $\alpha_0 = 3.34 \times 10^{-7}$ cm^{-1} for the modelled τ_0 and τ values. Assuming this simplest case holds then a plot of the absorption coefficient derived from exponential fitting,

α_{exp}, against the parameter $S(t = 0)$ should yield a curve that is well described by equation 8.5 and a fitting procedure should yield the optimum value of the proportionality constant k and indicate the degree of error introduced by the assumption that this simplest case holds.

Figure 8.8 shows the ringdown times derived from exponential fitting to ringdown traces with different initial saturation parameters (square black points). The ringdown times vary exactly as expected, looking unsaturated when $S(t = 0)$ is small (and thus returning a $\tau = 50\mu$s) and trending towards $\tau_0 = 100\mu$s when the saturation becomes large. Also shown in the figure are the absorption coefficients derived from exponential fitting (circular red points). These are fitted according to equation 8.5 with α_0 fixed and k allowed to vary. The optimum value of k is 0.165 (i.e. on average S_{avg} is 16.5% of $S(t = 0)$), the fit is shown by the red line in figure 8.8.

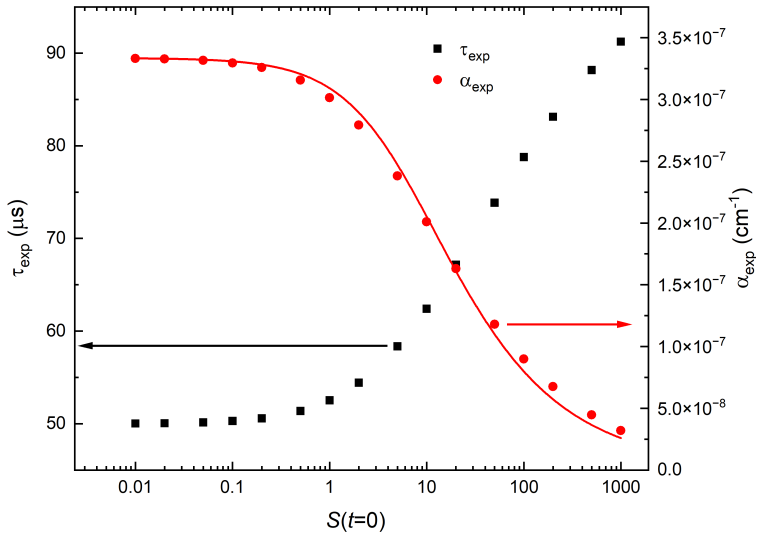

Figure 8.8: The effective ringdown time (black points) found when a saturated ringdown trace is fitted with an exponential fit. The ringdown time without absorption is set to 100 μs and with absorption (but with no saturation) is set to 50 μs. Also shown are the absorption coefficients (red points) derived from the exponential ringdown times showing clearly that saturations leads to a reduction in absorption coefficient. The red points are fitted according to equation 8.5 and the success of this fit indicates that fitting the saturated ringdown traces with an exponential function introduces only a small error.

The specific value of k is of minor importance compared to the conclusion that the process of fitting a non-exponential ringdown trace with an exponential function and

the simple interpretation of such fittings in order to find absorption coefficients only introduces less than 5% error for all values of $S(t = 0) < 50$. Additionally, because doubling $S(t = 0)$ makes very little difference to the deviation of the exponentially fitted absorption coefficients from the model (equation 8.5) the process of exponential fitting also conserves the shapes of Lamb dips (to within $\approx 5\%$). Finally, because the saturation coefficient is invariant with frequency (for inhomogeneously broadened transitions and ignoring Lamb dips) the Doppler width of the line as a whole is unaffected by saturation and also unaffected by the exponential fitting.

The fact the fit is not perfect is a result of the relationship between $S(t = 0)$ and S_{avg} not being as simple as assumed (in reality the ratio $S_{avg}/S(t = 0)$ decreases as $S(t = 0)$ becomes larger rather than being constant). Values of S_{avg} calculated using the equality in equation 8.5 are shown in figure 8.9, also shown are the values approximated using $S_{avg} = kS(t = 0)$ with $k = 0.165$.

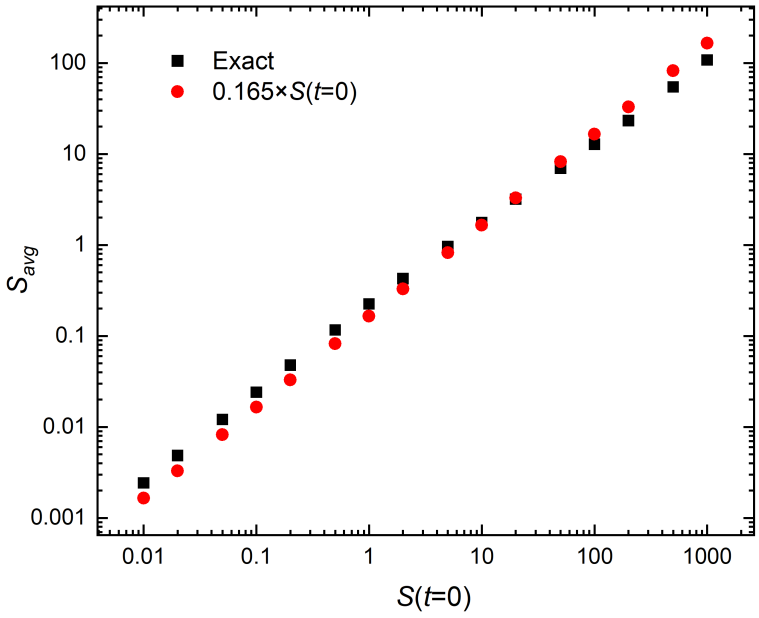

Figure 8.9: A comparison of the average saturation parameter, S_{avg}, during the course of the ringdown (which is the saturation parameter found by exponential fitting) against the saturation parameter at the beginning of the ringdown event (which can be controlled by changing the amplifier gain). The black points are found using the red points from figure 8.8 whilst the red points in this figure originate from the red line of best fit from figure 8.8.

It should be noted that the error introduced in the value of S_{avg} if it is calculated according to the approximation are significantly larger (as much as 40%) than the

errors in the absorption coefficient. This additional error arises due to the square root in equation 8.5 and because, for small saturation parameters, $\sqrt{1+S_{avg}} \approx 1$ and the $\approx 40\%$ error in S_{avg} has little influence on the absorption coefficient. Thus, both an experimental and theoretical examination of the exponential fitting process shows that consistent and meaningful saturation parameters can be found and unsaturated spectra can be deduced with reasonable confidence. This means that, as for the unsaturated case, densities and translational temperatures can be found using saturated CRDS with exponential fitting.

8.4 N_2^+ temperatures and densities

Fitting Gaussian profiles to the data in figure 8.7 (as depicted in figure 8.10) allows the determination of both temperatures and densities. By fitting each of the three spectra it was verified that Doppler widths are unaffected by saturation, as expected from the theory of optical saturation (section 2.6.2). The temperatures calculated from fits to the three spectra varied by less than 2% and indicate a value of 1475 ± 40 K for N_2^+ at 10 mTorr and 400 W.

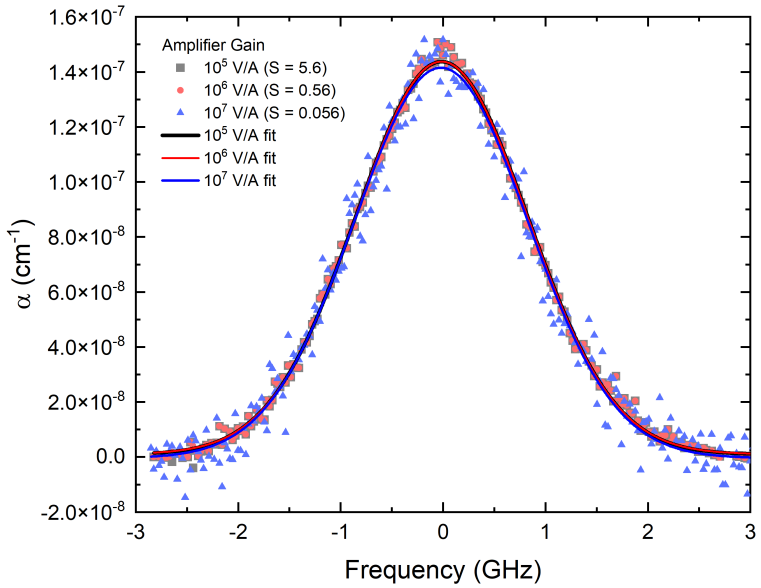

Figure 8.10: The three inferred unsaturated spectra from figure 8.7 fitted with Gaussian lineshape profiles.

These temperatures were used in conjunction with the previously mentioned PGOPHER simulation of the (2, 0) band of the Meinel system in order to find cross

sections. The cross sections produced by PGOPHER return the population in the vibrational state rather than the specific rotational level being probed. To do this PGOPHER uses a rotational temperature which is assumed here to be in equilibrium with the translational temperature indicated by the width of the fitted Doppler profiles. At 1474 K the relevant cross sections for the $P_{22}(7.5)$ transition is found to be 1.65×10^{-18} cm^2 cm^{-1} whilst the areas beneath the Gaussian curves are found to vary by less than 0.5 % and give an average value of $\alpha_{int} = 1.002 \times 10^{-8}$ cm^{-2} (note the conversion of GHz to wavenumbers). For N_2^+ wall loss in the baffle arms is expected to be extremely fast, both due to the acceleration of the ions towards the walls through the sheath and because the wall loss coefficient for ions is generally unity. For this reason it can be assumed that ions do not penetrate into the baffle arms and thus a length adjustment factor of 77/35 is appropriate in this case. The line of sight average number density of $N_2^+(X^2\Sigma_g^+, v = 0)$ is therefore $(1.3 \pm 0.1) \times 10^{10}$ cm^{-3}. The main source of uncertainty in this value is the fitting of the baseline ringdown time across the spectrum. It is found in nitrogen plasma that this baseline value changes significantly more than in oxygen plasma. When the plasma is running the baseline ringdown time decreases by 10s of μs over the course of a day (from ≈ 80 to as low as 30 μs). The cause of this change is yet to be unambiguously identified but it is always found that the ringdown time recovers to $\approx 80\mu$s after several hours without plasma. It is possible that some of the effect is due to the mirrors becoming heated (this would explain why the effect is bigger in the hotter nitrogen plasma than in the cooler oxygen plasma) or due to some temporary surface modification which might influence the mirror reflectivity.

The small size of the absorption in the saturated regime means that several hundred ringdowns must be averaged at each wavelength, and the desire to observe the Lamb dip requires that several hundred wavelengths are probed in the course of one spectrum. This leads to experimental times of the order of 1-2 hours and thus the baseline ringdown time can change considerably (and non-linearly) during the course of one spectral measurement. This baseline can prove rather challenging to fit and can lead to uncertainty up to 10% on the resulting spectral integrated areas (the uncertainty in the width and therefore temperature is found to be less significant)

8.4.1 Variation with power and pressure

CRD spectra were obtained at powers of 200, 300 and 400 W and pressures of 10, 50 and 100 mTorr with the amplifier set to the lowest (and hence most saturated) of the

settings discussed in the previous section. The resulting spectra are shown in figure 8.11.

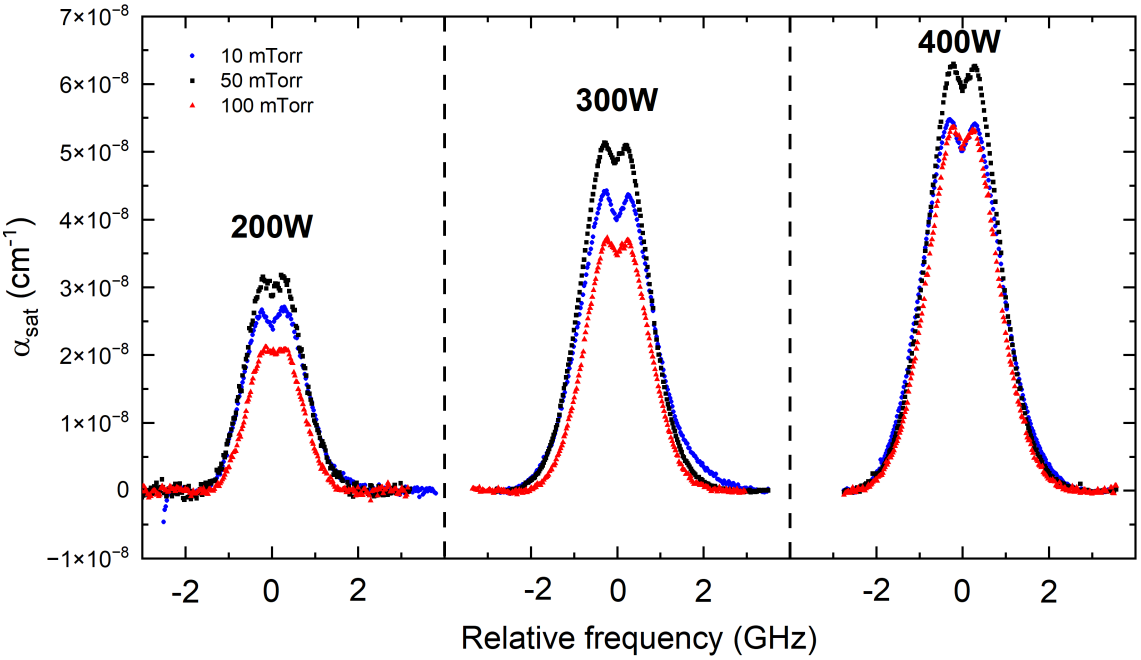

Figure 8.11: Saturated CRD spectra of the $P_{22}(7.5)$ rovibrational line of the (2, 0) band of the N_2^+ Meinel system as a function of plasma power and pressure.

Temperatures

Translational temperatures were obtained directly by fitting the data (excluding the Lamb dips) with a Gaussian function. The resulting translational temperatures are shown in figure 8.12. The translational temperatures show the expected increase with increasing plasma power as observed in the emission data and are also quite consistent with previous measurements of T_{rot} and T_{trans} of N_2^+. For example Gherman *et al.*[246] found ion temperatures of 1300 ± 100 K in a 300 W microwave discharge at 3.3 Torr using broadband-CEAS and Tuszewski[259] found values of around 1000 K in a 10 mTorr ICP operating at 0.46 MHz and also observed an increase of several hundred Kelvin as power increased from 200 to 900 W by measurement of the emission on the first negative system. Den Hartog *et al.*[213] also observed temperatures in excess of 1000 K by LIF on the first negative system downstream from an electron cyclotron resonance plasma operating at < 5 mTorr. Interestingly, the temperatures

measured here are considerably higher than the rotational and translational temperatures found by CEAS by Bakowski *et al.*[241] for $N_2(A^3\Sigma_u^+)$ in the same chamber (where the maximum was < 500 K even at 400 W).

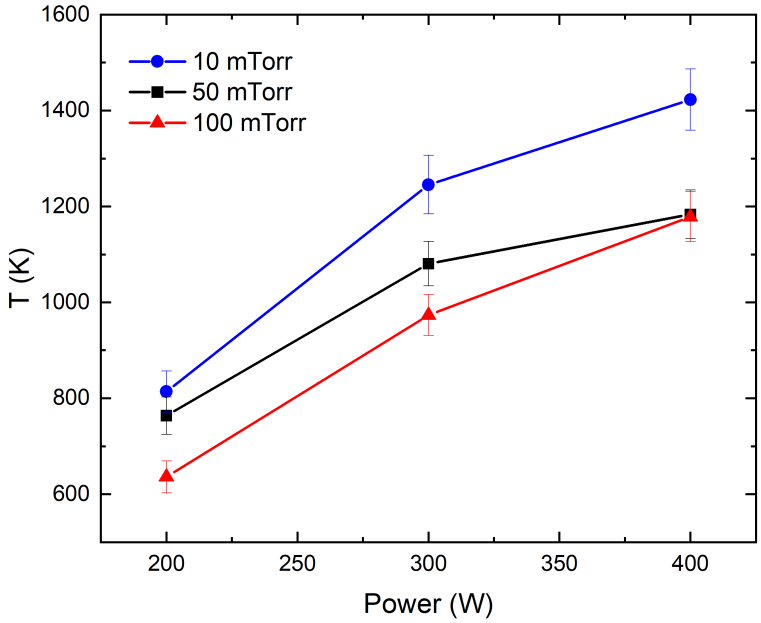

Figure 8.12: N_2^+ translational temperatures found by fitting the spectra in figure 8.11 with Gaussian lineshapes (and excluding the points on the Lamb dip).

Somewhat surprisingly the data shows a decrease in temperature as pressure increases, this in stark contrast to the rotational temperatures of $N_2(A^3\Sigma_u^+)$ (measured previously by Hancock *et al.*[153]) and $N_2(B^3\Pi_g)$ (measured by emission) which were found to increase slightly with increasing pressure but is in agreement with the observations of Den Hartog *et al.*[213] who observed a significant drop in ion temperature as pressure increased. Another surprising observation is that these line of sight averaged translational temperatures exceed the rotational temperatures measured by emission. As discussed at length for oxygen plasma, it would generally be expected that, because emission comes from the hottest parts of the plasma, emission derived temperatures should exceed those which are line of sight averaged. Possible explanations for this observation are given in the next section.

Densities

Number densities were obtained by use of the procedure described at the start of this section (section 8.4). The density of the vibrational ground state of the molecular ion in the plasma chamber, $[N_2^+(X^2\Sigma_g^+, v = 0)]$, is shown in figure 8.13.

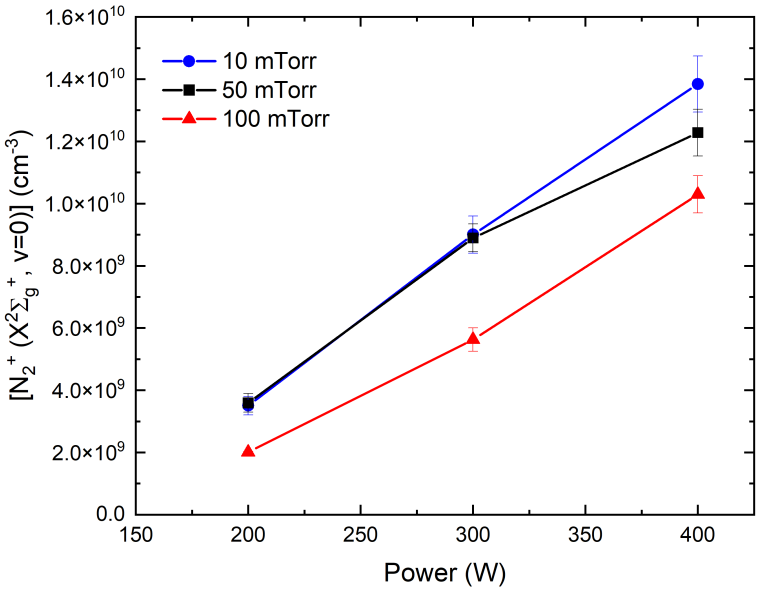

Figure 8.13: $N_2^+(X^2\Sigma_g^+, v = 0)$ densities found using the spectra in figure 8.11 and with cross sections calculated using PGOPHER and assuming that the rotational and translational temperatures of the cation are equilibrated.

It is desirable to quantify the degree of vibrational excitation of the cations (with vibrational temperature T_{vib}^{X+}) such that the total cation density can be calculated and the total electron density can be inferred. To do this spectroscopically would require the measurement of at least one (and preferably more than one) other vibrational bands of the Meinel system. Within the scanning range of the laser ($747 - 792$ nm) there are several possibilities: at the longer wavelength side of the (2, 0) band is the (8, 5) band, unfortunately the population of the $v'' = 5$ state proved too small for it to be observed in absorption. This provides some evidence that the vibrational temperature of $N_2^+(X^2\Sigma_g^+)$ is less than that of $N_2(B^3\Pi_g)$ or $N_2(C^3\Pi_u)$, because a simulation of the Meinel system with $T_{vib} = 8000$ K indicates that the (8, 5) band should be detectable. To shorter wavelengths of the (2, 0) Meinel band lie the (7, 4) and (6, 3) bands, these too are unfortunately unobservable (at $\approx$ 4000 K the stronger of the bands has a cross section around 3% of the (2, 0) band). The (7, 4) and (6, 3) bands of the Meinel system also overlap with the very strongly absorbing (2, 0) and (3, 1) bands of the first positive system which makes it very difficult to find any spectral window free from interference where a CRDS experiment might be attempted. The prime candidate for vibrational temperature measurement is the (3, 1) Meinel band, however its shortest wavelength band head occurs at 803 nm, still

too long for the laser to reach and thus a new laser would be needed to probe this band. Measurements on the (3, 1) band are a target for future investigations.

In the absence of the ability to measure the vibrational temperature an estimate is still possible. The inability to observe the (8, 5) band has already confirmed that $T_{vib}^{X+} < T_{vib}^{B}$. In fact the ion is sufficiently long lived that it can be reasonably assumed to be in vibrational equilibrium with the ground state molecules (*i.e.* $T_{vib}^{X} = T_{vib}^{X+}$). This was realised experimentally by Visser *et al.*[216] who observed that the change in ion temperatures upon extinction of a pulsed rf discharge (operating at 225 mTorr) was much slower than the rotational and vibrational relaxation rates expected for the ions. It was concluded that the ion temperatures were in fact following the cooling processes of the neutral molecules and were in equilibrium with them. In the discussion of the nitrogen emission data it was suggested that, because $N_2(A^3\Sigma_u^+)$ molecules are metastable they should be sufficiently long lived to reach vibrational equilibrium with ground state molecules. It is therefore reasonable to assume $T_{vib}^{A} = T_{vib}^{X} = T_{vib}^{X+}$ and therefore to assume that the vibrational temperatures of $N_2(A^3\Sigma_u^+)$, measured in this chamber previously[63,153], are a good estimate of the relevant temperatures for N_2^+, this was previously assumed by Hancock *et al.*[153]. This being the case the total number density of diatomic cations is given by

$$[N_2^+(X^2\Sigma_g^+)] = [N_2^+(X^2\Sigma_g^+, v = 0)]q_{vib}^0, \tag{8.6}$$

where q_{vib}^0 is the vibrational partition function of the cation (with energies taken relative to the ground vibrational state) and is calculated by a direct sum using the vibrational energy levels according to Shi *et al.*[260]. From Hancock *et al.*[153] a vibrational temperature of 3700 K is deemed reasonable for all the powers investigated here (the measured vibrational temperature shows only moderate changes with power and pressure for the conditions investigated here, a conclusion supported by the fact that the density ratio of the various vibrational states modelled by Thorsteinsson and Gudmundsson[261] varies little between 10 and 100 mTorr) and leads to $q_{vib}^0 \approx 1.77$. Thus total N_2^+ densities are expected to be approximately twice those shown in figure 8.13. The $v = 0$ ion densities in figure 8.13 show the expected increase with applied power and interesting behaviour with changing pressure; at high powers the ion density appears to decrease with increasing pressure whilst at lower powers the lower pressures appear to show similar ion densities whilst 100 mTorr still has the fewest ions. Whether this trend in $v = 0$ densities with pressure is reflected in the total ion densities could only be established by accurate measurement of the ionic vibrational temperature as a function of power and pressure, comparison with

previous measurements however can offer some insight into this observation as is now discussed.

8.4.2 Discussion

Temperature

As noted in section 8.4.1 the ion temperatures measured here are somewhat elevated compared to $N_2(A^3\Sigma_u^+)$ translational and rotational temperatures previously measured in the same chamber and particularly unusually they show the opposite trend with gas pressure. In order to verify the previously measured temperatures, further CRD spectra were taken, this time probing $N_2(A^3\Sigma_u^+)$ on the $Q_{11}(16)$ rotational line of the (7, 6) band of the first positive system at around 12721.94 cm^{-1}. This particular transition was chosen because it was conveniently close to the N_2^+ transition probed previously and free from interference from any Meinel band lines. Spectra of this transition as a function of power and pressure are shown in figure 8.14.

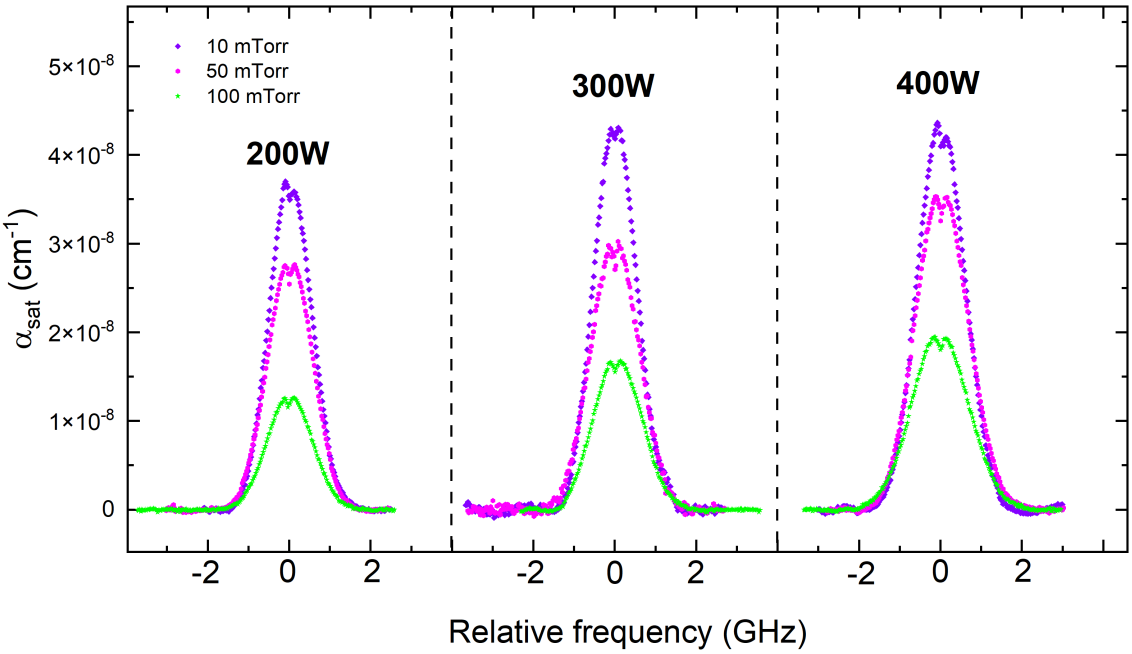

Figure 8.14: Saturated CRD spectra of the $Q_{11}(16)$ rotational line of the (7, 6) band of the first positive system of nitrogen.

It can be seen that these transitions are also optically saturated but in this case, because the primary aim of these measurement was to make temperature comparisons with the ions, it was decided not to go to the significant effort required to quantify the saturation parameter for this transition.

The Doppler temperatures that result from the spectra in figure 8.14 as well as those from figure 8.12 are shown in figure 8.15.

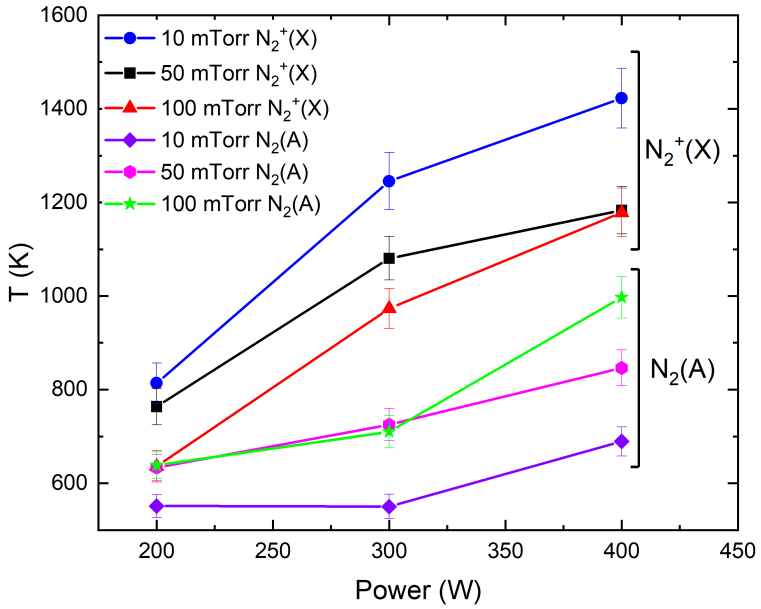

Figure 8.15: $N_2(A^3\Sigma_u^+, v = 6)$ translational temperatures found by fitting the the spectra in figure 8.14 with Gaussian lineshapes. Also shown is the data from figure 8.12 for comparison.

In comparison to the previous data of Thornton[63], measured by CEAS on the $Q_{12}(3)$ transition of the (3, 1) band, the temperatures are a little elevated (10 mTorr temperatures are typically around $100 - 150$ K higher than previously measured). Additionally, whereas the previous study suggested that the translational temperature changed little with gas pressure it can clearly be seen here that translational temperature actually increases with pressure exactly as was observed in the emission measurements but contrary to the observations of N_2^+ temperatures. This pressure variation of metastable temperature has been observed previously by Horikawa *et al.*[262] by CRDS in an ICP at 400 W and the temperatures measured in that work ($\approx$ 800 K at 20 mTorr and $\approx$ 1100 K at 100 mTorr) are in very good agreement with those observed here for comparable power and pressure regimes. The temperatures measured here are also rather similar to those measured for $N_2(B^3\Pi_g)$ by emission, probably because the $N_2(A^3\Sigma_u^+)$ state is quenched very efficiently at the chamber walls ($\gamma = 1$) and is thus largely confined to the central volume of the discharge where it is produced and where the majority of the plasma emission also originates.

From the data in figure 8.15 it is clear that there is a significant disparity between the apparent translational temperatures of the ions and the metastable neutrals in the plasma. This difference cannot be ascribed to plasma inhomogeneity because, if this were the cause, one would expect the temperatures between the different species would be most similar when the plasma is most uniform (*i.e.* at lower pressures). Instead it is seen that the temperature difference is biggest at low pressure and that the temperatures begin to converge as pressure is increased. This is by no means the first occasion on which ions have been observed to be hotter than the neutral species in the same plasma (indeed in some ICP models in oxygen the ion temperature is assumed to be twice that of the neutral species[91,149]). Foissac *et al.*[239,240,246] observed rotational temperatures for the two species in a flowing microwave discharge (433 MHz) at 3.3 Torr using ICLAS and found $T_{rot}^{X+} = 1300 \pm 100$ K and $T_{rot}^{A} = 945 \pm 50$ K; Tuszewski[259] observed $T_{rot}^{X+} = 900 - 1200$ K and $T_{rot}^{A} = 400 - 600$ K in a 0.46 MHz ICP operating between $1-15$ mTorr and $200-900$ W; finally Huang *et al.*[263] made observation of the second positive and first negative systems in a dual frequency (41 MHz and 2 MHz) CCP and found $T_{rot}^{X+} = 450-550$ K and $T_{rot}^{A} = 350-400$ K for a range of low frequency powers ($0-50$ W) and 100 W of high frequency power at 38 mTorr. The first of these studies attributed the selective heating of the ions to the weak ambipolar microfield of the plasma whilst the latter two suggested that the selective heating of the ions in their respective plasmas were results of the relatively low frequency rf fields being used (0.46 and 2 MHz respectively). The plasma in this work has a driving frequency (13.56 MHz) and pressure (10-100 mTorr) intermediate between those used in the previous studies where a temperature difference was observed and it is thus entirely plausible that either mechanism of ionic heating could be the cause of the hot ions seen here. The trends with pressure can be straightforwardly understood in terms of the frequency of collisions, at low pressure the infrequent collisions result in the hot ions remaining hot and the neutral species being much cooler, whilst at high pressures the more frequent collisions allow the translational energy of ions and neutrals to approach equilibrium. Thus, at higher pressures, the ions are cooled as they transfer energy to the neutrals. The heating of the neutrals with increasing pressure cannot be attributed to the ions alone (because they are present in much lower density than the neutrals), instead increased collision frequency also increases the transfer of translational energy from electrons and from vibrational modes and these effects also contribute to the translational heating of neutral species at higher pressure. It should also be pointed out that the rf and ambipolar fields that are likely responsible for translationally heating the ions ought not to have a significant effect on the ionic

vibrational temperature. Thus the observation of different rotational temperatures for the ions and metastable molecules does not necessarily invalidate the assumption made previously that the two species have the same vibrational temperature.

Density

The ion densities measured here are broadly in line with the literature which generally suggests that ion and electron densities in low pressure nitrogen plasma ought to range from a few 10^9 to a few 10^{11} cm^{-3}. Woodcock *et al.*[210] found ion densities by LIF of 10^{10} cm^{-3} in a 20 mTorr 200 W CCP, Gherman *et al.*[246] found densities of 10^9 cm^{-3} by broadband-CEAS in their microwave discharge and Visser *et al.*[216] found densities of 10^{11} cm^{-3} in a 22 mTorr 300 W pulsed rf discharge again using LIF. In terms of densities in ICP plasma Zhu *et al.*[24,25,264] found that the electron density increased from 2×10^9 cm^{-3} at 100 W to 10^{10} cm^{-3} at 500 W in a 15 mTorr 13.56 MHz ICP, Song *et al.*[26] found a value of $\approx 10^{10}$ cm^{-3} in an ICP using a Langmuir probe and the modelling of Thorsteinsson and Gudmundsson[261] predicted densities of a few 10^{11} cm^{-3} for a 500 W ICP at a range of pressures ($1-100$ mTorr). The previous spectroscopic measurements of N_2^+ in the ICP chamber used here consist of a few low signal to noise CEAS spectra[153] which found total ion densities of $\approx 3\times10^9$ cm^{-3}; these measurements utilised rather uncertain Doppler temperatures in deriving the total density (the lower temperatures make a factor of ≈ 2 difference in the relevant absorption cross sections) and required modulation broadening from use of wavelength modulation spectroscopy to be accounted for. CEAS also relies on accurate knowledge of "average" mirror reflectivity, R, which is usually inferred from the ringdown time of a low order cavity mode. The higher order modes actually used for CEAS are inherently more lossy than the low order modes used to determine R, use of the R value associated with the low order cavity modes can thus lead to a systematic underestimation of the absorption coefficient which could explain why the previous CEAS derived ion densities are so much lower than those found here.

Measurements utilising a movable planar probe also exist[64] and return ion densities of $\approx 2\times10^{10}$ cm^{-3} at 10 mTorr and 400 W falling to $\approx 7\times10^9$ cm^{-3} at 100 mTorr; this is in remarkably good agreement with the present work given that the different probes used by Bakowski[64] would only typically be expected to give electron and ion densities within a factor of ≈ 2. The work by Thorsteinsson and Gudmundsson[261] and the probe measurements of Bakowski[64] both indicate that the ion concentration goes through a maximum as pressure is increased in a nitrogen ICP. The former suggests that at 500 W the maximum in N_2^+ concentration occurs at around 20 mTorr,

whilst the work of Bakowski suggests that the maximum occurs at around 20 mTorr when power is low (100 W) but moves towards lower pressure (closer to 10 mTorr) when power is higher (400 W). These observations, particularly those of Bakowski, are consistent with the measurements of $N_2^+(X^2\Sigma_g^+,\ v = 0)$ presented here (and assuming that any difference in vibrational temperatures at the different pressures is small enough not to significantly effect the variation of ion density with pressure seen in amongst the $v = 0$ molecules). At the lower powers (200 and 300 W) the maximum in ion density is expected to be at around 20 mTorr and thus the 10 and 50 mTorr ion densities sit either side of the maximum and are similar. At the higher power (400 W) the maximum in density is expected to occur closer to 10 mTorr and thus the density decreases monotonically between 10 and 100 mTorr. The reasons for the observed density trends are directly related to the fall in electron temperature that arises when pressure increases, this is discussed in depth in the following chapter.

8.5 Conclusions

This chapter has detailed the measurement, by saturated CRDS, of the molecular N_2^+ cation which represents the most important reservoir of positive charge in inductively coupled nitrogen discharges. The experiments have utilised the electric dipole allowed absorption of the Meinel system ($N_2^+(A^2\Pi_u) \leftarrow N_2^+(X^2\Sigma_g^+)$), specifically the $P_{22}(7.5)$ rotational line of the (2, 0) vibrational band selected for its relatively large absorption cross section and separation from rotational lines of the first positive nitrogen system ($N_2(B^3\Pi_g) \leftarrow N_2(A^3\Sigma_u^+)$). The influence of saturation on the ringdown signal has been carefully considered and accounted for by the experimental determination of saturation parameters and this enables the determination of absolute number densities and translational temperatures as a function of both plasma power and pressure. The results for ions were compared to both emission and CRDS measurements on the first positive system of nitrogen. The rotational temperature of the $N_2(B^3\Pi_g)$ state observed by emission varies from approximately ambient at powers < 100 W up to temperatures in excess of 1000 K at 500 W. These values are found to be slightly (≈ 200 K) higher than the translational temperature of $N_2(A^3\Sigma_u^+)$ measured by absorption but the two show very similar trends, increasing with both increasing plasma power and pressure. The difference can be accounted for, as it was for oxygen plasma, by the fact that CRDS is line of sight averaged whilst emission measurements are weighted towards the hotter central volume of the plasma and the

measurements favour the conclusion that the rotational and translational motion of molecules in these two electronic states are in equilibrium.

In contrast, the CRDS measurements show that the translational temperatures of $N_2^+(X^2\Sigma_g^+)$ exceed those of $N_2(A^3\Sigma_u^+)$ and that the difference in their temperatures is largest at low pressures. This difference is attributed to the acceleration of the ions by the electromagnetic fields present in the plasma and is largest at low pressure because of the lower frequency of momentum transfer collisions between ions and neutrals under these conditions. Previous measurements on nitrogen discharges have observed a similar effect in the rotational temperatures of ionic and neutral species[240,246]. The aforementioned emission measurements also enable the determination of vibrational temperatures for the $N_2(B^3\Pi_g)$ state, and it is found that, for vibrational states with $v \leq 12$, the vibrational distribution function (VDF) is given by a Maxwell-Boltzmann distribution with high vibrational temperatures (> 3000 K) even at 10 W of plasma power and temperatures as high as 9000 K at higher powers (500 W). These vibrational temperatures are somewhat higher than those measured in the same plasma chamber by Thornton[63] by absorption on the first positive system. This difference can be explained by the fact that absorption measures the vibrational temperature of $N_2(A^3\Sigma_u^+)$ whereas emission measures the vibrational temperature of $N_2(B^3\Pi_g)$. These values can be significantly different because the population of vibrational levels is determined by the balance of various kinetic processes and these vary for the different electronic states[192]. Interestingly, states with $v > 12$ are found to have very low populations due to the fact that they are predissociated. The predissociation arising because $N_2(B^3\Pi_g, v > 12)$ can cross rapidly to the loosely bound $N_2(A'^5\Sigma_g^+)$ state.

The measured $N_2^+(X^2\Sigma_g^+,\ v = 0)$ densities lie in the range $(2-4) \times 10^9$ cm^{-3} at 200 W and increase markedly to $(1.0-1.4) \times 10^{10}$ cm^{-3} at 400 W. At each power the ion density is found to decrease with increasing pressure and this is closely related to a fall in electron temperature that is expected to accompany an increase in gas pressure (*vide infra*).

Chapter 9

Volume averaged kinetic modelling of nitrogen plasma

In order to interpret the nitrogen measurements a zero dimensional (volume averaged) kinetic model was constructed. The model is largely based on the work of Thorsteinsson and Gudmundsson[261] with some simplifications and some updated or adjusted rate coefficients. The model includes the same neutral species as Gudmundsson, namely ($N_2(X^1\Sigma_g^+)$, $N_2(A^3\Sigma_u^+)$, $N(^4S)$, $N(^2D)$ and $N(^2P)$) but only includes the most important cation ($N_2^+(X^2\Sigma_g^+)$), excluding N^+, N_3^+ and N_4^+. Because the ICP system described here only operates at pressures $\leq$ 100 mTorr no termolecular reactions are included (they are slow at low pressure). The final key difference with the model of Gudmundsson is the way in which vibrational excitation is included. Gudmundsson includes the lowest 7 vibrational states of the $N_2(X^1\Sigma_g^+)$ molecules individually, effectively treating them as separate species; this approach has the advantage that it allows the modelling of vibrational dynamics but it increases the number of reactions in the reaction set by an order of magnitude (the model of Gudmundsson includes around 450 processes). The aim with the model presented here is to achieve quantitatively useful results with the minimal complexity in the reaction set. In order to reduce the complexity this model accounts for vibrational excitation in a more limited but significantly simpler way.

9.1 Modelling vibrational excitation

Most of the literature regarding the rates of electron impact dissociation, ionisation and electronic excitation only report the rate for the vibrational ground state. Thus it is often necessary to estimate the rate for vibrationally excited molecules and this is done by the process of threshold shifting discussed previously. Thus, if the rate coefficient of some electron impact process for molecules in the vibrational ground state,

k_0, is known, then the rate coefficient for some excited vibrational state undergoing the same process may be approximated as:

$$k_v = k_0 \exp\left(\frac{E_v}{T_e}\right), \tag{9.1}$$

where E_v is the energy of the excited vibrational state relative to the ground state ($E_0 = 0$) expressed in eV. It is then also possible to express the total rate of the electron impact process, ν_{tot}, when all vibrational states are taken into account as:

$$\nu_{tot} = [e^-] \sum_{v=0}^{\infty} k_v[v] = k_0[e^-] \sum_{v=0}^{\infty} [v] \exp\left(\frac{E_v}{T_e}\right). \tag{9.2}$$

Working on the assumption that the vibrational energy levels follow a Boltzmann population distribution described by temperature T_v (expressed here for consistency in eV) then statistical mechanics allows the density in a given vibrational state, $[v]$, to be expressed in terms of the total density across all vibrational states, $[tot]$, and the partition function, $q_{vib} = \sum_{v=0}^{\infty} \exp\left(\frac{-E_v}{T_v}\right)$, as:

$$[v] = \frac{[tot] \exp\left(\frac{-E_v}{T_v}\right)}{q_{vib}} \tag{9.3}$$

Combining equations 9.2 and 9.3 gives

$$\nu_{tot} = \frac{k_0}{q_{vib}} [e^-][tot] \sum_{v=0}^{\infty} \exp\left(\frac{E_v}{T_e} - \frac{E_v}{T_v}\right). \tag{9.4}$$

Thus it is possible to write down an effective rate coefficient for the electron impact process with all vibrational states, k_{tot},

$$k_{tot} = \frac{k_0}{q_{vib}} \sum_{v=0}^{\infty} \exp\left(\frac{E_v}{T_e} - \frac{E_v}{T_v}\right), \tag{9.5}$$

and the ratio of this rate coefficient to k_0 which is often available in the literature is give by:

$$\frac{k_{tot}}{k_0} = \frac{1}{q_{vib}} \sum_{v=0}^{\infty} \exp\left(\frac{E_v}{T_e} - \frac{E_v}{T_v}\right) = \frac{\sum_{v=0}^{\infty} \exp\left(\frac{E_v}{T_e} - \frac{E_v}{T_v}\right)}{\sum_{v=0}^{\infty} \exp\left(\frac{-E_v}{T_v}\right)}. \tag{9.6}$$

If the vibrational levels are harmonic then each of the sums becomes a geometric series that can be evaluated, however, for the purposes of this model the sums are evaluated numerically using the (anharmonic) vibrational energy levels found by experiment or calculation for $N_2(X^1\Sigma_g^+)$[265], $N_2(A^3\Sigma_u^+)$[247] and $N_2^+(X^2\Sigma_g^+)$[260]. For $T_e = 2$ eV and $T_v = 0.32$ eV (= 3700 K) the k_{tot}/k_0 ratios for the three species are 1.12, 1.15 and 1.13 respectively. Thus, assuming only the threshold energy is changed, vibrational excitation enhances reaction rate by around $10 - 15\%$.

9.2 Reaction set

Electron impact rate coefficients

Table 9.1 shows the rates of the electron impact processes included in the model.

Table 9.1: Electron impact reactions and corresponding rate coefficients (T_e in eV).

#	Reaction	Rate Coefficient / $\mathrm{cm^3\,s^{-1}}$	ref.
1	$e^- + N_2(X^1\Sigma_g^+) \rightarrow e^- + N(^4S) + N(^2D)$	$1.13 \times 10^{-8} T_e^{0.52} \exp(-13.56/T_e)$	[261,266]*
2	$e^- + N_2(A^3\Sigma_u^+) \rightarrow e^- + N(^4S) + N(^2D)$	$k_1 \exp(6.169/T_e)$	[261,266]**
3	$e^- + N_2(X^1\Sigma_g^+) \rightarrow e^- + N_2^+(X^2\Sigma_g^+)$	$1.17 \times 10^{-8} T_e^{0.67} \exp(-17.84/T_e)$	[261,267]
4	$e^- + N_2(A^3\Sigma_u^+) \rightarrow e^- + N_2^+(X^2\Sigma_g^+)$	$1.08 \times 10^{-8} T_e^{0.71} \exp(-12.04/T_e)$	[261,268]
5	$e^- + N_2(X^1\Sigma_g^+) \rightarrow e^- + N^+ + N(^2D)$	$5.88 \times 10^{-10} T_e^{1.17} \exp(-22.36/T_e)$	[261,267]
6	$e^- + N_2(A^3\Sigma_u^+) \rightarrow e^- + N^+ + N(^2D)$	$1.2\ k_5 \exp(6.169/T_e)$	[261,267,268]†
7	$e^- + N_2(X^1\Sigma_g^+) \rightarrow e^- + N_2(A^3\Sigma_u^+)$	$2.101 \times 10^{-8} T_e^{-0.642} \exp(-9.348/T_e)$	[269]
8	$e^- + N_2(A^3\Sigma_u^+) \rightarrow e^- + N_2(X^1\Sigma_g^+)$	$1.881 \times 10^{-9} T_e^{0.050} \exp(-0.110/T_e)$	[269]
9	$e^- + N(^4S) \rightarrow e^- + N^+$	$4.99 \times 10^{-9} T_e^{0.77} \exp(-15.24/T_e)$	[261,270]
10	$e^- + N(^2D) \rightarrow e^- + N^+$	$1.67 \times 10^{-8} T_e^{0.5} \exp(-13.07/T_e)$	[261,270]
11	$e^- + N(^2P) \rightarrow e^- + N^+$	$9.42 \times 10^{-9} T_e^{0.67} \exp(-11.25/T_e)$	[261,270]
12	$e^- + N(^4S) \rightarrow e^- + N(^2D)$	$2.74 \times 10^{-8} T_e^{-0.4} \exp(-3.35/T_e)$	[261,271]
13	$e^- + N(^2D) \rightarrow e^- + N(^4S)$	$(4/10) k_{12} \exp(2.385/T_e)$	[261,271]‡
14	$e^- + N(^4S) \rightarrow e^- + N(^2P)$	$9.11 \times 10^{-9} T_e^{-0.45} \exp(-4.8/T_e)$	[261,271]
15	$e^- + N(^2P) \rightarrow e^- + N(^4S)$	$(4/6) k_{14} \exp(3.576/T_e)$	[261,271]‡
16	$e^- + N(^2D) \rightarrow e^- + N(^2P)$	$1.01 \times 10^{-8} T_e^{-0.18} \exp(-3.94/T_e)$	[261,271]
17	$e^- + N(^2P) \rightarrow e^- + N(^2D)$	$(10/6) k_{16} \exp(1.191/T_e)$	[261,271]‡
18	$e^- + N_2^+(X^2\Sigma_g^+) \rightarrow N(^4S) + N(^2D)$	$0.37 \times 1.9 \times 10^{-8} T_e^{-0.3}$	[261,272]§
19	$e^- + N_2^+(X^2\Sigma_g^+) \rightarrow N(^4S) + N(^2P)$	$0.11 \times 1.9 \times 10^{-8} T_e^{-0.3}$	[261,272]§
20	$e^- + N_2^+(X^2\Sigma_g^+) \rightarrow 2N(^2D)$	$0.52 \times 1.9 \times 10^{-8} T_e^{-0.3}$	[261,272]§
21	$e^- + N_2^+(X^2\Sigma_g^+) \rightarrow 2e^- + N^+ + N(^2D)$	$3.72 \times 10^{-8} T_e^{0.24} \exp(-8.63/T_e)$	[261,273]§§

* Product branching ratios from Cosby[266]

** Estimated by threshold adjustment of reaction 1

† Estimated by threshold adjustment of reaction 5 and scaled up by 20% (see[261])

‡ Estimated by detailed balancing

§ Product branching ratios from[272]

§§ data from[273] scaled up by 300% (see[261])

Where the rate coefficients are for electron-molecule reactions the k_0 rate is given and the value in the table is multiplied by the ratio k_{tot}/k_0 before being used in the

model. The only exception to this is the super-elastic process (reaction 8) where the threshold energy is ≈ 0 regardless of the initial vibrational state. For this reaction it is assumed that all vibrational states have the same rate coefficient. The coefficients in the table are largely taken from the modelling of Thorsteinsson[261] with the exception of reactions 7 and 8 which use the recent cross section calculations of Su *et al.*[269] to calculate rate coefficients as a function of electron temperature for $T_e < 4$ eV. These coefficients are fitted with an Arrhenius function (equation 5.1) to yield the values in the table. In reactions 1, 2, 5 and 6 there is evidence to suggest that the atomic products are predominantly formed in the states given in the table. Even though reactions 5, 6, 9, 10, 11 and 21 produce N^+ their rates are not sufficient (in the context of N^+ loss mechanisms) to produce significant amounts of this ion. These reactions are only included because they destroy or produce other species of interest.

Heavy species rate coefficients

The gas phase reactions included in the model that do not involve electrons are given in table 9.2. A few points of interest about these reactions are discussed here. Several of the reactions have rate coefficients with an unknown temperature dependence and for some reactions that do have a reported temperature dependence the reliability is somewhat questionable. In particular reaction 27 has a $T_{trans}^{-0.666}$ dependence in the table[274] but elsewhere a $T_{trans}^{-2.23}$ dependence is reported[240,275].

Reactions 30 and 31 take their temperature dependences from simple collision theory of gas phase kinetics[276] rather than from measurements whilst the magnitude of the rate coefficient is taken from Salmon *et al.*[277]. The reactions are also assumed to produce different atomic products. Reaction 30 is assumed to form $N(^2D)$ atoms in accordance with Dutuit *et al.*[278] because the production of ground state atoms is spin forbidden. Meanwhile reaction 31 is assumed to have the same rate as reaction 30, but is assumed to produce ground state atoms because there are no spin restrictions on the products.

Reactions 28 and 29 have temperature dependences that have been measured and calculated theoretically by Galvao *et al.*[279] but earlier measurements by Slanger and Black[280] showed a rather weaker temperature dependence (see Galvao *et al.*[279] for a comparison). The pooling reaction 26 is in fact accounting for several processes of the form

$$2N_2(A^3\Sigma_u^+) \rightarrow N_2^* + N_2(X^1\Sigma_g^+) \rightarrow N_2(A^3\Sigma_u^+) + N_2(X^1\Sigma_g^+) + h\nu \qquad (9.7)$$

where the excited state created by the quenching (N_2^*) is usually one of $N_2(B^3\Pi_g)$ or $N_2(C^3\Pi_u)$ both of which can rapidly radiatively cascade to the metastable $N_2(A^3\Sigma_u^+)$ state. Rather than include the pooling and cascade separately the model simply incorporates both processes in one. It should be noted that this rate coefficient is the one recommended by Herron[281] but that there could be other pooling pathways (*i.e.* via other excited states) not considered by Herron or in the work of Piper[195,196]. These pathways would enhance the rate coefficient and thus the true coefficient may exceed the value of 4×10^{-10} cm^{-3} s^{-1} in the table.

Table 9.2: Heavy species reactions and corresponding rate coefficients (T_{trans} in Kelvin).

#	Reaction	Rate Coefficient / cm^3 s^{-1}	ref
22	$N_2^+(X^2\Sigma_g^+) + N(^4S) \rightarrow N_2(X^1\Sigma_g^+) + N^+$	$2.4 \times 10^{-15} T_{trans}$	261,282
23	$N_2^+(X^2\Sigma_g^+) + N(^2D) \rightarrow N_2(X^1\Sigma_g^+) + N^+$	$2.4 \times 10^{-15} T_{trans}$	261,282
24	$N_2^+(X^2\Sigma_g^+) + N(^2P) \rightarrow N_2(X^1\Sigma_g^+) + N^+$	$2.4 \times 10^{-15} T_{trans}$	261,282
25	$N_2(A^3\Sigma_u^+) + N_2(X^1\Sigma_g^+) \rightarrow 2N_2(X^1\Sigma_g^+)$	3×10^{-18}	261,281,283
26	$2N_2(A^3\Sigma_u^+) \rightarrow N_2(A^3\Sigma_u^+) + N_2(X^1\Sigma_g^+)$	4×10^{-10}	195,196,281
27	$N_2(A^3\Sigma_u^+) + N(^4S) \rightarrow N_2(X^1\Sigma_g^+) + N(^2P)$	$4 \times 10^{-11} \left(\frac{300}{T_{trans}}\right)^{\frac{2}{3}}$	274,284
28	$N(^2D) + N_2(X^1\Sigma_g^+) \rightarrow N(^4S) + N_2(X^1\Sigma_g^+)$	$4.52 \times 10^{-14} T_{trans}^{0.678} \exp\left(\frac{-1437.7}{T_{trans}}\right)$	279
29	$N(^2D) + N_2(A^3\Sigma_u^+) \rightarrow N(^4S) + N_2(A^3\Sigma_u^+)$	$4.52 \times 10^{-14} T_{trans}^{0.678} \exp\left(\frac{-1437.7}{T_{trans}}\right)$	279*
30	$N(^2P) + N_2(X^1\Sigma_g^+) \rightarrow N(^2D) + N_2(X^1\Sigma_g^+)$	$1.732 \times 10^{-18} T_{trans}^{0.5}$	276–278
31	$N(^2P) + N_2(A^3\Sigma_u^+) \rightarrow N(^4S) + N_2(A^3\Sigma_u^+)$	$1.732 \times 10^{-18} T_{trans}^{0.5}$	276–278*
32	$N(^2P) + N(^4S) \rightarrow 2N(^4S)$	6.2×10^{-13}	261,281,285
33	$N(^2P) + N(^2D) \rightarrow N(^4S) + N(^2D)$	6.2×10^{-13}	261,281,285†
34	$2N(^2P) \rightarrow N(^4S) + N(^2P)$	6.2×10^{-13}	261,281,285†
35	$N(^2P) + N(^2D) \rightarrow e^- + N_2^+(X^2\Sigma_g^+)$	$\frac{1.92 \times 10^{-15} T_{trans}^{0.98}}{(1 - \exp(-3129/T_{trans}))}$	286
36	$2N(^2P) \rightarrow e^- + N_2^+(X^2\Sigma_g^+)$	$\frac{3.2 \times 10^{-15} T_{trans}^{0.98}}{(1 - \exp(-3129/T_{trans}))}$	286
* Rate coefficient assumed to be the same as for quenching by $N_2(X^1\Sigma_g^+)$ † Rate coefficient assumed to be the same as for quenching by $N(^4S)$			

Wall loss coefficients

The rate of loss of neutral species at the chamber walls is described, as for the oxygen plasma, by the approximation according to Chantry[125] (equation 4.5). The wall loss coefficients used for the important wall loss processes are listed in table 9.3. Metastable molecules are typically lost with unit probability whilst atom recombination has a wall loss coefficient that depends on the surface material. The atom recombination coefficient of $\gamma_N = 0.005$ for aluminium is taken from the lowest pressure measurement of Rouffet[287] (although there is a possibility the actual value may be somewhat higher, see for example the work of Sarrette *et al.*[138] who find a value of ≈ 0.02). This wall recombination coefficient is assumed to be the same for excited atoms as it is for the ground state. It is also assumed that excited atoms that meet the wall and do not recombine are relaxed into the electronic ground state, the wall relaxation coefficients for these processes are therefore $1 - \gamma_N$.

Table 9.3: Wall loss reactions and corresponding loss coefficients.

#	Reaction	Wall loss coefficient (γ)	ref.
37	$N_2(A^3\Sigma_u^+)$ + wall $\rightarrow N_2(X^1\Sigma_g^+)$	1	261,288,289
38	$N(^4S)$ + wall $\rightarrow \frac{1}{2}\ N_2(X^1\Sigma_g^+)$	0.005	287
39	$N(^2D)$ + wall $\rightarrow \frac{1}{2}\ N_2(X^1\Sigma_g^+)$	0.005	287
40	$N(^2D)$ + wall $\rightarrow N(^4S)$	0.995	see text
41	$N(^2P)$ + wall $\rightarrow \frac{1}{2}\ N_2(X^1\Sigma_g^+)$	0.005	287
42	$N(^2P)$ + wall $\rightarrow N(^4S)$	0.995	see text
43	$N_2^+(X^2\Sigma_g^+)$ + wall $\rightarrow N_2(X^1\Sigma_g^+)$	See text	3,261

Diffusion coefficients for metastable molecules are assumed to be the same as for ground state molecules and are taken from Winn[126], whilst all the atomic states are assumed to diffuse at the same rate and diffusion coefficients are taken from Morgan and Schiff[127]. Figure 9.1 shows the diffusion coefficients for molecular and atomic species fitted according to equation 4.12 which are used for the purposes of modelling wall loss of all the neutral species in table 9.3.

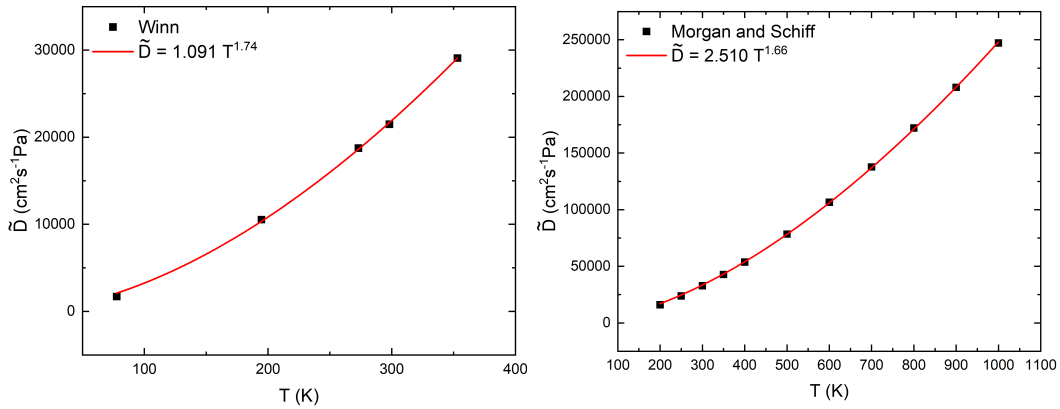

Figure 9.1: (a) Diffusion coefficient data for molecular nitrogen from Winn[126] fitted according to equation 4.12. (b) Diffusion coefficient data for atomic nitrogen from Morgan and Schiff[127] fitted according to equation 4.12.

Wall loss of ions

Ions undergo ambipolar diffusion to the chamber walls where they are lost with unit probability, thus wall loss is usually a significant loss process for positive ions in chamber based plasma. If a uniform electron temperature and gas density is assumed within the chamber it becomes possible to use a simple diffusive model to predict the spatial variation of ion density within the plasma. This yields a radial variation which follows a Bessel function and a variation with height (axial) in the plasma that is approximately described by a cosine function, thus the density peaks in the centre of the chamber[3]. The diffusive model is discussed in more depth in the next chapter in relation to the spatial variation of ion density. In reality this model is something of a simplification as there is significant spatial variation in electron temperature and gas density (mainly because of localised gas heating), nevertheless it is reasonable to use this model to estimate the ion wall losses (and indeed it is regularly used in ICP volume averaged modelling[3,16,90,124,129,261]).

The rate of loss at a particular chamber surface is proportional to the directional flux of ions entering the sheath at that surface given simply by $n_{i,s}v_B$ (where $n_{i,s}$ is the ion density at the sheath edge and v_B is the Bohm velocity) and the surface area (ions that enter the sheath can be thought of as lost, because they cannot re-enter the plasma). Summing across all the internal chamber surfaces will then give the number of ions leaving the plasma per unit time, this can be converted to a volume average loss rate by dividing by the total plasma volume. For a cylindrical geometry

therefore the rate of ion wall loss is given by:

$$k_{i,w}n_i = v_B \frac{2\pi R^2 n_{i,s}^H + 2\pi RH n_{i,s}^R}{\pi R^2 H}, \tag{9.8}$$

where n_i is the bulk ion density, v_B is the ion Bohm velocity, R and H are the chamber internal radius and height respectively and $n_{i,s}^H$ and $n_{i,s}^R$ are the ion densities at the sheath edge in the axial and radial directions respectively. Introducing the ion density ratios $h_H = \frac{n_{i,s}^H}{n_i}$ and $h_R = \frac{n_{i,s}^R}{n_i}$ the rate coefficient for ion loss can be written

$$k_{i,w} = v_B \frac{2\pi R^2 h_H + 2\pi RH h_R}{\pi R^2 H}. \tag{9.9}$$

The numerator of equation 9.9 is an effective area for ion loss whilst the ion density ratios can be approximated using a heuristic model according to Lee and Lieberman [290] as:

$$h_H \approx 0.86 \left(3 + \frac{H}{2\lambda_i} + \left(\frac{0.86 H v_B}{\pi D_a}\right)^2\right)^{-\frac{1}{2}} \tag{9.10}$$

and

$$h_R \approx 0.80 \left(4 + \frac{R}{\lambda_i} + \left(\frac{0.80 R v_B}{\chi_{01} J_1(\chi_{01}) D_a}\right)^2\right)^{-\frac{1}{2}}, \tag{9.11}$$

where λ_i is the ion mean free path, $\chi_{01} = 2.405$ is the first zero of the zeroth order Bessel function of the first kind, $J_1(\chi_{01}) = 0.519$ is the first order Bessel function of the first kind evaluated at χ_{01} and D_a is the ambipolar diffusion coefficient. The appropriate ion mean free path is given by:

$$\lambda_i = \frac{k_B T_{trans}}{\sigma p}, \tag{9.12}$$

where σ is the ion-neutral scattering cross section (taken as 2.5×10^{-18} m^2 for N_2-N_2^+ scattering [261,291]) and p is the total gas pressure. For simplicity it is assumed (for the purposes of calculating the ion mean free path) that ions only interact with nitrogen molecules. The ambipolar diffusion coefficient is directly related to the diffusion coefficient for the ions if their are no electrons present, D_i, according to:

$$D_a = D_i \left(1 + \frac{T_e}{T_{trans}}\right), \tag{9.13}$$

where the temperatures must be expressed in the same units. Finally the diffusion coefficient, D_i, can also be estimated according to:

$$D_i = \frac{k_B T_{trans} \lambda_i}{v_i m_i}, \tag{9.14}$$

where v_i is the mean ion velocity given by $v_i = \sqrt{\frac{8 k_B T_{trans}}{\pi m_i}}$.

9.3 Model results and discussion

Self-consistent cation densities and electron temperatures

Along with the reaction set the model also requires electron densities and temperatures, and neutral species temperatures in order to calculate the densities of the species which it seeks to model. For the purposes of modelling the electron densities are taken to be equal to $1.77[N_2^+(X^2\Sigma_g^+, v = 0)]$ calculated using quasi-neutrality and by assuming that no other cationic species are important and assuming an ion vibrational temperature of 3700 K as discussed earlier. The gas temperatures are taken from figure 8.15, the higher ion temperatures are not included because previous modelling[261] has found that including elevated ion temperatures has no influence on model results.

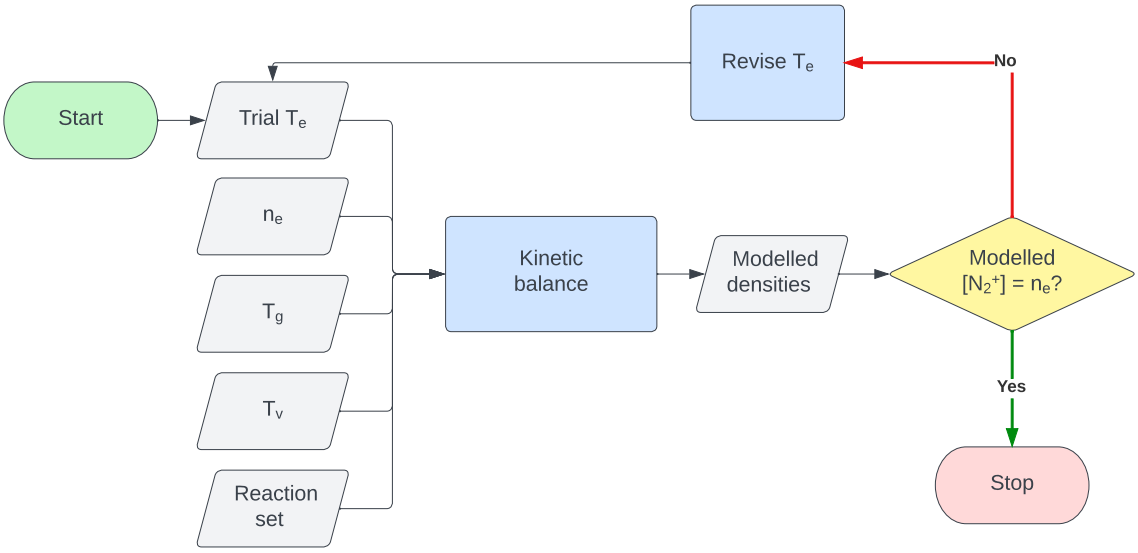

Figure 9.2: A flowchart indicating the iterative process used to find an electron temperature that reproduces the measured ion densities.

The electron temperature is treated as an independent variable which can be adjusted such that the model matches the experimental densities. The model then consists of a kinetic balance, constructed by equating the production and destruction rates of $N_2(A^3\Sigma_u^+)$, $N(^4S)$, $N(^2D)$, $N(^2P)$ and $N_2^+(X^2\Sigma_g^+)$, as well as equating the sum of their densities to the density corresponding to the total pressure and temperature in the

chamber (via the ideal gas law). This establishes a system of 6 simultaneous equations which can be solved for the densities of the species listed above plus $N_2(X^1\Sigma_g^+)$. In order for the model to be self-consistent the ion density it predicts ought to be the same as the electron density input. The electron temperature is adjusted, as depicted in figure 9.2, until self-consistency is achieved.

The electron temperatures found by the self-consistent modelling approach as a function of power and pressure are shown in figure 9.3 along with an exponential fit at each power (the fit is simply included as a guide to the eye, not because there is any physical reason to expect exponential behaviour). The figure also depicts the results of planar probe measurements, in the same chamber, made by Bakowski[64]. Given the huge difference in the two methods of deriving electron temperatures and the inherent simplifying assumptions, both in the kinetic modelling and the analysis of probe results, the agreement is remarkably good. Not only is the agreement good in terms of the variation of electron temperature with pressure, it is also good in absolute terms across the pressure range (always within 0.3 eV of the exponential best fit line).

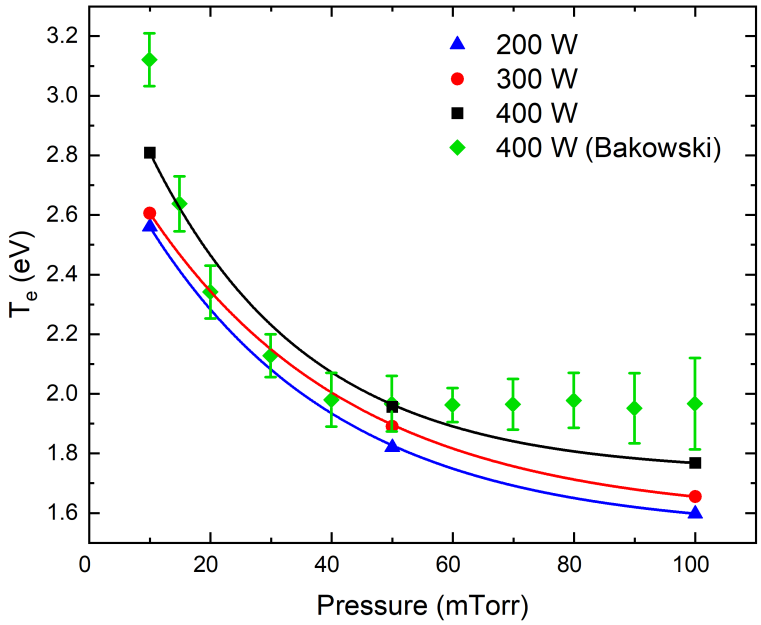

Figure 9.3: Electron temperatures found by the self-consistent model and compared to the planar probe measurements of Bakowski[64].

In terms of the kinetics of the cations, their production is by electron impact on $N_2(X^1\Sigma_g^+)$ molecules (reaction 3) whilst they are lost predominantly at the walls at

low pressure, with dissociative recombination (reactions 18, 19 and 20) also becoming important at higher pressures. As pressure increases the increase in feedstock gas density will increase the ion production rate whilst also reducing the rate of diffusion to the walls and, *ceteris paribus*, this will result in an increased ion density. Experiments (figure 8.13) show this not to be the case, ion and electron densities show a modest decrease with pressure, and the only explanation is that something offsets this increase in feedstock density. The increasing relative importance of dissociative recombination with increasing pressure plays a small role in counteracting the effects of increased pressure, the main influence however, comes from the rapidly dropping electron temperature as pressure increases. Ionisation is a high threshold process and thus a small change in electron temperature can have a significant effect on the proportion of electrons with sufficient energy to cause ionisation and thereby produce cations.

Densities of other species

The densities of the other species predicted by the self-consistent model are shown as a function of both pressure and power in figure 9.4. The trends for the various species are only discussed briefly here. In general the results of this model are broadly in line with the results of the model of Thorsteinsson and Gudmundsson on which it is based[261] with the caveat that the (measured) electron densities used here are somewhat lower and as a result the densities of all excited species are shifted to some extent towards lower values. The density of ground state molecules naturally increases with the gas pressure because it is the feedstock gas, whilst its density is observed to decrease with power largely due to the translational heating of the plasma but also in part due to the greater mole fraction of excited state species present at higher powers. Ground state atoms are predominantly produced by electron impact processes with high threshold energies or from the excited atomic states ($N(^2P)$ and $N(^2D)$) being quenched, both at the chamber walls and also in the gas phase (in particular by $N_2(X^1\Sigma_g^+)$) at the higher pressures. Loss of the $N(^4S)$ atoms is dominated by excitation to the electronically excited atomic states, recombination at the chamber walls and, at higher pressures, by the energy exchange with $N_2(A^3\Sigma_u^+)$ (reaction 27). Several of these production and loss processes rapidly interconvert the three atomic states present in the chamber and thus determine the relative density of the three atomic states. Meanwhile the total atom content of the plasma is mainly controlled

by the rate of electron impact dissociation processes and wall recombination. Electron impact dissociation is generally a high energy threshold process and the density of ground state atoms thus approximately follows the electron temperature.

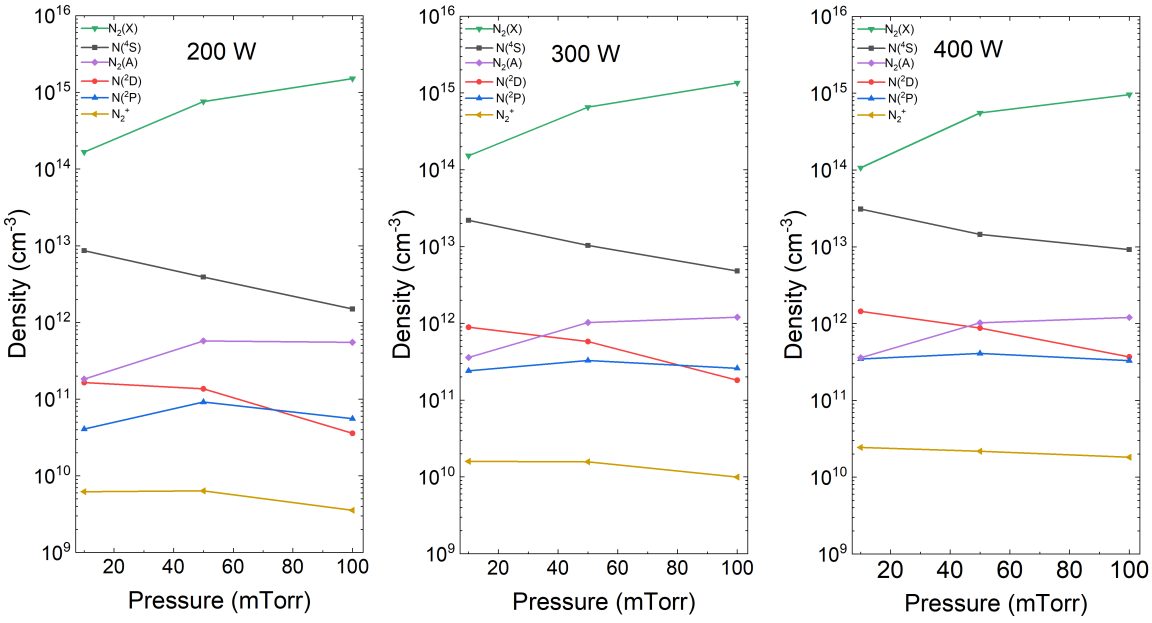

Figure 9.4: Species densities predicted by the self consistent model as a function of plasma power and pressure.

Within the model solutions shown in figure 9.4, $N_2(A^3\Sigma_u^+)$ is produced entirely by electron impact excitation on the molecular ground state. At low pressure (10 mTorr 400 W) the loss of the metastable molecules is due to wall quenching (reaction 37), gas phase atomic quenching (reaction 27) and energy pooling (reaction 26) in a ratio of $\approx$ 70 : 25 : 5 whilst at high pressures (100 mTorr 400 W) diffusion is slower and the ratios become $\approx$ 45 : 15 : 40, with the pooling reaction becoming much more important. The excitation process has a lower energy threshold than ionisation or dissociation, so the rate of $N_2(A^3\Sigma_u^+)$ production is less electron temperature dependent than these other processes in the range $T_e \approx 1-3$ eV. The dominant effects defining the trend in $N_2(A^3\Sigma_u^+)$ density with pressure are an increase in feedstock density from which $N_2(A^3\Sigma_u^+)$ is produced and slower diffusion losses at higher pressures. These are sufficient to overcome the effects of the changing electron temperature and the model predicts that the metastable density should increase with increasing pressure.

The density of $N(^2D)$ atoms is closely tied to the density of $N(^4S)$, it is mainly produced by electron impact excitation of $N(^4S)$ or electron impact dissociation of

$N_2(X^1\Sigma_g^+)$ and lost by wall or gas phase quenching to form $N(^4S)$ or by wall recombination. The rapid interconversion between the two lowest atomic state, combined with their shared, higher threshold production process (reaction 1) means that their densities change similarly with pressure.

$N(^2P)$ shows much less variation with gas pressure than do the other two atomic states. There are a couple of reasons for this: first, $N(^2P)$ is not produced in significant quantities by electron impact dissociation of ground state molecules and secondly, it has an important production pathway that is not by electron impact but is instead by the energy transfer process (reaction 27). Thus the decreasing density with pressure seen by the other atomic species is offset in the case of $N(^2P)$ by the increasing density of $N_2(A^3\Sigma_u^+)$ from which it can be produced.

Comparing with experiments-revising the model

The variation of the species densities predicted by the model with power and pressure are consistent with the conclusions of Thorsteinsson and Gudmundsson[261] as indeed are the main conclusions as to which processes are most important in the production and loss of the important species. The true success of the model however must be judged by comparing its solutions to measurements. By virtue of the self-consistent approach the densities of ions produced by the model are in agreement with the measurements already presented here (with the caveat that vibrational temperatures are somewhat uncertain) however, comparison with measurements of the other species will serve to test the model's capabilities.

The metastable $N_2(A^3\Sigma_u^+)$ state has been observed in ICP plasmas on several occasions. Most relevant to the modelling here are the measurements of Thornton *et al.*[63,153,241], Agarwal *et al.*[292] and Horikawa *et al.*[262,289] all of whom make measurements in 13.56 MHz ICPs operating at powers and pressures directly relevant to this work. All three of these works find metastable densities in the range of a few 10^{11}-a few 10^{12} cm^{-3} and two of them[153,262] make measurements at different powers and find a modest increase in density with plasma power. In these respects the kinetic model is rather successful at reproducing experimental $N_2(A^3\Sigma_u^+)$ densities. It is also possible to use the CRDS results in figure 8.14 to infer the relative variations in $N_2(A^3\Sigma_u^+)$ density with power and pressure. Despite the lack of knowledge of saturation parameter for this transition the translational temperature can still be used to calculate absorption cross sections and the ratio of integrated absorption coefficient to cross section should still be proportional to the density. In this way the relative densities in figure 9.5 were found. Although these are technically relative densities

in the $v = 6$ vibrational level, a comparison with the work of Hancock *et al.*[153] suggests that this is generally a constant proportion of the total $N_2(A^3\Sigma_u^+)$ density (*i.e.* vibrational temperature is approximately constant) and thus the trends are useful for comparison. These densities too show a modest increase with plasma power and agree in that respect with both the model and previous work.

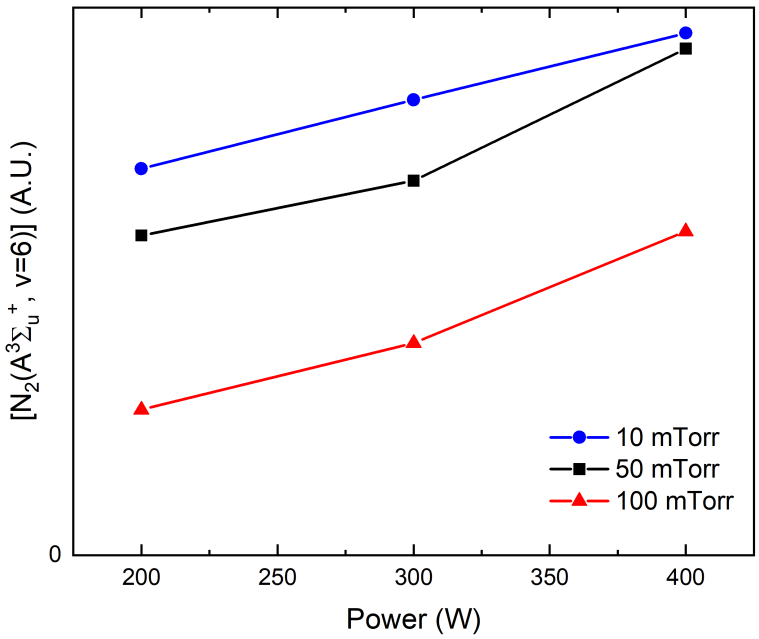

Figure 9.5: Relative density of $N_2(A^3\Sigma_u^+)$ in the $v = 6$ vibrational state found by the fitting of absorption spectra (figure 8.14).

The other important observation from figure 9.5 is that the density of $N_2(A^3\Sigma_u^+)$ decreases significantly with increasing pressure (by a factor of $\approx 2-3$ across this power range for a change in pressure from 10 to 100 mTorr). This is an observation made consistently in nitrogen ICP measurements with Hancock *et al.*[153,241] observing a change in density by a factor of ≈ 5 between 10 and 100 mTorr in the same chamber operating at 100 W; Horikawa *et al.*[262] observing a decrease in density by approximately an order of magnitude between 10 and 100 mTorr at 400 W and Agarwal *et al.*[292] measuring a factor of 2 decrease in density between 50 and 200 mTorr at 750 W. These observations are in stark contrast to the modelled pressure variation and have previously defied any straightforward explanation in terms of the widely accepted important kinetic processes. Agarwal *et al.*[292] assert that molecular quenching of $N_2(A^3\Sigma_u^+)$ should become important at higher pressures, but offer no

specific quenching processes or any kinetic considerations; Horikawa *et al.*[262] consider the problem more carefully but conclude that their observed density variations cannot be explained by the literature rate coefficients for the loss of $N_2(A^3\Sigma_u^+)$ whilst Bilek *et al.*[293] conclude that their model is likely to be missing important quenching processes and consider whether the rate of atom quenching or pooling might actually be faster than literature suggests, but without reaching a firm conclusion on which of those processes (if either) could account for any discrepancy. Bakowski *et al.*[241] do manage to produce a model which indicates a decreasing $N_2(A^3\Sigma_u^+)$ density with increasing pressure, however the model typically underestimates the rate of diffusive losses and thus concludes that atom quenching is the dominant loss process for $N_2(A^3\Sigma_u^+)$ at all pressures between 10 and 100 mTorr. The model then lets the atomic density vary so as to achieve the desired metastable density rather than modelling the atomic density, as the model presented here attempts to. Even with their model's success Bakowski *et al.*[241] note that the high (and variable) atom densities that they predict could be masking flaws in their model. Most recently of all Mignogna *et al.*[294] have found their kinetic model unable to reproduce measured metastable densities and have explored several options including careful consideration of the quenching rate coefficient for $N_2(A^3\Sigma_u^+)$ and the densities of the possible quenchers.

Where the previous works fail to explain the steep drop in metastable density with pressure an additional quenching process is usually invoked. This is mainly because kinetic calculations tend to agree best at low pressures (where wall loss dominates and quenching density is expected to be low) and become worse at higher pressures (where the unknown quenching is more likely to come into play) and that is the case here. The work of Hancock *et al.*[153] suggests that the modelled $N_2(A^3\Sigma_u^+)$ density of a few 10^{11} cm^{-3} is reasonable at 10 mTorr and 400 W but that the predicted density of $\approx 10^{12}$ cm^{-3} at 100 mTorr 400 W is likely to be around an order of magnitude too high. If it is supposed that a metastable density of $\approx 2 \times 10^{11}$ cm^{-3} should be obtained at 100 mTorr and 400W (by assuming a factor of 2 reduction from the density at 10 mTorr 400 W based on figure 9.5) then, from the kinetics previously discussed, the energy pooling (reaction 26) would become unimportant and thus the loss of $N_2(A^3\Sigma_u^+)$ would be either at the walls or by gas phase quenching by some species, Q. Assuming that $N_2(A^3\Sigma_u^+)$ production is by electron impact excitation the following balance can be constructed:

$$k_7[e^-][N_2(X^1\Sigma_g^+)] = (k_{37} + k_Q[Q])[N_2(A^3\Sigma_u^+)], \tag{9.15}$$

and from this the required quasi-first-order quenching rate coefficient ($k_Q[Q]$) necessary for $[N_2(A^3\Sigma_u^+)]= 2\times10^{11}$ cm^{-3} can be estimated. Taking k_7 from table 9.1 with T_e from figure 9.3 (1.768 eV), k_{37} from the Chantry equation (4.5)[125] and taking $[e^-]$ and $[N_2(X^1\Sigma_g^+)]$ from the model results yields $k_Q[Q] \approx 6800$ s^{-1}.

A fast quenching process could have a rate coefficient, k_Q, of the order of a few 10^{-10} cm^3 s^{-1} (see Dutuit *et al.*[278] for examples of such processes) and the quenching species would therefore need to be present with a density of a few 10^{13} cm^{-3}. The only species expected to be present in the chamber near to or above this level are $N_2(X^1\Sigma_g^+)$ and N(^{4}S) atoms, however, quenching by each of these species is already included in the model. The rate of quenching by ground state molecules is rather uncertain[281] but is definitely slow (with rate coefficient no larger than 10^{-16} cm^{3}s^{-1}) whilst the quenching by atoms has a rate coefficient of $4\times10^{-11}\left(\frac{300}{T_{trans}}\right)^{\frac{2}{3}}$ cm^3 s^{-1}. Even if the somewhat questionable temperature dependence is ignored, a rate coefficient of 4×10^{-11} cm^3 s^{-1} would require an atom density of 1.7×10^{14} cm^{-3} (*i.e.* $\approx 17\%$ of the total chamber density) to reach the required metastable quenching rate. Such a high degree of dissociation is not expected in nitrogen ICPs, with experimental atomic mole fractions in ICPs ranging from $\approx 0.05\%$ measured by Horikawa *et al.*[262] (at 100 mTorr 400 W) through 1.4% (20 mTorr and 200 W) and 0.1% (200 mTorr and 200 W) found by Kang *et al.*[295] up to ≈ 3 or 4% measured by Agarwal *et al.*[292] at 750 W and at a range of pressures below 200 mTorr. It therefore seems unlikely that our plasma will attain the required degree of dissociation to enable sufficiently fast atom quenching of metastable species.

With this conclusion in mind one must consider the possibility that the literature rate coefficient for the quenching of $N_2(A^3\Sigma_u^+)$ by atomic nitrogen may be unreliable. The rate coefficient for this reaction which is used most often is that found by Piper[197] and a few other measurements also exist which agree to within $\approx 20\%$ with the value of 4×10^{-11} cm^3 s^{-1}[281]. All of these measurements however utilise a flowing discharge and monitor $N_2(A^3\Sigma_u^+)$ density downstream by optical emission (Piper utilises the Vegard-Kaplan emission). This method relies on the assumption that, within the downstream region, $N_2(A^3\Sigma_u^+)$ is no longer being produced and thus the changing emission signal along the flow tube is purely indicative of the loss processes at play.

More recent work however, suggests that this assumption might not be a good one. The extensive work of Sadeghi *et al.*[239,240,246] utilised a flowing nitrogen discharge, the plasma was generated by a microwave cavity and measurements of a number of species performed in the short-lived afterglow (SLA). Importantly the density of metastable molecules was observed to decrease immediately downstream from the

discharge before increasing to a secondary maximum around 20 cm down stream (which corresponded to ≈ 15 ms of flow) before dropping off again at greater distances downstream. One key conclusion of these studies is that the $N_2(A^3\Sigma_u^+)$ molecules observed far downstream are not those that are produced by the microwave cavity (these molecules are lost or quenched on a timescale of 0.1 ms), but are instead produced in the afterglow. The importance of downstream $N_2(A^3\Sigma_u^+)$ production processes is corroborated by the fact that the $N_2(A^3\Sigma_u^+)$ signal in the late afterglow persists for much longer (*i.e.* further downstream) than would be predicted based on the expected quenching rate for this species. Sadeghi *et al.* propose that downstream electrons will have insufficient energy to produce $N_2(A^3\Sigma_u^+)$ in significant amounts and that downstream production must therefore be via atomic and molecular gas phase chemistry. They propose a number of possible sources of the downstream $N_2(A^3\Sigma_u^+)$, in particular they invoke the termolecular process (which can be important in their 3.3 Torr system):

$$N(^4S) + N(^4S) + N_2(X^1\Sigma_g^+) \rightarrow N_2(A^3\Sigma_u^+) + N_2(X^1\Sigma_g^+). \tag{9.16}$$

Based on the observations of Sadeghi *et al.* it is certainly possible that the experiments of Piper[197] which utilise the downstream emission of an Ar/N_2 microwave discharge at 1.8 Torr could also exhibit downstream $N_2(A^3\Sigma_u^+)$ production. Such production processes would lengthen the apparent $N_2(A^3\Sigma_u^+)$ lifetimes exhibited in the afterglow and, because the production processes are not accounted for in the kinetic scheme, this would lead to an underestimate of the quenching rate coefficient. This conclusion is, to some extent, supported by the work of Piper himself. Piper measures the rate of the quenching process (reaction 27) in two ways. First is the measurement already discussed of the Vegard-Kaplan system which finds the rate coefficient of 4×10^{-11} cm^3 s^{-1} whilst the second method involves observation of the forbidden emission from the excited atomic product ($N(^2P) \rightarrow N(^4S)$) at 346.6 nm. Given that reaction 27 is expected to be the only source of $N(^2P)$ in the afterglow it would be expected that the two methods should find the same rate coefficient for the quenching process, but this is not the case. Piper finds that $N(^2P)$ is produced with a rate coefficient of 1.9×10^{-10} cm^3 s^{-1}, a factor of 5 greater than the apparent quenching rate coefficient of $N_2(A^3\Sigma_u^+)$. Downstream production of $N_2(A^3\Sigma_u^+)$ provides a potential explanation for this disparity, in which case the larger rate coefficient found from atomic emission represents the true rate of the quenching process while the smaller rate coefficient from the Vegard-Kaplan measurement is influenced by both quenching and production processes.

Taking the rate coefficient of 1.9×10^{-10} cm^3 s^{-1} for reaction 27 would (according to equation 9.16) require an atomic density of 3.6×10^{13} cm^{-3} in order to obtain the required quenching rate to give an equilibrium metastable density of 2×10^{11} cm^{-3}. This corresponds to an atom mole fraction of $3 - 4\%$ which is within the bounds of previous measurements.

Given that the preceding discussion in relation to the modelling of metastable densities focused largely on the role of atomic nitrogen, it is necessary also to discuss the dissociation kinetics in nitrogen plasma. As with the metastable state, the kinetics of atomic nitrogen has also caused a significant amount of consternation amongst the plasma community. As noted recently by Volynets *et al.*[276], dissociation in nitrogen plasma is complex and, despite being the focus of much work over many years, is still an open problem with significant interest. Experimental measurements of atom density[262,276,292] show an increase in density with pressure. Once again these observations are at odds with the modelling results (figure 9.4) and it is therefore likely that the model is not successfully capturing the kinetics of dissociation within the plasma.

Perhaps the biggest source of uncertainty, in terms of the atoms densities in the plasma studied here, is the wall recombination coefficient of the atoms. This is the main pathway by which atoms are destroyed (other processes forming N(^{2}D) and N(^{2}P) are fast but these excited states are largely recycled back into N(^{4}S)) yet without recombination coefficients specific to the chamber under investigation its rate is rather uncertain, especially because recombination coefficients typically depend on the surface materials and on the condition of the surface (for example on surface roughness and thickness of oxidised or nitrided layers). To compound this issue, the recombination coefficient can also be strongly pressure dependent and few measurements of wall recombination coefficients exist at pressures as low as $10 - 100$ mTorr. This uncertainty makes the wall recombination coefficient the natural parameter to vary in order to ensure the model produces sufficient atoms in order to quench the metastable molecules.

Using the rate coefficient of 1.9×10^{-10} cm^3 s^{-1} for reaction 27 along with a reduced recombination coefficient for N(^{4}S) atoms of 0.001 provides a model which is much more successful at producing reasonable metastable densities at 400 W and 100 mTorr. With these new rate coefficients a slightly reduced electron temperature is required to achieve self-consistent ions densities ($T_e = 1.677$ eV). This results in a metastable density of 2.05×10^{11} cm^{-3} and an N(^{4}S) density of 2.54×10^{13} cm^{-3}. The atom concentration required to reduce the metastable density to a reasonable value is somewhat lower than the value of 3.6×10^{13} cm^{-3} found using equation 9.16

because of the slightly reduced electron temperature in this revised simulation which reduces the production rate of metastable molecules within the model.

Similar calculations can be performed with the new rate coefficient for reaction 27 at the lower pressures, with electron temperatures and atomic wall loss coefficients varied in order to achieve self consistent and physically reasonable densities of ions and metastable molecules, respectively. The parameters used in this revised modelling are shown in figures 9.6(a) and (b) whilst the densities predicted by the model (keeping all other variables the same as before) for a 400 W plasma are shown in figure 9.6(c).

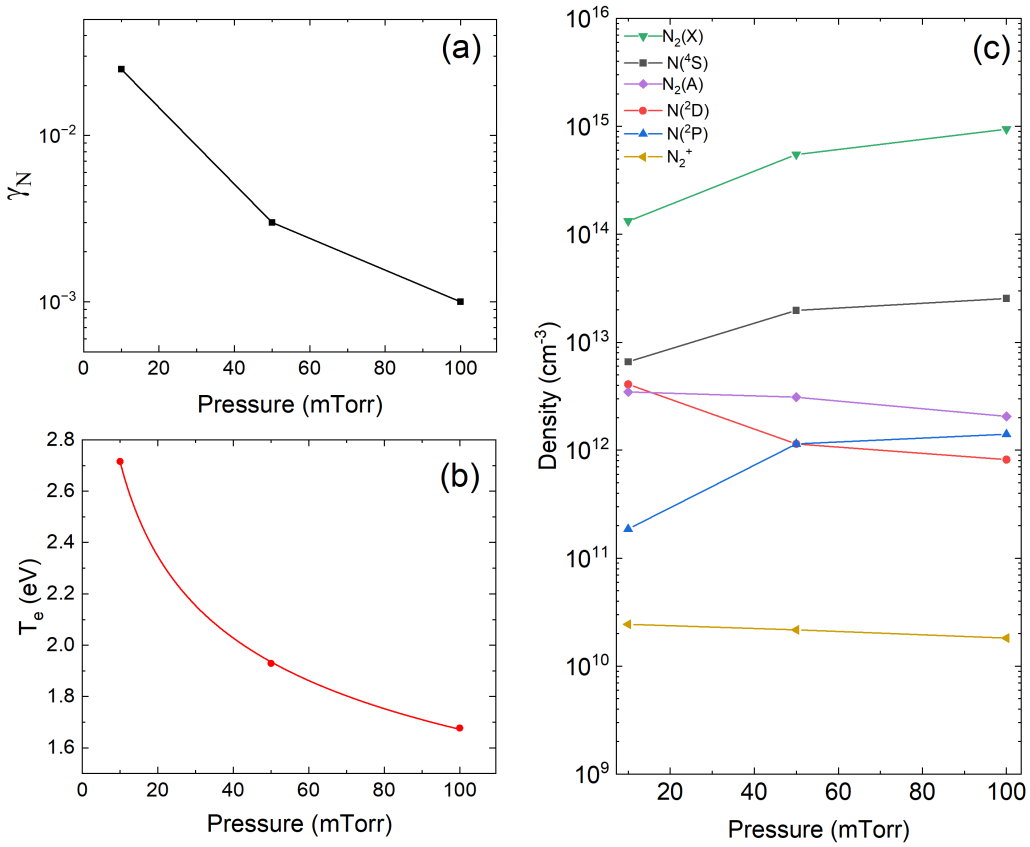

Figure 9.6: (a) Pressure variation of atom wall loss coefficient required in order to produce the expected trends in atomic and metastable density within the revised model at 400 W. (b) The electron temperatures required in the revised model to achieve self consistent ion densities at 400 W. (c) The species densities found by the revised model.

The trends with pressure for ground state atoms and metastable molecules are more in line with experimental values, but in order to produce this trend a rapid

decrease in the wall recombination coefficient with increasing pressure is required. Several previous studies have observed wall loss coefficients for atomic nitrogen that decrease with increasing pressure for various materials[138,287,296]. This trend has been justified by considering the effects of increased pressure on physisorbed atoms. It is suggested that, at higher pressures, a greater fraction of physisorption sites are occupied by nitrogen molecules and any atoms that do physisorb are therefore less likely to migrate on the surface and reach a chemisorption site from which they can undergo Eley-Rideal or Langmuir-Hinshelwood recombination. Additionally, the higher pressure increases the rate of collision-induced desorption of physisorbed atoms and this also reduces the recombination probability[138]. The work of Sarrette *et al.*[138] observes a decrease in γ by one order of magnitude as pressure increases from 1 to 15 Torr with γ changing much more rapidly with pressure at lower pressures. The change in γ implied by the model presented here is by more than an order of magnitude as pressure increases from 10 to 100 mTorr, this rate of change with pressure is clearly much greater than the previous measurements, but this model is under a much lower pressure regime and so a stronger dependence of γ on pressure is expected.

Other possible explanations

Although the revised model is able to produce atomic and molecular number densities in better agreement with what is expected based on previous experiments, it only represents one possible explanation as to why the initial modelling might fail in the cases of atoms and metastable molecules. There are naturally several other variables and unknowns that might be responsible.

Vibrational excitation can have a very great influence on the plasma chemistry. The model used here has made several assumptions with relation to the vibrational excitation of the N_2 molecules within the chamber, these are: i) that the vibrational distribution function (VDF) is well described by a Boltzmann distribution, ii) that the vibrational temperature of $N_2(X^1\Sigma_g^+)$ is well approximated by the corresponding temperature of $N_2(A^3\Sigma_u^+)$, and iii) that the vibrationally excited molecules react with a rate coefficient either identical to the vibrational ground state or with a shifted threshold energy for electron impact processes. Each of these assumptions could account (in part) for the disagreement between this model and experiments and the possible errors in each of the assumptions will be discussed in turn here.

First it is assumed that the vibrational excitation is well described by a Boltzmann distribution, this assumption is largely based on measurements of several vibrational levels of the metastable molecule by Thornton[63]. Those measurements

probe $v = 0, 1, 3$ and 6 and find densities that are well represented by a single vibrational temperature (*i.e.* by a Boltzmann distribution). In reality, vibrational energy distributions often deviate from a Boltzmann distribution. If the vibrational states populations are controlled by electron impact vibrational excitation followed by V-V energy transfer then one expects a Treanor distribution, in which the higher vibrational states exhibit a population inversion and thus high vibrational states are significantly overpopulated compared to a Boltzmann distribution. Alternatively, if V-T collisions dominate, then a Boltzmann distribution with a temperature equal to the gas translational temperature would be expected. Generally, in a nitrogen plasma, the low vibrational states are in the Treanor regime and the high vibrational states in the Boltzmann regime with the two regions joined by a plateau[297,298]. This type of vibrational distribution function is referred to as a Treanor-Gordiets distribution and such distributions have been observed in various nitrogen plasmas[297,299,300]. For the purpose of illustration the two limiting VDFs are shown in figure 9.7 along with data from Kozak and Bogaerts[301] that shows the VDF of a real plasma with the characteristics of a Treanor-Gordiets distribution. The dashed lines in the figure are positioned to indicate the three regions of the Treanor-Gordiets distribution, with Treanor behaviour on the left, the plateau in the middle and Boltzmann behaviour on the right. The figure is adapted from de la Fuente *et al.*[10].

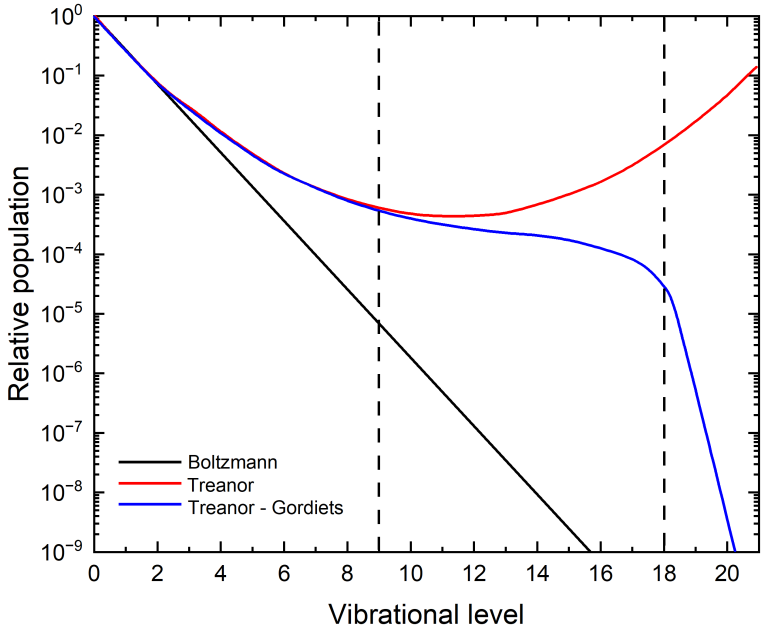

Figure 9.7: Examples of the possible vibrational energy distribution functions relevant to nitrogen plasma. Adapted from de la Fuente *et al.*[10]

It is certainly possible that the relatively low vibrational states measured by Thornton[63] could appear close to linear on a Boltzmann plot whilst, in fact, following a Treanor-Gordiets function with a plateau in population at higher vibrational levels and thus this assumption of the model would underestimate the importance of higher vibrational states.

One way to clarify the situation would be to measure more vibrational states of $N_2(A^3\Sigma_u^+)$ in absorption to probe the exact shape of the VDF. This could be achieved by repeating the CRDS experiments presented here on other vibrational bands (with different lasers if necessary) or through the use of a broadband light source (*e.g.* a supercontinuum source) that would, in combination with cavity enhancement, allow many vibrational bands of the first positive system to be probed simultaneously.

A second important assumption inherent in the above discussion is that the vibrational temperature of the $N_2(A^3\Sigma_u^+)$ is representative of the vibrational temperature of $N_2(X^1\Sigma_g^+)$ molecules. The metastable state is more likely to be in vibrational equilibrium with the ground state than, for example, the radiative $N_2(B^3\Pi_g)$ state, however, given the rapid quenching of metastable molecules by atomic nitrogen and the uncertainty as to the vibrational state dependence of this process it is difficult to say with certainty that the VDFs of the two species will be the same. The assumption that the two species are in vibrational equilibrium is necessary however, because ground state molecules are extremely difficult to access spectroscopically and thus direct measurement of their vibration distribution function is challenging. The distribution of high vibrational states in oxygen plasma have been measured using a laser-driven light source to observe absorption on the oxygen Schumann-Runge system between $220 - 400$ nm[141], however, similar allowed systems in nitrogen only occur at even shorter wavelengths so equivalent measurements in nitrogen would require photons in the VUV (< 200 nm), which makes such measurements very technically challenging. Alternatively, the use of a UV optical cavity can enable absorption measurements on the forbidden Lyman-Birge-Hopfield system ($N_2(a^1\Pi_g)$-$N_2(X^1\Sigma_g^+)$)(see for example Macko *et al.*[302] who made measurements of $N_2(X^1\Sigma_g^+, v = 18)$ at ≈ 227 nm) or Raman scattering can be used (see for example Kuhfeld *et al.*[303]). A final alternative that could enable high vibrational states of $N_2(X^1\Sigma_g^+)$ to be probed is CRDS on the forbidden Vegard-Kaplan systems ($N_2(A^3\Sigma_u^+)$-$N_2(X^1\Sigma_g^+)$), the vibrational bands of which extend through the visible and into the near infrared (*e.g.* the (6, 22) band occurs at around 750 nm[304]). Einstein A coefficients for the Vegard-Kaplan bands in the visible and near infrared are typically between 10^{-2} and 10^{-3} s^{-1} and would

therefore only be observable if the much stronger lines of the allowed first positive and Meinel systems could be avoided.

On the face of it, given that the adjustments for vibrational excitation in the model typically only lead to a change of around 10% in the rate coefficient for electron impact processes, it ought to make little difference if the model underestimates the number of molecules in high vibrational levels (which are small compared to $v = 0$ even for a Treanor-Gordiets distribution). Likewise, if the VDF for $N_2(X^1\Sigma_g^+)$ is somewhat different to that for $N_2(A^3\Sigma_u^+)$, this too would be expected only to have a small effect. However, it is possible that vibrationally excited species might react significantly more quickly than ground state molecules in ways not accounted for by simple threshold shifting, or indeed that they might be able to undergo additional gas phase processes by virtue of their significant vibrational energy. One example of such a process is electron impact dissociation. In the model a simple threshold shift is applied, however the theoretical work of Laporta *et al.*[305] shows this to be a gross oversimplification. In fact it is found that, as well as having a lower threshold energy, the electron impact dissociation of vibrationally excited molecules have significantly greater cross sections (for example $v = 10$ molecules have a threshold nearly 3 eV lower than $v = 0$ but also cross sections approximately two orders of magnitude greater). Such enhanced cross sections for vibrationally excited molecules combined with the plateau expected for a Treanor-Gordiets VDF could make such processes extremely important in determining the plasma chemistry. Likewise the reactions between heavy species could conceivably have rates that depend strongly on vibration state, although in this case data for vibrationally excited molecules is often not available. The rate of reaction 27 was measured by Piper[197] for both $v = 0$ and $v = 1$ $N_2(A^3\Sigma_u^+)$ molecules and there was no conclusive evidence of different rate coefficients for the two vibrational states, but this possibility cannot be discounted. Similarly, reaction 25 (metastable quenching by ground state molecules) is known to be slow for $N_2(X^1\Sigma_g^+, v = 0)$ but could be significantly faster for vibrationally excited molecules, in which case this quenching could be important for loss of metastable molecules, while the pooling reaction (reaction 26) could also change the balance of the various species if it were more efficient amongst vibrationally excited molecules (again Piper[195,196] probed rate coefficients for $v = 0$ and $v = 1$ molecules and in this case some vibrational state dependence was observed).

Finally, vibrationally excited molecules are capable of undergoing addition reactions by virtue of their additional internal energy. In particular Sadeghi *et al.*[240] and

Volynets *et al.*[276] include the following reactions:

$$N_2(X^1\Sigma_g^+, v \geq 12) + N_2(X^1\Sigma_g^+, v \geq 12) \rightarrow N_2(X^1\Sigma_g^+) + N_2(A^3\Sigma_u^+) \tag{9.17}$$

$$N_2(X^1\Sigma_g^+, v \geq 10) + N(^2P) \rightarrow N_2(A^3\Sigma_u^+) + N(^4S) \tag{9.18}$$

$$N_2(X^1\Sigma_g^+, v \geq 14) + N(^2D) \rightarrow N_2(A^3\Sigma_u^+) + N(^4S) \tag{9.19}$$

$$N_2(X^1\Sigma_g^+, v \geq 25) + N(^4S) \rightarrow N_2(A^3\Sigma_u^+) + N(^4S). \tag{9.20}$$

These reactions are used to account for the production of $N_2(A^3\Sigma_u^+)$ in the short lived afterglow (SLA)[240]. Although, within the constraints of the current model none of these reactions are significant, a non-Boltzmann VDF could increase their importance markedly.

A final possibility that could explain the disagreements between model and experiment is the choice of electron energy distribution function (EEDF). For the sake of simplicity the model assumes a Maxwellian EEDF in calculating its rate coefficients. In reality, the EEDF is likely to deviate from a Maxwellian, with the extent of the deviation strongly influenced by gas pressure and plasma power. Previous work utilising Langmuir probes in Nitrogen ICPs[28] found EEDFs that were close to Maxwellian in the H-mode for electron energies less than ≈ 12 eV but showed a depletion in the density of electrons with energy greater than ≈ 12 eV at 100 mTorr. In the E-mode, the deviation from a Maxwellian distribution was much more significant, in particular, a significant hole in the EEDF is observed at around 3 eV (the energy at which the electron impact vibrational excitation cross section peaks).

All the data measured here utilised the H-mode of the plasma, hence the depleted high energy electrons are the most important effect. Crucially, it is precisely these high energy electrons which are responsible for producing N_2^+ by electron impact ionisation (which has a threshold energy ≈ 16 eV). The model uses the kinetic balance of these ions to find an electron temperature and thus the ion production kinetics are vital to the success of the model. The electron temperature found by the model is the value that ensures the correct fraction of the electrons have sufficient energy to cause ionisation, such that production and loss of the ions are balanced and the equilibrium concentration matches the experimental value. For a realistic alternative EEDF (with depleted high energy electrons) a higher mean electron energy would be required to obtain the same fraction of electrons with sufficient energy to cause ionisation. Thus, the electron temperature found by the model would represent an underestimate of the mean energy of the electrons actually present in the plasma. This would have a knock on effect on the other electron impact processes in the model. Electron impact

dissociation and excitation have lower threshold energies than ionisation ($\approx$ 12 and 8 eV respectively). This means that the real EEDF (with a higher average energy but depleted electron densities at high energy) would be expected to have higher densities of electrons with energy sufficient to cause dissociation and excitation than the Maxwellian found by the model. In other words, if the real EEDF has depleted high energy electrons but the model uses a Maxwellian, then the modelled electron temperature which successfully balances ion production and loss will underestimate the production rates of atoms and excited molecules. The increased production rates of atoms and metastable molecules that would be found if a more realistic non-Maxwellian EEDF was used could also have a significant impact on the modelled results.

9.4 Conclusions

In order to support the results of the CRDS measurements on N_2^+ a kinetic model of the plasma was constructed which can reproduce measured ionic densities using reasonable electron temperatures. This model predicts that electron temperature decreases with pressure, in line with previous planar probe measurements[64]. Despite this success the model fails to agree with experimental $N_2(A^3\Sigma_u^+)$ and $N(^4S)$ densities. This is a difficulty that has arisen repeatedly in nitrogen plasma models presented in the literature and plausible reasons for the disparity between model and experiment in this case were discussed at length. In the future, the understanding of the important kinetic processes occurring in the plasma would be enhanced significantly by several additional measurements. Quantifying the atom content of the plasma is made difficult by a lack of allowed transitions but would add clarity to the discussion regarding atomic quenching of metastable molecules. Detection would probably be best achieved by TALIF utilising two photons of 206.72 nm[106,306]. The role of vibrationally excited molecules is also of interest in the plasma chemistry and hence direct measurements of the vibrational distribution of ground state nitrogen molecules would also be of significant interest. This too would be a very challenging measurement, with multiphoton processes, VUV absorption or Raman scattering (possible including four-wave mixing in the form of Coherent Anti-Stokes Raman Spectroscopy) the most likely possibilities and all presenting significant practical challenges. Finally the quenching process:

$$N_2(A^3\Sigma_u^+) + N(^4S) \rightarrow N_2(X^1\Sigma_g^+) + N(^2P) \tag{9.21}$$

has been widely acknowledged to play an important role in the kinetics of both atomic and metastable species in nitrogen plasma yet its rate is somewhat uncertain. Measurements to verify the rate coefficient of this process and extend the data to quenching rates for higher vibrational states of metastable molecules would be extremely beneficial to understanding nitrogen ICP.

Chapter 10

Approaching the plasma sheath

Chapter 8 has demonstrated the ability of saturated CRDS to quantify the density of nitrogen cations present in the bulk of the plasma. Of even greater interest, however, is the spatial variation of this density (and the cation temperatures) as the surface of the plasma chamber is approached. This interest in the behaviour of ions in the plasma sheath arises predominantly from their ability to induce surface chemistry, once they have been accelerated across the sheath. Based on the idea that the flux of ions within a collisionless sheath is conserved, it is expected that the ion density should drop through the sheath and also that they should be accelerated in the direction of the chamber wall (as described in section 1.1.6).

10.1 Experimental changes

The optical arrangement used to probe ion and metastable densities near to the lower electrode is identical to that used in the chapter 8 (and described in chapter 1) to probe the plasma bulk. Such ringdown systems are highly sensitive and it would therefore be prohibitively difficult to translate the optical cavity in order to make measurements at different distances from the electrode surface without misaligning it. Instead the old lower electrode assembly is removed and a new, translatable assembly is constructed. The new assembly consists of a grounded and water-cooled planar electrode similar to the original (but with a wider 25 cm diameter) which is now mounted on a vacuum compatible precision translation mount (Zaber) which has a 20 mm range of motion and a precision and reproducibility better than 1 μm. This mount raises the electrode height by $\approx$ 50 mm (refer to figure 1.9) such that, within the 20 mm range of motion of the mount, the electrode clips the cavity modes (see later) and spectra can thus be taken close to the electrode surface. On either side of the electrode there are 5 cm gaps to the chamber side walls (the chamber diameter

is 35 cm). These regions would be expected to contain ions and metastable species when the plasma is on and thus the absorption from these regions might be expected to mask the absorption from directly above the electrode surface, where the signal is expected to be small because of a depletion in ion density within the sheath. To avoid this confounding factor, small steel inserts were constructed that could be placed inside the chamber baffle arms and could protrude 5 cm into the plasma in order to effectively extend the arms right to the edge of the new electrode. The expectation was that, because of the narrow arm diameter and the high wall loss coefficients, these extended arms would be virtually free from $N_2^+(X^2\Sigma_g^+)$ and $N_2(A^3\Sigma_u^+)$ and thus any absorption that is observed will be due to species that are definitely close to the surface of the new electrode. A diagram illustrating these changes is shown in figure 10.1.

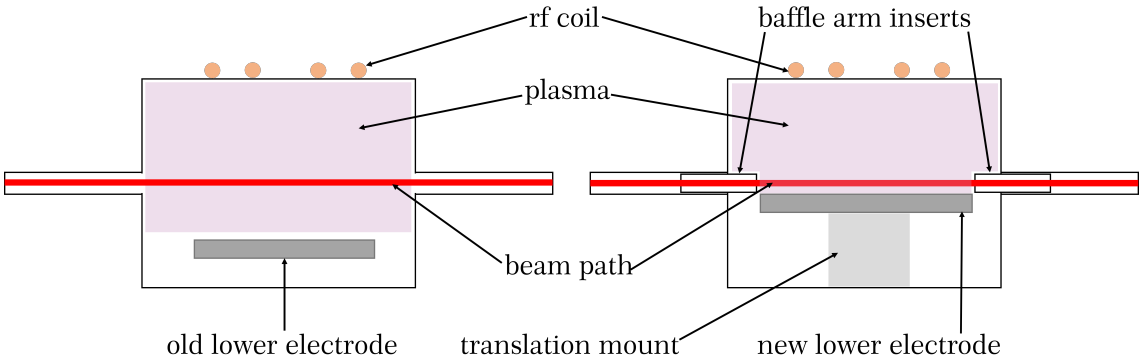

Figure 10.1: A schematic showing the chamber cross section before (left) and after (right) the new, translatable lower electrode was added. Also shown in the new set up are the two inserts added to the baffle arms to ensure that ions being observed are directly above the lower electrode surface.

Figure 10.2 provides a schematic of the various distances which are relevant when describing the new chamber set up, in particular in the geometric considerations of the following section. It should be noted that as the electrode height, h, increases, the distance, d, decreases (*i.e.* $d = h_0 - h$ where h_0 is the (constant) height for which the electrode surface is exactly at the centre of the cavity mode).

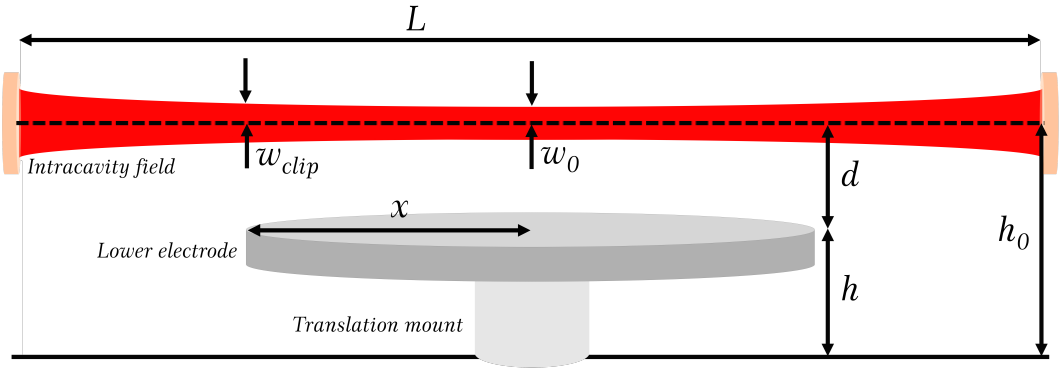

Figure 10.2: A schematic of the distances used to describe the new chamber set up. Of particular importance is the distance d which represents the adjustable separation of the electrode surface and the beam centre.

10.2 Calibration of the cavity-electrode separation

When the optical cavity used for CRDS is precisely aligned the exact height, within the plasma chamber, through which the cavity mode propagates depends on the exact trajectory of the input beam as well as the cavity mirror alignment. Thus, during the course of optimising the ringdown system (*i.e.* aligning the cavity mirrors to excite the TEM_{00} mode as selectively as possible) the exact position of the cavity mode within the chamber may change. Such changes are usually only on the mm scale but given the desire to measure ringdown time as a function of electrode position with an accuracy better than 1 mm these changes need to be accounted for.

Conveniently, as discussed in section 2.5.1, the change in ringdown time as the cavity mode clips the electrode surface means that, as the electrode approaches the cavity mode, the change in ringdown time can be used to precisely calibrate the position of the cavity mode relative to the position of the electrode surface. Recalling that

$$\frac{\tau_0}{\tau_{clip}} = 1 + \frac{\ln f}{\ln R}, \tag{10.1}$$

where τ_{clip} and τ_0 are the ringdown times with and without clipping of the beam, R is the mirror reflectivity and f is the fraction of the beam that is not clipped by the electrode, given by

$$f = \frac{1}{2}\left(1 + \mathrm{erf}\left(\frac{d\sqrt{2}}{w_{clip}}\right)\right), \tag{10.2}$$

where d is the distance between the electrode and the beam centre and w_{clip} is the spot size of the beam in the cavity. From equation A.9 the beam parameter at the centre of the optical cavity, q_0, is given by

$$q_0 = \left(\frac{\pi w_0^2}{\lambda}\right) i. \tag{10.3}$$

It is therefore possible to calculate the beam parameter at the edge of the lower (non-driven) electrode (*i.e.* the point at which the beam will clip the electrode) using the beam propagation matrix for propagation through free space (equation A.10) with the propagation distance x set equal to the radius of the electrode. This yields (by equation A.11) a beam parameter at the electrode edge, q_{clip}, of

$$q_{clip} = \left(\frac{\pi w_0^2}{\lambda}\right) i + x. \tag{10.4}$$

Rationalising this expression, and noting the relationship between its real and imaginary parts and the beam radius of curvature and spot size (see equation A.9) yields a spot size given by:

$$w_{clip}^2 = \left(\frac{x\lambda}{\pi w_0}\right)^2 + w_0^2. \tag{10.5}$$

For the set up used in this chapter $\lambda = 786$ nm, $w_0 = 356$ μm (from equation A.7) and $x = 0.125$ m giving $w_{clip} = 367$ μm. This indicates that the cavity mode is actually fairly well collimated across the diameter of the electrode. With this beam spot size in hand it is possible, by measuring the ringdown time as a function of electrode position, to ascertain the separation of electrode and cavity mode. Figure 10.3 shows measured ringdown times (away from any absorption features) as the electrode height h is varied. Large h corresponds to a small separation, d, between the electrode surface and the cavity mode. A fit of the data according to equation 10.1 is shown in figure 10.3; the fit was performed with $w = w_{clip} = 367\mu$m and with R, τ_0 and h_0 floating and returned values of $R = 0.999962$, $\tau_0 = 68.67\mu$s and $h_0 = 19.83$ mm. Thus the exact separation between the cavity mode and the electrode was calibrated for all electrode heights. This calibration was performed each time the cavity was realigned and thus data taken with different cavity alignments can be compared.

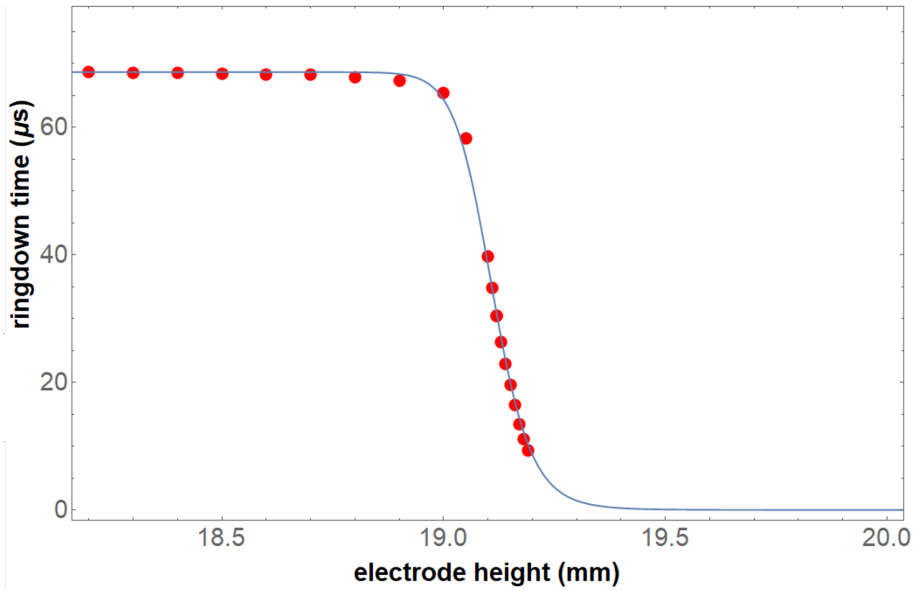

Figure 10.3: The measured change in ringdown time as the height of the electrode (h) was changed (red) fitted according to equation 10.1. The fitting reveals the absolute separation of the electrode and the beam centre.

Another important point to make about the data in figure 10.3 is that, even though the electrode is positioned at 19.83 mm, the ringdown time drops below 10 μs at electrode heights of around 19.2 mm. This is because, with mirror losses being around 1 part in every 25,000, only a very small amount of the beam has to be clipped for clipping losses to be comparable to mirror losses. This means that probing any closer than about 0.5 mm from the chamber wall with this technique is likely to be rather difficult.

10.3 Spatial variation of $N_2^+(X^2\Sigma_g^+)$ density and temperature

10.3.1 Saturation revisited

This chapter utilises the same optical cavity and transition (the $P_{22}(7.5)$ rovibrational line of the (2, 0) band of the N_2^+ Meinel system) as the bulk measurements and thus optical saturation will be important and the saturation parameter should be similar. In order to verify that the deconstruction and reconstruction of the plasma chamber in a new configuration had no effect on the saturation parameter the experiments detailed in section 8.3.2 were repeated in the new set up. In order to optimise the

precision with which saturation parameters can be measured it is important to maximise the absorption signal, and for that reason, the lower electrode was set to its lowest position (to maximise baseline ringdown time) and the plasma was set to high power (400 W) and low pressure (10 mTorr) conditions in order to maximise cation density. Figure 10.4 shows: three spectra taken under different levels of saturation (amplifier gains of $10^5 - 10^7$ V/A) (10.4a); the inferred unsaturated spectra showing very good agreement between the three different conditions (10.4b); and the saturation parameters appropriate for the most saturated conditions (10.4c), found in the same way as before, which enable the unsaturated spectrum to be inferred from the saturated data.

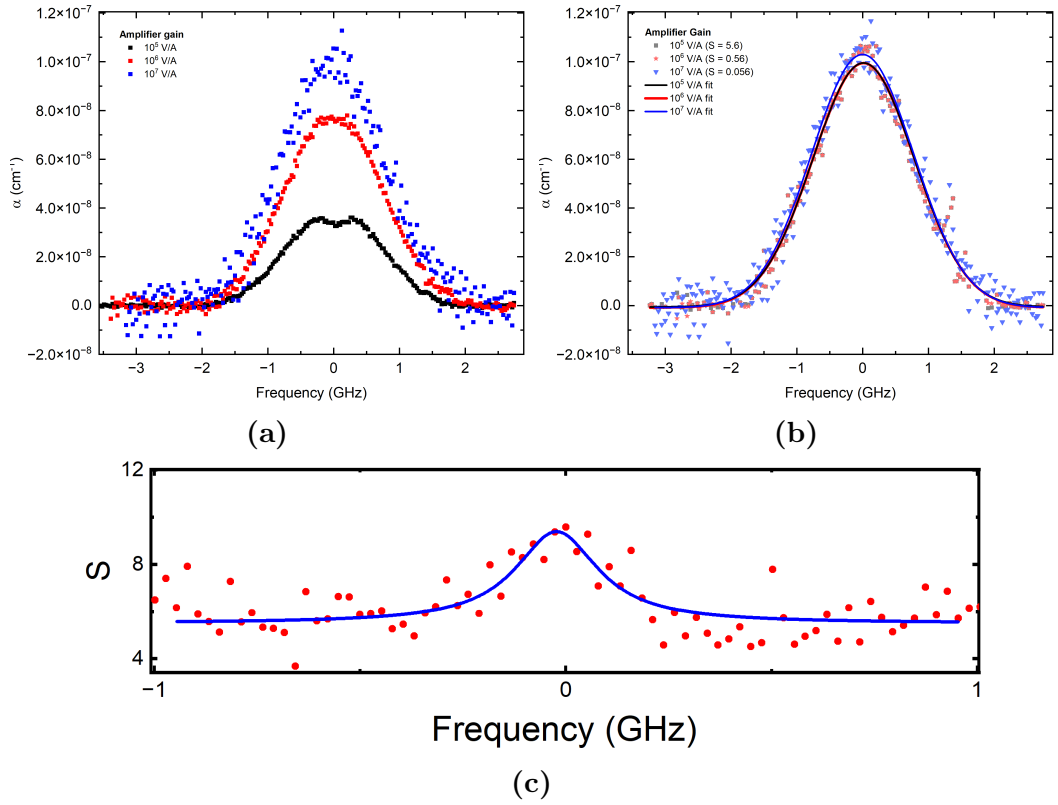

Figure 10.4: (a) Three spectra taken with plasma power of 400 W, pressure of 10 mTorr and different levels of optical saturation. (b) The three inferred unsaturated spectra, each fitting with a Gaussian and showing good agreement. (c) the saturation parameters used to infer unsaturated spectra and found (as before) by using the ratio of the spectra in (a).

Not only is this technique once again successful in allowing unsaturated spectra to be obtained from saturated measurements, it also shows that $S = 5.6 \pm 0.2$ for the most saturated conditions, in excellent agreement with the bulk measurement.

The data also show the approximate doubling of the saturation parameter at the line centre, as is expected for a Lamb dip. It was therefore concluded that rearranging the chamber and realigning the optical cavity had no influence on the level of optical saturation attained in the cavity during a CRDS measurement. The spectra in figure 10.4 correspond to $T_{trans} = 1260 \pm 65$ K and $[N_2^+(X^2\Sigma_g^+, v = 0)] = (1.06 \pm 0.1) \times 10^{10}$ cm^{-3}.

10.3.2 Absorption profiles

Figure 10.5 shows saturated CRD spectra of the $P_{22}(7.5)$ rovibrational line of the (2, 0) band of the N_2^+ Meinel system, taken as a function of the separation between the lower electrode and the beam centre, d, (calibrated as described previously) and with the plasma operating at 10 mTorr and 300 W. The spectra were taken with amplifier gain of 10^6 V/A (*i.e.* with a saturation parameter of 0.56) because it was found that this made for the best signal to noise ratio when d was small. Also shown are Gaussian fits to the data, in each case the data points at the centre of the spectrum (shown slightly faded) were excluded from the fit in order to avoid the fit being unduly influenced by the Lamb dip (which, although difficult to see, is still present).

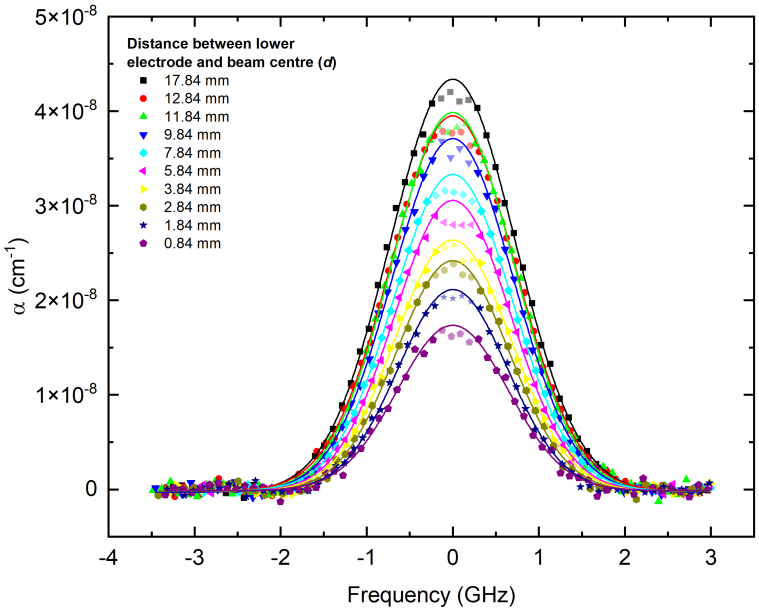

Figure 10.5: A series of spectra, all taken with plasma power of 300 W and pressure of 10 mTorr but with varying electrode height. A clear decrease in absorption coefficients is seen when the beam is very close to the electrode surface. All spectra are fitted with a Gaussian lineshape.

The translational temperatures, T_{trans}, derived from the widths of Gaussian fits to the data in figure 10.5 are shown in figure 10.6 and show a nearly linear change in temperature, with the lowest values found close to the electrode surface ($\approx$ 850 K at $\approx$ 1 mm) and the highest values closest to the plasma bulk ($\approx$ 1100 K at $\approx$ 18 mm). Given that the new lower electrode is water-cooled it is no surprise that species near to its surface are also cooled. Interestingly these temperatures show no sign of the ion acceleration expected near to the chamber wall an observation that will be discussed in detail later.

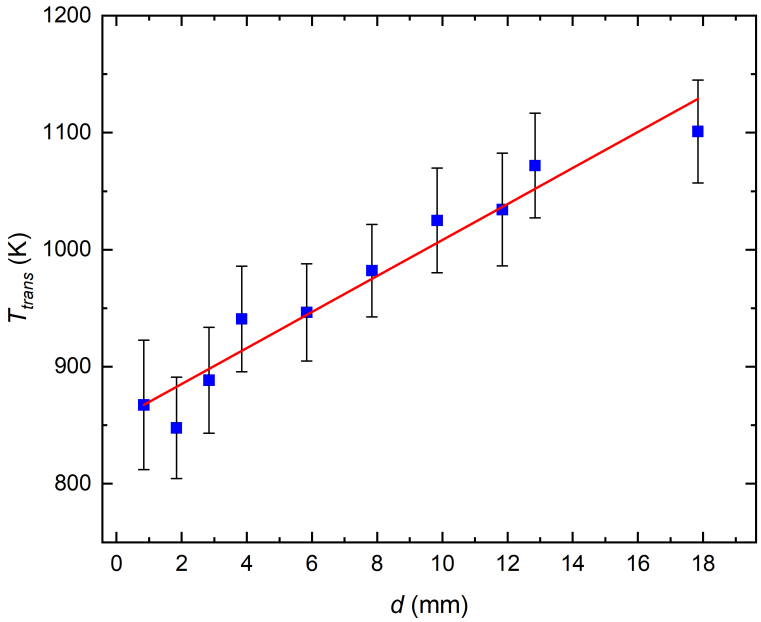

Figure 10.6: Variation of translational temperature with d found using the Gaussian fits from figure 10.5. Gas pressure was 10 mTorr and power 300 W.

As with the bulk measurements, the translational temperatures measured spectroscopically are assumed to be equal to the rotational temperatures, which are used to calculate absorption cross sections at each height for this transition. The resulting densities are, of course, line of sight averaged and thus a length adjustment factor must be applied. In the case of the new set up the appropriate factor is 77/25 and this results in the $v = 0$ ion densities shown in figure 10.7.

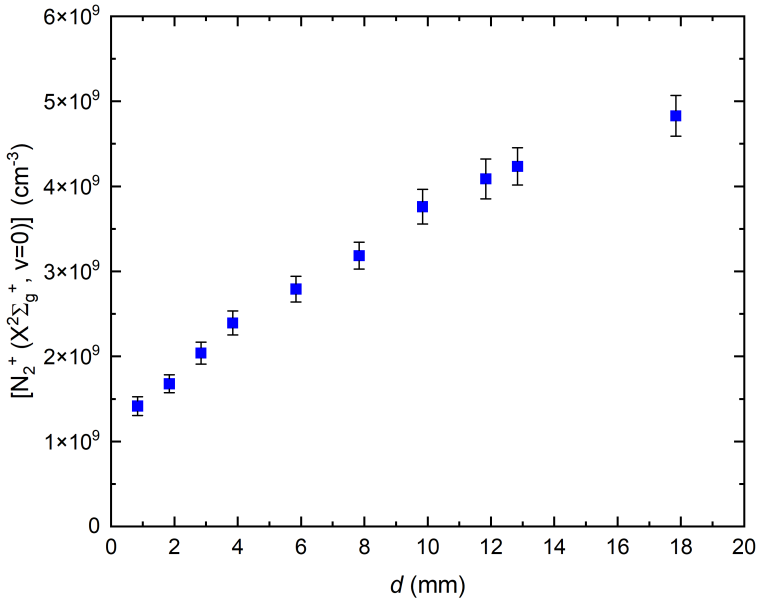

Figure 10.7: Density of $N_2^+(X^2\Sigma_g^+, v = 0)$ as a function of d found from the Gaussian fits to the spectra in figure 10.5 and accounting for saturation and the baffle arms as discussed in the text. Operating conditions are 300W and 10 mTorr.

The ion densities show a monotonic increase as the measurement moves further from the chamber wall with density increasing by a factor of ≈ 4 in the space of 2 cm. There is also a slight curvature to the density profile indicating that the density may be levelling off at larger distances as might be expected as it approaches the bulk value. Chapter 8 found a bulk density of $\approx 9 \times 10^9$ cm^{-3} under these conditions, somewhat higher than the highest value measured here. This indicates either that the change in chamber geometry has altered the bulk cation density and/or that the density continues to increase at distances greater than 2 cm from the electrode.

10.3.3 Wavelength switching

Although complete absorption profiles are required in order to obtain translational temperatures and to obtain the most reliable densities, it is possible (and much quicker) to obtain density information by simply measuring the ringdown time on and off of the absorption resonance. Ideally, in the unsaturated case, the on resonance measurement would be taken on the maximum of the absorption and thus, by calculating the expected Doppler width from the line of fit in figure 10.6, the integrated absorption and hence number density could be inferred. In the case where there is saturation the maximum in the absorption profile is reduced by the presence

of the Lamb dip and hence calculation of the expected area under the full Gaussian profile is difficult (small deviation from the exact centre of the Lamb dip would mean lead to large uncertainties in the saturation parameter). Nevertheless such measurements can still be used to find the relative $v = 0$ ion densities as a function of separation between the cavity mode and the electrode surface. This is possible because the saturated absorption coefficient at line centre, $\alpha_s(\nu_0)$, will be directly proportional to the unsaturated absorption coefficient at line centre, $\alpha_0(\nu_0)$:

$$\alpha_s(\nu_0) \propto \alpha_0(\nu_0). \tag{10.6}$$

The product of this (maximum) absorption coefficient and the FWHM (calculated from figure 10.6) is then proportional to the integrated absorption coefficient, α_{INT}, which is in turn equal to the product of number density and integrated cross section (calculated using PGOPHER at the temperatures taken from figure 10.6).

$$\alpha_0(\nu_0) \times \text{FWHM} \propto \alpha_{INT} = [\text{N}_2^+(\text{X}^2\Sigma_g^+, v = 0)]\sigma_{INT}. \tag{10.7}$$

Thus relative densities can be found according to

$$[\text{N}_2^+(\text{X}^2\Sigma_g^+, v = 0)] \propto \frac{\alpha_s(\nu_0) \times \text{FWHM}}{\sigma_{INT}}. \tag{10.8}$$

These relative densities can then be put on an absolute footing by comparison with results derived from full spectra, and in this way a full density profile can be found whilst only requiring a few full spectra (in order to estimate the temperature profile and to put densities on an absolute footing) to be recorded.

Wavelength switching experiments were carried out under conditions of 300 W and 10 mTorr, 300 W and 100 mTorr and 200 W and 100 mTorr. Under each set of conditions at least 3 full absorption profiles were also obtained (at different separations, d) in order to observe the expected temperature variation as a function of distance from the surface and also to allow the wavelength switching measurements to be scaled to give absolute densities. The resulting Doppler temperatures are depicted in figure 10.8a (note that the blue data points are simply reproduced from figure 10.6). Temperatures at 300 W show a clear drop close to the lower electrode surface whilst at 200 W the temperature varies little with d. Figure 10.8b shows how the density of $v = 0$ ions changes, as a function of distance from the electrode surface, for the three sets of plasma conditions. The filled squares show the data from the switching experiments whilst the empty circles are values derived from the full spectra. The 300 W 10 mTorr switching densities are scaled to match the values from the full spectra

at a distance of 10 mm whilst the other two data sets which having fewer full spectra available are scaled to agree at ≈ 18 mm. Across all the plasma conditions the good agreement between the full spectra and the wavelength switching demonstrate that the latter is effective in finding number densities with good accuracy. Both 300 W data sets show a reduction in density by a factor of $\approx 4-5$ over the 2 cm nearest the wall whilst the 200 W data shows a decrease by one order of magnitude.

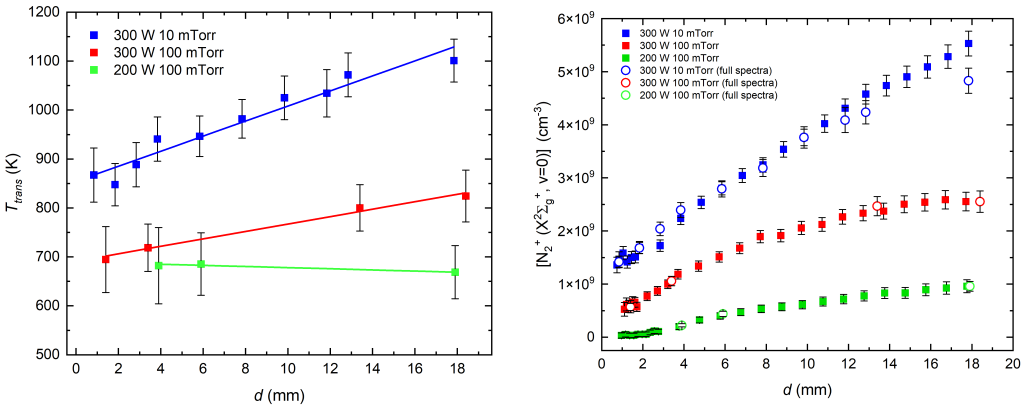

(a) **(b)**

Figure 10.8: (a) Variation of $N_2^+(X^2\Sigma_g^+)$ translational temperatures with d for three different plasma conditions. (b) Variation in $N_2^+(X^2\Sigma_g^+, v=0)$ with d for three plasma conditions showing the good agreement in density trends between the data derived from full spectra (unfilled points) and those found by switching the laser on and off resonance (filled points).

10.4 Discussion

10.4.1 Temperatures

It is clear from the data that, at 300 W, the translational temperature of the ions varies strongly over the full 2 cm range of motion of the translation mount. The temperatures at ≈ 2 cm from the surface are somewhat below those measured in the bulk in chapter 8 (*e.g.* at 300 W 10 mTorr the highest temperature is ≈ 1100 K whilst the bulk measurements found a temperature of ≈ 1250 K). This difference indicates that the temperature is likely to continue to rise for some distance beyond the 2 cm limit of these measurements, although it should be noted that the introduction of the translation mount significantly reduces the plasma volume and this could have an influence on the plasma parameters. On the other hand, the lower power data (200 W) shows a temperature that is virtually constant with position and equal to the bulk value measured in chapter 8. This could be related to the fact this data was

taken after the high power data and the chamber wall may thus have remained hot (effectively chamber hysteresis) but it certainly warrants further investigation as to its reproducibility.

The 200 and 300 W data taken at 100 mTorr both appear to show the same temperature as $d \to 0$ whilst the 10 mTorr data shows a somewhat higher temperature at the wall. This is consistent with the electrode being held at a constant temperature by the water cooling with the adjacent gas being cooled to a greater or lesser extent depending on the pressure and thus the collision frequency with the wall. Interestingly the temperature data shows no sign of the ion acceleration expected near to the chamber wall. This is probably because CRDS necessarily measures temperatures using light that propagates along the optical cavity (parallel to the electrode surface) and acceleration towards the electrode will be perpendicular to the measurement direction.

If the ions undergo relatively few collisions as they traverse the sheath (likely at 10 mTorr) then the acceleration is unlikely to be apparent in the velocity component parallel to the electrode surface. The fact that there is no sign of heating in the "parallel" translational temperature as the wall is approached gives confidence to the assumption that this translational temperature and the rotational distribution of the ions are still in approximate thermal equilibrium in the sheath/presheath (an assumption used to find absorption cross sections). This conclusion is also corroborated by the measurements of Gerassimou *et al.*[214] who found that the rotational temperature of N_2^+ dropped close to the chamber surface in a manner very similar to the drop observed here in parallel translational temperature. Despite this, it is possible that, if the sheath is not collisionless, some of the energy conferred to the ions by the sheath potential could cause some parallel translational heating but that this effect is dominated by the net cooling of the gas close to the water cooled chamber walls. One way of probing if this is the case is to probe how the translational temperature of a neutral species changes close to the chamber wall. Such a species will not be accelerated by the sheath and thus should be cooled by at least as much as the ions near to the wall. The metastable $N_2(A^3\Sigma_u^+)$ state is one such neutral target species.

Comparison with the metastable state

Saturated CRD spectra of the $R_{33}(14)$ rotational line of the (2,0) band of nitrogen's first positive system were obtain at several electrode positions and saturation parameters found in a manner identical to that described in the preceding sections of this

chapter. Despite having a similar absorption cross section to the Meinel band transition these new spectra are found to be significantly more saturated ($S \approx 115$ for spectra taken with 10^5 VA^{-1} amplifier gain) presumably because, whilst the pumping rates are similar for both transitions, the relaxation rate for $N_2^+(A^2\Pi_u)$ must be somewhat higher than that for $N_2(B^3\Pi_g)$ leading to a smaller relative population of the excited state in the former case and thus less saturation. The Doppler width derived translational temperatures for $N_2(A^3\Sigma_u^+)$, found from these spectra, are shown in figure 10.9.

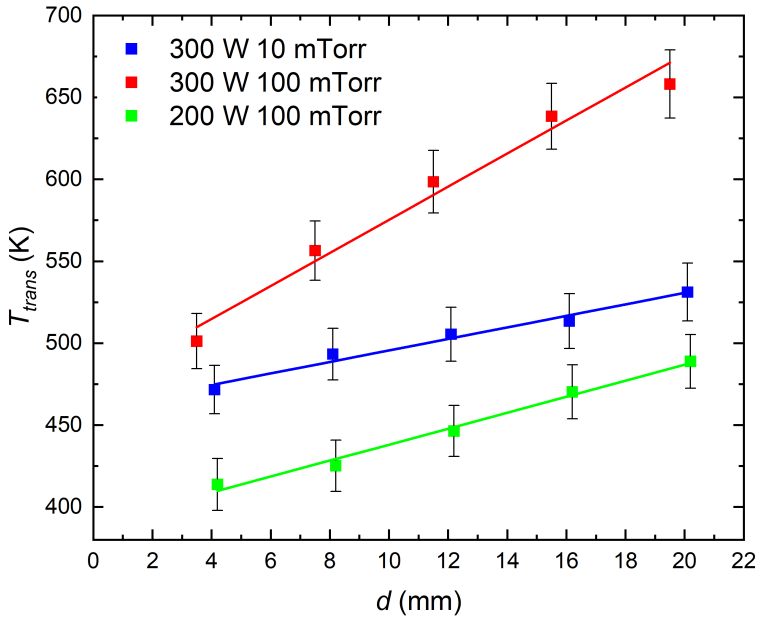

Figure 10.9: Variation of the translational temperature of $N_2(A^3\Sigma_u^+, v = 0)$ with d found by Gaussian fitting of saturated CRDS spectra.

As for the bulk data in chapter 8, it is found that the $N_2(A^3\Sigma_u^+)$ translational temperature is consistently ≈ 200 K lower than the translational temperature for $N_2^+(X^2\Sigma_g^+)$. Both species do, however, show remarkably similar translational temperature variation with height, falling by 150-200 K in the 2 cm near to the wall, and this indicates, as expected for these pressures, that the sheath is not highly collisional and thus the ion acceleration remains in the direction perpendicular to the surface.

10.4.2 Densities

The clear reduction in density shown in figure 10.8b when the electrode surface is approached is testament to the sensitivity of the CRDS technique and verifies that it

is of sufficient sensitivity to detect the sorts of changes in ion density expected in an ICP sheath (see predictions for a Child-Langmuir sheath that are depicted in figure 1.5). Despite this, in the absence of spatially resolved electron density measurements close to the wall, it is impossible to say unequivocally whether these measurements are truly probing the sheath or if there is simply a spatial variation in ion density in the bulk plasma (with the sheath being too small to observe with this technique). Several experiments and models on a range of different rf plasmas (including CCPs and ICPs in argon, neon and nitrogen) indicate that the density of ions varies spatially, even in the regions where quasi-neutrality is conserved, and usually peaks in the middle of the chamber and decreases towards the walls. For example the argon ICP model of Lucken *et al.*[307] found significant breakdown in quasi-neutrality occurred only in a region of about 2 mm thickness next to the wall but found ion density variation in the bulk over several cm. Gerassimou *et al.*[214] observed a nitrogen CCP sheath width of 5 mm (based on the change in ion lifetimes with position) but ion densities that, again, varied over several cm. In this case, under all the plasma conditions, it is found that the $N_2^+(X^2\Sigma_g^+, v = 0)$ density at 2 cm from the chamber wall is only ever around half of the value measured in the bulk in chapter 8. This indicates strongly (despite the change is discharge geometry due to the new translation mount) that the ion density continues to increase significantly beyond the 2 cm measurement region.

There are several reasons for such spatial variation in ion density near to chamber walls on scales much larger than the sheath length. First, because the walls are significant sinks of ions (and high energy electrons) both of these species exist with density gradients from the centre of the chamber towards the walls down which the charged species undergo (ambipolar) diffusion. Within a simple diffusion based model the spatial variation of ion density (n_i) is given by Fick's law[3]:

$$D\nabla^2 n_i(z,r) + k_{iz} n_i(z,r) = 0, \tag{10.9}$$

where the first term accounts for diffusion and the second term accounts for production of cations in the plasma volume (this production is by electron impact but since the plasma is quasi-neutral $k_{iz} n_e(z,r) = k_{iz} n_i(z,r)$). The production term neglects the spatial variation of electron temperature and for an ICP chamber it also neglects the fact that power is delivered into the skin layer rather than uniformly across the plasma. Nevertheless it provides a simple insight into why ion density might vary significantly in the bulk of a plasma confined to a chamber. The lowest order solution within this diffusion controlled approximation consists of the following spatial

variation in ion density[3]:

$$n_i(z,r) = n_0 J_0\left(\frac{2.405r}{R}\right)\cos\left(\frac{\pi z}{H}\right) \tag{10.10}$$

where J_0 is the zeroth order Bessel function of the first kind. This solution assumes as its boundary conditions that the density of ions is zero at the walls. This is clearly unrealistic since zero density but a finite flux of ions towards the walls would imply infinite ion velocity. This solution is displayed graphically in figure 10.10, simply to illustrate the strong spatial variation in ion density that can be inferred without any consideration of sheath effects, the figure also shows a slice through the 2D density profile.

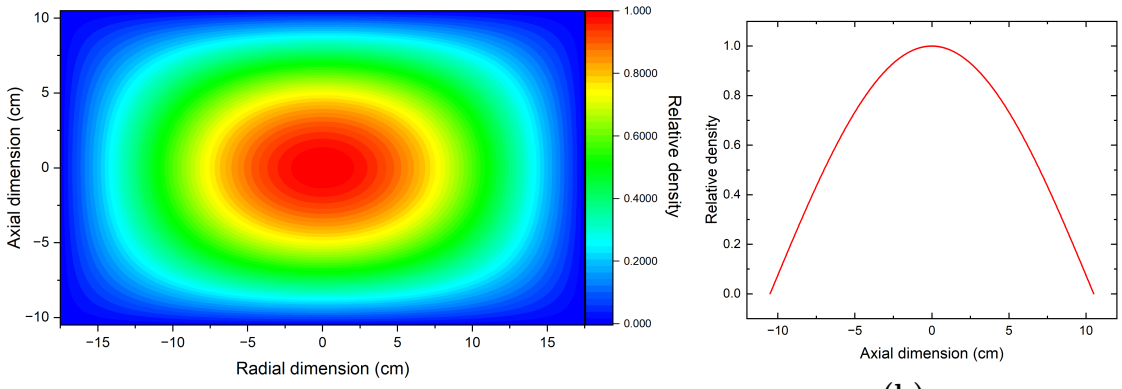

(a) **(b)**

Figure 10.10: (a) Modelled ion density variation in a plasma where ions are only produced by electron impact and only lost by diffusing out of the plasma volume. This figure illustrates the significant ion density gradients that can be present even when sheath effects are neglected. (b) A density profile slice taken from (a) with the radial dimension fixed at 0 and the axial dimension varied.

The real axial density gradient in a nitrogen ICP will be strongly influenced by the fact that power is delivered into the skin region near the top of the chamber. The ionisation of nitrogen molecules requires electron energy in excess of 15 eV and these processes are thus largely localised near to the top of chamber in the vicinity of the rf coil where electron temperatures are highest and from where the ions diffuse into the rest of the chamber (see for example the work of Han *et al.*[308]). The density profile will also be strongly influenced by non-diffusive losses of ions that take place in the bulk, in particular dissociative recombination, which can be an important loss process for molecular cations (see modelling in the previous chapter). Most importantly, the fact that ion density is likely to vary spatially in the bulk of the plasma makes it

somewhat difficult to discern whether or not the measured reduction in density is truly representative of the sheath/presheath or if it is simply a result of diffusion. There are several ways that the situation could be clarified and these are explored in the remainder of this chapter.

Expected sheath characteristics

One way to establish if these data are truly probing the sheath is to estimate how thick the sheath ought to be, either theoretically or by comparison with measurements on similar plasmas (either ICPs in noble gases or nitrogen CCPs). The sheath formed next to an unbiased electrode (or wall) in an ICP ought to be well described by the simple (low voltage) sheath model presented in Chapter 1. Indeed measurements by Tsankov and Czarnetzki[309] in a 10 mTorr 600 W neon plasma found ion energies at the wall reached the value expected for an ion falling through a sheath towards a wall at the floating potential, V_f (see equation 1.37):

$$\langle E \rangle = \frac{eT_e}{2}\left(\ln\frac{m_i}{2\pi m_e}+1\right). \tag{10.11}$$

In the chamber currently under investigation electrical probe measurements by Bakowski[64] in an argon plasma found a voltage drop across the sheath of $3.7T_e$ (compared to $4.7T_e$ expected from equation 10.11). The disparity could be due to the breakdown of the assumption that the sheath is collisionless. A similar effect was seen in simulations by Beving *et al.*[310] where a fluid simulation of the sheath potential drop (*i.e.* equation 10.11) found values that were greater than the potential drop calculated by a more realistic particle in cell (PIC) simulation by a constant offset of the order of T_e, this difference was attributed to particle kinetics that were captured by PIC but not by the fluid model, but no specific kinetic processes were mentioned. Such a sheath is expected to be several times the Debye length at the sheath edge. Tsankov and Czarnetzki[309] observed a sheath thickness of ≈ 10 Debye lengths in a neon plasma, this was typically on the order of 1 mm, whilst the PIC simulations of Beving *et al.*[310] also predict sheath thicknesses of ≈ 10 Debye lengths at 10-100 mTorr. Notably the simpler fluid simulations of Beving *et al.* underestimate the sheath thickness by a factor of 3 for pressure below 1 Torr compared to the PIC results. The Debye length in a plasma with $T_e = 2$ eV and $n_e = 10^{10}$ cm^{-3} (typical of the plasma probed here) is ≈ 0.1 mm (and may be a little bigger at the sheath edge, where electron density is reduced). Thus a sheath thickness of ≈ 1 mm might also be expected in this plasma. The CRDS technique is certainly capable of probing on a sub-mm length

scale and thus the possibility that these measurements are probing the sheath cannot be discounted.

In the region closest to the electrode surface (*i.e.* on the expected length scale of the sheath) the ion density is generally observed to plateau. In the context of the behaviour of a high voltage sheath depicted in figure 1.5b (not strictly applicable here but useful for the sake of comparison) and the similar observations of Woodcock *et al.*[210], Goeckner *et al.*[311] and Fivaz *et al.*[312] this flattening can be tentatively attributed to sheath like behaviour. If the plateau is representative of the sheath then it appears that the sheath is largest (≈ 2 mm) at 200 W and 100 mTorr but smaller at the higher powers. If the sheath is ≈ 10 Debye lengths thick then the change in sheath thickness should be related directly to the change in Debye length with power. At low powers the electron density is small and thus the Debye length (and therefore the sheath) are large. This argument is consistent with these observations and with those of Mutsukura *et al.*[22] who found that the sheath in a nitrogen CCP decreased in thickness as pressure was increased. This can be understood in terms of the decreasing Debye length, caused by an decrease in electron temperature, as pressure is increased. On this basis it would be expected that the plateau in ion density should be more spatially extended for the 10 mTorr 300 W plasma than for the 100 mTorr 300 W case, although the data are inconclusive in this regard.

Comparison with the metastable state

As for the temperature data, a useful comparison can also be made with the metastable density, as a function of position, near the chamber wall. The comparison is particularly useful because both species are produced predominantly by electron impact and thus any spatial variation that arises from non-uniform electron density distributions should be the same for both species. Any difference in their spatial density variation must therefore be due to factors other than electron density changes, *e.g.* spatial variation in electron temperature, the importance of different gas phase processes (atom quenching of the metastable state) or, sheath type behaviour of the ions. As before for the cation, a series of full spectra (which were used to find the translational temperatures in figure 10.9) were used to find absolute densities of $N_2(A^3\Sigma_u^+)$ using saturation parameters found by taking spectra at different levels of saturation. The switching experiment was then used to obtain more complete density profiles and scaled to agree with the full spectra. The results for three plasma conditions are shown in figure 10.11. The densities of $N_2(A^3\Sigma_u^+, v = 0)$ are at least 50 times larger than the densities of cations (figure 10.8b) under the same conditions. Taking the 300

W 100 mTorr data as an example, between 20 mm and 8 mm away from the chamber wall the density of $N_2^+(X^2\Sigma_g^+,\ v=0)$ drops by ≈ 25 % whilst the density of $N_2(A^3\Sigma_u^+,\ v=0)$ drops by ≈ 15 %. In other words their spatial variation in this region is rather similar and this region is certainly not the sheath. On the other hand, between 8 mm and 1 mm the density of $N_2^+(X^2\Sigma_g^+,\ v=0)$ falls by ≈ 75 % whilst the density of $N_2(A^3\Sigma_u^+,\ v=0)$ falls only by around ≈ 25 %. This pattern, with ion densities changing much more rapidly than metastable densities close to the wall is repeated under other plasma conditions and sheath or presheath like behaviour of the ions in this region could contribute to this very different behaviour between the two species. However, a spatially varying EEDF and the importance of dissociative recombination and atomic quenching to the destruction of $N_2^+(X^2\Sigma_g^+)$ and $N_2(A^3\Sigma_u^+)$, respectively, could also conceivably explain the differences in the spatial distributions of the two species. Either way, the spatial distribution of $N_2(A^3\Sigma_u^+,\ v=0)$ is interesting in its own right and the ability of this technique to measure this spatial density variation is of greater potential utility.

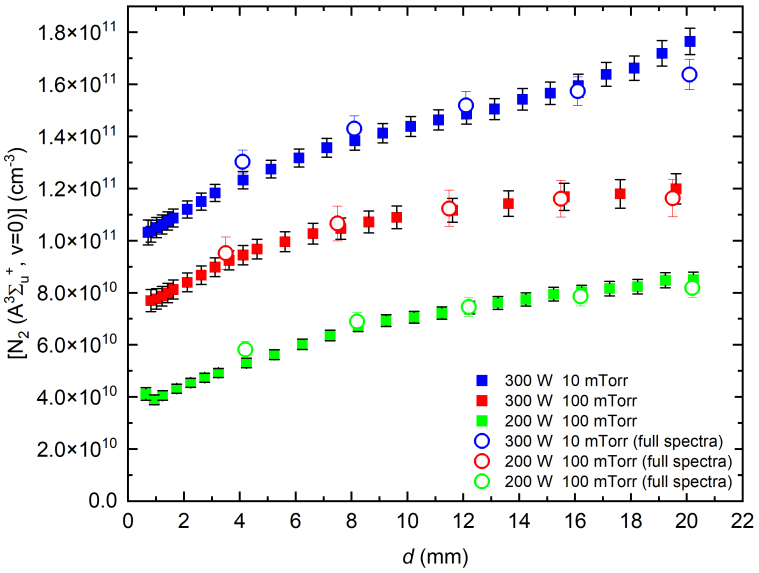

Figure 10.11: Variation in $N_2(A^3\Sigma_u^+,\ v=0)$ density with d, again showing good agreement between full spectra and laser switching experiments and notably a much less significant decrease in density than the corresponding ion profile.

10.4.3 Conclusions

This chapter has described the successful implementation of a unique experimental arrangement to probe the spatial variation of $N_2^+(X^2\Sigma_g^+, v = 0)$ and $N_2(A^3\Sigma_u^+, v = 0)$ density as a function of distance from the surface of an unbiased electrode using saturated CRDS. A very clear and reproducible reduction in the densities of each species is observed as the electrode surface is approached, but it is very difficult to say with any certainty that the sheath is in fact being probed, even for the smallest values of d (≈ 0.5 mm). The spatial limits of the CRD technique in terms of approaching the surface are very similar to the expected extent of the sheath and it is therefore impossible to discern whether the observed variation in ion density with position is simply a result of diffusive losses towards the walls or if sheath like behaviour is indeed being observed. The observed plateau in number density, its extent (as a function of plasma power and pressure) and the difference in behaviour observed for cationic and neutral species both provide some degree of support for the idea that the sheath is indeed being probed but none of these observations are definitive. Nevertheless, the results do represent the first demonstration of the use of CRDS to probe sheath behaviour. The spatial resolution that has been achieved, although on the limit for probing an unbiased sheath, is certainly sufficient to probe the sheath close to a biased electrode and would enable the observation of changes in sheath properties as a function of bias voltage. By considering figure 1.5 it is clear that a DC bias of a few hundred Volts would be expected to produce sheath thicknesses of the order of a cm for the plasma considered here (where the density of electrons at the sheath edge, $n_{e,s}$ is a few 10^9 cm^{-3}). Under these conditions it would also be expected that the ion density profile would be reasonably approximated by Child's law (equation 1.42) or by some collisional alternative (Table 1.1) and the data could then be interpreted, for example, to investigate the collisionality of the sheath at different pressures. Such studies are now being undertaken.

Chapter 11

Saturated CRDS for Doppler-free spectroscopy

The preceding chapters have focused on the measurements of densities and temperatures of species produced in nitrogen plasma using saturated CRDS. The spectra consistently show Lamb dips which, thus far, have been largely ignored as they do not significantly impact the determination of these physicochemical plasma properties. The observation of Lamb dips in the spectra of molecular ions using tunable laser absorption spectroscopy is itself rather novel, with the first such observation coming as recently as 2010[229,230]. This chapter seeks to investigate and understand the characteristics of the Lamb dips, in particular their width. Lamb dips are Doppler free and as such their width should be representative of the other broadening mechanisms which contribute to the total linewidth, namely: pressure, lifetime, transit-time and power broadening. In particular, the dependence of linewidth on transit time through the beam means that ion acceleration through the plasma sheath has implications for the Lamb dip width. Additional contributions to the lineshape can also be caused by unresolved hyperfine structure and this is relevant here because the vast majority of nitrogen atoms are ^{14}N and have a nuclear spin $I = 1$ and thus the transitions probed display hyperfine structure. In certain circumstances, such is the slender nature of the Lamb dip, that when additional broadening effects are small, it can be used to probe the linewidth of cw lasers (see for example Pinto *et al.*[313]). It is concluded in this work that the Lamb dip widths are primarily influenced both by unresolved hyperfine structure in the transitions and by optical power broadening. The inability of these experiments to resolve the hyperfine structure is due predominantly to power broadening of the hyperfine components, and is a necessary consequence of the high sensitivity required to probe ion densities via saturated CRDS. Nevertheless, the potential exists to utilise the sub-Doppler resolution inherent in Lamb dip spectroscopy

to probe ion dynamics in some of the more active regions of the plasma, such as the plasma sheath.

11.1 Lamb dip widths in the plasma bulk

Lamb dips, being Doppler free, are significantly narrower than the absorption lineshape in the elevated temperature and low pressure environment of the plasma. The accurate characterisation of the dips therefore requires much smaller laser frequency steps. In order to achieve the required acquisition resolution the CRD spectra shown in the preceding three chapters were taken with many more points than those taken under unsaturated conditions reported in part II of this thesis (compare, for example, the saturated spectra of figures 8.11 and 8.14 with the unsaturated spectra of figure 4.10 and 4.14). This resolution comes at a significant cost in terms of acquisition time but does mean that many of the spectra already presented in this thesis provide sufficient detail to allow accurate characterisation of the Lamb dip.

In order to find the Lamb dip width the data must be fitted. Fitting according to equation 2.60 is possible, however, the complexity of this function means that inevitably there is interdependence between the fit parameters. Additionally, because this equation attempts to fit the entire absorption profile and the Lamb dip is only a small part of the profile, the least squares fitting sometimes results in poor fitting of the Lamb dip while improving the fit to the rest of the absorption profile. A simpler alternative is to fit a Gaussian baseline (excluding the points which constitute the Lamb dip) and to subtract this from the experimental spectrum to leave only the Lamb dip signal, which can then be fitted with an appropriate lineshape; this simpler approach is utilised in this chapter and examples of this process are shown in figure 11.1. Figures 11.1(a) and 11.1(c) show a Gaussian baseline fitted to the 400 W 100 mTorr data for the $P_{22}(7.5)$ (2, 0) Meinel transition (from figure 8.11) and the $Q_{11}(16)$ (7, 6) first positive transition (from figure 8.14), respectively, whilst 11.1(b) and 11.1(d) show the corresponding Lamb dips with fits. Most broadening mechanisms responsible for the Lamb dip widths (pressure, lifetime and power broadening) are expected to produce a Lorentzian lineshape. Some mechanisms however can lead to Gaussian contributions to the lineshape, for example, transit time broadening[43] or laser linewidth broadening, perhaps as a result of stray rf fields from the plasma power supply (see for example the work of Ciaffoni *et al.*[314] and Pinto *et al.*[313]). For these reasons, exemplar Gaussian and Lorentzian fits to the data are shown in figure 11.1.

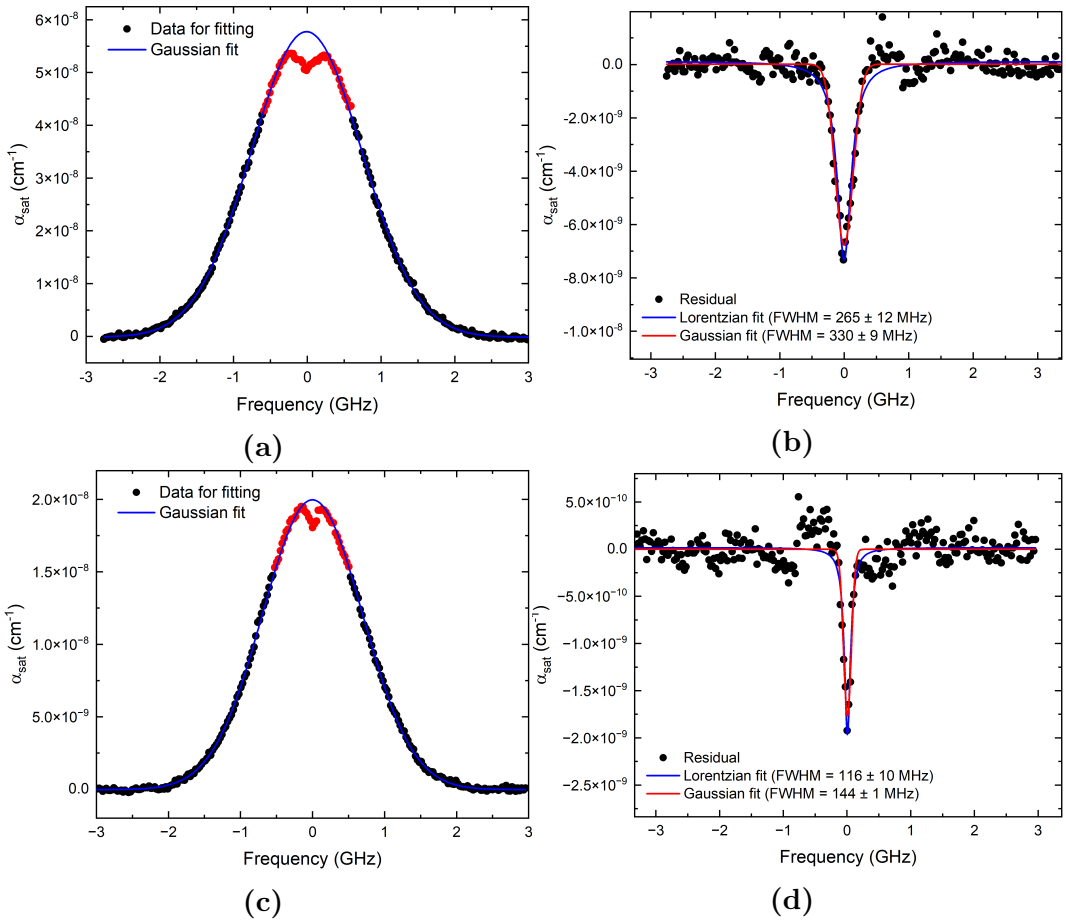

Figure 11.1: (a) The Gaussian baseline fitted to the CRD spectrum of the $P_{22}(7.5), (2,0)$ transition of the N_2^+ Meinel system at 400 W and 100 mTorr. Red points, which constitute the Lamb dip, are excluded from the baseline fit. (b) The residual of the fit in (a) showing the Lamb dip fitted with a Lorentzian and a Gaussian lineshape. (c) The baseline fitting for the $Q_{11}(16)(7,6)$ transition of the N_2 first positive system at 400 W and 100 mTorr. (d) The residual of (c) with the Lamb dip fitted with a Lorentzian and a Gaussian lineshape.

Figure 11.1 shows a couple of interesting features. First, the widths of the Lamb dips for both species are relatively large, taking values of 330 MHz for $N_2^+(X^2\Sigma_g^+)$ and 116 MHz for $N_2(A^3\Sigma_u^+)$; this is remarkably wide compared with expected Lamb dip widths of the order of 100s of kHz at such low pressures (dependent on the transition Einstein A-factor and pressure broadening parameters, *vide infra*). The possible reasons for this extraordinary width is the focus of much of this chapter. Secondly, the two species show Lamb dip widths that differ by a factor of 2-3, this too is not necessarily expected and its origin will also be considered in this chapter. Finally, it should be noted that these measurements show excellent sensitivity, with CRDS showing baseline deviations $< 5 \times 10^{-10}$ cm^{-1} in many of the spectra.

One salient point to consider is whether the choice to fit saturated ringdown signals with an exponential function markedly affects the resulting Lamb dip width. The arguments made previously (section 8.3.3) suggest that the Doppler free lineshapes found using exponential fitting should be meaningful and this conclusion is supported by the use of exponential fittings in similar experiments used to observe Lamb dips in water[257] and acetylene[315]. The recent work of Aiello *et al.*[316] is also particularly useful as it investigates the difference between fitting with a simple exponential or fully accounting for the effects of saturation on the ringdown signal. The different fitting approaches result in dips that differ in width by $\approx 40\%$, a difference that arises because the exponential fitting can only give an approximate (although consistent) quantification of the saturation and therefore produces Lamb dips which still exhibit the influence of power broadening. In the non-exponential model the power broadening information is encapsulated in a separate fitting parameter and lineshapes can be retrieved that are free from the influence of power broadening, and are consequently narrower than those determined using simple exponential fitting. Nevertheless, the work of Aiello *et al.*[316] clearly indicates that Lamb dips found by fitting saturated CRDS signals with an exponential function do yield results that are physically meaningful, provided one remembers that the treatment does not intrinsically address saturation effects (*e.g.* power broadening).

Before the likely broadening mechanisms for the Lamb dips are considered in detail the variation in dip width with various experimental conditions is worthy of investigation, which should give some indication as to which broadening mechanisms are significant. As a first example, figure 11.2 shows how the Lamb dip widths vary for $N_2^+(X^2\Sigma_g^+)$ and $N_2(A^3\Sigma_u^+)$ as a function of plasma power and pressure. The widths once again show a clear difference between the two species, but no clear trends with either plasma power or pressure are apparent. This indicates that neither electron impact processes nor collisions with parent molecules contribute significantly to changes in the optical saturation over these operating conditions. The scatter on the data, particularly at low power for $N_2^+(X^2\Sigma_g^+)$, is a result of the difficulty in background subtraction at such a small level of absorption (both when finding absorption coefficients from ringdown data and when subtracting the Gaussian baseline to fit the data).

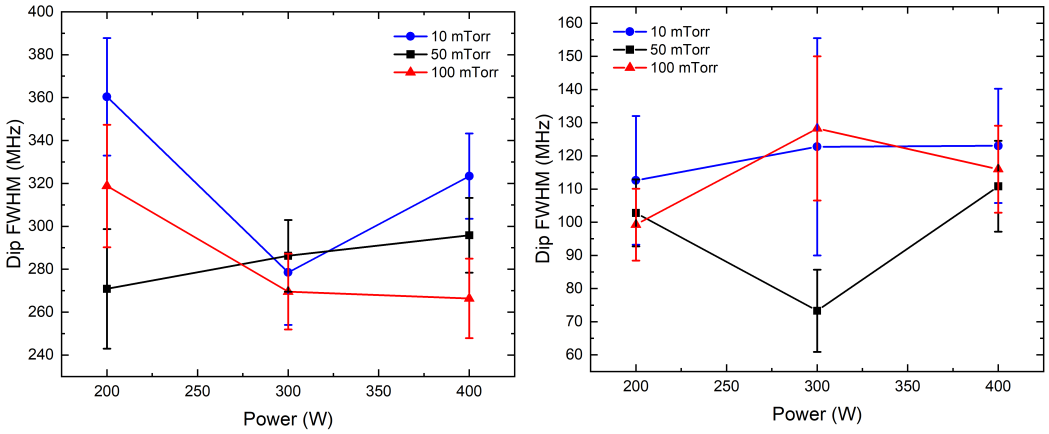

Figure 11.2: (a) The variation of Lamb dip width with plasma power and pressure for the $P_{22}(7.5)(2,0)$ transition of the Meinel system of N_2^+. (b) The variation of Lamb dip width with plasma power and pressure for the $Q_{11}(16)(7,6)$ transition of the first positive system of N_2.

The contribution of power broadening to the Lamb dip width can be investigated by varying the intracavity saturation parameter and observing the outcome. The $P_{22}(7.5)$ spectra for N_2^+ are shown in figure 11.3(a) and (c) for amplifier gains of 10^5 and 10^6 V A^{-1}, respectively, with the corresponding Lamb dips shown in figure 11.3(b) and (d), these may be compared with data shown previously in figure 8.5. As expected, the less saturated spectrum shows a narrower Lamb dip width (206±30 MHz vs 302 ± 18 MHz). Interestingly, it is not just narrower than the dip in figure 11.3(a) and (b) but also narrower than all the widths presented in figure 11.2 which were taken under the more saturated conditions (10^5 V A^{-1}). This provides convincing evidence that the Lamb dip is power broadened, as would be expected given the saturation parameters found in the preceding chapters.

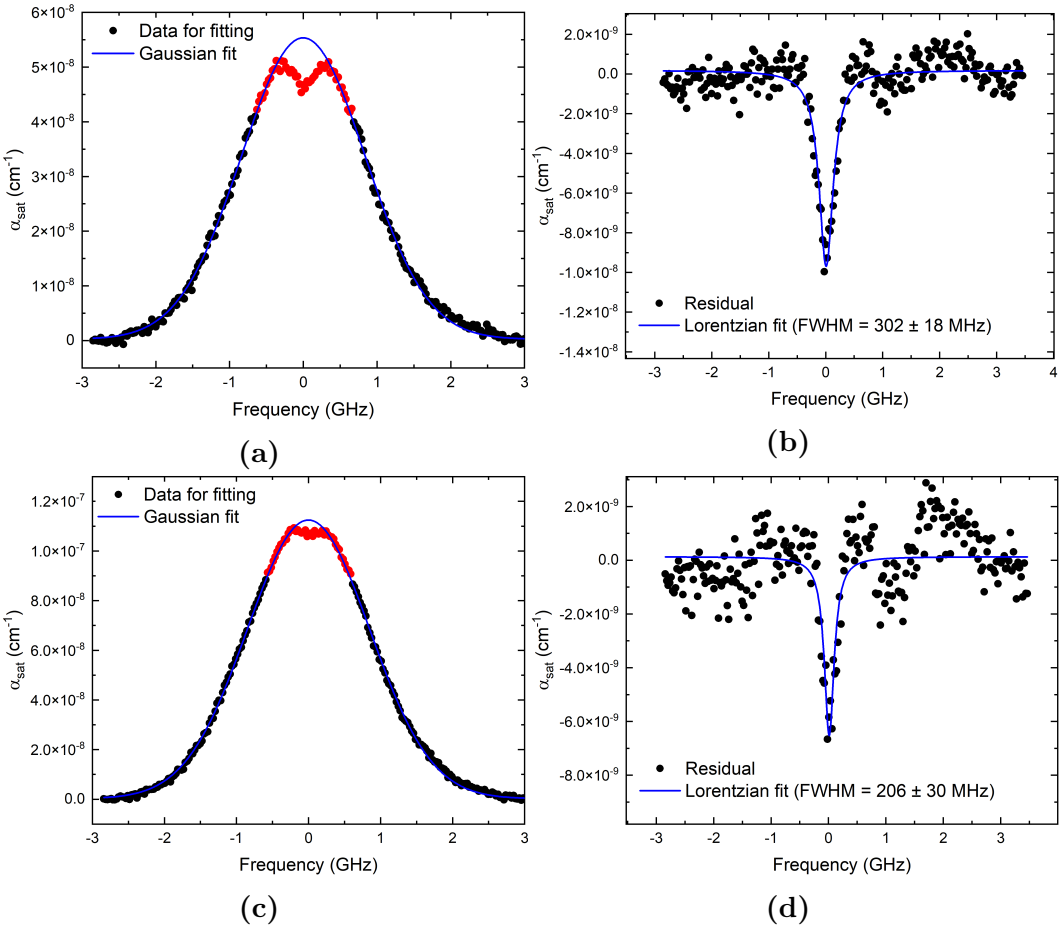

Figure 11.3: (a) The Gaussian baseline fittings to the $P_{22}(7.5)$ Meinel system spectrum taken at 400 W and 10 mTorr, with a transimpedance amplifier gain of 10^5 V A^{-1}. Red points are excluded from the baseline fitting. The resulting Lorentzian fit of the residual dip is shown in (b). Panels (c) and (d) show the equivalent spectra and Lamb dip for a transimpedance amplifier gain of 10^6 V A^{-1}.

As discussed in chapter 2, for a power broadened Lamb dip, the width, $\Delta\nu_{L,S}$, can be expressed as:

$$\Delta\nu_{L,S} \approx \Delta\nu_L\sqrt{1+S}. \tag{11.1}$$

where $\Delta\nu_L$ is the homogeneous width without power broadening and S is the saturation parameter[58,70]. Taking $S = 5.6$ and $S = 0.56$ for the two cases from chapter 8 allows $\Delta\nu_L$ to be estimated for each of the spectra in figure 11.3. For the more saturated spectrum (10^5 V A^{-1}) this yields $\Delta\nu_L = 118 \pm 7$ MHz whilst for the less saturated spectrum (10^6 V A^{-1}) one finds $\Delta\nu_L = 165 \pm 24$ MHz. Although these two values are not in perfect agreement it is worth noting that the errors on the values are simply derived from the error in the fitting parameters. The data in figure 11.2 indicates that the uncertainty associated with the reproducibility of the experiment

is somewhat larger than this fitting error. With this in mind it is certainly plausible that the difference in Lamb dip widths observed in figure 11.3 can be explained by power broadening. This leaves a homogenous width excluding power broadening of $\approx 140 \pm 40$ MHz which remains to be accounted for by other broadening mechanisms.

11.2 Approaching the plasma sheath

The adjustments to the chamber described in the previous chapter make it possible to observe the Lamb dip as a function of the distance, d, between the beam centre and the electrode surface. The spectra in chapter 9 generally have frequency steps too large to make reliable Lamb dip widths retrievable and therefore additional spectra were obtained in order to investigate if the dip width changes significantly with d. Figure 11.4 shows Lamb dip data extracted from the high resolution spectra of the $P_{22}(7.5)(2,0)$ transition of the N_2^+ Meinel system. Spectra were taken at three electrode heights and all of the residuals show a significant scatter about the baselines as a result of the small absorption coefficients close to the electrode surface. This scatter makes the extraction of reliable Lamb dip widths difficult, although figures 11.4(a) and (b) suggest Lamb dip widths of (246 ± 33) and (298 ± 36) MHz, in keeping with the bulk measurements on this transition. Meanwhile a spectrum at $d = 6$ mm (not shown) only yields a signal to noise ratio of ≈ 2 and its width of 396 ± 98 MHz is therefore not statistically significantly different from the others.

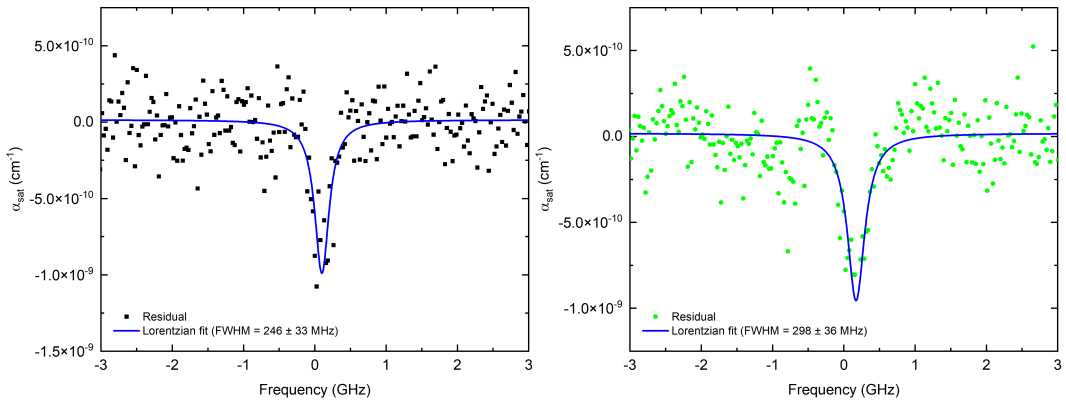

(a) $d = 18.0$ mm **(b)** $d = 8.0$ mm

Figure 11.4: Lamb dips for the $P_{22}(7.5)(2,0)$ transition of the Meinel system at two different electrode-beam separations, d, in a 200 W 100 mTorr plasma. The resulting Lamb dips are shown for (a) $d = 18$ mm and (b) $d = 8$ mm.

In order to attempt to be more definite about potential d-dependent behaviour a second Meinel system transition was investigated. The $Q_{22}(11.5)(2,0)$ transition was

chosen because of its larger cross section (around twice that for $P_{22}(7.5)$ at typical plasma temperatures) and because of its good separation from first positive system transitions. Spectra at two different electrode heights (for 100 mTorr and 300 W) were obtained for the $Q_{22}(11.5)$ transition and showed a significantly improved signal to noise ratio compared to $P_{22}(7.5)$ and the same Doppler width (as expected). The Lamb dip fits for these two spectra are shown in figures 11.5(a) and (b) and both show almost identical dip widths (109 ± 5 MHz at 19.5 mm from the electrode surface and 106 ± 16 MHz at 2.5 mm from the electrode surface). It is notable that this transition shows Lamb dips that are significantly deeper and narrower (≈ 100 MHz) than those for the $P_{22}(7.5)$ transition. Given that these are measurements of the same species (except for the different rotational states), the significant difference in the dip widths is a rather curious observation and worthy of further investigation.

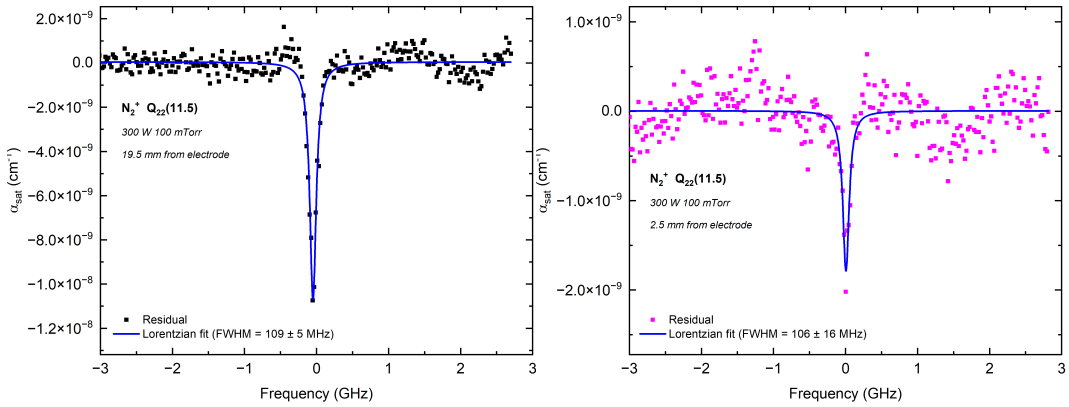

(a) $d = 19.5$ mm **(b)** $d = 2.5$ mm

Figure 11.5: Lamb dips for the $Q_{22}(11.5)$ (2, 0) transition of the Meinel system at two distances from the chamber lower electrode: (a) $d = 19.5$ mm and (b) $d = 2.5$ mm. Spectra were obtain with plasma power of 300 W and an operating pressure of 100 mTorr.

One clear question that arises is whether the differences in width occur because the transitions belong to different rotational branches, or if they are a result of the different rotational states from which the transitions originate. In order to investigate this, spectra were taken of the complementary $P_{22}(11.5)$ (figure 11.6(a)) and $Q_{22}(7.5)$ (figure 11.6(b)) rotational lines. The $P_{22}(11.5)$ transition (figure 11.6(a)) shows a Lamb dip width of 328 ± 40 MHz, in good agreement with the widths observed for the $P_{22}(7.5)$ transition (figure 11.4). Meanwhile the $Q_{22}(7.5)$ transition (figure 11.6(b)) shows a width of 114 ± 7 MHz, in good agreement for the dips measured for $Q_{22}(11.5)$ (figure 11.5). Clearly, the dip widths are most strongly influenced by

rotational branch rather than rotational state in the range of J values investigated here.

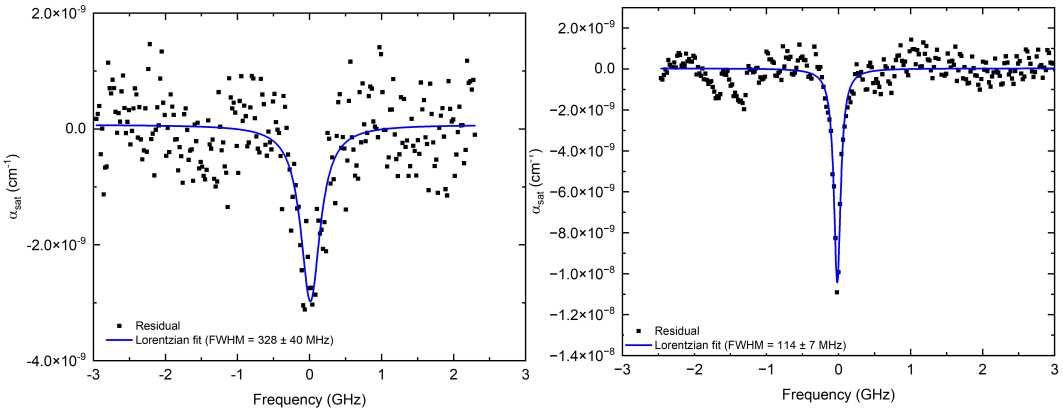

(a) $P_{22}(11.5)$ **(b)** $Q_{22}(7.5)$

Figure 11.6: Lamb dips from (a) the $P_{22}(11.5)$ (2, 0) transition and (b) the $Q_{22}(7.5)$ (2, 0) transition of the Meinel system at $d = 19.5$ mm. Spectra were obtain with plasma power of 300 W and an operating pressure of 100 mTorr.

Within the local wavelength region (≈ 770 nm) once again it is also convenient to compare these Meinel system transitions with transitions in the first positive system; thus probing $N_2(A^3\Sigma_u^+)$ as the electrode height is varied. Figure 11.7 shows spectra of the $Q_{22}(15)$ rotational transition of the $(2, 0)$ band of the first positive system. The observed Lamb dip widths are 133 ± 15 and 105 ± 10 MHz at $d = 19.8$ and 2.8 mm, respectively. Further spectra of the $R_{33}(14)$ transition show widths between 112 and 143 MHz with no clear trend with d. Both transitions show (within the experimental uncertainty) identical Lamb dip widths, suggesting that the dip widths for $N_2(A^3\Sigma_u^+)$ are not as strongly dependent on the rotational branch as they are for $N_2^+(X^2\Sigma_g^+)$, at least for this limited set of transitions.

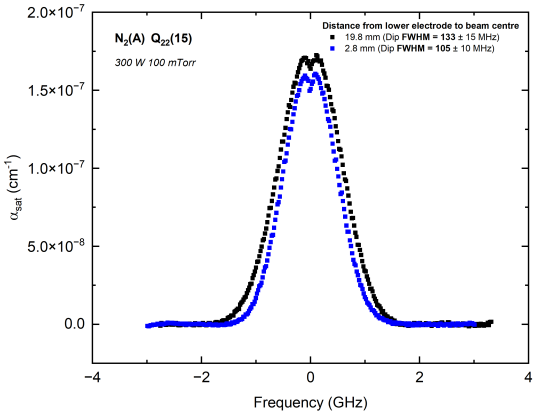

Figure 11.7: Spectra of the $Q_{22}(15)$ transition of the (2, 0) band of the first positive system at two separations d. The Lamb dip widths are reported in the figure legend and show no significant variation with d. Spectra were obtain with plasma power of 300 W and an operating pressure of 100 mTorr.

Table 11.1: The transitions and their associated Lamb dip widths reported in this chapter (because the dip widths show no clear change with plasma conditions or height above the lower electrode, the values are taken from the most significant data).

Vibronic transition	Rotational transition	Dip width / MHz
$N_2^+(A^2\Pi_u, v=2) \leftarrow N_2^+(X^2\Sigma_g^+, v=0)$	$P_{22}(7.5)$	302 ± 18
$N_2^+(A^2\Pi_u, v=2) \leftarrow N_2^+(X^2\Sigma_g^+, v=0)$	$P_{22}(11.5)$	328 ± 40
$N_2^+(A^2\Pi_u, v=2) \leftarrow N_2^+(X^2\Sigma_g^+, v=0)$	$Q_{22}(7.5)$	114 ± 7
$N_2^+(A^2\Pi_u, v=2) \leftarrow N_2^+(X^2\Sigma_g^+, v=0)$	$Q_{22}(11.5)$	109 ± 5
$N_2(B^3\Pi_g, v=7) \leftarrow N_2(A^3\Sigma_u^+, v=6)$	$Q_{11}(16)$	116 ± 10
$N_2(B^3\Pi_g, v=2) \leftarrow N_2(A^3\Sigma_u^+, v=0)$	$R_{33}(14)$	112 ± 10
$N_2(B^3\Pi_g, v=2) \leftarrow N_2(A^3\Sigma_u^+, v=0)$	$Q_{22}(15)$	133 ± 15

To summarise, the transitions for which Lamb dips have been observed and which are reported in this chapter are presented in table 11.1. The observations show that, whilst the Lamb dips associated with absorption by $N_2(A^3\Sigma_u^+)$ and $N_2^+(X^2\Sigma_g^+)$ show no change with the electrode separation d, the Lamb dips for the ions seem to show an unusual effect whereby the widths of the Lamb dips depend on the rotational branch to which the transition belongs (*i.e.* the Q_{22} branch transitions are consistently over 150 MHz narrower than the P_{22} branch transitions). As noted previously, both species show Lamb dips that are unusually wide and this persists into the pre-sheath region.

11.3 Discussion

In order to try to understand the extraordinarily wide Lamb dips observed in this work it is worth considering carefully the likely magnitude of the contributions to the dip width from the various line broadening mechanisms at play. This section considers first the possibility that the laser linewidth might be responsible and secondly the likely sources of broadening arising from the absorber itself.

11.3.1 Broadening due to the laser: a self-heterodyne beat note study

Perhaps the most obvious contributor to the Lamb dip width is the laser linewidth. In order to verify that this is not the dominant contribution here, *i.e.* that the laser linewidth is negligible compared to the width of the Lamb dips, a self-heterodyne beat note experiment was performed. The basic principle of a beat note experiment to measure the laser linewidth is as follows. If the laser beam is coaligned with a reference beam of narrow linewidth onto a detector of suitable bandwidth then the resultant signal contains frequency components at both the sum and difference of the laser and the reference frequencies. Provided the difference frequency is sufficiently small (*e.g.* of the order of 10s or 100s MHz) then it can be detected by a fast detector (*e.g.* a photodiode or photomultiplier tube). When this so called beat note signal is analysed using a spectrum analyser, a peak is observed at the difference frequency and the width of this peak corresponds to the laser linewidth.

In practise an arbitrarily narrow reference signal is hard to come by, ultrastable atomic clock signals can be used but these fail to fulfil the requirement that the difference frequency should be small for most laser frequencies. An alternative is to produce two beams from a single laser and beat those against one another. This is achieved by using an AOM which, as well as diverting the diffracted beams spatially also shifts their frequency by the AOM drive frequency (in the case of these experiments 200 MHz). The zeroth and first order beams therefore have a difference frequency of 200 MHz and thus a beat note signal can be detected when they are coincident on a detector.

The laser linewidth is associated with phase noise and the more often the output of the laser changes phase the less well defined its frequency and hence the broader its linewidth[317]. The characteristic time between substantial random changes in the phase of the laser output is known as the coherence time. The laser coherence however leads to a problem when combining the two output beams which originate from the

same source as they will necessarily have the same phase noise and their phases will be strongly correlated, and thus their beat note will not be representative of the laser linewidth. One way in which the phases of the two beams can be decorrelated, to give two beams with a quasi-random phase relationship, is by delaying one of the beams (*e.g.* by passing it through a long optical fibre) for a time much longer than the coherence time of the laser. This ensures that the non-delayed beam undergoes several changes of phase whilst the other beam is delayed, such that, when they arrive at the detector they have a near random phase relationship[318,319].

This is the basis of the self heterodyne beat note experiment, the experimental arrangement for which is shown in figure 11.8. In this case the laser is passed through the AOM and the zeroth order beam is launched into a 1 km delay fibre whilst the first order beam is coupled into a short fibre. The two beams are then combined in a fibre coupler (FC) then directed into a photomultiplier tube detector (PMT). Finally the signal is amplified by a transimpedance amplifier and passed to a spectrum analyser (SA).

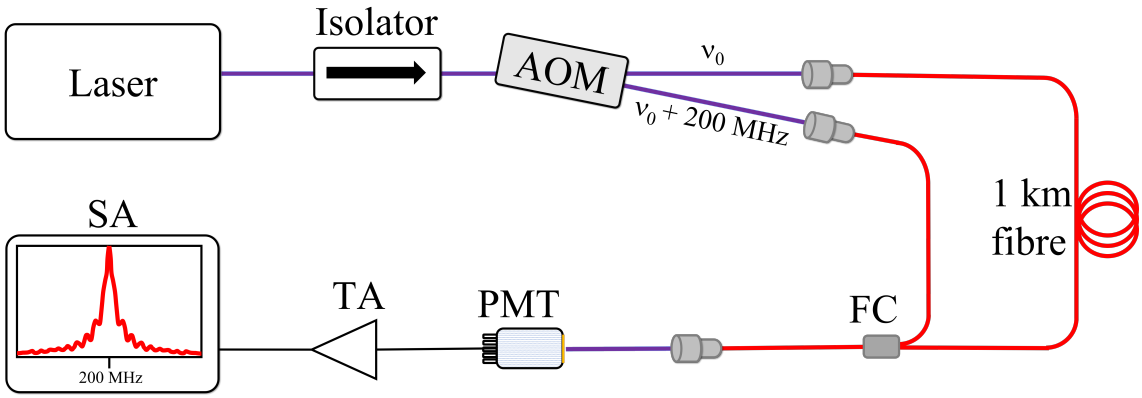

Figure 11.8: Experimental arrangement utilised for Self-Heterodyne beat note detection. Of particular importance are the frequency shifting effect of the AOM and the long delay fibre (in this case 1 km).

If it is assumed that the phase noise of the laser is white then the laser lineshape will

be Lorentzian and the self-heterodyne spectrum, $S(\omega)$, is given by[318,319]:

$$S(\omega) = 2I_1 I_2 \exp\left(\frac{-\tau_D}{\tau_C}\right)\delta(\omega - \omega_{\mathrm{AOM}})$$

$$+\frac{(2I_1 I_2 \tau_C/\pi)}{1+(\omega-\omega_{\mathrm{AOM}})^2\tau_C^2}\left(1-\left(\exp\left(\frac{-\tau_D}{\tau_C}\right)\left(\cos((\omega-\omega_{\mathrm{AOM}})\tau_D)+\frac{\sin((\omega-\omega_{\mathrm{AOM}})\tau_D)}{(\omega-\omega_{\mathrm{AOM}})\tau_D}\right)\right)\right), \tag{11.2}$$

where I_1 and I_2 are the intensities of the two beams, τ_D is the delay time, τ_C is the laser coherence time (related to the laser optical spectrum FWHM, $\Delta\nu$, by $\tau_C = (2\pi\Delta\nu)^{-1}$), δ is the Dirac delta function and ω_{AOM} is the driving (angular) frequency of the AOM (here $\omega_{\mathrm{AOM}} = 2\pi\nu_{\mathrm{AOM}} = 2\pi \times 200$ MHz). In the limit where the delay time is much greater than the laser coherence time ($\tau_D >> \tau_C$) equation 11.2 reduces to a Lorentzian function whose width is twice the width of the laser's optical spectrum (because the signal is broadened by the phase noise of both beams). Alternatively, if τ_D is very small the theoretical beat note signal becomes a delta function (because of the identical phase noise between the beams predicted in this limit) and provides no information about the laser linewidth. At intermediate delay times the self-heterodyne spectrum appears as a delta function from the first term in equation 11.2 (often broadened when the signal is time integrated due to low frequency jitter in the laser central frequency[318]) on top of a broad pedestal, with oscillations in the wings which arise from the second term in equation 11.2. Figure 11.9 shows the theoretical self-heterodyne signal for various delay times τ_D and for a fixed laser coherence time of $\tau_C = 1\mu$s. Ideally, a sufficient length of optical fibre would be used so that ($\tau_D >> \tau_C$) and a Lorentzian signal would be detected. In reality however, particularly for very stable lasers where coherence times (τ_C) in excess of 1μs are routinely found, it can become prohibitively expensive to purchase the necessary fibres. In this case an analysis of the pedestal region, as well as the oscillations in the wings of the self-heterodyne signal can provide laser linewidth information.

Self-heterodyne beat note data taken for the laser used for measuring CRDS spectra of the nitrogen plasma is shown in figure 11.10. The measurement was made at 786 nm with a few seconds integration time and the data are divided, by colour coding, into three sections: in black are the points that cover the (broadened) delta function; in red are points that constitute the wings and in blue the remaining points that effectively form the pedestal upon which the delta function sits. The data are

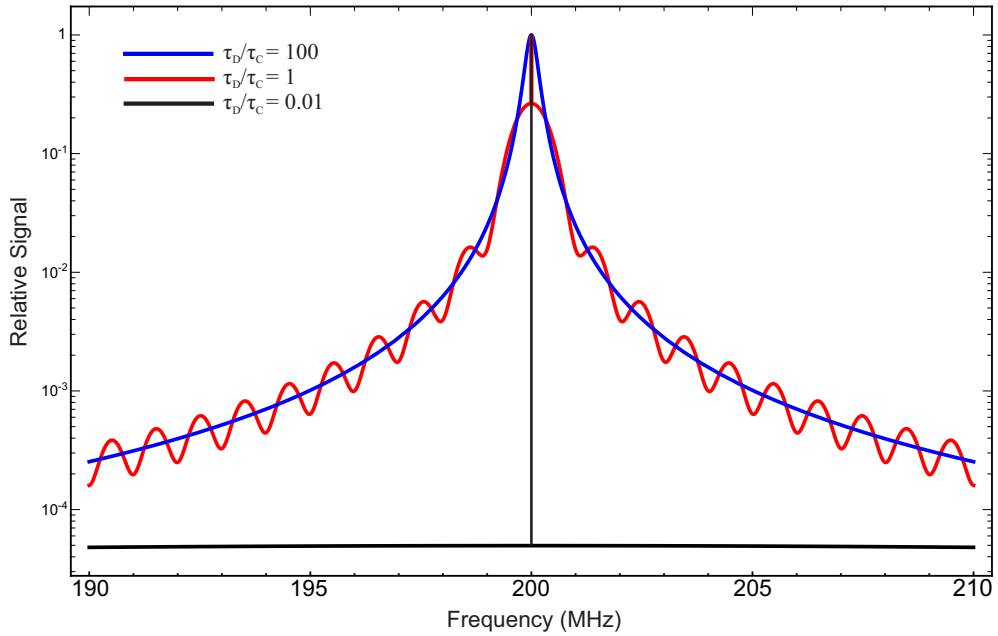

Figure 11.9: Simulated beat note signals for cases assuming the laser phase noise is white noise and when the delay time in the long fibre delay line is much greater than the laser coherence time ($\tau_D/\tau_C = 100$); equal to the laser coherence time ($\tau_D/\tau_C = 1$); and much shorter than the laser coherence time ($\tau_D/\tau_C = 0.01$). The three cases are discussed in more detail in the text.

fitted with equation 11.2 but excluding the delta function (which is, in reality, broadened) and including an additional offset. A fit to the red data points returns the red line, which is a good fit of the modulation in the wings of the signal but much poorer in the centre; if the blue points are also included in the fit, the blue line is returned. The blue line is much more successful at reproducing the pedestal but fails to describe the correct modulation depth in the wings. Neither fitted curve represents the data in a wholly satisfactory way. This poor fitting has however been observed previously[318,319] and is a reflection of the fact that the phase noise of the laser is not strictly white but has additional low frequency fluctuations. In the previous work of Van Exter *et al.*[319] it is concluded however that the wings of the data are only influenced by the phase perturbing effects of spontaneous emission in the laser, and thus the wings are representative of the quantum-limited laser linewidth which describes the Lorentzian wings of the laser optical spectrum. The pedestal region on the other hand is the region that is representative of the more commonly defined FWHM of the lasers optical spectrum (because the half maximum signal excluding the delta function region falls on the pedestal) and is influenced by other phase perturbing effects such as mechanical and thermal instability as well as spontaneous emission.

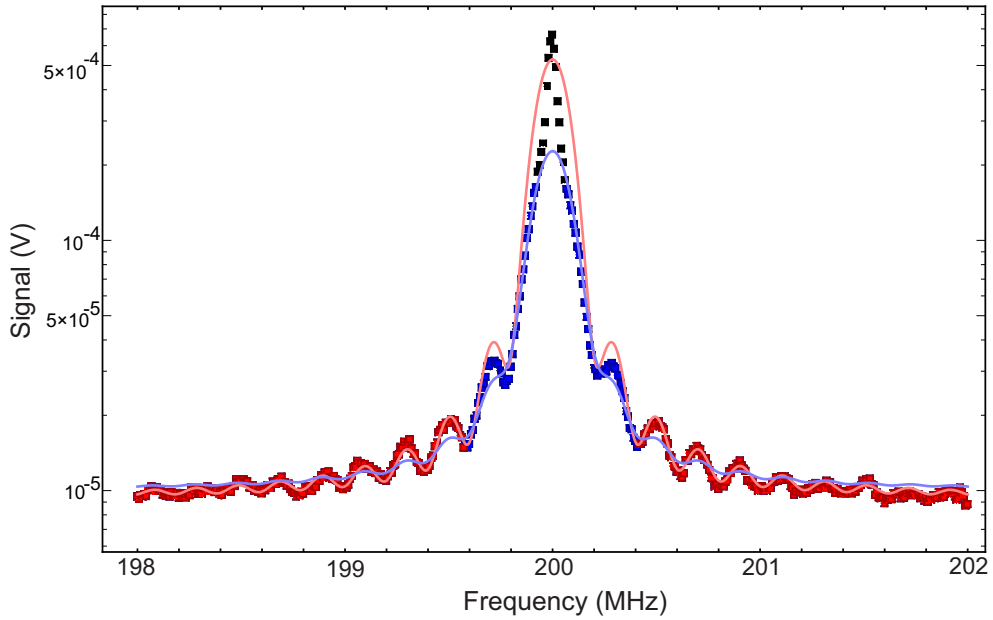

Figure 11.10: Experimental beat note signal showing clearly that the delay time is similar to the coherence time. Fittings are performed using only the second term in equation 11.2. The black points are influenced by the (broadened) delta function from the first term of equation 11.2 and are thus excluded from fitting. The blue fit line (which includes both the red and blue data points) yields a laser linewidth of 67 kHz, but is rather unsuccessful at reproducing the modulation depth in the wings of the signal. The red fit line (which only includes the red data points) yields a laser linewidth of 26 kHz and is much more successful at reproducing the modulation depth in the wings, but less successful at reproducing the behaviour close to 200 MHz. The implications of these two fits (and the reasons why neither is perfect) are discussed in the text.

Thus the following coherence lengths and linewidths can be determined from the data: the red fit provides $\tau_C = 6.18\mu$s and therefore a quantum-limited FWHM linewidth of $\Delta\nu = 26$ kHz whilst the blue fit provides $\tau_C = 2.83\mu$s and thus an effective FWHM for practical purposes of $\Delta\nu = 67$ kHz. The linewidth quoted by the manufacturer (Toptica) for this laser is $10 - 300$ kHz and the measurements certainly concur with this specification.

The separation of the fringes in the self-heterodyne signal is indicative of the delay time τ_D and the red fit which models these fringes best returns a delay time of 4.95μs (the blue fit also provides a value within 0.6% of this). For the 1 km delay fibre this implies a refractive index of 1.48 which is close to the literature value of 1.454 for fused silica at 786 nm[320]. Finally, it was also found that there was no change

to the linewidth when the rf power supply to the plasma was turned on, indicating that the laser is impervious to this potential source of perturbation. Importantly this experiment demonstrates conclusively that the laser linewidth is significantly narrower than the Lamb dip and thus cannot be contributing significantly to the observed Lamb dip widths.

11.3.2 Broadening due to the absorber

Having discounted the laser as a source of the broad Lamb dips one must consider carefully the physical mechanisms of line broadening acting on the absorbing molecules or ions. It should be noted that, in some pump-probe experiments where the two beams are not fully counter-propagating, residual Doppler broadening of the dip can occur, but in the experiments described here the optical cavity ensures no such misalignment can occur and thus the Doppler width of the Lamb dip must be exactly zero. Other potential mechanisms are as follows:

Power broadening

As discussed above, the Lamb dip data obtained with varying saturation parameter shows a change in width that can be attributed to power broadening. Through the use of equation 2.63 with saturation parameters taken as 5.6 and 0.56 for amplifier gain values of 10^5 and 10^6 V A^{-1} (see chapter 8) it is still expected that in the absence of power broadening the Lamb dip widths will be in excess of 100 MHz. Therefore, although power broadening is an important factor in explaining the observed Lamb dips it cannot fully account for the widths and other possible broadening mechanisms must be considered.

Natural broadening

For both the Meinel and the first positive system, the most important factor determining the natural linewidth is the radiative lifetime of the upper state accessed in a given transition. For the vibration states studied here lifetimes can be found in the literature[321] and it is found that $N_2^+(A^2\Pi_u, v = 2)$, $N_2(B^3\Pi_g, v = 2)$ and $N_2(B^3\Pi_g, v = 7)$ have radiative lifetimes of 11.9×10^{-6} s, 7.1×10^{-6} s and 5.3×10^{-6} s, respectively. These lifetimes correspond to linewidths ($= 1/2\pi\tau$) of the order of 10's of kHz, far too narrow to explain the observed dip widths.

Pressure broadening

Mills, Siller and McCall[229,230] are virtually the only other group of researchers to have made similar observations of Lamb dips in the spectra of the N_2^+ Meinel system, in their case they utilised the (1, 0) band rather than the (2, 0) band used here. They first used cavity enhanced velocity modulation spectroscopy and later added a heterodyne detection technique to demonstrate Noise Immune Cavity Enhanced Optical Heterodyne Velocity Modulation Spectroscopy (NICE-OHVMS).

They were able to observe pressure broadening of Lamb dips and reported a pressure broadening coefficient of $\approx$ 8 MHz Torr^{-1}. This indicates that the pressure broadening contribution to the Lamb dips measured here ought to be $\approx$ 80 kHz at 10 mTorr and $\approx$ 800 kHz at 100 mTorr. It is no surprise therefore, given the resolution of the experiments here and the small absorption coefficients, that this pressure broadening could not be observed. This leads to the conclusion that pressure broadening is not an important broadening mechanism in these experiments. Intriguingly, in the previous work by McCall *et al.*[229,230] it was found that, if the data were extrapolated to zero pressure, a dip width of 32 MHz persisted, which could only be explained by invoking additional broadening mechanisms - see later. It should be noted that a pressure broadening parameter of 8 MHz Torr^{-1} is rather larger than typical values expected from a Langevin capture theory based collision cross section (calculated by Mills *et al.*[229]) and Hodges and McCall[234] similarly found that it underestimates pressure broadening in H_3^+ velocity modulation spectra. In the latter case the authors offered a possible explanation, that the appropriate quantity for describing pressure broadening is the *momentum-transfer* cross section, which they estimate to be a factor of 4π larger than the Langevin collision cross section; the larger cross section corresponds to a higher frequency of phase changing collisions for the ions and thus a larger pressure broadening parameter. However, even with this enhancement the resulting pressure broadening parameter is insufficient to explain the widths observed in this work.

Transit time broadening

Transit time broadening arises due to the finite time which absorbing species spend within the cavity mode field. The transit time linewidth can be approximated as $\Delta\nu_{TT} \approx 0.4\bar{v}/w$[43,58] where $\bar{v}$ is the mean speed with which the species traverse the beam and w is the beam waist, which can be calculated from the cavity geometry using equation A.7, and here takes a value $w = 356$ μm. Woodcock *et al.*[210] observed

directional ion velocities in a high voltage sheath as high as 4×10^4 ms^{-1} which would produce a corresponding transit time width of ≈ 45 MHz. This is significant enough that it might be observable in the Lamb dip width, although the experiments presented here are unlikely to have probed a region of pure sheath-like behaviour and indeed were unable to detect any change in dip width as a function of electrode distance d. In a thermal sample of N_2 even for $T_{trans} = 1250$ K the mean molecular speed is ≈ 1000 m s^{-1} and the resulting transit time linewidth is expected to be ≈ 1 MHz. Once again this is far too small to explain the observed Lamb dip widths.

Hyperfine structure

There is a possibility that the broad Lamb dips could be the result of unresolved hyperfine structure. This was also considered by Kassi *et al.*[257] and in their work on $^{17}O^{12}C^{16}O$ they were able to resolve such hyperfine structure. If hyperfine structure is responsible for the dip width then it would be expected that the width would change with rotational state (because the hyperfine splitting would also change), however, in neither this work, nor in the previous work by McCall *et al.*[229,230,322] were any changes in dip width as a function of rotational level of N_2^+ identified. Hyperfine splitting could offer an explanation of the change in dip width with rotational branch observed for N_2^+. Hyperfine structure hasn't been observed spectroscopically in the Meinel system, however, calculated values of the isotropic hyperfine coupling constant, A_{iso}, of the two electronic states involved yield values of < 10 and 88 ± 10 MHz for the $N_2^+(X^2\Sigma_g^+)$ and $N_2^+(A^2\Pi_u)$ states, respectively[323,324]. These values are sufficient to result in hyperfine splitting of 10s or 100s MHz, although the exact splitting in the spectra depends on the precise rotational transition under investigation.

More experimental work exists in the case of the first positive system of N_2[325,326]. The extensive experimental work of Geisen *et al.*[325] is particularly useful and focuses on the hyperfine structure of the (10, 6) band of the first positive system in the $^{14}N_2$ molecule. Geisen *et al.*[325] note that measurements on other vibrational bands show only a weak dependence of the hyperfine splitting on vibrational state and demonstrate that hyperfine coupling leads to splitting in the spectra that can be as large as several hundred MHz, and that it can vary significantly with rotational state. The observations of Geisen *et al.* also show significant variation in the magnitude of hyperfine splitting for different rotational branches. The hyperfine structure observed in the spectra is dictated not only by the splitting of the hyperfine levels in the upper and lower states but also by the selection rule that dictates the allowed hyperfine

transitions, the relevant rule is $\Delta F = 0, \pm 1$ but not $0 \leftrightarrow 0$ and it is found that transitions for which $\Delta F = \Delta J$ are the most intense. Although these observations are on $N_2(A^3\Sigma_u^+)$ they add some confidence to the suggestion that the change in dip width with rotational branch in N_2^+ could have its origin in hyperfine interactions. For the R_{33} and Q_{22} branches of the first positive system (transitions of which were measured in this thesis (figure 11.7) the higher J spectra reported by Geisen *et al.* (up to $J'' = 12$) show hyperfine components which span ≈ 100 MHz, in very good agreement with the observed Lamb dip widths. This possibility therefore warrants further investigation. In particular, future experiments should target those transitions which Geisen *et al.* identify as having the largest hyperfine splitting, for example the $Q_{33}(2)$ transition which has components spanning ≈ 500 MHz, in order to maximise the possibility of resolving the hyperfine transitions and thus identifying this broadening mechanism unequivocally.

Other broadening effects

McCall *et al.*[229,230,322] attempted to identify both power broadening (albeit in a lower finesse cavity, $\mathscr{F} = 250$) and hyperfine structure in their work but were unable to observe these effects. They also concluded (as here) that other mechanisms are insufficient to explain their observed dip widths (*e.g.* pressure broadening). They posit that their velocity modulation method itself could influence the Lamb dip width; as the ions are accelerated by the applied field they only spend a very short time in the velocity group that contributes to the Lamb dip and so the effective interaction time between the laser and the molecules is very short and the Lamb dips are therefore broadened. This mechanism could also operate here. Certainly, the observed translational heating of the ions in the plasma relative to the neutrals suggests that the ions are indeed accelerated by electromagnetic fields within the plasma and this could offer an alternative explanation (as opposed to hyperfine structure) as to why the Lamb dips for $N_2^+(X^2\Sigma_g^+)$ are broader than those of $N_2(A^3\Sigma_u^+)$. This mechanism cannot, however, readily explain why such broad Lamb dips should be observed for the $N_2(A^3\Sigma_u^+)$ molecules which, being uncharged, ought not to experience such acceleration. Nor can it explain the rotational branch dependence of Lamb dip widths in the Meinel system. Indeed, although they suggest this additional broadening mechanism[229] the group of McCall later conclude that the dip widths are not fully understood[322].

11.4 Conclusions

This chapter has presented an initial investigation into the widths of the Lamb dips that occur in the saturated CRD spectra of both $N_2(A^3\Sigma_u^+)$ and $N_2^+(X^2\Sigma_g^+)$. The observations clearly show that both species exhibit Lamb dips that are unusually wide (FWHM of $100 - 400$ MHz); that the Lamb dips show laser power broadening but don't vary either with plasma conditions or when the plasma sheath is approached; and that for N_2^+ the dip widths depend on the rotational branch being probed, with the Q_{22} branch transitions significantly narrower than P_{22} branch transitions.

These observations are carefully considered in terms of the most likely Lamb dip broadening mechanisms. The laser linewidth is measured by a self-heterodyne technique and found to be 67 kHz, much smaller than the Lamb dip widths. Other broadening mechanisms such as pressure and transit time broadening are also insignificant compared to the measured widths. The most likely explanation for the observations is that the Lamb dips for each species consist of many unresolved hyperfine components. Both species have hyperfine coupling constants of a similar magnitude and it is expected that the hyperfine splitting of their spectra should be of the order of 10s−100s MHz. The inability of this technique to resolve the hyperfine transitions is likely a result of the power broadening of each hyperfine transition, whilst the observation that the power broadening does not follow equation 11.1 perfectly can be explained by the presence of hyperfine structure and the fact that the intensity of the different hyperfine components will depend on the laser intensity (because the most intense hyperfine transitions will be affected more by saturation that the weaker components). Additionally, hyperfine structure is the sole mechanism proposed here that provides an explanation of the different dip widths for different rotational branches and this is one of the reasons why this is preferred, for example, over the explanation given by McCall *et al.*[229] which invokes dephasing related to ions experiencing AC fields within the plasma. That neither in this work, nor the work reported in McCall *et al.*, was a change in Lamb dip width with rotational state observed, can be explained simply by the fact that many rotational transitions have comparable hyperfine splitting and thus appear to have the same dip width within the limited resolution of these experiments.

The Lamb dips are certainly worthy of further investigation. At present, although hyperfine structure provides the most plausible explanation, the conclusions about the most important broadening mechanisms largely originate from circumstantial evidence. Unequivocal proof could be obtained if it were possible to resolve hyperfine

structure in a Lamb dip and any future work to resolve this question should focus in particular on measuring those rotational transitions for which the largest hyperfine splittings are expected. In addition, every effort should also be made to take the highest quality data possible under optimum conditions of saturation, that is, conditions where the saturation is sufficient to observe the Lamb dip but not so high as to power broaden the hyperfine components of the transition and thereby lead to their coalescence. It should be emphasised however that the quality of the saturated CRDS data increases as the degree of saturation increases and thus obtaining optimum, hyperfine-resolved, Lamb dips will be an experimental challenge. If this becomes possible, however, then the door is opened to the exciting prospect of probing transit time broadening within the plasma sheath, with routinely achievable ion energies ($\approx$ 10 eV) expected to result in transit time broadening of the hyperfine components of $\approx$ 10 MHz.

Nitrogen plasma conclusions

This section of the thesis details the application of saturated cavity ringdown spectroscopy to probe nitrogen plasma. In particular, an external cavity diode laser operating in the range $747 - 792$ nm has been used to probe the (2,0) band of the Meinel system ($N_2^+(A^2\Pi_u) \rightarrow N_2^+(X^2\Sigma_g^+)$) and the (7,6) and (2,0) bands of the first positive system ($N_2(B^3\Pi_g) \leftarrow N_2(A^3\Sigma_u^+)$). Careful analysis of the effects of saturation allows the extraction of densities and translational temperatures from the spectra.

In the bulk of the plasma the translational temperature of $N_2^+(X^2\Sigma_g^+, v = 0)$ is found to increase with increasing power (from ≈ 600 K at 200 W, 100 mTorr up to ≈ 1200 K at 400 W, 100 mTorr) and decrease with increasing pressure, with translational temperatures at 10 mTorr consistently ≈ 250 K hotter than those at 100 mTorr. The density of $N_2^+(X^2\Sigma_g^+, v = 0)$ is also found to increase with increasing power (from $\approx 3 \times 10^9$ cm^{-3} at 200 W to $\approx 10^{10}$ cm^{-3} at 400 W) and to decrease modestly with increasing pressure. Similar measurements on $N_2(A^3\Sigma_u^+, v = 6)$ yield two interesting points of comparison: first, the translational temperatures are consistently lower than those measured for the ions, with the difference as large as 700 K at 400 W and 10 mTorr; and second, the temperatures increase with increasing pressure, the opposite to the trend observed for the ions. These observations are a consequence of ion acceleration by the plasma electromagnetic fields and the subsequent transfer of this translational energy to the neutral species, which becomes more efficient at higher pressures.

The saturated CRDS measurements are supported by wavelength resolved emission measurements. Comparison with high precision spectral simulations of the first positive system allows rotational and vibrational temperatures of $N_2(B^3\Pi_g)$ to be deduced. It is found that rotational temperatures increase from ≈ 300 K at $0 - 100$ W up to ≈ 1000 K at 500 W, approximately in line with the absorption measurements (bearing in mind the different spatial selectivities of the two techniques, discussed at length for oxygen plasma). Vibrationally it is found that, amongst states with $v \leq 12$ the apparent vibrational temperature is high even at low powers (≈ 5000 K at powers < 50 W) and increases with increasing power (to ≈ 8000 K at 500 W). In contrast, emission from states with $v > 12$ is not observed due to their predissociation. The

emission measurements also show that the E/H switchover in this nitrogen ICP occurs at 50 W at 10 mTorr and at 150 W at 100 mTorr.

The bulk measurements are supported by a volume averaged kinetic model. This model is rather successful at reproducing measured ion densities and from it, reasonable electron temperatures are inferred. The model is less successful in the case of $N_2(A^3\Sigma_u^+)$, running into a contradiction which is common in the literature, namely, that the literature values for $N_2(A^3\Sigma_u^+)$ quenching rate coefficients are insufficient to explain the observed reduction in $N_2(A^3\Sigma_u^+)$ density as pressure increases. Possible causes and resolutions of this issue are discussed in detail.

The section moves on to describe an experimental adjustment to the chamber electrode assembly which enables the measurement of height profiles for both temperature and density of $N_2^+(X^2\Sigma_g^+)$ and $N_2(A^3\Sigma_u^+)$. These measurements are fundamentally interesting because of the importance of the plasma sheath in plasma processing. For the ions it is found that the ion temperature falls from $\approx$ 1100 K 18 mm from the electrode surface to $\approx$ 850 K 1 mm from the electrode. Ion densities drop by approximately an order of magnitude, from $\approx 10^{10}$ cm^{-3} to $\approx 10^9$ cm^{-3}, as the surface is approached and show the same trends with pressure and power as observed in the plasma bulk. The temperatures and densities measured for $N_2(A^3\Sigma_u^+)$ show more modest reductions close the electrode surface and, as for the bulk, temperatures are significantly lower than those measured for $N_2^+(X^2\Sigma_g^+)$. The key conclusion of this chapter is that it demonstrates the ability of the new experimental arrangement to probe close enough to the surface to make it applicable to sheath measurements, particular of sheaths close to biased surfaces.

Finally, this section considers carefully the possible origins of the unusually wide Lamb dips observed for both $N_2^+(X^2\Sigma_g^+)$ and $N_2(A^3\Sigma_u^+)$ spectra. A laser linewidth measurement allows this to be discounted as a significant source of broadening and it is concluded that unresolved hyperfine structure is the key contributor to Lamb dip widths of 100s MHz.

In the case of the nitrogen plasma there are considerably more open questions which require further investigation, than there are for oxygen. Foremost among these is the issue of $N_2(A^3\Sigma_u^+)$ kinetics, specifically the inconsistency between measured and modelled densities as a function of pressure. Several possible causes of this inconsistency have been discussed and further experimentation could provide much needed clarity on this issue. Firstly, uncertainty in the rate of quenching of $N_2(A^3\Sigma_u^+)$ by $N(^4S)$ is worthy of investigation, and taking note of the important mechanisms

suggested to account for the downstream production of $N_2(A^3\Sigma_u^+)$ in a flowing afterglow[240], the vibrational state dependence of the quenching rate must also be clarified. Secondly, the effects of non-Boltzmann vibrational distribution functions (VDFs) should be determined, and for $N_2(A^3\Sigma_u^+)$ this could be achieved by extending the current CRDS measurements on the first positive system to additional vibrational bands, for example by using broadband cavity enhanced spectroscopy (BBCEAS). However, for the crucial case of molecules in the ground electronic state the VDF would be considerably more challenging to measure, probably requiring VUV photons. Fluid dynamical modelling of the nitrogen plasma could also provide valuable insight into the plasma behaviour and any such modelling would also benefit greatly from knowledge of the VDFs for $N_2(X^1\Sigma_g^+)$, $N_2(A^3\Sigma_u^+)$, $N_2(B^3\Pi_g)$ and $N_2^+(X^2\Sigma_g^+)$. Such modelling would also provide information on plasma inhomogeneity and a more rigorous test of the reaction set presented in chapter 9 and these could provide insight into the outstanding questions regarding $N_2(A^3\Sigma_u^+)$ quenching.

In addition to the investigations aimed at understanding the kinetics of nitrogen plasma, it is also apposite to pursue measurements that would clarify the nature of the Lamb dips and enhance our understanding of the hyperfine structure in the spectra of N_2^+. In this work is has been concluded that the Lamb dip widths are largely determined by hyperfine structure, yet no such structure has been definitively observed (by this work or that of others). The pursuit of Lamb dip measurements on lower rotational states (if the signal to noise ratio is sufficiently high) alongside the development of a fitting routine to explicitly deal with the effects of saturation will help clarify these conclusions. Realisation of these experiments would further enhance the prospect of using the Lamb dips to probe transit time effects in the plasma sheath.

Chapter 12

General conclusions and outlook

Ultimately the aim of the work described here is to push the boundaries of spectroscopic measurements on plasma. This is achieved by employing state-of-the-art sensitive quantitative techniques and tailoring their application to cope with the relatively harsh environment of the plasma, to provide significant improvements in sensitivity over previously reported measurements. These methods make it possible to quantify species in plasma systems that have previously defied precise measurement. The novelty however, is not confined to the application of quantitative techniques of exceptional sensitivity, but is also manifest in their application within a plasma chamber of flexible geometry in which different regions of the plasma can now be interrogated, especially those that directly interact with plasma facing surfaces. While work on this is in its infancy, it already shows promise that future measurements pertinent to the surface converging flux of important ionic and excited-state species relevant to surface processing can be made with excellent spatial resolution.

The key conclusions and possible future directions that this work could take are discussed in the conclusions at the end of sections II and III of this thesis. The spatial inhomogeneity of the plasma is highlighted as one characteristic that needs to be better understood in order to improve the quantitative understanding of these systems. From an experimental point of view, inhomogeneity could be examined by measuring line of sight radial profiles (chords through the plasma chamber) and using Abel inversion techniques to retrieve true spatially resolved species' absolute number densities. However, the design of the current plasma chamber renders this impossible. A good alternative is to model the plasma system in 2D using a combined computational fluid dynamics/chemical kinetics approach, a process that is already begun.

It is clear that considering optimal kinetic modelling, even of the plasmas formed from relatively simple homonuclear diatomic species such as oxygen and nitrogen,

there are several unknowns, or gaps in our collective understanding which require further research on basic mechanisms for their resolution, for example, on quenching, electron attachment and wall loss. In this work, this is particularly an issue for $N_2(A^3\Sigma_u^+)$. Quantitative, or even semi-quantitative measurements on other – kinetics defining – species in a nitrogen plasma, especially $N(^4S)$ would undoubtedly help. However, this is a problematic species to probe, intractable to current CRDS methods, and is usually probed (if at all) by two photon laser induced fluorescence.

There is no doubt that low pressure ICPs will continue to be a fruitful area of research, especially as the latest industrial methods evolve to more atomic scale surface processing, where plasma enhanced atomic layer etching and deposition are important. Understanding the nature of species impinging on the surface becomes ever more critical, not only to maintain etch fidelity on the nanometre length scales, but also to possibly devise new plasma-based techniques for the next generations of 3D semiconductor architectures. Clearly, the impact of this work has the potential to extend well beyond plasma science.

References

[1] I. Langmuir, "Oscillations in Ionized Gases," *Proceedings of the National Academy of Sciences*, vol. 14, no. 8, pp. 627–637, 1928.

[2] D. A. Gurnett and W. S. Kurth, "Plasma densities near and beyond the heliopause from the Voyager 1 and 2 plasma wave instruments," *Nature Astronomy*, vol. 3, no. 11, pp. 1024–1028, 2019.

[3] M. A. Lieberman and A. J. Lichtenberg, *Principles of Plasma Discharges and Materials Processing*. Hoboken, New Jersey: Wiley, 2nd ed., 2005.

[4] A. Fridman, *Plasma Chemistry*. Cambridge University Press, 2008.

[5] K. Weman, "Arc welding: an overview," *Welding Processes Handbook*, pp. 31–50, 2012.

[6] H. F. Sterling and R. C. G. Swann, "Chemical vapour deposition promoted by r.f. discharge," *Solid-State Electronics*, vol. 8, pp. 653–654, 1965.

[7] J. C. Angus, H. A. Will, and W. S. Stanko, "Growth of Diamond Seed Crystals by Vapor Deposition," *Journal of Applied Physics*, vol. 39, no. 6, pp. 2915–2922, 1968.

[8] M. Laroussi, S. Bekeschus, M. Keidar, A. Bogaerts, A. Fridman, X. Lu, K. Ostrikov, M. Hori, K. Stapelmann, V. Miller, S. Reuter, C. Laux, A. Mesbah, J. Walsh, C. Jiang, S. M. Thagard, H. Tanaka, D. Liu, D. Yan, and M. Yusupov, "Low-Temperature Plasma for Biology, Hygiene, and Medicine: Perspective and Roadmap," *IEEE Transactions on Radiation and Plasma Medical Sciences*, vol. 6, no. 2, pp. 127–157, 2022.

[9] F. F. Chen, *Introduction to Plasma Physics and Controlled Fusion*. Cham: Springer International Publishing, 2016.

[10] J. F. De La Fuente, S. H. Moreno, A. I. Stankiewicz, and G. D. Stefanidis, "A new methodology for the reduction of vibrational kinetics in non-equilibrium microwave plasma: Application to CO_2 dissociation," *Reaction Chemistry and Engineering*, vol. 1, no. 5, pp. 540–554, 2016.

[11] J. T. Gudmundsson, I. G. Kouznetsov, K. K. Patel, and M. A. Lieberman, "Electronegativity of low-pressure high-density oxygen discharges," *Journal of Physics D: Applied Physics*, vol. 34, no. 7, pp. 1100–1109, 2001.

[12] G. Colonna and A. D'Angola, *Plasma Modeling Methods and Applications*. IOP Publishing, 2016.

[13] C. D. Child, "Discharge From Hot CaO," *Physical Review (Series I)*, vol. 32, no. 5, pp. 492–511, 1911.

[14] I. Langmuir, "The Effect of Space Charge and Residual Gases on Thermionic Currents in High Vacuum," *Physical Review*, vol. 2, no. 6, pp. 450–486, 1913.

[15] P. Chabert, T. V. Tsankov, and U. Czarnetzki, "Foundations of capacitive and inductive radio-frequency discharges," *Plasma Sources Science and Technology*, vol. 30, art. 024001, 2021.

[16] P. Chabert and N. Braithwaite, *Physics of Radio-Frequency Plasmas*. Cambridge: Cambridge University Press, 2011.

[17] T. Panagopoulos and D. J. Economou, "Plasma sheath model and ion energy distribution for all radio frequencies," *Journal of Applied Physics*, vol. 85, no. 7, pp. 3435–3443, 1999.

[18] N. F. Mott and R. W. Gurney, *Electronic Processes in Ionic Crystals*. Oxford: Clarendon Press, 1940.

[19] R. Warren, "Interpretation of Field Measurements in the Cathode Region of Glow Discharges," *Physical Review*, vol. 98, no. 6, pp. 1658–1664, 1955.

[20] M. S. Benilov, "The Child-Langmuir law and analytical theory of collisionless to collision-dominated sheaths," *Plasma Sources Science and Technology*, vol. 18, art. 014005, 2009.

[21] S. Naggary, D. Engel, L. Kroll, and R. P. Brinkmann, "Bridging Child-Langmuir and Warren: Exact and approximate solutions for the unipolar sheath of intermediate pressure," *Plasma Sources Science and Technology*, vol. 28, art. 015003, 2019.

[22] N. Mutsukura, K. Kobayashi, and Y. Machi, "Plasma sheath thickness in radio-frequency discharges," *Journal of Applied Physics*, vol. 68, no. 6, pp. 2657–2660, 1990.

[23] J. Schleitzer, V. Schneider, and H. Kersten, "Investigations of the sheath in a dual-frequency capacitively coupled rf discharge by optically trapped microparticles," *Physics of Plasmas*, vol. 28, art. 083506, 2021.

[24] X. M. Zhu and Y. K. Pu, "Using OES to determine electron temperature and density in low-pressure nitrogen and argon plasmas," *Plasma Sources Science and Technology*, vol. 17, art. 024002, 2008.

[25] X. M. Zhu and Y. K. Pu, "Optical emission spectroscopy in low-temperature plasmas containing argon and nitrogen: Determination of the electron temperature and density by the line-ratio method," *Journal of Physics D: Applied Physics*, vol. 43, art. 403001, 2010.

[26] M. A. Song, Y. W. Lee, and T. H. Chung, "Characterization of an inductively coupled nitrogen-argon plasma by Langmuir probe combined with optical emission spectroscopy," *Physics of Plasmas*, vol. 18, art. 023504, 2011.

[27] C. Ong, O. Chin, M. Nisoa, and B. Paosawatyanyang, "Langmuir probe measurement in a radio frequency inductively coupled argon plasma," *Jurnal Fizik Malaysia*, vol. 25, no. 3-4, pp. 97–102, 2004.

[28] H. C. Lee, J. K. Lee, and C. W. Chung, "Evolution of the electron energy distribution and E-H mode transition in inductively coupled nitrogen plasma," *Physics of Plasmas*, vol. 17, art. 033506, 2010.

[29] H. C. Lee, S. Oh, and C. W. Chung, "Experimental observation of the skin effect on plasma uniformity in inductively coupled plasmas with a radio frequency bias," *Plasma Sources Science and Technology*, vol. 21, art. 035003, 2012.

[30] J. T. Gudmundsson, A. M. Marakhtanov, K. K. Patel, V. P. Gopinath, and M. A. Lieberman, "On the plasma parameters of a planar inductive oxygen

discharge," *Journal of Physics D: Applied Physics*, vol. 33, no. 11, pp. 1323–1331, 2000.

[31] J. Bredin, P. Chabert, and A. Aanesland, "Langmuir probe analysis of highly electronegative plasmas," *Applied Physics Letters*, vol. 102, art. 154107, 2013.

[32] M. Fiebrandt, M. Oberberg, and P. Awakowicz, "Comparison of Langmuir probe and multipole resonance probe measurements in argon, hydrogen, nitrogen, and oxygen mixtures in a double ICP discharge," *Journal of Applied Physics*, vol. 122, art. 013302, 2017.

[33] F. Karouta, "A practical approach to reactive ion etching," *Journal of Physics D: Applied Physics*, vol. 47, art. 233501, 2014.

[34] K. Racka-Szmidt, B. Stonio, J. Żelazko, M. Filipiak, and M. Sochacki, "A review: Inductively coupled plasma reactive ion etching of silicon carbide," *Materials*, vol. 15, art. 123, 2022.

[35] K. J. Kanarik, T. Lill, E. A. Hudson, S. Sriraman, S. Tan, J. Marks, V. Vahedi, and R. A. Gottscho, "Overview of atomic layer etching in the semiconductor industry," *Journal of Vacuum Science and Technology A: Vacuum, Surfaces, and Films*, vol. 33, art. 020802, 2015.

[36] G. S. Oehrlein, D. Metzler, and C. Li, "Atomic Layer Etching at the Tipping Point: An Overview," *ECS Journal of Solid State Science and Technology*, vol. 4, no. 6, pp. N5041–N5053, 2015.

[37] R. Vallat, R. Gassilloud, B. Eychenne, and C. Vallée, "Selective deposition of Ta_2O_5 by adding plasma etching super-cycles in plasma enhanced atomic layer deposition steps ," *Journal of Vacuum Science and Technology A: Vacuum, Surfaces, and Films*, vol. 35, art. 01B104, 2017.

[38] S. K. Song, H. Saare, and G. N. Parsons, "Integrated Isothermal Atomic Layer Deposition/Atomic Layer Etching Supercycles for Area-Selective Deposition of TiO_2," *Chemistry of Materials*, vol. 31, no. 13, pp. 4793–4804, 2019.

[39] G. L. Kabongo, B. M. Mothudi, and M. S. Dhlamini, "Advanced Development of Sustainable PECVD Semitransparent Photovoltaics: A Review," *Frontiers in Materials*, vol. 8, art. 762030, 2021.

[40] M. C. Vasudev, K. D. Anderson, T. J. Bunning, V. V. Tsukruk, and R. R. Naik, "Exploration of plasma-enhanced chemical vapor deposition as a method for thin-film fabrication with biological applications," *ACS Applied Materials and Interfaces*, vol. 5, no. 10, pp. 3983–3994, 2013.

[41] M. F. Ceiler, P. A. Kohl, and S. A. Bidstrup, "Plasma-Enhanced Chemical Vapor Deposition of Silicon Dioxide Deposited at Low Temperatures," *Journal of The Electrochemical Society*, vol. 142, no. 6, pp. 2067–2071, 1995.

[42] H. B. Profijt, S. E. Potts, M. C. M. van de Sanden, and W. M. M. Kessels, "Plasma-Assisted Atomic Layer Deposition: Basics, Opportunities, and Challenges," *Journal of Vacuum Science and Technology A: Vacuum, Surfaces, and Films*, vol. 29, art. 050801, 2011.

[43] W. Demtröder, *Laser Spectroscopy 1: Basic Principles*. Berlin Heidelberg: Springer-Verlag, 5th ed., 2014.

[44] E. Condon and G. H. Shortley, *The Theory of Atomic Spectra*. Cambridge: Cambridge University Press, 1964.

[45] P. R. Bunker and P. Jensen, *Molecular Symmetry and Spectroscopy*. Ottawa: Canadian Science Publishing, 2nd ed., 2012.

[46] E. E. Whiting, A. Schadee, J. B. Tatum, J. T. Hougen, and R. W. Nicholls, "Recommended conventions for defining transition moments and intensity factors in diatomic molecular spectra," *Journal of Molecular Spectroscopy*, vol. 80, no. 2, pp. 249–256, 1980.

[47] M. Larsson, "Conversion formulas between radiative lifetimes and other dynamical variables for spin-allowed electronic transitions in diatomic molecules," *Astronomy and Astrophysics*, vol. 128, pp. 291–298, 1983.

[48] A. Schadee, "Unique definitions for the band strength and the electronic-vibrational dipole moment of diatomic molecular radiative transitions," *Journal of Quantitative Spectroscopy and Radiative Transfer*, vol. 19, pp. 451–453, 1978.

[49] J. B. Tatum, "The Interpretation of Intensities in Diatomic Molecular Spectra," *The Astrophysical Journal Supplement Series*, vol. 14, pp. 21–55, 1967.

[50] J. F. Noxon, "Observation of the $b^1\Sigma_g^+$-$a^1\Delta_g$ transition in O_2," *Canadian Journal of Physics*, vol. 39, no. 8, pp. 1110–1119, 1961.

[51] S. Williams, M. Gupta, T. Owano, D. S. Baer, A. O'Keefe, D. R. Yarkony, and S. Matsika, "Quantitative detection of singlet O_2 by cavity-enhanced absorption," *Optics Letters*, vol. 29, no. 10, p. 1066, 2004.

[52] M. Gupta, T. Owano, D. S. Baer, A. O'Keefe, and S. Williams, "Quantitative determination of singlet oxygen density and temperature for Oxygen-Iodine Laser Applications," *Chemical Physics Letters*, vol. 400, no. 1-3, pp. 42–46, 2004.

[53] I. Kovács, *Rotational Structure in the Spectra of Diatomic Molecules*. New York: American Elsevier Publishing Company Inc., 1969.

[54] E. E. Whiting, J. A. Paterson, I. Kovács, and R. W. Nicholls, "Computer checking of rotational line intensity factors for diatomic transitions," *Journal of Molecular Spectroscopy*, vol. 47, no. 1, pp. 84–98, 1973.

[55] C. M. Western, "PGOPHER: A program for simulating rotational, vibrational and electronic spectra," *Journal of Quantitative Spectroscopy and Radiative Transfer*, vol. 186, pp. 221–242, 2017.

[56] I. E. Gordon, L. S. Rothman, R. J. Hargreaves, R. Hashemi, E. V. Karlovets, F. M. Skinner, E. K. Conway, C. Hill, R. V. Kochanov, Y. Tan, P. Wcisło, A. A. Finenko, K. Nelson, P. F. Bernath, M. Birk, V. Boudon, A. Campargue, K. V. Chance, A. Coustenis, B. J. Drouin, J. M. Flaud, R. R. Gamache, J. T. Hodges, D. Jacquemart, E. J. Mlawer, A. V. Nikitin, V. I. Perevalov, M. Rotger, J. Tennyson, G. C. Toon, H. Tran, V. G. Tyuterev, E. M. Adkins, A. Baker, A. Barbe, E. Canè, A. G. Császár, A. Dudaryonok, O. Egorov, A. J. Fleisher, H. Fleurbaey, A. Foltynowicz, T. Furtenbacher, J. J. Harrison, J. M. Hartmann, V. M. Horneman, X. Huang, T. Karman, J. Karns, S. Kassi, I. Kleiner, V. Kofman, F. Kwabia-Tchana, N. N. Lavrentieva, T. J. Lee, D. A. Long, A. A. Lukashevskaya, O. M. Lyulin, V. Y. Makhnev, W. Matt, S. T. Massie, M. Melosso, S. N. Mikhailenko, D. Mondelain, H. S. Müller, O. V. Naumenko, A. Perrin, O. L. Polyansky, E. Raddaoui, P. L. Raston, Z. D. Reed, M. Rey, C. Richard, R. Tóbiás, I. Sadiek, D. W. Schwenke, E. Starikova, K. Sung, F. Tamassia, S. A. Tashkun, J. Vander Auwera, I. A. Vasilenko, A. A. Vigasin, G. L. Villanueva, B. Vispoel, G. Wagner, A. Yachmenev, and S. N. Yurchenko, "The HITRAN2020 molecular spectroscopic database," *Journal of Quantitative Spectroscopy and Radiative Transfer*, vol. 277, art. 107949, 2022.

[57] P. Atkins and R. Friedman, *Molecular Quantum Mechanics*. Oxford: Oxford University Press, 4th ed., 2005.

[58] V. S. Letokhov and V. P. Chebotayev, *Nonlinear Laser Spectroscopy*. Berlin Heidelberg: Springer-Verlag, 1977.

[59] G. Hancock, V. L. Kasyutich, and G. A. Ritchie, "Wavelength-modulation spectroscopy using a frequency-doubled current-modulated diode laser," *Applied Physics B: Lasers and Optics*, vol. 74, no. 6, pp. 569–575, 2002.

[60] G. C. Bjorklund, "Measuring Weak Absorptions and Dispersions," *Optics letters*, vol. 5, no. 1, pp. 15–17, 1980.

[61] J. U. White, "Long Optical Paths of Large Aperture," *Journal of the Optical Society of America*, vol. 32, no. 5, p. 285, 1942.

[62] D. R. Herriott and H. J. Schulte, "Folded Optical Delay Lines," *Applied Optics*, vol. 4, no. 8, p. 883, 1965.

[63] L. Thornton, *Diode Laser Absorption Studies of Gas Phase Species*. DPhil, University of Oxford, 2006.

[64] B. Bakowski, *Laser Studies of Species in Plasma*. DPhil, University of Oxford, 2003.

[65] R. Peverall, S. D. A. Rogers, and G. A. D. Ritchie, "Quantitative measurements of oxygen atom and negative ion densities in a low pressure oxygen plasma by cavity ringdown spectroscopy," *Plasma Sources Science and Technology*, vol. 29, art. 045004, 2020.

[66] S. D. A. Rogers, A. Bond, R. Peverall, G. Hancock, C. M. Western, and G. A. D. Ritchie, "Quantitative measurements of singlet molecular oxygen in a low pressure ICP," *Plasma Sources Science and Technology*, vol. 30, art. 09LT02, 2021.

[67] G. Berden and R. Engeln, *Cavity Ring-Down Spectroscopy: Techniques and Applications*. Chichester: Wiley, 2009.

[68] A. E. Siegman, *Lasers*. Mill Valley, California: Univeristy Science Books, 1986.

[69] O. Svelto, *Principles of Lasers*. New York Dordrecht Heidelberg London: Springer, 5th ed., 2010.

[70] W. Demtröder, *Laser spectroscopy 2: Experimental techniques*. Berlin Heidelberg: Springer-Verlag, 5th ed., 2015.

[71] W. R. Bennett Jr., "Hole Burning Effects in a He-Ne Optical Maser," *Physical Review*, vol. 126, no. 2, pp. 580–593, 1962.

[72] W. E. Lamb, "Theory of an Optical Maser," *Physical Review*, vol. 134, no. 6A, pp. A1429–A1450, 1964.

[73] G. Herzberg, *Atomic spectra and atomic structure*. New York: Dover Publications, 2nd ed., 1944.

[74] A. Kramida, Yu. Ralchenko, J. Reader, and NIST ASD Team. NIST Atomic Spectra Database (ver. 5.10), [Online]. Available: `https://physics.nist.gov/asd` [2022]. National Institute of Standards and Technology, Gaithersburg, Maryland, 2022.

[75] F. R. Gilmore, "Potential energy curves for N_2, NO, O_2 and corresponding ions," *Journal of Quantitative Spectrosocpy and Radiative Transfer*, vol. 5, no. 2, pp. 369–390, 1965.

[76] F. Hund, "Zur Deutung der Molekelspektren I," *Zeitschrift für Physik*, vol. 40, pp. 742–764, 1927.

[77] F. Hund, "Zur Deutung der Molekelspektren II," *Zeitschrift für Physik*, vol. 42, pp. 93–120, 1927.

[78] G. Herzberg, *Molecular Spectra and Molecular Structure I. Spectra of Diatomic Molecules*. Princeton, New Jersey: D. Van Nostrand Company inc., 2nd ed., 1950.

[79] B. J. Drouin, D. C. Benner, L. R. Brown, M. J. Cich, T. J. Crawford, V. M. Devi, A. Guillaume, J. T. Hodges, E. J. Mlawer, D. J. Robichaud, F. Oyafuso, V. H. Payne, K. Sung, E. H. Wishnow, and S. Yu, "Multispectrum analysis of the oxygen A-band," *Journal of Quantitative Spectroscopy and Radiative Transfer*, vol. 186, pp. 118–138, 2017.

[80] A. B. Meinel, "The auroral spectrum from 6200 to 8900 A*," *The Astrophysical Journal*, vol. 113, p. 583, 1951.

[81] R. N. Franklin, "The role of $O_2(a^1\Delta_g)$ metastables and associative detachment in discharges in oxygen," *Journal of Physics D: Applied Physics*, vol. 34, no. 12, pp. 1834–1839, 2001.

[82] M. W. Kiehlbauch and D. B. Graves, "Inductively coupled plasmas in oxygen: Modeling and experiment," *Journal of Vacuum Science and Technology A: Vacuum, Surfaces, and Films*, vol. 21, no. 3, pp. 660–670, 2003.

[83] W. Yang and C. A. Wolden, "Plasma-enhanced chemical vapor deposition of TiO_2 thin films for dielectric applications," *Thin Solid Films*, vol. 515, no. 4, pp. 1708–1713, 2006.

[84] B. A. Langowski and K. E. Uhrich, "Oxygen plasma-treatment effects on Si transfer," *Langmuir*, vol. 21, no. 14, pp. 6366–6372, 2005.

[85] C. M. Chan, T. M. Ko, and H. Hiraoka, "Polymer surface modification by plasmas and photons," *Surface Science Reports*, vol. 24, no. 1-2, pp. 1–54, 1996.

[86] D. J. Milliron, I. G. Hill, C. Shen, A. Kahn, and J. Schwartz, "Surface oxidation activates indium tin oxide for hole injection," *Journal of Applied Physics*, vol. 87, no. 1, pp. 572–576, 2000.

[87] V. Krastev, I. Reid, C. Galassi, G. Hughes, and E. McGlynn, "Influence of $C_4F_8/Ar/O_2$ plasma etching on SiO_2 surface chemistry," *Journal of Materials Science: Materials in Electronics*, vol. 16, no. 8, pp. 541–547, 2005.

[88] M. K. Singh, A. Ogino, and M. Nagatsu, "Inactivation factors of spore-forming bacteria using low-pressure microwave plasmas in an N_2 and O_2 gas mixture," *New Journal of Physics*, vol. 11, art. 115027, 2009.

[89] C. S. Corr, S. Gomez, and W. G. Graham, "Discharge kinetics of inductively coupled oxygen plasmas: Experiment and model," *Plasma Sources Science and Technology*, vol. 21, art. 055024, 2012.

[90] J. T. Gudmundsson, T. Kimura, and M. A. Lieberman, "Experimental studies of O_2/Ar plasma in a planar inductive discharge," *Plasma Sources Science and Technology*, vol. 8, no. 1, pp. 22–30, 1999.

[91] J. Meichsner and T. Wegner, "Evaluation of oxygen species during E–H transition in inductively coupled RF plasmas: combination of experimental results with global model," *European Physical Journal D*, vol. 72, no. 5, pp. 1–15, 2018.

[92] T. Czerwiec, J. Gavillet, T. Belmonte, H. Michel, and A. Ricard, "Determination of O atom density in Ar-O_2 and Ar-O_2-H_2 flowing microwave discharges," *Surface and Coatings Technology*, vol. 98, no. 1-3, pp. 1411–1415, 1998.

[93] J. Jašík, P. Macko, V. Martišovitš, P. Lukáč, and P. Veis, "Time resolved actinometric study of pulsed RF oxygen discharge," *Czechoslovak Journal of Physics*, vol. 54, no. 6, pp. 661–676, 2004.

[94] J. P. Booth and N. Sadeghi, "Oxygen and fluorine atom kinetics in electron cyclotron resonance plasmas by time-resolved actinometry," *Journal of Applied Physics*, vol. 70, no. 2, pp. 611–620, 1991.

[95] A. Granier, D. Chéreau, K. Henda, R. Safari, and P. Leprince, "Validity of actinometry to monitor oxygen atom concentration in microwave discharges created by surface wave in O_2-N_2 mixtures," *Journal of Applied Physics*, vol. 75, no. 1, pp. 104–114, 1994.

[96] J. P. Booth, A. Chatterjee, O. Guaitella, J. S. Sousa, D. Lopaev, S. Zyryanov, T. Rakhimova, D. Voloshin, Y. Mankelevich, N. de Oliveira, and L. Nahon, "Determination of absolute $O(^3P)$ and $O_2(a^1\Delta_g)$ densities and kinetics in fully modulated O_2 dc glow discharges from the $O_2(X^3\Sigma_g^-)$ afterglow recovery dynamics," *Plasma Sources Science and Technology*, vol. 29, art. 115009, 2020.

[97] N. Sharma, M. Chakraborty, P. K. Saha, A. Mukherjee, N. K. Neog, and M. Bandyopadhyay, "Effect of argon and oxygen gas concentration on mode transition and negative ion production in helicon discharge," *Journal of Applied Physics*, vol. 128, art. 183303, 2020.

[98] D. V. Lopaev, A. V. Volynets, S. M. Zyryanov, A. I. Zotovich, and A. T. Rakhimov, "Actinometry of O, N and F atoms," *Journal of Physics D: Applied Physics*, vol. 50, art. 075202, 2017.

[99] S. M. Newman, A. J. Orr-Ewing, D. A. Newnham, and J. Ballard, "Temperature and pressure dependence of line widths and integrated absorption intensities for the $O_2(a^1\Delta_g - X^3\Sigma_g^-$ (0,0) transition," *Journal of Physical Chemistry A*, vol. 104, no. 42, pp. 9467–9480, 2000.

[100] M. Kang and J. W. Hahn, "Analytical calculation of the light-collection efficiency of an optical emission spectrometer with the effective solid-angle method," *Applied Optics*, vol. 55, no. 15, p. 3909, 2016.

[101] E. J. Collart, J. A. Baggerman, and R. J. Visser, "Excitation mechanisms of oxygen atoms in a low pressure O_2 radio-frequency plasma," *Journal of Applied Physics*, vol. 70, no. 10, pp. 5278–5281, 1991.

[102] G. Dilecce, M. Vigliotti, and S. D. Benedictis, "A TALIF calibration method for quantitative oxygen atom density measurement in plasma jets," *Journal of Physics D: Applied Physics*, vol. 33, no. 6, pp. 53–56, 2000.

[103] P. Peze, A. Paillous, J. Siffre, and B. Dubreuil, "Quantitative measurements of oxygen atom density using LIF," *Journal of Physics D: Applied Physics*, vol. 26, no. 10, pp. 1622–1629, 1993.

[104] G. Hancock and M. J. Toogood, "Laser-induced fluorescence of oxygen atoms in a plasma reactor," *Applied Physics Letters*, vol. 60, no. 1, pp. 35–37, 1992.

[105] S. Gomez, P. G. Steen, and W. G. Graham, "Atomic oxygen surface loss coefficient measurements in a capacitive/inductive radio-frequency plasma," *Applied Physics Letters*, vol. 81, no. 1, pp. 19–21, 2002.

[106] R. Peverall and G. A. Ritchie, "Spectroscopy techniques and the measurement of molecular radical densities in atmospheric pressure plasmas," *Plasma Sources Science and Technology*, vol. 28, art. 073002, 2019.

[107] K. Niemi, V. Schulz-Von Der Gathen, and H. F. Döbele, "Absolute atomic oxygen density measurements by two-photon absorption laser-induced fluorescence spectroscopy in an RF-excited atmospheric pressure plasma jet," *Plasma Sources Science and Technology*, vol. 14, no. 2, pp. 375–386, 2005.

[108] A. F. Van Gessel, S. C. Van Grootel, and P. J. Bruggeman, "Atomic oxygen TALIF measurements in an atmospheric-pressure microwave plasma jet with in situ xenon calibration," *Plasma Sources Science and Technology*, vol. 22, art. 055010, 2013.

[109] C. M. Western, J. P. Booth, A. Chatterjee, and N. de Oliveira, "Rydberg spectra of singlet metastable states of O_2," *Molecular Physics*, vol. 119, art. e1741714, 2021.

[110] X. Yang, K. Sasaki, and M. Nagatsu, "Self-absorption-calibrated vacuum ultraviolet absorption spectroscopy for absolute oxygen atomic density measurement," *Plasma Sources Science and Technology*, vol. 24, art. 055019, 2015.

[111] H. Nagai, M. Hiramatsu, M. Hori, and T. Goto, "Measurement of oxygen atom density employing vacuum ultraviolet absorption spectroscopy with microdischarge hollow cathode lamp," *Review of Scientific Instruments*, vol. 74, no. 7, pp. 3453–3459, 2003.

[112] T. Kitajima, K. Noro, T. Nakano, and T. Makabe, "Influence of driving frequency on oxygen atom density in O_2 radio frequency capacitively coupled plasma," *Journal of Physics D: Applied Physics*, vol. 37, no. 19, pp. 2670–2676, 2004.

[113] K. Niemi, D. O'Connell, N. De Oliveira, D. Joyeux, L. Nahon, J. P. Booth, and T. Gans, "Absolute atomic oxygen and nitrogen densities in radio-frequency driven atmospheric pressure cold plasmas: Synchrotron vacuum ultra-violet high-resolution Fourier-transform absorption measurements," *Applied Physics Letters*, vol. 103, no. 3, pp. 1–5, 2013.

[114] F. G. Celii, H. R. Thorsheim, M. A. Hanratty, and J. E. Butler, "Oxygen atom detection using third harmonic generation," *Applied Optics*, vol. 29, no. 21, p. 3135, 1990.

[115] S. J. Harris and A. M. Weiner, "Detection of atomic oxygen by intracavity spectroscopy," *Optics Letters*, vol. 6, no. 3, p. 142, 1981.

[116] A. Teslja and P. J. Dagdigian, "Determination of oxygen atom concentrations by cavity ring-down spectroscopy," *Chemical Physics Letters*, vol. 400, no. 4-6, pp. 374–378, 2004.

[117] M. Gupta, T. Owano, D. Baer, and A. O'Keefe, "Quantitative determination of the $O(^3P)$ density via visible cavity-enhanced spectroscopy," *Applied Physics Letters*, vol. 89, no. 24, pp. 1–4, 2006.

[118] G. Hancock, R. Peverall, G. A. Ritchie, and L. J. Thornton, "The number density of ground state atomic oxygen ($O(^3P_2)$) measured in an inductively coupled plasma chamber by cavity enhanced absorption," *Journal of Physics D: Applied Physics*, vol. 40, no. 15, pp. 4515–4518, 2007.

[119] V. S. Pazyuk, Y. P. Podmar'kov, N. A. Raspopov, and M. P. Frolov, "Direct detection of singlet oxygen $O_2(a^1\Delta_g)$ by absorption at the $a^1\Delta_g \rightarrow b^1\Sigma_g^+$ transition using intracavity laser spectroscopy," *Quantum Electronics*, vol. 31, pp. 363–366, 2001.

[120] S. Williams, S. Popovic, and M. Gupta, "Microwave plasma generation and filtered transport of $O_2(a^1\Delta_g)$," *Plasma Sources Science and Technology*, vol. 18, art. 035014, 2009.

[121] T. Földes, P. Čermák, M. Macko, P. Veis, and P. Macko, "Cavity ring-down spectroscopy of singlet oxygen generated in microwave plasma," *Chemical Physics Letters*, vol. 467, pp. 233–236, 2009.

[122] R. L. Sharpless and T. G. Slanger, "Surface chemistry of metastable oxygen. II. Destruction of $O_2(a^1\Delta_g)$," *The Journal of Chemical Physics*, vol. 91, pp. 7947–7950, 1989.

[123] J. T. Gudmundsson, "Recombination and detachment in oxygen discharges: The role of metastable oxygen molecules," *Journal of Physics D: Applied Physics*, vol. 37, no. 15, pp. 2073–2081, 2004.

[124] D. A. Toneli, R. S. Pessoa, M. Roberto, and J. T. Gudmundsson, "On the formation and annihilation of the singlet molecular metastables in an oxygen discharge," *Journal of Physics D: Applied Physics*, vol. 48, art. 325202, 2015.

[125] P. J. Chantry, "A simple formula for diffusion calculations involving wall reflection and low density," *Journal of Applied Physics*, vol. 62, no. 4, pp. 1141–1148, 1987.

[126] E. B. Winn, "The temperature dependence of the self-diffusion coefficients of argon, neon, nitrogen, oxygen, carbon dioxide, and methane," *Physical Review*, vol. 80, pp. 1024–1027, 1950.

[127] J. E. Morgan and H. I. Schiff, "Diffusion Coefficients of O and N Atoms in Inert Gases," *Canadian Journal of Chemistry*, vol. 42, no. 10, pp. 2300–2306, 1964.

[128] P. H. Vidaud, R. P. Wayne, and M. Yaron, "Diffusion Coefficient Measurement of $O_2^*(^1\Delta_g)$ in ground state O_2," *Chemical Physics Letters*, vol. 38, pp. 306–309, 1976.

[129] J. T. Gudmundsson and E. G. Thorsteinsson, "Oxygen discharges diluted with argon: Dissociation processes," *Plasma Sources Science and Technology*, vol. 16, pp. 399–412, 2007.

[130] S. J. Cubley and E. A. Mason, "Atom-molecule and molecule-molecule potentials and transport collision integrals for high-temperature air species," *Physics of Fluids*, vol. 18, no. 9, pp. 1109–1111, 1975.

[131] K. S. Yun, S. Weissman, and E. A. Mason, "High-temperature transport properties of dissociating nitrogen and dissociating oxygen," *Physics of Fluids*, vol. 5, no. 6, pp. 672–678, 1962.

[132] T. R. Marrero and E. A. Mason, "Gaseous Diffusion Coefficients," *Journal of Physical and Chemical Reference Data*, vol. 1, no. 1, pp. 3–118, 1972.

[133] J. Krištof, P. Macko, and P. Veis, "Surface loss probability of atomic oxygen," *Vacuum*, vol. 86, no. 6, pp. 614–619, 2012.

[134] G. Cartry, X. Duten, and A. Rousseau, "Atomic oxygen surface loss probability on silica in microwave plasmas studied by a pulsed induced fluorescence technique," *Plasma Sources Science and Technology*, vol. 15, no. 3, pp. 479–488, 2006.

[135] A. Bousquet, G. Cartry, and A. Granier, "Investigation of O-atom kinetics in O_2, CO_2, H_2O and O_2/HMDSO low pressure radiofrequency pulsed plasmas by time-resolved optical emission spectroscopy," *Plasma Sources Science and Technology*, vol. 16, no. 3, pp. 597–605, 2007.

[136] E. N. Fuller, P. D. Schettler, and J. C. Giddings, "A new method for prediction of binary gas-phase diffusion coefficients," *Industrial and Engineering Chemistry*, vol. 58, no. 5, pp. 18–27, 1966.

[137] S. Wickramanayaka, S. Meikle, T. Kobayashi, N. Hosokawa, and Y. Hatanaka, "Measurements of catalytic efficiency of surfaces for the removal of atomic oxygen using NO_2^* continuum ," *Journal of Vacuum Science and Technology A: Vacuum, Surfaces, and Films*, vol. 9, no. 6, pp. 2999–3002, 1991.

[138] J. P. Sarrette, B. Rouffet, and A. Ricard, "Determination of nitrogen atoms loss probabilities on copper, aluminium, alumina, brass and nylon surfaces," *Plasma Processes and Polymers*, vol. 3, pp. 120–126, 2006.

[139] G. Cartry, L. Magne, and G. Cernogora, "Atomic oxygen recombination on fused silica: experimental evidence of the surface state influence," *Journal of Physics D: Applied Physics*, vol. 32, pp. L53–L56, 1999.

[140] J. P. Booth, O. Guaitella, A. Chatterjee, C. Drag, V. Guerra, D. Lopaev, S. Zyryanov, T. Rakhimova, D. Voloshin, and Y. Mankelevich, "Oxygen (^{3}P) atom recombination on a Pyrex surface in an O_2 plasma," *Plasma Sources Science and Technology*, vol. 28, art. 055005, 2019.

[141] A. Annušová, D. Marinov, J. P. Booth, N. Sirse, M. L. D. Silva, B. Lopez, and V. Guerra, "Kinetics of highly vibrationally excited O_2(X) molecules in inductively-coupled oxygen plasmas," *Plasma Sources Science and Technology*, vol. 27, art. 045006, 2018.

[142] A. R. Gibson, M. Foucher, D. Marinov, P. Chabert, T. Gans, M. J. Kushner, and J. P. Booth, "The role of thermal energy accommodation and atomic recombination probabilities in low pressure oxygen plasmas," *Plasma Physics and Controlled Fusion*, vol. 59, art. 024004, 2017.

[143] M. Génévriez, K. M. Dunseath, M. Terao-Dunseath, A. Hibbert, A. Dochain, R. Marion, and X. Urbain, "Absolute total, partial, and differential cross sections for photodetachment of O," *Physical Review A*, vol. 98, no. 3, pp. 1–14, 2018.

[144] L. C. Lee and G. P. Smith, "Photodissociation and photodetachment of molecular negative ions. VI. Ions in $O_2/CH_4/H_2O$ mixtures from 3500 to 8600 Å," *The Journal of Chemical Physics*, vol. 70, no. 4, pp. 1727–1735, 1979.

[145] Z. E. Helou, S. Churassy, G. Wannous, R. Bacis, and E. Boursey, "Absolute cross sections of ozone at atmospheric temperatures for the Wulf and the Chappuis bands," *Journal of Chemical Physics*, vol. 122, art. 244311, 2005.

[146] E. Stoffels, W. W. Stoffels, D. Vender, M. Kando, G. M. Kroesen, and F. J. De Hoog, "Negative ions in a radio-frequency oxygen plasma," *Physical Review E*, vol. 51, no. 3, pp. 2425–2435, 1995.

[147] B. J. Drouin, H. Gupta, S. Yu, C. E. Miller, and H. S. Müller, "High resolution spectral analysis of oxygen. II. Rotational spectra of $a^1\Delta_g$ O_2 isotopologues," *Journal of Chemical Physics*, vol. 137, art. 024305, 2012.

[148] P. Werle, R. Mucke, and F. Slemr, "The limits of signal averaging in atmospheric trace-gas monitoring by tunable diode-laser absorption spectroscopy," *Applied Physics B*, vol. 57, pp. 131–139, 1993.

[149] T. Wegner, C. Küllig, and J. Meichsner, "On the E-H transition in inductively coupled radio frequency oxygen plasmas: I. Density and temperature of electrons, ground state and singlet metastable molecular oxygen," *Plasma Sources Science and Technology*, vol. 26, art. 025006, 2017.

[150] A. Derzsi, T. Lafleur, J. P. Booth, I. Korolov, and Z. Donkó, "Experimental and simulation study of a capacitively coupled oxygen discharge driven by tailored voltage waveforms," *Plasma Sources Science and Technology*, vol. 25, art. 015004, 2016.

[151] R. P. Wayne, "Singlet Molecular Oxygen," *Advances in Photochemistry*, vol. 7, pp. 311–371, 1969.

[152] S. Yu, B. J. Drouin, and C. E. Miller, "High resolution spectral analysis of oxygen. IV. Energy levels, partition sums, band constants, RKR potentials, Franck-Condon factors involving the $X^3\Sigma_g^-$, $a^1\Delta_g$ and $b^1\Sigma_g^+$ states," *Journal of Chemical Physics*, vol. 141, art. 174302, 2014.

[153] G. Hancock, R. Peverall, G. A. D. Ritchie, and L. J. Thornton, "Absolute number densities of vibrationally excited $N_2(A^3\Sigma_u^+)$ produced in a low pressure rf plasma," *Journal of Physics D: Applied Physics*, vol. 39, pp. 1846–1852, 2006.

[154] G. P. Perram, D. A. Determan, J. A. Dorian, B. F. Lowe, and T. L. Thompson, "Radial diffusion between coaxial cylinders and surface deactivation of $O_2(b^1\Sigma_g^+)$," *Chemical Physics*, vol. 162, pp. 427–432, 1992.

[155] E. G. Thorsteinsson and J. T. Gudmundsson, "The low pressure Cl_2/O_2 discharge and the role of ClO," *Plasma Sources Science and Technology*, vol. 19, art. 055008, 2010.

[156] J. P. Booth, A. Chatterjee, O. Guaitella, D. Lopaev, S. Zyryanov, A. Volynets, T. Rakhimova, D. Voloshin, A. Chukalovsky, Y. Mankelevich, and V. Guerra, "Quenching of $O_2(b^1\Sigma_g^+)$ by $O(^3P)$ atoms. Effect of gas temperature," *Plasma Sources Science and Technology*, vol. 31, art. 065012, 2022.

[157] P. D. Burrow, "Dissociative attachment from the $O_2(a^1\Delta_g)$ state," *The Journal of Chemical Physics*, vol. 59, pp. 4932–4936, 1973.

[158] N. C. M. Fuller, M. V. Malyshev, V. M. Donnelly, and I. P. Herman, "Characterization of transformer coupled oxygen plasmas by trace rare gases-optical emission spectroscopy and langmuir probe analysis," *Technol*, vol. 9, pp. 116–127, 2000.

[159] V. Laporta, R. Celiberto, and J. Tennyson, "Dissociative electron attachment and electron-impact resonant dissociation of vibrationally excited o2 molecules," *Physical Review A - Atomic, Molecular, and Optical Physics*, vol. 91, art. 012701, 2015.

[160] M. Tashiro, K. Morokuma, and J. Tennyson, "R-matrix calculation of differential cross sections for low-energy electron collisions with ground-state and electronically excited-state O_2 molecules," *Physical Review A - Atomic, Molecular, and Optical Physics*, vol. 74, art. 022706, 2006.

[161] J. T. Gudmundsson, "A critical review of the reaction set for a low pressure oxygen processing discharge (technical report rh-16-2004)," tech. rep., Science Institute, University of Iceland, 2004.

[162] A. V. Phelps, "Tabulations of Collision Cross Sections and Calculated Transport and Reaction Coefficients for Electron Collisions with O_2: Technical Report 28, JILA Information Center Report," tech. rep., University of Colorado, Boulder, Colorado, 1985.

[163] R. Peverall, S. Rosén, J. R. Peterson, M. Larsson, A. Al-Khalili, L. Vikor, J. Semaniak, R. Bobbenkamp, A. Le Padellec, A. N. Maurellis, and W. J. Van Der Zande, "Dissociative recombination and excitation of O_2^+: Cross sections, product yields and implications for studies of ionospheric airglows," *Journal of Chemical Physics*, vol. 114, no. 15, pp. 6679–6689, 2001.

[164] R. Atkinson, D. L. Baulch, R. A. Cox, R. F. Hampson, J. A. Kerr Chairman, and J. Troe, "Evaluated Kinetic and Photochemical Data for Atmospheric Chemistry: Supplement III. IUPAC Subcommittee on Gas Kinetic Data Evaluation for Atmospheric Chemistry," *Journal of Physical and Chemical Reference Data*, vol. 26, no. 3, pp. 521–1011, 1997.

[165] D.-X. Liu, M.-Z. Rong, X.-H. Wang, F. Iza, M. G. Kong, and P. Bruggeman, "Main Species and Physicochemical Processes in Cold Atmospheric-pressure He + O_2 Plasmas," *Plasma Processes and Polymers*, vol. 7, no. 9-10, pp. 846–865, 2010.

[166] A. V. Volynets, D. V. Lopaev, T. V. Rakhimova, O. V. Proshina, A. A. Chukalovsky, and J. P. Booth, "Fast quenching of metastable $O_2(a^1\Delta_g)$ and $O_2(b^1\Sigma_g^+)$ molecules by $O(^3P)$ atoms at high temperature," *Plasma Sources Science and Technology*, vol. 29, art. 115020, 2020.

[167] D. A. Toneli, R. S. Pessoa, M. Roberto, and J. T. Gudmundsson, "A volume averaged global model study of the influence of the electron energy distribution and the wall material on an oxygen discharge," *Journal of Physics D: Applied Physics*, vol. 48, art. 495203, 2015.

[168] S. G. Belostotsky, D. J. Economou, D. V. Lopaev, and T. V. Rakhimova, "Negative ion destruction by O(3P) atoms and O2(a 1Δg) molecules in an oxygen plasma," *Plasma Sources Science and Technology*, vol. 14, no. 3, pp. 532–542, 2005.

[169] A. Midey, I. Dotan, S. Lee, W. T. Rawlins, M. A. Johnson, and A. A. Viggiano, "Kinetics for the reaction of O^- and O_2^- with $O_2(a^1\Delta_g)$ Measured in a Selected Ion Flow Tube at 300 K.," *Journal of Physical Chemistry A*, vol. 111, no. 24, pp. 5218–5222, 2007.

[170] A. Midey, I. Dotan, and A. A. Viggiano, "Temperature Dependences for the Reactions of O^- and O_2^- with $O_2(a^1\Delta_g)$ from 200 to 700 K.," *Journal of Physical Chemistry A*, vol. 112, no. 14, pp. 3040–3045, 2007.

[171] D.-C. Seo and T.-H. Chung, "Observation of the transition of operating regions in a low-pressure inductively coupled oxygen plasma by Langmuir probe measurement and optical emission spectroscopy," *Journal of Physics D: Applied Physics J. Phys. D: Appl. Phys*, vol. 34, pp. 2854–2861, 2001.

[172] W. X. Ding, L. A. Pinnaduwage, C. Tav, and D. L. McCorkle, "Role of high Rydberg states in enhanced O^- formation in a pulsed O_2 discharge," *Plasma Sources Science and Technology*, vol. 8, no. 3, pp. 384–391, 1999.

[173] J. A. Wagner and H. M. Katsch, "Negative oxygen ions in a pulsed RF-discharge with inductive coupling in mixtures of noble gases and oxygen," *Plasma Sources Science and Technology*, vol. 15, no. 1, pp. 156–169, 2006.

[174] L. D. Landau and E. M. Lifshitz, *Fluid Mechanics*. Oxford: Permagon Press, second ed., 1987.

[175] E. W. Lemmon and R. T. Jacobsen, "Viscosity and Thermal Conductivity Equations for Nitrogen, Oxygen, Argon, and Air," *International Journal of Thermophysics*, vol. 25, no. 1, pp. 21–69, 2004.

[176] A. Parent, M. Morin, and P. Lavigne, "Propagation of super-Gaussian field distributions," *Optical and Quantum Electronics*, vol. 24, no. 9, pp. 1071–1079, 1992.

[177] D. C. Duncan, "The excitation of the spectra of nitrogen by electron impacts," *The Astrophysical Journal*, vol. 62, no. 3, pp. 145–167, 1925.

[178] S. E. Williams, "The efficiency of excitation of the nitrogen first positive bands by electron impact," *Proceedings of the Physical Society*, vol. 47, pp. 420–423, 1935.

[179] R. B. Bates, "The intensity distribution in the nitrogen band systems emitted from the earth's upper atmosphere," *Proceedings of the Royal Society of London. Series A. Mathematical and Physical Sciences*, vol. 196, no. 1045, pp. 217–250, 1949.

[180] D. C. Tyte, "Some observations on the nitrogen first negative system," *Proceedings of the Physical Society*, vol. 81, pp. 163–170, 1963.

[181] C. Biloiu, X. Sun, Z. Harvey, and E. Scime, "An alternative method for gas temperature determination in nitrogen plasmas: Fits of the bands of the first positive system ($B^3\Pi_g \rightarrow A\ ^3\Sigma_u^+$)," *Journal of Applied Physics*, vol. 101, art. 073303, 2007.

[182] F. Becker, I. W. Rangelow, K. Maßeli, and R. Kassing, "Diagnostic on N_2 plasma with an energy resolved quadrupole mass spectrometer at the powered electrode in a reactive ion etching system: ion energy distribution of N_2^+ and N^+," *Surface and Coatings Technology*, vol. 74-75, pp. 485–490, 1995.

[183] J. Cho, S. Han, Y. Lee, O. K. Kim, G. H. Kim, Y. W. Kim, H. Lim, and M. Suh, "Measurement of nitrogen ion species ratio in inductively coupled plasma source ion implantation," *Surface and Coatings Technology*, vol. 136, no. 1-3, pp. 106–110, 2001.

[184] J. Benedikt, A. Hecimovic, D. Ellerweg, and A. Von Keudell, "Quadrupole mass spectrometry of reactive plasmas," *Journal of Physics D: Applied Physics*, vol. 45, art. 403001, 2012.

[185] C. J. Gillan, O. Nagy, P. G. Burke, L. A. Morgan, and C. J. Noble, "Electron scattering by nitrogen molecules," *Journal of Physics B: Atomic and Molecular Physics*, vol. 20, no. 17, pp. 4585–4603, 1987.

[186] A. Bourdon and P. Vervisch, "Electron-vibration energy exchange models in nitrogen plasma flows," *Physical Review E - Statistical Physics, Plasmas, Fluids, and Related Interdisciplinary Topics*, vol. 55, no. 4, pp. 4634–4641, 1997.

[187] D. T. Birtwistle and A. Herzenberg, "Vibrational excitation of N_2 by resonance scattering of electrons," *Journal of Physics B: Atomic and Molecular Physics*, vol. 4, no. 1, pp. 53–70, 1971.

[188] S. De Benedictis, G. Dilecce, M. Simek, and M. Vigliotti, "Experimental study of N_2 RF plasma jet by optical methods," *Plasma Sources Science and Technology*, vol. 7, no. 4, pp. 557–571, 1998.

[189] Q. Y. Zhang, D. Q. Shi, W. Xu, C. Y. Miao, C. Y. Ma, C. S. Ren, C. Zhang, and Z. Yi, "Determination of vibrational and rotational temperatures in highly constricted nitrogen plasmas by fitting the second positive system of N_2 molecules," *AIP Advances*, vol. 5, art. 057158, 2015.

[190] C. Biloiu, X. Sun, Z. Harvey, and E. Scime, "Determination of rotational and vibrational temperatures of a nitrogen helicon plasma," *Review of Scientific Instruments*, vol. 77, art. 10F117, 2006.

[191] P. Paris, M. Aints, F. Valk, T. Plank, A. Haljaste, K. V. Kozlov, and H. E. Wagner, "Intensity ratio of spectral bands of nitrogen as a measure of electric field strength in plasmas," *Journal of Physics D: Applied Physics*, vol. 38, no. 21, pp. 3894–3899, 2005.

[192] G. Dilecce, P. F. Ambrico, L. M. Martini, and P. Tosi, "On the determination of the vibrational temperature by optical emission spectroscopy," *Plasma Sources Science and Technology*, vol. 31, art. 077001, 2022.

[193] H. Fatima, M. U. Ullah, S. Ahmad, M. Imran, S. Sajjad, S.Hussain, and A. Qayyum, "Spectroscopic evaluation of vibrational temperature and electron density in reduced pressure radio frequency nitrogen plasma," *SN Applied Sciences*, vol. 3, art. 646, 2021.

[194] A. M. Pointu, E. Mintusov, and P. Fromy, "Study of an atmospheric pressure flowing afterglow in N_2/NO mixture and its application to the measurement of N_2(A) concentration," *Plasma Sources Science and Technology*, vol. 19, art. 015018, 2010.

[195] L. G. Piper, "State-to-state $N_2(A^3\Sigma_u^+)$ energy pooling reactions. II. The formation and quenching of $N_2(B^3\Pi_g, v' = 1\text{–}12)$," *The Journal of Chemical Physics*, vol. 88, no. 11, pp. 6911–6921, 1988.

[196] L. G. Piper, "State-to-state $N_2(A^3\Sigma_u^+)$ energy-pooling reactions. I. The formation of $N_2(C^3\Pi_u)$ and the Herman infrared system," *The Journal of Chemical Physics*, vol. 88, no. 1, pp. 231–239, 1988.

[197] L. G. Piper, "The excitation of $N(^2P)$ by $N_2(A^3\Sigma_u^+, v' = 0, 1)$," *The Journal of Chemical Physics*, vol. 90, no. 12, pp. 7087–7095, 1989.

[198] M. Šimek, "Determination of $N_2(A^3\Sigma_u^+)$ metastable density produced by nitrogen streamers at atmospheric pressure: 1. Design of diagnostic method," *Plasma Sources Science and Technology*, vol. 12, no. 3, pp. 421–431, 2003.

[199] D. W. Ferguson, K. Narahari Rao, P. A. Martin, and G. Guelachvili, "High resolution infrared Fourier transform emission spectra of the $^{14}N_2^+$ Meinel system: $A^2\Pi_u$ -$X^2\Sigma_g^+$," *Journal of Molecular Spectroscopy*, vol. 153, pp. 599–609, 1992.

[200] B. Krames, T. Glenewinkel-Meyer, and J. Meichsner, "Spatial density profiles of the N_2 metastable state $A^3\Sigma_u^+$, the $B^3\Pi_g$ and $C^3\Pi_u$ states in an asymmetric rf discharge," *Journal of Physics D: Applied Physics*, vol. 34, no. 12, pp. 1789–1798, 2001.

[201] B. Krames, T. Glenewinkel-Meyer, and J. Meichsner, "In situ determination of absolute number densities of nitrogen molecule triplet states in an rf-plasma sheath," *Journal of Applied Physics*, vol. 89, no. 6, pp. 3115–3120, 2001.

[202] S. De Benedictis and G. Dilecce, "Rate constants for deactivation of $N_2(A)$ $v = 2$–7 by O, O_2, and NO," *The Journal of Chemical Physics*, vol. 107, no. 16, pp. 6219–6229, 1997.

[203] S. De Benedictis, G. Dilecce, and M. Simek, "Time-resolved LIF spectroscopy on $N_2(A)$ metastable in a He/N_2 pulsed rf discharge," *Chemical Physics*, vol. 178, no. 1-3, pp. 547–560, 1993.

[204] S. Nemschokmichal, F. Bernhardt, B. Krames, and J. Meichsner, "Laser-induced fluorescence spectroscopy of $N_2(A^3\Sigma_u^+)$ and absolute density calibration by Rayleigh scattering in capacitively coupled rf discharges," *Journal of Physics D: Applied Physics*, vol. 44, art. 205201, 2011.

[205] R. Ono, C. Tobaru, Y. Teramoto, and T. Oda, "Laser-induced fluorescence of $N_2(A^3\Sigma_u^+)$ metastable in N_2 pulsed positive corona discharge," *Plasma Sources Science and Technology*, vol. 18, art. 025006, 2009.

[206] S. De Benedictis, G. Dilecce, and M. Simek, "LIF measurement of $N_2(A^3\Sigma_u^+, v = 4)$ population density in a pulsed rf discharge," *Journal of Physics D: Applied Physics*, vol. 31, no. 10, pp. 1197–1205, 1998.

[207] G. Dilecce, P. F. Ambrico, and S. De Benedictis, "OODR-LIF direct measurement of $N_2(C^3\Pi_u, v = 0 - 4)$ electronic quenching and vibrational relaxation rate coefficients by N_2 collision," *Chemical Physics Letters*, vol. 431, no. 4-6, pp. 241–246, 2006.

[208] M. Šimek, P. F. Ambrico, and V. Prukner, "LIF study of $N_2(A^3\Sigma_u^+, v = 0 - 10)$ vibrational kinetics under nitrogen streamer conditions," *Journal of Physics D: Applied Physics*, vol. 48, art. 265202, 2015.

[209] G. D. Stancu, M. Janda, F. Kaddouri, D. A. Lacoste, and C. O. Laux, "Time-resolved CRDS measurements of the $N_2(A^3\Sigma_u^+)$ density produced by nanosecond discharges in atmospheric pressure nitrogen and air," *Journal of Physical Chemistry A*, vol. 114, no. 1, pp. 201–208, 2010.

[210] B. K. Woodcock, J. R. Busby, T. G. Freegarde, and G. Hancock, "Doppler spectroscopic measurements of sheath ion velocities in radio-frequency plasmas," *Journal of Applied Physics*, vol. 81, no. 9, pp. 5945–5949, 1997.

[211] K. Konthasinghe, K. Fitzmorris, M. Peiris, A. J. Hopkins, B. Petrak, D. K. Killinger, and A. Muller, "Laser-induced fluorescence from N_2^+ ions generated by a corona discharge in ambient air," *Applied Spectroscopy*, vol. 69, no. 9, pp. 1042–1046, 2015.

[212] J. M. Cook, T. A. Miller, and V. E. Bondybey, "Laser induced fluorescence detection and characterization of ionic and metastable reaction products," *The Journal of Chemical Physics*, vol. 69, no. 6, pp. 2562–2568, 1978.

[213] E. A. Den Hartog, H. Persing, and R. C. Woods, "Laser-induced fluorescence measurements of transverse ion temperature in an electron cyclotron resonance plasma," *Applied Physics Letters*, vol. 57, no. 7, pp. 661–663, 1990.

[214] D. E. Gerassimou, S. Cavadias, D. Mataras, and D. E. Rapakoulias, "Nitrogen ion dynamics in low-pressure nitrogen plasma and plasma sheath," *Journal of Applied Physics*, vol. 67, no. 1, pp. 146–153, 1990.

[215] T. A. Miller, T. Suzuki, and E. Hirota, "High resolution, cw laser induced fluorescence study of the $A^2\Pi_u$ -$X^2\Sigma_g^+$ system of N_2^+," *The Journal of Chemical Physics*, vol. 80, no. 10, pp. 4671–4678, 1984.

[216] R. J. Visser, J. A. Baggerman, J. P. Poppelaars, and E. J. Collart, "The time evolution of the ion density and the gas temperature in pulsed radio frequency plasmas," *Journal of Applied Physics*, vol. 71, no. 12, pp. 5792–5798, 1992.

[217] A. Lucca Fabris, C. V. Young, and M. A. Cappelli, "Time-resolved laser-induced fluorescence measurement of ion and neutral dynamics in a Hall thruster during ionization oscillations," *Journal of Applied Physics*, vol. 118, art. 233301, 2015.

[218] C. V. Young, A. Lucca Fabris, and M. A. Cappelli, "Ion dynamics in an e × B Hall plasma accelerator," *Applied Physics Letters*, vol. 106, art. 044102, 2015.

[219] B. Jacobs, W. Gekelman, P. Pribyl, and M. Barnes, "Phase-Resolved Measurements of Ion Velocity in a Radio-Frequency Sheath," *Physical Review Letters*, vol. 105, art. 075001, 2010.

[220] E. Kawamura, V. Vahedi, M. A. Lieberman, and C. K. Birdsall, "Ion energy distributions in rf sheaths; review, analysis and simulation," *Plasma Sources Science and Technology*, vol. 8, pp. R45–R64, 1999.

[221] J. W. Coburn and E. Kay, "Positive-ion bombardment of substrates in rf diode glow discharge sputtering," *Journal of Applied Physics*, vol. 43, no. 12, pp. 4965–4971, 1972.

[222] R. J. Hoekstra and M. J. Kushner, "Predictions of ion energy distributions and radical fluxes in radio frequency biased inductively coupled plasma etching reactors," *Journal of Applied Physics*, vol. 79, no. 5, pp. 2275–2286, 1996.

[223] T. Fukuchi, "Detection of metastable excited molecules $N_2(A^3\Sigma_u^+)$ in an atmospheric pressure nitrogen discharge by Raman scattering," *Electronics and Communications in Japan*, vol. 93, no. 6, pp. 34–40, 2010.

[224] E. Carbone and S. Nijdam, "Thomson scattering on non-equilibrium low density plasmas: Principles, practice and challenges," *Plasma Physics and Controlled Fusion*, vol. 57, art. 014026, 2015.

[225] S. Hübner, E. Carbone, J. M. Palomares, and J. van der Mullen, "Afterglow of Argon Plasmas with H_2, O_2, N_2, and CO_2 Admixtures Observed by Thomson Scattering," *Plasma Processes and Polymers*, vol. 11, pp. 482–488, art. 015018, 2014.

[226] I. Hadj Bachir, T. R. Huet, J. L. Destombes, and M. Vervloet, "Laser optogalvanic spectroscopy of N_2 from the $A^3\Sigma_u^+$ metastable state in a corona excited supersonic expansion," *Chemical Physics Letters*, vol. 270, no. 5-6, pp. 533–537, 1997.

[227] I. Hadj Bachir, H. Bolvin, C. Demuynck, J. Destombes, and A. Zellagui, "High-Resolution Optogalvanic Spectrum of N_2^+ Using a Ti:Sapphire Laser: The (2,0) Vibrational Band of the Meinel System $A^2\Pi_u$ - $X^2\Sigma_g^+$," *Journal of Molecular Spectroscopy*, vol. 166, pp. 88–96, 1994.

[228] D. Collet, J. L. Destombes, I. Hadj Bachir, and T. R. Huet, "Rotational analysis of the vibrational hot bands of N_2^+ ($A^2\Pi_u$ -$X\ ^2\Sigma_g^+$) in the near-infrared region using velocity modulation spectroscopy," *Chemical Physics Letters*, vol. 286, pp. 311–316, 1998.

[229] A. A. Mills, B. M. Siller, and B. J. McCall, "Precision cavity enhanced velocity modulation spectroscopy," *Chemical Physics Letters*, vol. 501, pp. 1–5, 2010.

[230] B. M. Siller, A. A. Mills, and B. J. McCall, "Cavity-enhanced velocity modulation spectroscopy," *Optics Letters*, vol. 35, no. 8, p. 1266, 2010.

[231] Y. D. Wu, J. W. Ben, N. Li, L. J. Zheng, Y. Q. Chen, and X. H. Yang, "Study of (2, 0) band of $A^2\Pi_u$ -$X^2\Sigma_g^+$ system of N_2^+ by optical heterodyne detected velocity modulation spectroscopy," *Chinese Journal of Chemical Physics*, vol. 20, no. 3, pp. 285–290, 2007.

[232] Y. Liu, C. Duan, S. Wu, H. Zhuang, and Y. Chen, "The rotational structure of the (7, 4) and (7, 2) bands of the $A^2\Pi_u$ -$X^2\Sigma_g^+$ system of N_2^+ studied by velocity modulation laser spectroscopy," *Journal of Molecular Spectroscopy*, vol. 208, no. 1, pp. 144–147, 2001.

[233] Y. P. Zhang, L. H. Deng, J. Zhang, and Y. Q. Chen, "Rotational Analysis of $A^2\Pi_u$ -$X^2\Sigma_g^+$ System of $^{14}N_2^+$," *Chinese Journal of Chemical Physics*, vol. 28, no. 2, pp. 134–142, 2015.

[234] J. N. Hodges and B. J. McCall, "Quantitative velocity modulation spectroscopy," *Journal of Chemical Physics*, vol. 144, art. 184201, 2016.

[235] O. Oldenberg, D. G. Bills, and N. P. Carleton, "Measurement of Weak Absorption by Molecules," *Journal of the Optical Society of America*, vol. 51, no. 5, p. 526, 1961.

[236] G. Cernogora, L. Hochard, M. Touzeau, and C. M. Ferreira, "Population of $N_2(A^3\Sigma_u^+)$ metastable states in a pure nitrogen glow discharge," *Journal of Physics B: Atomic and Molecular Physics*, vol. 14, pp. 2977–2987, 1981.

[237] G. Cernogora, C. M. Ferreira, L. Hochard, M. Touzeau, and J. Loureiro, "Vibrational populations of $N_2(A^3\Sigma_u^+)$ in a pure nitrogen glow discharge," *Journal of Physics B: Atomic and Molecular Physics*, vol. 17, no. 21, pp. 4429–4437, 1984.

[238] E. Augustyniak and J. Borysow, "Kinetics of the $(A^3\Sigma_u^+, v = 0)$ state of N_2 in the near afterglow of a nitrogen pulsed discharge," *Journal of Physics D: Applied Physics*, vol. 27, pp. 652–660, 1994.

[239] C. Foissac, A. Campargue, A. Kachanov, P. Supiot, G. Weirauch, and N. Sadeghi, "Intracavity laser absorption spectroscopy applied to measure the

absolute density and temperature of $N_2(A^3\Sigma_u^+)$ metastable molecules in a flowing N_2 microwave discharge," *Journal of Physics D: Applied Physics*, vol. 33, no. 19, pp. 2434–2441, 2000.

[240] N. Sadeghi, C. Foissac, and P. Supiot, "Kinetics of $N_2(A^3\Sigma_u^+)$ molecules and ionization mechanisms in the afterglow of a flowing N_2 microwave discharge," *Journal of Physics D: Applied Physics*, vol. 34, no. 12, pp. 1779–1788, 2001.

[241] B. Bakowski, G. Hancock, R. Peverall, G. A. Ritchie, and L. J. Thornton, "Characterization of an inductively coupled N_2 plasma using sensitive diode laser spectroscopy," *Journal of Physics D: Applied Physics*, vol. 37, no. 15, pp. 2064–2072, 2004.

[242] M. Kotterer, J. Conceicao, and J. P. Maier, "Cavity ringdown spectroscopy of molecular ions: $A^2\Pi_u \leftarrow X^2\Sigma_g^+$ (6-0) transition of N_2^+," *Chemical Physics Letters*, vol. 259, no. 1-2, pp. 233–236, 1996.

[243] M. Aldener, B. Lindgren, A. Pettersson, and U. Sassenberg, "Cavity Ringdown Laser Absorption Spectroscopy - Nitrogen cation," *Physica Scripta*, vol. 61, pp. 62–65, 2000.

[244] A. P. Yalin, C. O. Laux, C. H. Kruger, and R. N. Zare, "Spatial profiles of N_2^+ concentration in an atmospheric pressure nitrogen glow discharge," *Plasma Sources Science and Technology*, vol. 11, no. 3, pp. 248–253, 2002.

[245] S. L. Widicus Weaver, M. B. Wiczer, B. Negru, J. P. DiGangi, B. A. Tom, and B. J. McCall, "Continuous-wave cavity ringdown spectroscopy of the N_2^+ Meinel system (2, 1) band," *Journal of Molecular Spectroscopy*, vol. 249, no. 1, pp. 14–22, 2008.

[246] T. Gherman, E. Eslami, D. Romanini, S. Kassi, J. C. Vial, and N. Sadeghi, "High sensitivity broad-band mode-locked cavity-enhanced absorption spectroscopy: measurement of $Ar^*(^3P_2)$ atom and N_2^+ ion densities," *Journal of Physics D: Applied Physics*, vol. 37, no. 17, pp. 2408–2415, 2004.

[247] C. M. Western, L. Carter-Blatchford, P. Crozet, A. J. Ross, J. Morville, and D. W. Tokaryk, "The spectrum of N_2 from 4,500 to 15,700 cm^{-1} revisited with PGOPHER," *Journal of Quantitative Spectroscopy and Radiative Transfer*, vol. 219, pp. 127–141, 2018.

[248] F. R. Gilmore, R. R. Laher, and P. J. Espy, "Franck–Condon Factors, r-Centroids, Electronic Transition Moments, and Einstein Coefficients for Many Nitrogen and Oxygen Band Systems," *Journal of Physical and Chemical Reference Data*, vol. 21, no. 5, pp. 1005–1107, 1992.

[249] K. Shibusawa and M. Funatsu, "Radiative characteristics of N_2 first positive band in visible and near-infrared regions for microwave-discharged nitrogen plasma," *Transactions of the Japan Society for Aeronautical and Space Sciences*, vol. 62, no. 2, pp. 86–92, 2019.

[250] H. Geisen, D. Neuschäfer, and C. Ottinger, "State-specific predissociation of $N_2(B^3\Pi_g)$ measured by laser-induced fluorescence on a molecular beam," *The Journal of Chemical Physics*, vol. 92, no. 1, pp. 104–115, 1990.

[251] M. Mavadat, A. Ricard, C. Sarra-Bournet, and G. Laroche, "Determination of ro-vibrational excitations of N_2(B, v) and N_2(C, v) states in N_2 microwave discharges using visible and IR spectroscopy," *Journal of Physics D: Applied Physics*, vol. 44, art. 155207, 2011.

[252] N. Britun, M. Gaillard, A. Ricard, Y. M. Kim, K. S. Kim, and J. G. Han, "Determination of the vibrational, rotational and electron temperatures in N_2 and Ar-N_2 rf discharge," *Journal of Physics D: Applied Physics*, vol. 40, no. 4, pp. 1022–1029, 2007.

[253] P. Supiot, O. Dessaux, and P. Goudmand, "Spectroscopic analysis of the nitrogen short-lived afterglow induced at 433 MHz," *Journal of Physics D: Applied Physics*, vol. 28, no. 9, pp. 1826–1839, 1995.

[254] Z. D. Kang and Y. K. Pu, "Molecular nitrogen vibrational temperature in an inductively coupled plasma," *Chinese Physics Letters*, vol. 19, no. 2, pp. 211–213, 2002.

[255] A. French, *High sensitivity spectroscopic studies in low pressure molecular plasma systems*. Part II, University of Oxford, 2017.

[256] I. M. El-Fayoumi, I. R. Jones, and M. M. Turner, "Hysteresis in the E- to H-mode transition in a planar coil, inductively coupled rf argon discharge," *Journal of Physics D: Applied Physics*, vol. 31, no. 21, pp. 3082–3094, 1998.

[257] S. Kassi, T. Stoltmann, M. Casado, M. Daëron, and A. Campargue, "Lamb dip CRDS of highly saturated transitions of water near 1.4 μm," *Journal of Chemical Physics*, vol. 148, art. 054201, 2018.

[258] D. Romanini, P. Dupré, and R. Jost, "Non-linear effects by continuous wave cavity ringdown spectroscopy in jet-cooled NO_2," *Vibrational Spectroscopy*, vol. 19, no. 1, pp. 93–106, 1999.

[259] M. Tuszewski, "Ion and gas temperatures of 0.46 MHz inductive plasma discharges," *Journal of Applied Physics*, vol. 100, art. 053301, 2006.

[260] D. Shi, W. Xing, J. Sun, Z. Zhu, and Y. Liu, "Spectroscopic constants and molecular properties of $X^2\Sigma_g^+$, $A^2\Pi_u$, $B^2\Sigma_u^+$ and $D^2\Pi_g$ electronic states of the N_2^+ ion," *Computational and Theoretical Chemistry*, vol. 966, pp. 44–53, 2011.

[261] E. G. Thorsteinsson and J. T. Gudmundsson, "A global (volume averaged) model of a nitrogen discharge: I. Steady state," *Plasma Sources Science and Technology*, vol. 18, art. 045001, 2009.

[262] Y. Horikawa, K. Kurihara, and K. Sasaki, "Absolute densities of $N_2(A^3\Sigma_u^+)$, $N(^4S)$, and $N(^2D)$ in an inductively coupled nitrogen plasma source," *Japanese Journal of Applied Physics*, vol. 49, art. 026101, 2010.

[263] X. J. Huang, Y. Xin, L. Yang, Q. H. Yuan, and Z. Y. Ning, "Spectroscopic study on rotational and vibrational temperature of N_2 and N_2^+ in dual-frequency capacitively coupled plasma," *Physics of Plasmas*, vol. 15, art. 113504, 2008.

[264] Y. K. Pu, Z. G. Guo, Aman-Ur-Rehman, Z. D. Yu, and J. Ma, "Tuning effect of inert gas mixing on electron energy distribution function in inductively coupled discharges," *Plasma Physics and Controlled Fusion*, vol. 48, no. 1, pp. 61–70, 2006.

[265] M. Lino da Silva, V. Guerra, J. Loureiro, and P. A. Sá, "Vibrational distributions in N_2 with an improved calculation of energy levels using the RKR method," *Chemical Physics*, vol. 348, no. 1-3, pp. 187–194, 2008.

[266] P. C. Cosby, "Electron-impact dissociation of nitrogen," *The Journal of Chemical Physics*, vol. 98, no. 12, pp. 9544–9559, 1993.

[267] C. Tian and C. R. Vidal, "Electron impact ionization of N_2 and O_2: contributions from different dissociation channels of multiply ionized molecules," *Journal of Physics B: Atomic, Molecular and Optical Physics*, vol. 31, pp. 5369–5381, 1998.

[268] R. S. Freund, R. C. Wetzel, and R. J. Shul, "Measurements of electron-impact-ionization cross sections of N_2, CO, CO_2, CS, S_2, CS_2, and metastable N_2," *Physical Review A*, vol. 41, no. 11, pp. 5861–5868, 1990.

[269] H. Su, X. Cheng, H. Zhang, and J. Tennyson, "Electro collisions with molecular nitrogen in its ground and electronically excited states using the R-matrix method," *Journal of Physics B: Atomic, Molecular and Optical Physics*, vol. 54, art. 115203, 2021.

[270] Y. K. Kim and J. P. Desclaux, "Ionization of carbon, nitrogen, and oxygen by electron impact," *Physical Review A - Atomic, Molecular, and Optical Physics*, vol. 66, art. 012708, 2002.

[271] S. S. Tayal and O. Zatsarinny, "B-spline R-matrix with pseudostates approach for electron impact excitation of atomic nitrogen," *Journal of Physics B: Atomic, Molecular and Optical Physics*, vol. 38, no. 20, pp. 3631–3645, 2005.

[272] J. R. Peterson, A. Le Padellec, H. Danared, G. H. Dunn, M. Larsson, A. Larson, R. Peverall, C. Strömholm, S. Rosén, M. Af Ugglas, and W. J. Van Der Zande, "Dissociative recombination and excitation of N_2^+: Cross sections and product branching ratios," *Journal of Chemical Physics*, vol. 108, no. 5, pp. 1978–1988, 1998.

[273] E. M. Bahati, J. J. Jureta, D. S. Belic, H. Cherkani-Hassani, M. O. Abdellahi, and P. Defrance, "Electron impact dissociation and ionization of N_2^+," *Journal of Physics B: Atomic, Molecular and Optical Physics*, vol. 34, no. 15, pp. 2963–2973, 2001.

[274] B. F. Gordiets, C. M. Ferreira, V. L. Guerra, J. M. Loureiro, J. Nahorny, D. Pagnon, M. Touzeau, and M. Vialle, "Kinetic Model of a Low-Pressure N_2–O_2 Flowing Glow Discharge," *IEEE Transactions on Plasma Science*, vol. 23, no. 4, pp. 750–768, 1995.

[275] R. Flagan and J. Appleton, "Excitation mechanism of thenitrogen first positive and first negative radiation at high temperature," *Journal of Chemical Physics*, vol. 56, no. 3, pp. 1163–1173, 1971.

[276] A. V. Volynets, D. V. Lopaev, T. V. Rakhimova, A. A. Chukalovsky, Y. A. Mankelevich, N. A. Popov, A. I. Zotovich, and A. T. Rakhimov, "N_2 dissociation and kinetics of $N(^4S)$ atoms in nitrogen DC glow discharge," *Journal of Physics D: Applied Physics*, vol. 51, art. 364002, 2018.

[277] A. Salmon, N. A. Popov, G. D. Stancu, and C. O. Laux, "Quenching rate of $N(^2P)$ atoms in a nitrogen afterglow at atmospheric pressure," *Journal of Physics D: Applied Physics*, vol. 51, art. 314001, 2018.

[278] O. Dutuit, N. Carrasco, R. Thissen, V. Vuitton, C. Alcaraz, P. Pernot, N. Balucani, P. Casavecchia, A. Canosa, S. L. Picard, J. C. Loison, Z. Herman, J. Zabka, D. Ascenzi, P. Tosi, P. Franceschi, S. D. Price, and P. Lavvas, "Critical review of N, N^+, N_2^+, N^{++}, and N_2^{++} main production processes and reactions of relevance to titan's atmosphere," *Astrophysical Journal, Supplement Series*, vol. 204, no. 20, pp. 1–45, 2013.

[279] B. R. Galvão, A. J. Varandas, J. P. Braga, and J. C. Belchior, "Electronic quenching of $N(^2D)$ by N_2: Theoretical predictions, comparison with experimental rate constants, and impact on atmospheric modeling," *Journal of Physical Chemistry Letters*, vol. 4, no. 14, pp. 2292–2297, 2013.

[280] T. G. Slanger and G. Black, "Quenching of $N(^2D)$ by N_2 and H_2O," *The Journal of Chemical Physics*, vol. 64, no. 11, pp. 4442–4444, 1976.

[281] J. T. Herron, "Evaluated chemical kinetics data for reactions of $N(^2D)$, $N(^2P)$, and $N_2(A^3\Sigma_u^+)$ in the gas phase," *Journal of Physical and Chemical Reference Data*, vol. 28, no. 5, pp. 1453–1483, 1999.

[282] I. A. Kossyi, A. Y. Kostinsky, A. A. Matveyev, and V. P. Silakov, "Kinetic scheme of the non-equilibrium discharge in nitrogen-oxygen mixtures," *Plasma Sources Science and Technology*, vol. 1, no. 3, pp. 207–220, 1992.

[283] D. Levron and A. V. Phelps, "Quenching of $N_2(A^3\Sigma_u^+, v = 0, 1)$ by N_2 , Ar, and H_2," *The Journal of Chemical Physics*, vol. 69, no. 5, pp. 2260–2262, 1978.

[284] Y. A. Lebedev and V. A. Shakhatov, "Diagnostics of a nonequilibrium nitrogen plasma from the emission spectra of the second positive system of N_2," *Plasma Physics Reports*, vol. 32, no. 1, pp. 56–71, 2006.

[285] R. A. Young and O. J. Dunn, "The excitation and quenching of $N(^2P)$," *The Journal of Chemical Physics*, vol. 63, no. 3, pp. 1150–1153, 1975.

[286] A. A. Matveyev and V. P. Silakov, "Theoretical study of the role of ultraviolet radiation of the non-equilibrium plasma in the dynamics of the microwave discharge in molecular nitrogen," *Plasma Sources Science and Technology*, vol. 8, no. 1, pp. 162–178, 1999.

[287] B. Rouffet, F. Gaboriau, and J. P. Sarrette, "Pressure dependence of the nitrogen atom recombination probability in late afterglows," *Journal of Physics D: Applied Physics*, vol. 43, art. 185203, 2010.

[288] W. G. Clark and D. W. Setser, "Energy transfer reactions of $N_2(A^3\Sigma_u^+)$. 5. Quenching by hydrogen halides, methyl halides, and other molecules," *Journal of Physical Chemistry*, vol. 84, no. 18, pp. 2225–2233, 1980.

[289] Y. Horikawa, T. Hayashi, and K. Sasaki, "Lifetime of molecular nitrogen at metastable $A^3\Sigma_u^+$ state in afterglow of inductively-coupled nitrogen plasma," *Japanese Journal of Applied Physics*, vol. 51, art. 126301, 2012.

[290] C. Lee and M. A. Lieberman, "Global model of Ar, O_2, Cl_2, and Ar/O_2 high-density plasma discharges," *Journal of Vacuum Science and Technology A: Vacuum, Surfaces, and Films*, vol. 13, no. 2, pp. 368–380, 1995.

[291] A. V. Phelps, "Cross Sections and Swarm Coefficients for Nitrogen Ions and Neutrals in N_2 and Argon Ions and Neutrals in Ar for Energies from 0.1 eV to 10 keV," *Journal of Physical and Chemical Reference Data*, vol. 20, no. 3, pp. 557–573, 1991.

[292] S. Agarwal, B. Hoex, M. C. Van De Sanden, D. Maroudas, and E. S. Aydil, "Absolute densities of N and excited N_2 in a N_2 plasma," *Applied Physics Letters*, vol. 83, no. 24, pp. 4918–4920, 2003.

[293] P. Bílek, L. Kuthanová, T. Hoder, and M. Šimek, "Atmospheric pressure Townsend discharge in pure nitrogen - a test case for $N_2(A^3\Sigma_u^+)$ kinetics under low E/N conditions," *Plasma Sources Science and Technology*, vol. 31, art. 084004, 2022.

[294] D. Mignogna, E. R. Jans, S. Raskar, and I. V. Adamovich, "Generation and decay of $N_2(A^3\Sigma_u^+)$ molecules in reacting CO_2 and CH_4 plasmas," *Plasma Sources Science and Technology*, vol. 31, art. 115005, 2022.

[295] N. Kang, S. G. Oh, F. Gaboriau, and A. Ricard, "Determination of the Absolute Nitrogen Atom Density in an Ar-N_2 ICP Discharge," *Applied Spectroscopy*, vol. 59, no. 5, pp. 3031–3036, 2011.

[296] S. F. Adams and T. A. Miller, "Surface and volume loss of atomic nitrogen in a parallel plate rf discharge reactor," *Plasma Sources Science and Technology*, vol. 9, no. 3, pp. 248–255, 2000.

[297] M. Capitelli and M. Dilonardo, "Nonequilibrium vibrational populations of diatomic species in electrical discharges: Effects on the dissociation rates," *Chemical Physics*, vol. 24, no. 3, pp. 417–427, 1977.

[298] B. F. Gordiets and S. S. Mamedov, "Vibrational distribution functions and relaxation rate in anharmonic-oscillator systems," *Journal of Applied Mechanics and Technical Physics*, vol. 15, no. 3, pp. 297–304, 1975.

[299] M. Capitelli, C. Gorse, and G. D. Billing, "V—V pumping up in non-equilibrium nitrogen: Effects on the dissociation rate," *Chemical Physics*, vol. 52, no. 3, pp. 299–304, 1980.

[300] G. Colonna, V. Laporta, R. Celiberto, M. Capitelli, and J. Tennyson, "Non-equilibrium vibrational and electron energy distributions functions in atmospheric nitrogen ns pulsed discharges and μs post-discharges: the role of electron molecule vibrational excitation scaling-laws," *Plasma Sources Science and Technology*, vol. 24, art. 035004, 2015.

[301] T. Kozàk and A. Bogaerts, "Splitting of CO_2 by vibrational excitation in non-equilibrium plasmas: A reaction kinetics model," *Plasma Sources Science and Technology*, vol. 23, art. 045004, 2014.

[302] P. Macko, G. Cunge, and N. Sadeghi, "Density of $N_2(X^1\Sigma_g^+;\ v = 18)$ molecules in a dc glow discharge measured by cavity ringdown spectroscopy at 227 nm; validity domain of the technique," *Journal of Physics D: Applied Physics*, vol. 34, no. 12, pp. 1807–1811, 2001.

[303] J. Kuhfeld, D. Luggenhölscher, and U. Czarnetzki, "Vibrational CARS measurements in a near-atmospheric pressure plasma jet in nitrogen: II. Analysis," *Journal of Physics D: Applied Physics*, vol. 54, art. 305204, 2021.

[304] L. G. Piper, "Reevaluation of the transition-moment function and Einstein coefficients for the $N_2(A^3\Sigma_u^+ - X^1\Sigma_g^+)$ transition," *The Journal of Chemical Physics*, vol. 99, no. 5, pp. 3174–3181, 1993.

[305] V. Laporta, D. A. Little, R. Celiberto, and J. Tennyson, "Electron-impact resonant vibrational excitation and dissociation processes involving vibrationally excited N_2 molecules," *Plasma Sources Science and Technology*, vol. 23, art. 065002, 2014.

[306] K. Niemi, V. Schulz-von Der Gathen, and H. F. Döbele, "Absolute calibration of atomic density measurements by laser-induced fluorescence spectroscopy with two-photon excitation," *Journal of Physics D: Applied Physics*, vol. 34, no. 15, pp. 2330–2335, 2001.

[307] R. Lucken, V. Croes, T. Lafleur, J.-L. Raimbault, A. Bourdon, and P. Chabert, "Edge-to-center plasma density ratios in two-dimensional plasma discharges," *Plasma Sources Science and Technology*, vol. 27, art. 035004, 2018.

[308] J. Han, P. Pribyl, W. Gekelman, A. Paterson, S. J. Lanham, C. Qu, and M. J. Kushner, "Three-dimensional measurements of plasma parameters in an inductively coupled plasma processing chamber," *Physics of Plasmas*, vol. 26, art. 103503, 2019.

[309] T. V. Tsankov and U. Czarnetzki, "Information hidden in the velocity distribution of ions and the exact kinetic Bohm criterion," *Plasma Sources Science and Technology*, vol. 26, art. 055003, 2017.

[310] L. P. Beving, M. M. Hopkins, and S. D. Baalrud, "How sheath properties change with gas pressure: modeling and simulation," *Plasma Sources Science and Technology*, vol. 31, art. 084009, 2022.

[311] M. J. Goeckner, J. Goree, and T. E. Sheridan, "Measurements of ion velocity and density in the plasma sheath," *Physics of Fluids B*, vol. 4, no. 6, pp. 1663–1670, 1992.

[312] M. Fivaz, S. Brunner, W. Schwarzenbach, A. A. Howling, and C. Hollenstein, "Reconstruction of the time-averaged sheath potential profile in an argon radiofrequency plasma using the ion energy distribution," *Plasma Sources Science and Technology*, vol. 4, no. 3, pp. 373–378, 1995.

[313] T. H. P. Pinto, J. M. R. Kirkbride, and G. A. D. Ritchie, "Broadening the optical bandwidth of quantum cascade lasers using RF noise current perturbations," *Optics Letters*, vol. 43, no. 8, p. 1931, 2018.

[314] L. Ciaffoni, J. Couper, G. Hancock, R. Peverall, P. A. Robbins, and G. A. D. Ritchie, "RF noise induced laser perturbation for improving the performance of non-resonant cavity enhanced absorption spectroscopy," *Optics Express*, vol. 22, no. 14, p. 17030, 2014.

[315] V. Di Sarno, R. Aiello, M. De Rosa, I. Ricciardi, S. Mosca, G. Notariale, P. De Natale, L. Santamaria, and P. Maddaloni, "Lamb-dip spectroscopy of buffer-gas-cooled molecules," *optica*, vol. 6, pp. 436–441, 2019.

[316] R. Aiello, V. Di Sarno, M. G. D. Santi, M. De Rosa, I. Ricciardi, G. Giusfredi, P. De Natale, L. Santamaria, and P. Maddaloni, "Lamb-dip saturated-absorption cavity ring-down rovibrational molecular spectroscopy in the near-infrared," *Photonics Research*, vol. 10, no. 8, p. 1803, 2022.

[317] A. L. Schawlow and C. H. Townes, "Infrared and optical masers," *Physical Review*, vol. 112, no. 6, pp. 1940–1949, 1958.

[318] L. E. Richter, H. I. Mandelberg, M. S. Kruger, and P. A. McGrath, "Linewidth Determination From Self-Heterodyne Measurements With Subcoherence Delay Times.," *IEEE Journal of Quantum Electronics*, vol. QE-22, no. 11, pp. 2070–2074, 1986.

[319] M. P. van Exter, S. J. Kuppens, and J. P. Woerdman, "Excess Phase Noise in Self-Heterodyne Detection," *IEEE Journal of Quantum Electronics*, vol. 28, no. 3, pp. 580–584, 1992.

[320] I. H. Malitson, "Interspecimen Comparison of the Refractive Index of Fused Silica," *Journal of the Optical Society of America*, vol. 55, no. 10, p. 1205, 1965.

[321] A. Lofthus and P. H. Krupenie, "The spectrum of molecular nitrogen," *Journal of Physical and Chemical Reference Data*, vol. 6, no. 1, pp. 113–307, 1977.

[322] B. M. Siller, M. W. Porambo, A. A. Mills, and B. J. McCall, "Noise immune cavity enhanced optical heterodyne velocity modulation spectroscopy," *Optics Express*, vol. 19, pp. 24822–24827, 2011.

[323] P. J. Bruna and F. Grein, "The $X^2\Sigma_g^+$ and $B^2\Sigma_u^+$ states of N_2^+: Hyperfine and nuclear quadrupole coupling constants, electric quadrupole moments, and electron-spin g -factors. A theoretical study," *Journal of Molecular Spectroscopy*, vol. 227, no. 1, pp. 67–80, 2004.

[324] P. J. Bruna and F. Grein, "The A $^2\Pi_u$ state of N_2^+ : Electric properties, fine and hyperfine coupling constants, and magnetic moments (g-factors). A theoretical study," *Journal of Molecular Spectroscopy*, vol. 250, no. 2, pp. 75–85, 2008.

[325] H. Geisen, D. Neuschäfer, and C. Ottinger, "Hyperfine structure of N_2 (B $^3\Pi_g$ and A $^3\Sigma_u^+$) from LIF measurements on a beam of metastable N_2 molecules," *Zeitschrift für Physik D Atoms, Molecules and Clusters*, vol. 4, pp. 263–290, 1987.

[326] D. Forthomme, C. P. McRaven, G. E. Hall, and T. J. Sears, "Hyperfine structures in the v = 1-0 vibrational band of the $B^3\Pi_g$ - $A^3\Sigma_u^+$ of N_2," *Journal of Molecular Spectroscopy*, vol. 282, no. 1, pp. 50–55, 2012.

[327] F. Träger, *Springer Handbook of Lasers and Optics*. Berlin Heidelberg: Springer-Verlag, 2nd ed., 2012.

[328] H. N. R. Saunders and F. A., "New Regularities in the Spectra of the alkaline earths," *Astrophysical Journal*, vol. 61, pp. 38–69, 1925.

[329] A. Yariv, *Optical Electronics in Modern Communications, 5th ed.* New York, Oxford: Oxford University Press, 5th ed., 1997.

[330] S. O'Hagan, T. Pinto, P. Ewart, and G. A. Ritchie, "Multi-mode absorption spectroscopy using a quantum cascade laser for simultaneous detection of NO and H_2O," *Applied Physics B: Lasers and Optics*, vol. 122, no. 8, pp. 1–10, 2016.

[331] F. Duarte, *Tunable Lasers Handbook*. San Diego: Academic Press, 1995.

Part IV

Appendices

Appendix A

The properties of passive optical cavities

A.1 Resonance

This appendix serves to introduce the fundamentals of optical cavities. Fundamentally an optical cavity is a set of mirrors arranged such that radiation inside the cavity is trapped along a recirculating path. Within this path the radiation can exhibit interference, either constructive or destructive depending on the radiation wavelength and the mirror geometry. The simplest optical cavity is linear and coaxial, consisting of two mirrors facing one another; this is the type of cavity used throughout this thesis. In a linear cavity constructive interference occurs when the radiation frequency, ν, and cavity length, L, are related by:[68]

$$\nu = \frac{kc}{2nL} \tag{A.1}$$

where k is a positive integer and n the refractive index of the intracavity medium. When this condition is met the laser and a cavity are said to be in resonance and a *longitudinal mode* of the cavity is excited. It should be noted that this expression is equivalent to the requirement that the cavity round trip distance is an integer number of radiation wavelengths. Additionally, equation A.1 implies that for a given cavity length, as the radiation frequency is scanned it will come into resonance every $(c/(2nL))$ Hz. This difference in frequency between successive resonant modes is referred to as the free spectral range (FSR) of the cavity:[68]

$$\mathrm{FSR} = \frac{c}{2nL}. \tag{A.2}$$

Cavity transmission intensity as a function of radiation frequency is given by the Airy function:[327]

$$\frac{I_{trans}}{I_0} = \frac{1}{1 + \frac{4R}{(1-R)^2}\sin^2(2\pi\nu L)} \tag{A.3}$$

where $\frac{I_{trans}}{I_0}$ is the normalised transmission intensity, R is the (geometric mean) mirror reflectivity and ν is the detuning frequency from an arbitrarily chosen resonance. Figure A.1 demonstrates the form of the Airy function for a range of mirror reflectivities for a caivty geometry where FSR= 0.5 GHz.

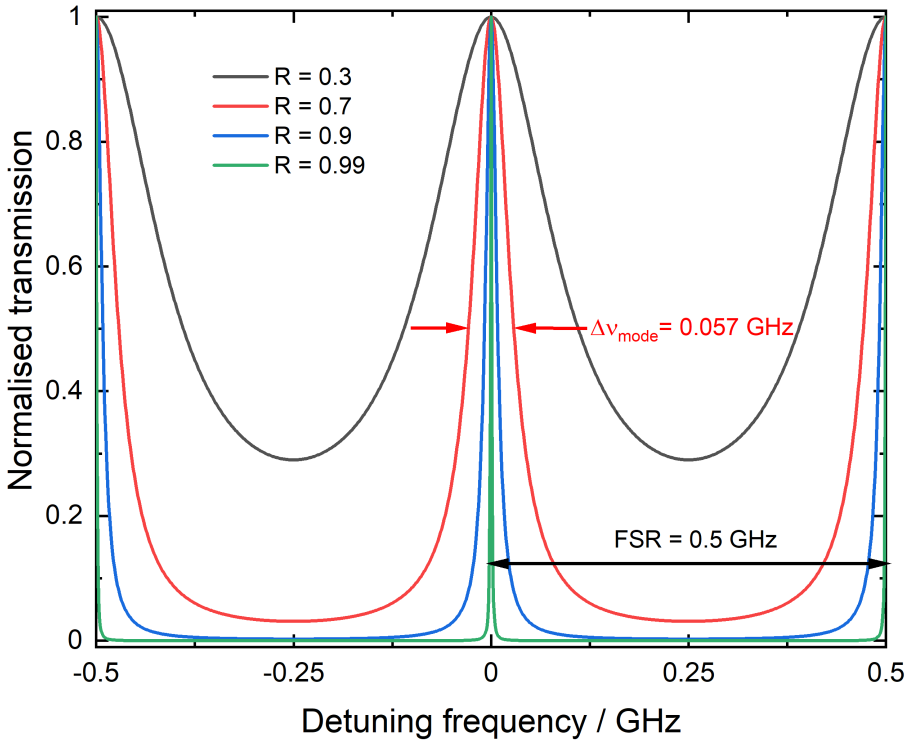

Figure A.1: A series of Airy functions demonstrating the narrowing of cavity transmission as mirror reflectivity increases. All the cavities have a free spectral range of 0.5 GHz.

As the reflectivity of the mirrors from which a cavity is constructed increases, the transmission peaks in the Airy function become more well defined. For low reflectivity cavity mirrors the peaks in transmission intensity as a function of frequency are broad, but for high reflectivity mirrors, only frequencies that match the resonance condition very closely are transmitted because there is a requirement to maintain phase over a much longer distance and the resulting resonances are narrow. One useful quantity

in defining the quality of an optical cavity is the ratio of the FSR to the bandwidth of the resonant modes, $\Delta\nu_{\text{mode}}$. This ratio is referred to as the finesse, $\mathscr{F}$, of the cavity and can be written in terms of the mirror reflectivity, R, as:[68]

$$\mathscr{F} = \frac{\text{FSR}}{\Delta\nu_{\text{mode}}} \approx \frac{\pi\sqrt{R}}{1-R}. \tag{A.4}$$

The longitudinal resonance condition (A.1) dictates which frequencies of radiation can be supported by an optical cavity. This restriction fundamentally arises from the fact that interference is constructive only if the phase of the radiation field is conserved after each round trip of the cavity. What this condition does not account for is the potential for different transverse distributions which give rise to *transverse modes* of the cavity. Within the paraxial ray approximation (*i.e.* assuming that the intracavity laser beam consists of rays that propagate in a direction that is close to parallel with the cavity's optical axis, or alternatively that the intracavity beam is only weakly convergent or divergent) the transverse modes have field distributions that are given by Hermite-Gaussian functions and are labelled TEM_{nm} modes where n and m refer to the number of nodes that exist in the x and y directions respectively.[68] When carrying out cavity enhanced spectroscopic measurements it is often important to be as selective as possible when exciting transverse modes and this will be discussed in more detail later in this chapter when considering mode matching. For now a simple illustration of the lowest order Hermite-Gaussian modes is given in figure A.2.

A.2 Optical stability

In order to trap radiation in an optical cavity (crucial to pathlength increases in spectroscopic applications) it is insufficient to simply arrange any two mirrors opposite one another. One must also consider the optical stability of the cavity, in other words, whether the mirrors have radii of curvature and separation conducive to supporting cavity modes. For clarity, one obvious example of an unstable cavity is one constructed from two convex mirrors, in this case the spot size of a Gaussian beam within the cavity becomes bigger and bigger with each round trip and quickly intensity spills over the edge of the cavity mirrors and the radiation is no longer effectively trapped.

The mirror g-parameters, g_i, are useful in quantifying if a given cavity geometry will be stable and are defined for mirror i, with mirror radius of curvature, R_i, forming

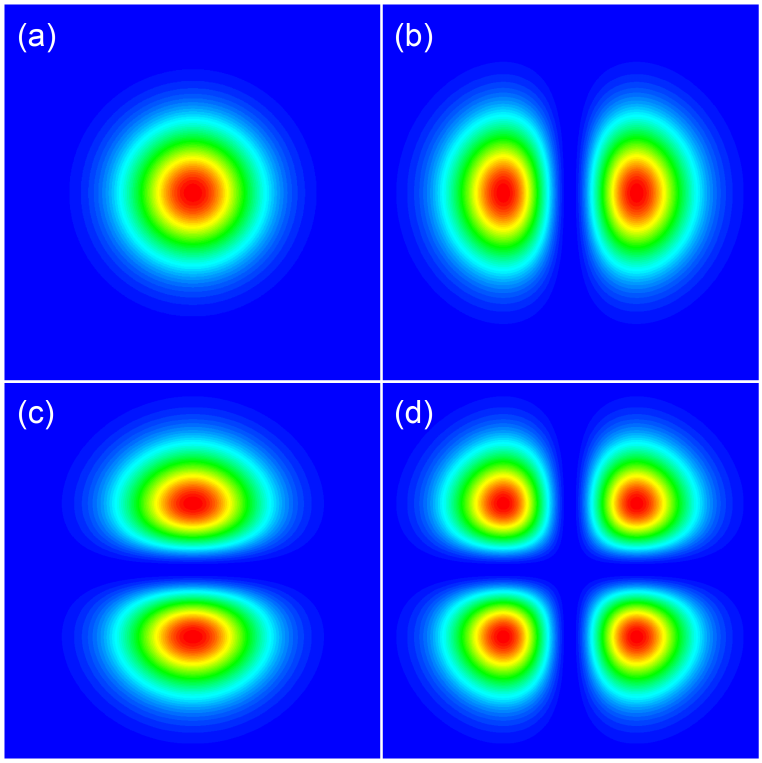

Figure A.2: Intensity distributions of the (a) TEM_{00} transverse mode, (b) TEM_{10} transverse mode, (c) TEM_{01} transverse mode and (d) TEM_{11} transverse mode.

a linear cavity with length, L, as:[68]

$$g_i = 1 - \left(\frac{L}{R_i}\right). \tag{A.5}$$

Using the g-parameters for the two mirrors in a linear cavity allows the stability condition to be expressed as:[68]

$$0 < g_1 g_2 < 1. \tag{A.6}$$

An expression which is most easily satisfied by selecting two concave mirrors ($R > 0$) and arranging them such that $L < R$.

A.3 The intracavity beam shape

When a cavity is formed from concave mirrors the radius of curvature, r, and spot size, w, of the intracavity beam varies as a function of position within the cavity (where the spot size is defined as the distance from the beam centre at which the intensity drops to $1/e^2$ of its maximum value). Note that the radius of curvature of the beam (which varies spatially) is denoted with a lowercase r to distinguish it from

the mirror radii of curvature R which are fixed. At the centre of a symmetrical cavity ($g_1 = g_2 \equiv g$) the radius of curvature for the TEM_{00} mode is infinite and the spot size, w_0 (which, at the cavity focus, is also called the beam waist), can be found from:

$$w_0^2 = \frac{L\lambda}{\pi}\sqrt{\frac{1+g}{4(1-g)}}, \tag{A.7}$$

Where λ is the wavelength of the radiation. Meanwhile, at the cavity mirrors the radius of curvature of the mode is the same as the radius of curvature of the mirrors and the spot size, w_1 is given by

$$w_1^2 = \frac{L\lambda}{\pi}\sqrt{\frac{1}{(1-g^2)}} \tag{A.8}$$

More generally the change in w and r as a Gaussian beam propagates (through space or through optical elements) can be calculated by first defining the complex beam parameter, q, given by:

$$\frac{1}{q} = \frac{1}{r} - \frac{\lambda}{\pi w^2}i, \tag{A.9}$$

and also defining an ABCD transformation matrix for the given optical element through which the beam propagates (in an alternative formulation the beam parameter can be expressed as a vector which can be linearly transformed by this matrix to find the new beam parameter after propagation). As an example, for propagation through free space by a distance x the ABCD matrix is given by:

$$\begin{pmatrix} A & B \\ C & D \end{pmatrix} = \begin{pmatrix} 1 & x \\ 0 & 1 \end{pmatrix} \tag{A.10}$$

The beam parameter after the propagation, q_1, is then related to the beam parameter before the propagation, q_0, according to the so called ABCD law:

$$q_1 = \frac{Aq_0 + B}{Cq_0 + D}. \tag{A.11}$$

If the beam propagates through several optical elements the transformation matrices for these elements can be multiplied in turn to find the total transformation matrix then the ABCD law can be applied (the matrix corresponding to the first optical element through which the beam propagated should appear on the right of the matrix product). For example if the beam passes through element 1 followed by element 2 the total matrix would be given by

$$\begin{pmatrix} A_{tot} & B_{tot} \\ C_{tot} & D_{tot} \end{pmatrix} = \begin{pmatrix} A_2 & B_2 \\ C_2 & D_2 \end{pmatrix}\begin{pmatrix} A_1 & B_1 \\ C_1 & D_1 \end{pmatrix} \tag{A.12}$$

Appendix B

Atomic and molecular terms and Hund's cases

B.1 Atomic terms

Electrons associated with atoms can be thought of as existing in atomic orbitals. A given arrangement of electrons within these orbitals is referred to as a configuration and the energy levels that arise from this configuration depend on the coupling of electronic orbital and spin angular momenta belonging to the electrons. In particular it is electrons that exist outside of filled subshells that determine the energy levels (those in filled subshells have no net angular momentum). These electrons each have an orbital angular momentum (quantised by the *orbital angular momentum quantum number* l) and a spin angular momentum (quantised by the *spin angular momentum quantum number* s). The most appropriate coupling scheme for light atoms (*i.e.* in the first row of the periodic table) is that of Russell-Saunders coupling[328]. Suppose there were only 2 electrons outside of closed subshells, within the Russell-Saunders scheme the orbital angular momenta of these two electrons couple strongly together as do their spin angular momenta to form a total orbital angular momentum, **L**, with quantum number $L = l_1 + l_2, l_1 + l_2 - 1, ...|l_1 - l_2|$ and a total spin angular momentum, **S** with quantum number $S = s_1 + s_2, s_1 + s_2 - 1, ...|s_1 - s_2|$. These two angular momenta then couple more weakly (via spin-orbit coupling) to form the total angular momentum, **J**, with quantum number $J = L + S, L + S - 1, ...|L - S|$. The levels that arise are then denoted by a atomic term symbol ${}^{2S+1}L$ or level symbol ${}^{2S+1}L_J$, where $L = 0, 1, 2...$ are given the labels S, P, D... respectively.

B.2 Molecular terms

Similar to the atomic case, electrons in molecules can be thought of as existing in molecular orbitals and a given configuration can lead to several terms of different energy. Molecular term symbols for diatomic molecules are similar to those for atoms with the form: ${}^{2S+1}|\Lambda|^{+/-}_{g/u}$ where S is again the total spin angular momentum quantum number, Λ is the quantum number for the projection of the orbital angular momentum on the internuclear axis (the projection being given by $|\Lambda|\hbar$), g/u refers to the inversion symmetry of the electronic wavefunction (if the molecule is centrosymmetric) and $+/-$ refers to its symmetry with respect to reflection in a plane containing the internuclear axis.[78]. $|\Lambda| = 0, 1, 2...$ are labelled $\Sigma, \Pi, \Delta...$ respectively.

B.3 Hund's cases (a) and (b)

Only two of Hund's cases need concern us here, the cases (a) and (b). Vector diagrams of Hund's coupling cases (a) and (b) are shown in figure B.1.

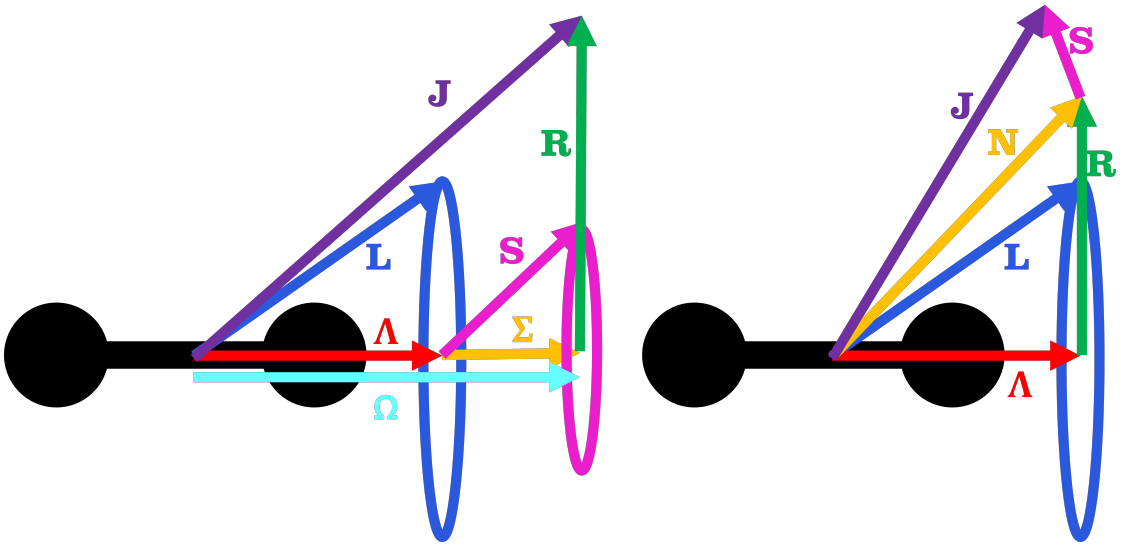

Figure B.1: The relationships between the various angular momenta in Hund's cases (a) (on the left) and (b) (on the right).

In Hund's case (a) the electronic orbital angular momentum **L** is strongly electrostatically coupled to the internuclear axis such that the projection of this angular momentum on the internuclear axis, **Λ**, is defined by the good quantum number Λ.

The electronic spin angular momentum $\mathbf{S}$ also couples strongly to the internuclear axis thus defining the spin projection $\mathbf{\Sigma}$ with quantum number Σ (not to be confused with Σ electronic terms). These two projections then couple (by spin-orbit coupling) to one another to form the total electronic angular momentum projection $\mathbf{\Omega} = \mathbf{\Lambda} + \mathbf{\Sigma}$ with quantum number $\Omega = ||\Lambda| + \Sigma|, ||\Lambda| + \Sigma - 1|, ..., ||\Lambda| - \Sigma|$. Finally the total electronic angular momentum couples weakly to the angular momentum arising from molecular rotation, $\mathbf{R}$ to give the total angular momentum $\mathbf{J} = \mathbf{\Omega} + \mathbf{R}$ ($J = \Omega, \Omega + 1, \Omega + 2, ...$). For Hund's case (a) coupling the rotational states can be arranged in groups according to their Ω value (see for example the upper states in figures 2.10 and 2.11). By convention these groups are labelled sequentially, with the lowest in energy labelled F_1, the next F_2 and so on, the energy ordering that arises in any specific case depends on the sign of the spin-orbit coupling constants.

Hund's case (b) differs from case (a) in that the electronic spin angular momentum is not strongly coupled to the internuclear axis or to the electronic orbital angular momentum (thus $\mathbf{\Sigma}$ and $\mathbf{\Omega}$ are not well defined). The electronic orbital angular momentum projection $\mathbf{\Lambda}$ therefore couples most strongly to the rotational angular momentum $\mathbf{R}$ to give the total angular momentum excluding spin $\mathbf{N} = \mathbf{\Lambda} + \mathbf{R}$ ($N = |\Lambda|, |\Lambda|+1, ...$). Finally the weak coupling between $\mathbf{N}$ and the spin angular momentum $\mathbf{S}$ gives the total angular momentum $\mathbf{J} = \mathbf{N} + \mathbf{S}$ with quantum number $J = N + S, N + S - 1, ..., |N - S|$. In Hund's case (b) the levels with the maximum value of J for a given N, (*i.e.* $J = N + S$) are labelled F_1, the next highest ($J = N + S - 1$) labelled F_2 and so on. It should be noted that if the spin angular momentum $\mathbf{S} = \mathbf{0}$ then Hund's cases (a) and (b) become equivalent.

In addition to being labelled with their quantum numbers and F_i labels, the rotational energy levels associated with each electronic state are also assigned symmetry labels ($\oplus$, $\ominus$, s and a). The $\oplus$ and $\ominus$ symmetry labels refer to the parity of the total spatial wavefunction, this is simply a combination of the $+/-$ symmetry of the electronic term symbol and the parity of the rotational wavefunction (symmetric for even R and asymmetric for odd R). For a diatomic molecule the vibrational wavefunction always has even parity so it doesn't change the overall parity of the wavefunction. By way of an example: the electronic wavefunction of $O_2(X^3\Sigma_g^-)$ has $-$ symmetry so that its even R states are overall $\ominus$ and its odd R states are overall $\oplus$. Conversely the $O_2(b^1\Sigma_g^+)$ state has $+$ symmetry so its even R states are $\oplus$ and its odd R states are $\ominus$. The s and a symmetry labels refer to the symmetry of the total spatial wavefunction with respect to exchanging the identical nuclei (s being symmetric and a antisymmetric). This label can be deduced from the $\oplus/\ominus$ symmetry of the rotational

level and the g/u symmetry of the electronic state. If the state is g then $\oplus$ levels are s and $\ominus$ levels are a, whereas if the state is u then $\oplus$ levels are a and $\ominus$ levels are s[78].

Appendix C

Experimental optical hardware

C.1 Lasers

In order to observe many of the phenomena described in chapter 2 (for example line broadening, cavity modes and Lamb dips) it is highly desirable to have a narrow linewidth, tunable light source. Provided the linewidth of the source is significantly smaller than the width of the spectral feature begin probed (be it an absorption or a Lamb dip or something else) then the source can thought of as effectively monochromatic and the line profile is dependent only on the factors already discussed. Over the past several decades lasers have emerged as the ideal tool for producing narrow linewidth radiation and many lasers also provide some ability to tune the wavelength in a continuous fashion.

Many of the species of interest in both oxygen and nitrogen plasmas only have allowed transitions in the vacuum ultraviolet (VUV). VUV radiation is very hard to handle (it is absorbed by air) and difficult to produce. In terms of VUV lasers, the only options suitable for use in a normal laboratory are excimer lasers which produce only a very limited number of wavelengths and are not widely or easily tunable. Free electron lasers (FELs) can produce tunable VUV radiation but FEL facilities are expensive to establish and their are only a few facilities worldwide. Other VUV sources (lamps or synchrotrons) produce broadband radiation and this makes analysis of resulting spectra difficult (see specific examples in later chapters).

Much more well developed are lasers in the visible ($400-750$nm) and near infrared ($750-2000$nm), in particular lasers with wavelengths in the so called 'telecommunications window' ($1310-1550$nm) are mass produced for industrial use in electronics and sensors as well as telecommunications. Lasers at these wavelengths are relatively cheap as well as being robust, reliable and compact. Additionally many of the plasma bourne species in the plasmas discussed in this thesis have forbidden transitions that

are accessible with such lasers. In combination with cavity enhanced spectroscopic techniques it becomes possible to probe these species whilst taking advantage of the availability and tunability of the most well developed laser technology.

Diodes

Fundamentally a laser requires a material in which a population inversion can be produced (i.e. pumping can be achieved such that the upper state of some transition has a greater population than the lower state) so that the rate of stimulated emission is greater than that of absorption and any resonant photons entering this so called *gain medium* are amplified rather than being absorbed.

One way of producing such a gain medium that has been widely utilised in commercial lasers is by joining together a p-doped semiconductor and an n-doped semiconductor. A device with such a junction is called a diode[329] and by applying a forward bias voltage diodes can be made to produce light due to electron-hole recombination that occurs because of the resulting population inversion at the p-n junction, indeed light emitting diodes (LEDs) have become ubiquitous in everyday life. Even more usefully, by tuning the materials and dopants used in the two semiconductors and thus altering the bandgap a range of wavelengths can be produced using diodes. The band diagram of an unbiased and a forward biased diode are shown in figure C.1 (a) and (b) respectively.

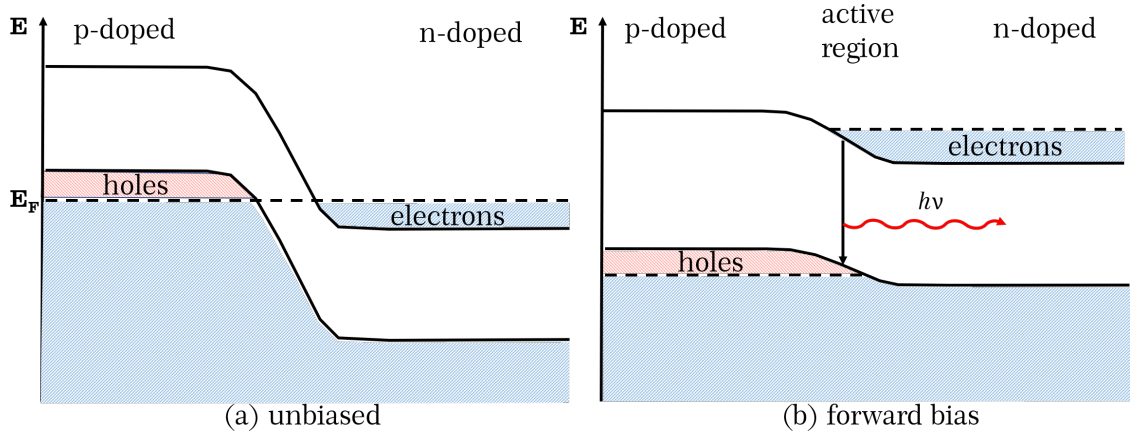

Figure C.1: (a) A band diagram showing the junction between a p-doped semiconductor (with additional holes near the valence band) and an n-doped semiconductor (with additional filled levels near the conduction band) forming a diode. (b) A schematic of how biasing a diode can cause light emission by electron-hole recombination creating an LED.

Making a diode into a laser

Radiation produced by diodes is not coherent, nor is it narrow linewidth (i.e. A diode alone is not a laser). In order to make a diode laser some form of wavelength selective feedback is required. The simplest way of achieving such feedback is by coating one end facet of the diode chip with a high reflectivity (HR) coating and the other end with a partially reflective (PR) coating (to allow some light to leave the diode). These coatings then form a low finesse optical cavity (a Fabry-Perot resonator). A schematic of a Farby-Perot diode laser is shown in figure C.2(a) Wavelengths of light corresponding to resonant cavity modes are amplified by stimulated emission as they pass repeatedly through the gain medium whilst other wavelengths are suppressed by destructive interference. Fabry-Perot diode lasers are relatively simple but they have some disadvantages. Even when short resonators are used (with large FSR) it is sometimes the case that the diode emits light that is resonant with several longitudinal modes of the resonator. If this is the case the laser may produce several frequencies of light simultaneously (each frequency separated from the next by the FSR of the resonator) and this multimode operation is generally undesirable for precision spectroscopy (although it can be utilised to probe several transitions simultaneously, for example in multi-mode absorption spectroscopy (MUMAS)[330]). When single mode operation can be achieved Fabry-Perot lasers' frequency can be tuned by adjusting the refractive index of the semiconductors and hence changing the resonance frequency within the cavity according to equation A.1. This can be achieved by tuning the chip temperature, which also changes the cavity length and the bandgap (i.e the gain curve) of the diode by changing the lattice parameter. The wavelength may also be tuned by changing the current applied to the laser chip, this changes the density of electrons and holes within the bands which in turn alters the refractive index.

Despite this tunability, Fabry-Perot lasers show a propensity to hop between resonator modes and this mode hoping means that not all frequencies within the gain curve of the diode are accessible (because the large FSR means modes are well separated in frequency). Finally, the bandwidth of the optical cavity, $\Delta\nu_{cav}$ defines the linewidth of the laser $\Delta\nu_{las}$ according to the Schawlow–Townes equation.[329] The important result of this equation is that

$$\Delta\nu_{las} \propto (\Delta\nu_{cav})^2 \propto \frac{1}{L^2} \tag{C.1}$$

where L is the cavity length. Thus the short cavities used in Fabry-Perot lasers lead to large laser linewidths (typically of the order of 100 MHz). This means that Fabry-Perot lasers are limited in their ability to probe fine details of absorption profiles (such as Lamb dips).

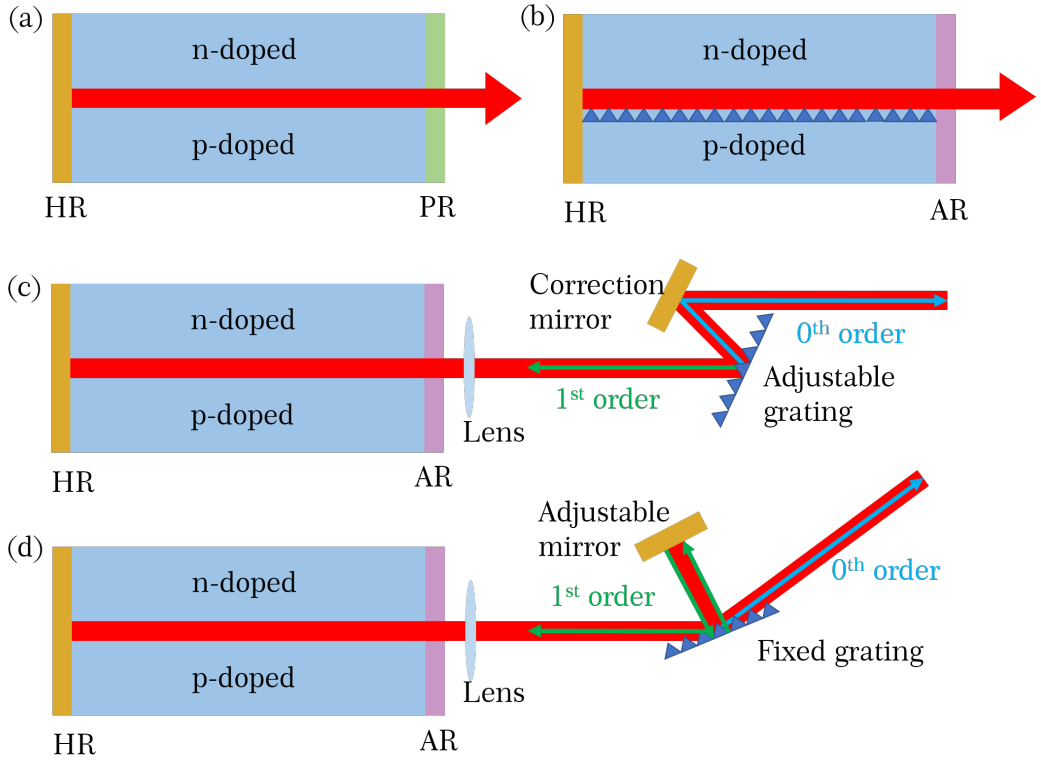

Figure C.2: Diagrams illustrating how an LED can be turned into a laser by addition of (wavelength selective) feedback optics. (a) a Fabry-Perot arrangement, (b) a ditributed feedback (DFB) arrangement, (c) an external cavity diode laser (ECDL) in the Littrow configuration and (d) an ECDL in the Littman-Metcalf configuration.

Several more sophisticated feedback mechanisms exist that allow for continuous tunability and narrower linewidths. The two types of diode laser utilised in this work are distributed feedback (DFB) and external cavity diode lasers (ECDL).

Distributed feedback (DFB) diode lasers

Within a DFB diode laser chip the back facet is high reflectivity (HR) coated (as in a Fabry-Perot device) whilst the front facet of the chip is anti-reflection (AR) coated, allowing light to pass through. The wavelength selective feedback is provided by a

periodic structuring of the gain medium. This periodic structure acts as a Bragg reflector selectively reflecting a single wavelength of radiation and suppressing all others due to destructive interference. A schematic view of a DFB diode laser is shown in figure C.2(b) with the distributed Bragg reflector represented by the blue triangles. The wavelength selectivity of the laser is defined by the spacing of the Bragg grating and hence if precise grating spacings can be achieved then extremely good wavelength selectivity is possible. DFB diode lasers routinely achieve linewidths of the order of $1 - 10$ MHz in the near infrared. These laser can also be tuned by adjusting the diode refractive index either by adjusting temperature or current with single mode scanning of several hundred GHz possible in the near infrared.

External cavity diode lasers (ECDLs)

An external cavity diode laser (ECDL) utilises an optical cavity that is much larger than the chip itself. This is done by HR coating one end of the chip and AR coating the other (as in a DFB laser). Wavelength selective feedback is then provided by a diffraction grating which is mounted typically several centimeters from the AR coated front facet of the chip.[329] Two configurations of ECDL are frequently employed: the Littrow configuration and the Littman-Metcalf configuration.[331] In the former (shown in figure C.2(c)) the first order diffracted beam provides feedback directly into the diode whilst the zeroth order beam is the output of the laser, by finely adjusting the grating (typically with a piezoelectric transducer) the wavelength that is fed back to the laser can be tuned. In the latter configuration (figure C.2(d)) the zeroth order beam again forms the output whilst the first order beam is reflected off an additional mirror before being fed back to the diode by the grating, in this arrangement the additional mirror is adjusted to tune the laser. The Littman-Metcalf configuration offers an advantage because wavelength tuning doesn't change the path of the output beam unlike the basic Littrow arrangement. Meanwhile the Littrow arrangement is capable of producing greater laser powers and with the addition of a correction mirror can also achieve wavelength tuning without beam path alterations. Both arrangements offer similar levels of performance with a single laser able to cover $> 10,000$ GHz (with mode hop free scanning over 10's GHz) and narrow linewidths of $10 - 100$ kHz made possible by the much larger cavity length in these lasers (equation C.1).

C.2 Detectors

Two types of photon detectors are used in the work in this thesis. At wavelengths < 1000 nm a photomultiplier tube (PMT) is used. Photomultipliers consist of a photocathode which emits a photoelectron when an incident photon has energy greater than its workfunction. This photoelectron is directed by a focusing electrode onto a dynode and causes the emission of several secondary electrons which are accelerated onto a second dynode (held at a higher potential) and begin an avalanche of electrons across many dynodes of increasing potential. Eventually the initial photoelectron is multiplied by a factor of $\approx 10^8$ and this large number of electrons lead a current spike at the PMT anode.[329] This multiplication of signal makes PMT detector extremely sensitive (capable of single photon detection) and therefore ideal for CRDS studies (where high reflectivity mirrors mean that, even for large intracavity intensities, the photon flux at the detector can be small).

It is difficult to produce a photocathode materials that produce photoelectrons at wavelengths longer than ≈ 1700 nm. At these wavelengths therefore an alternative type of detector is required. Photodiodes are a well established technology for light detection, they effectively work in the same way as LED's but in reverse. An incident photon excites an electron across the band gap into the conduction band, the electron then drifts towards the n-doped semiconductor (which has a lower energy conduction band) and this flow of electrons can be measured as a current.[329] The most common photodiode detectors are those based on Si which operate between ≈ 400 nm and ≈ 1100 nm and those based on InGaAs which typically operate between ≈ 900 nm and ≈ 1700 nm but can be extended (for example by tuning the relative abundance of In and Ga and altering the method of layer deposition used in diode construction) to 2500 nm.

C.3 Acousto-optic modulators (AOMs)

Acousto-optic modulators (or AOMs) are used several times throughout the experiments in this thesis, first as an optical switch in cavity ringdown spectroscopy and later as a frequency shifter for self heterodyne beatnote experiments designed to measure laser linewidth. It is therefore pertinent to introduce them briefly here. An AOM consists of an acousto-optic crystal (here TeO_2) attached to a piezoelectric transducer which is supplied with a high frequency oscillating voltage (200 MHZ in these experiments). The rapid oscillation of the piezo creates ultrasonic waves in the crystal,

these waves are associated with wavefronts of compression in the material. When an acousto-optic material is compressed it's local refractive index changes and thus the acoustic waves establish what is effectively a diffraction grating within the material.[68] This grating effects a laser beam passing through the AOM crystal in two ways. First it produces several beams of different diffraction orders. The first order beam is then used in CRDS experiments and can be rapidly extinguished by switching off the AOM piezo, thus allowing ringdown events to be observed. Secondly, because the sound waves in the crystal are propagating through it, the diffracted beams take on a Doppler shift, thus for a 200 MHz AOM the zeroth order beam will remain at its incident frequency, ν/MHz, whilst the first order diffracted beams will be frequency shifted to $(\nu + 200)$/MHz. This is utilised in the beat note experiments as will be detailed later in this thesis. These two effects are shown in figure C.3 which depicts an AOM schematically.

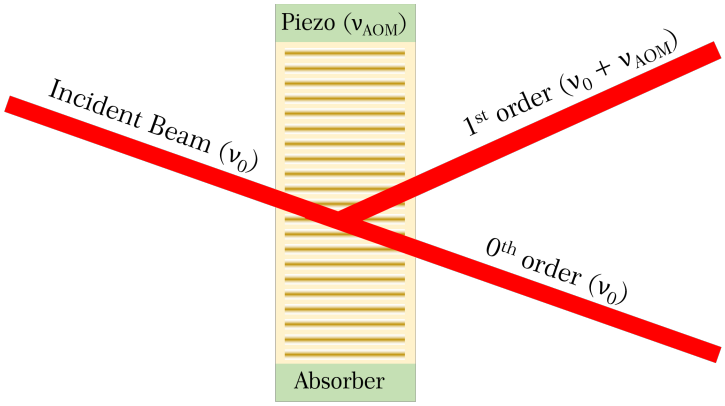

Figure C.3: A schematic of an acousto-optic modulator (AOM) showing both the splitting of the input beam by diffraction and the frequency shifting of the diffracted beam by the AOM frequency.

Appendix D

Lists of transitions and lasers

Table D.1: Transitions probed in this thesis, assignments are explained in the previous appendices and chapter 2. The laser number refers to the values in table D.2.

Electronic	Vibrational	Rotational	Wavenumber / cm^{-1}	Laser number
$O(^1D_2) \leftarrow O(^3P_2)$	N/A	N/A	15867.862	#1
$O(^1D_2) \leftarrow O(^3P_1)$	N/A	N/A	15718.597	#1
$O_2(b^1\Sigma_g^+) \leftarrow O_2(a^1\Delta_g)$	(0, 0)	$Q(4)$	5237.962	#2
$O_2(b^1\Sigma_g^+) \leftarrow O_2(a^1\Delta_g)$	(0, 0)	$Q(6)$	5237.378	#2
$O_2(b^1\Sigma_g^+) \leftarrow O_2(a^1\Delta_g)$	(0, 0)	$Q(10)$	5235.570	#2
$O_2(b^1\Sigma_g^+) \leftarrow O_2(a^1\Delta_g)$	(0, 0)	$Q(12)$	5234.345	#2
$O_2(b^1\Sigma_g^+) \leftarrow O_2(X^3\Sigma_g^-)$	(0, 0)	${}^pP_{12}(1)$	13118.045	#3
$O_2(b^1\Sigma_g^+) \leftarrow O_2(X^3\Sigma_g^-)$	(0, 0)	${}^rQ_{11}(18)$	13158.744	#3
$O_2(b^1\Sigma_g^+) \leftarrow O_2(X^3\Sigma_g^-)$	(0, 0)	${}^rR_{12}(19)$	13158.679	#3
$O_2(b^1\Sigma_g^+) \leftarrow O_2(X^3\Sigma_g^-)$	(0, 0)	${}^rQ_{11}(28)$	13165.166	#3
$O_2(b^1\Sigma_g^+) \leftarrow O_2(X^3\Sigma_g^-)$	(0, 0)	${}^rQ_{11}(30)$	13165.249	#3
$O_2(b^1\Sigma_g^+) \leftarrow O_2(X^3\Sigma_g^-)$	(0, 0)	${}^pP_{12}(31)$	12988.723	#3
$O_2(b^1\Sigma_g^+) \leftarrow O_2(X^3\Sigma_g^-)$	(1, 1)	${}^rR_{12}(7)$	12988.480	#3
$O_2(b^1\Sigma_g^+) \leftarrow O_2(X^3\Sigma_g^-)$	(1, 1)	${}^rQ_{11}(16)$	13003.448	#3
$O_2(b^1\Sigma_g^+) \leftarrow O_2(X^3\Sigma_g^-)$	(1, 1)	${}^rR_{12}(17)$	13003.548	#3
$O_2(b^1\Sigma_g^+) \leftarrow O_2(X^3\Sigma_g^-)$	(1, 1)	${}^rQ_{11}(22)$	13008.894	#3
$N_2^+(A^2\Pi_u) \leftarrow N_2^+(X^2\Sigma_g^+)$	(2, 0)	$P_{22}(7.5)$	12716.722	#3
$N_2^+(A^2\Pi_u) \leftarrow N_2^+(X^2\Sigma_g^+)$	(2, 0)	$P_{22}(11.5)$	12679.979	#3
$N_2^+(A^2\Pi_u) \leftarrow N_2^+(X^2\Sigma_g^+)$	(2, 0)	$Q_{22}(7.5)$	12742.673	#3
$N_2^+(A^2\Pi_u) \leftarrow N_2^+(X^2\Sigma_g^+)$	(2, 0)	$Q_{22}(11.5)$	12719.712	#3
$N_2(B^3\Pi_g) \leftarrow N_2(A^3\Sigma_u^+)$	(7, 6)	$Q_{11}(16)$	12721.942	#3
$N_2(B^3\Pi_g) \leftarrow N_2(A^3\Sigma_u^+)$	(2, 0)	$R_{33}(14)$	13029.829	#3
$N_2(B^3\Pi_g) \leftarrow N_2(A^3\Sigma_u^+)$	(2, 0)	$Q_{22}(15)$	12969.272	#3

Table D.2: Details of the lasers used in this thesis.

Laser number	Make	Model	ID number	Operating range / cm^{-1}
#1	Toptica	DL100	LD-0633-0100-1	15711 – 15898
#2	Eblana	EP1909	DXT0250	5233 – 5244
#3	Toptica	DLPro	LD-0780-0100-AR-1	12625 – 13376